Transonic Aeroelastic Instability Searches Using a Hierarchy of Aerodynamic Models

Thesis submitted in accordance with the requirements of
the University of Liverpool for the degree of Doctor in Philosophy
by
Sebastian Timme (Dipl.–Ing.)

June 2010

Abstract

The use of a hierarchy of high fidelity computational fluid dynamics models in routine aircraft aeroelastic stability analyses is investigated. An instability of the time–linearised aeroelastic system is predicted by a small nonlinear eigenvalue problem, with the normal mode structural problem corrected by an interaction matrix to represent the flow response which is simulated by different nonlinear aerodynamic models. These are given by the full potential, Euler, and Reynolds–averaged Navier–Stokes equations. The task of searching for aeroelastic instability over a flight envelope, which is a multidimensional parameter space, is accomplished by introducing searches for the approximation of the interaction matrix. This matrix is approximated by reconstruction based on true samples which are computed in the frequency or time domain. For the task of reconstruction, kriging interpolation is discussed.

The kriging approach is derived and thoroughly investigated for two structural models describing the dynamics of two degrees–of–freedom aerofoil cases and realistic aircraft structures. It is demonstrated that the results from the approximation are in excellent agreement with the predictions of the exact full order eigenvalue solver for the stability analysis over the whole flight envelope. First, the stability results of the NACA 0012 aerofoil case are compared for all considered flow models discussing the influence of physical effects and numerical discretisation. Secondly, the kriging formulation for the symmetric Goland wing cases with and without tip store is shown to be equivalent to the aerofoil formulation with only minor modifications. Thirdly, the MDO wing case, fully accounting for the effects of aerostatic deformation, requires an expanded parameter space for the instability search including the response frequency, freestream Mach number and altitude.

To search the flight envelope, while assuming little prior knowledge of the stability behaviour, several sampling techniques are considered for the aerofoil cases. Risk–based sampling is found to be efficient in detecting the instability points accurately in multidimensional parameter spaces. This is then shown for the aerostatically deformed MDO wing using a four dimensional search space adding the freestream angle of attack. Finally, the stability analysis based on flow models of variable fidelity is demonstrated for the NACA 0012 aerofoil case and the Goland wing/store configuration using both an augmented set of samples and co–kriging for the task of reconstruction.

Acknowledgements

I would like to acknowledge my supervisors Professor K. J. Badcock and Professor J. E. Mottershead. I would also like to extend my thanks to Professor G. N. Barakos for his generous support and all the colleagues, both past and present, in the Computational Fluid Dynamics Laboratory at the University of Liverpool for fruitful discussions and for creating a stimulating working environment over the past three years.

I particularly wish to thank Professor K. J. Badcock without whom I would certainly have been lost. His encouragement and ideas were of utmost help to this work and are very much appreciated.

Last, but not least, my friends and family, near and far, shall not be forgotten for their support and patience.

This research forms part of the programme of the Marie Curie Excellence Team "Ecerta" financially supported by the European Union under contract MEXT–CT–2006–042383.

Declaration

I confirm that the thesis is my own work, that I have not presented anyone else's work as my own and that full and appropriate acknowledgement has been given where reference has been made to the work of others.

Sebastian Timme
June 2010

List of Publications

Timme, S., Marques, S. and Badcock, K. J., "Transonic Aeroelastic Stability Analysis Using a Kriging–Based Schur Complement Formulation," Submitted to the AIAA Journal.

Timme, S., Marques, S. and Badcock, K. J., "Transonic Aeroelastic Stability Analysis Using a Kriging–Based Schur Complement Formulation," *AIAA Paper 2010-8228*, Presented at the AIAA Atmospheric Flight Mechanics Conference, Toronto, Canada, 2010.

Timme, S., Rampurawala, A. and Badcock, K. J., "Applying Interpolation Techniques to Search for Transonic Aeroelastic Instability: ANN vs Kriging," Presented at the RAeS Aerodynamics Conference 2010, Bristol, United Kindom, 2010.

Timme, S. and Badcock, K. J., "Searching for Transonic Aeroelastic Instability Using an Aerodynamic Model Hierarchy," Submitted to the AIAA Journal.

Timme, S. and Badcock, K. J., "Searching for Transonic Aeroelastic Instability Using an Aerodynamic Model Hierarchy," *AIAA Paper 2010-3048*, Presented at the 51st AIAA/ASME/ASCE/AHS/ASC Structures, Structural Dynamics, and Materials Conference, Orlando, FL, 2010.

Badcock, K. J., Timme, S. and Marques, S., "Implementing the Schur Complement Eigenvalue Formulation in the DLR TAU Code," Tech. Rep., Computational Fluid Dynamics Laboratory, University of Liverpool, Liverpool, United Kingdom, 2010.

Timme, S. and Badcock, K. J., "oFPfoil (v1.0) – User Guide," Tech. Rep., Computational Fluid Dynamics Laboratory, University of Liverpool, Liverpool, United Kingdom, 2010, available at http://cfd4aircraft.com/4downloads.php.

Timme, S. and Badcock, K. J., "Oscillatory Behavior of Transonic Aeroelastic Instability Boundaries," *AIAA Journal*, Vol. 47, No. 6, 2009, pp. 1590–1592.

Timme, S. and Badcock, K. J., "Aeroelasticity based on Bifurcation Theory," Proceedings of the 5th European Congress on Computational Methods in Applied Sciences and Engineering (ECCOMAS 2008), Venice, Italy, 2008.

Table of Contents

List of Figures

List of Tables

List of Symbols

A	=	Jacobian matrix ($= \partial \boldsymbol{R}/\partial \boldsymbol{w}$)
a	=	speed of sound
a_1, a_2	=	constants in boundary layer model
$\widehat{a}$	=	amplitude of forced sinusoidal motion
B	=	matrix of unsteady terms in boundary layer model
C_1, C_2, C_3	=	matrices in approximation model ($A_{ss} = C_1 + \vartheta C_2$ and $A_{sf} = \vartheta C_3$)
C_D	=	dissipation coefficient
C_f	=	skin friction coefficient
C_l, C_m	=	coefficients of lift and pitching moment
C_p	=	pressure coefficient
C_τ	=	shear–stress coefficient
$\boldsymbol{c}$	=	real–valued constant vector
c_p, c_v	=	coefficients of specific heat
D, E	=	matrices in structural state–space model
$\mathcal{D}$	=	dissipation integral
E_P, E_K	=	potential and kinetic energy
e_t	=	specific total energy
$\boldsymbol{F}^i$, $\boldsymbol{F}^v$	=	inviscid and viscous fluxes
F	=	regression matrix in kriging model
$\boldsymbol{f}$	=	vector of aerodynamic forces
$\boldsymbol{f}$	=	vector of basis functions in kriging model
f	=	frequency ($= 1/T$)
f_{v1}	=	near wall damping function in Spalart–Allmaras turbulence model
H	=	boundary layer shape parameter
H_k	=	boundary layer kinematic shape parameter
H^*	=	boundary layer kinetic energy shape parameter
H^{**}	=	boundary layer density thickness shape parameter
H_{θ_ρ}	=	boundary layer auxiliary density shape factor
$\boldsymbol{h}$	=	heat–flux vector
h_r	=	altitude

h	=	specific enthalpy
h, $\dot{h}$	=	plunge and plunge rate
I	=	identity matrix
i	=	imaginary unit ($= \sqrt{-1}$)
K	=	number of terms in truncated exponential Fourier series
K_c	=	constant in boundary layer model
k	=	reduced frequency
k	=	turbulence kinetic energy
L	=	Lagrangian ($= E_K - E_P$)
L	=	dissipation length
$\boldsymbol{l}$	=	arbitrary closed curve
l_{mix}	=	mixing length
M, C, K	=	matrices of mass, damping and stiffness
M_e, M_r	=	local edge Mach number and freestream Mach number
$\mathcal{N}$	=	normal distribution
$\boldsymbol{n}$	=	unit normal vector
n	=	real time level
n	=	number of unknowns or normal modes
n	=	number of samples in kriging model
$\boldsymbol{P}$	=	pseudo residual vector
$\mathcal{P}$, $\mathcal{D}$, $\mathcal{W}$, $\mathcal{C}$	=	operators of production, diffusion, dissipation and cross–diffusion
Pr, Pr_t	=	Prandtl number and turbulent Prandtl number
$\boldsymbol{p}$	=	eigenvector
$\boldsymbol{p}$	=	vector of smoothness parameters in kriging model
p	=	pressure
Q	=	matrix of aerodynamic influence coefficients ($= Q_1 + \lambda Q_2$)
$\mathcal{Q}$	=	operator of velocity gradient in boundary layer model
$\boldsymbol{q}$	=	vector of Cartesian velocity components
q	=	magnitude of velocity vector
$\boldsymbol{R}$	=	residual vector
R	=	correlation matrix in kriging model
R	=	gas constant
$\mathcal{R}$	=	residual operator
Re, Re_θ	=	chord and momentum thickness Reynolds number
$\boldsymbol{r}$	=	vector of correlations in kriging model
r_α	=	radius of gyration about elastic centre
S	=	area of control volume
S	=	Schur complement matrix ($= S^s + S^c$)
S^s, S^c	=	structural and interaction term of Schur complement matrix
$\widehat{S}^c$	=	kriging approximation of Schur interaction term

$\mathcal{S}$, $\mathcal{T}$	=	spatial and temporal operator in boundary layer model
$\boldsymbol{s}$	=	vector of input parameters at sample location in kriging model
T	=	temperature
T	=	period ($= 2\pi/\omega$)
$\boldsymbol{t}$	=	unit tangential vector
t	=	real time
U_s	=	equivalent normalised wall slip velocity in boundary layer model
u, v	=	velocity components in streamwise and wall normal coordinates
$\bar{u}$	=	reduced velocity
V, ∂V	=	control volume and control volume boundary
V	=	flutter speed index ($= \bar{u}/\sqrt{\mu_s}$)
W	=	work done by generalised forces
$\boldsymbol{w}, \dot{\boldsymbol{w}}$	=	vectors of unknowns and corresponding temporal derivatives
$\boldsymbol{x}$, $\dot{\boldsymbol{x}}$	=	vectors containing grid location and velocity
$\boldsymbol{x}$	=	vector of input parameters at unsampled location in kriging model
x_{tr}	=	boundary layer transition location
x_α	=	offset between centre of gravity and elastic centre
$\boldsymbol{y}$	=	solution vector of linear system
$\boldsymbol{y}_s$	=	vector of true system responses in kriging model
y	=	true system response in kriging model
$\widehat{y}$	=	approximated system response in kriging model

Greek Symbols

$\boldsymbol{\alpha}_k$	=	vector of Fourier coefficients for fluid response
α	=	freestream angle of attack
α, $\dot{\alpha}$	=	pitch angle and pitch rate
$\boldsymbol{\beta}$	=	vector of regression parameters in kriging model
$\boldsymbol{\beta}_k$	=	vector of Fourier coefficients for structural forcing
Γ	=	circulation
γ	=	ratio of specific heats
δ	=	boundary layer thickness
δ^*	=	boundary layer displacement thickness
δ^{**}	=	boundary layer density thickness
δ_u^*	=	auxiliary boundary layer thickness
$\dot{\boldsymbol{\epsilon}}$	=	rate of deformation (strain–rate) tensor
ϵ	=	increment
ζ	=	structural damping ratio
$\boldsymbol{\eta}$, $\dot{\boldsymbol{\eta}}$	=	vectors of generalised coordinates and velocities

$\boldsymbol{\theta}$	=	vector of correlation parameters in kriging model
θ	=	boundary layer momentum thickness
θ^*	=	boundary layer kinetic energy thickness
ϑ	=	mass ratio in modal structural model
λ	=	eigenvalue
λ	=	thermal conductivity
μ, μ_t	=	dynamic viscosity and turbulent (eddy) viscosity
μ	=	independent/bifurcation parameter
μ_s	=	aerofoil–to–fluid mass ratio in aerofoil structural model
$\widetilde{\nu}$	=	intermediate variable of Spalart–Allmaras turbulence model
ν	=	pseudo time level
ξ, η	=	streamwise and wall normal coordinates
ϱ	=	density
σ	=	eigenvalue's real part (damping)
σ	=	standard deviation
σ^2	=	process variance in kriging model
ς	=	entropy defined to become zero under freestream conditions
$\boldsymbol{\tau}$	=	stress tensor
τ	=	pseudo time
Φ	=	velocity potential
$\boldsymbol{\Phi}$	=	matrix of mode shapes
Φ	=	cumulative distribution function of standard normal distribution
ϕ	=	probability density function of standard normal distribution
φ	=	standard error in kriging model
ψ	=	slope limiter
Ω	=	constant of the power law
$\boldsymbol{\omega}$	=	vorticity vector
ω	=	eigenvalue's imaginary part (circular frequency)
ω	=	specific turbulence dissipation rate (turbulence frequency)
ω_r	=	ratio of natural frequencies ($= \omega_h/\omega_\alpha$)

Subscripts

b	=	wall blowing
cg	=	centre of gravity
cv	=	control volume
d, u	=	downstream and upstream of shock location
e	=	values at edge of boundary layer
ec	=	elastic centre

eq	=	equilibrium values in boundary layer solution
F	=	critical/instability point
f	=	fluid
h	=	halo value
p	=	nonlinear potential model including wake correction
r	=	reference value (typically related to the freestream)
s	=	structural
v	=	viscous model
W	=	wall
ε	=	small variation
0	=	steady state solution, mean value or initial value

Acronyms

CFD	=	computational fluid dynamics
CVT	=	constant volume tetrahedron
DLR	=	German Aerospace Center (Deutsches Zentrum für Luft- und Raumfahrt)
EGO	=	efficient global optimization
EGRA	=	efficient global reliability analysis
EI/EIF	=	expected improvement/expected improvement function
FP/FPv	=	full potential/full potential with viscous correction
IPM	=	shifted inverse power method
LCO	=	limit–cycle oscillation
LH	=	latin hypercube
LPv	=	linear potential with viscous correction
MDO	=	multidisciplinary optimisation
MSE	=	mean squared error
MUSCL	=	monotonic upstream–centered scheme for conservation laws
NS	=	Navier–Stokes
PMB	=	parallel multiblock
RANS	=	Reynolds–averaged Navier–Stokes
ROM	=	reduced order model
SA	=	Spalart–Allmaras
SST	=	shear–stress transport
STD	=	standard deviation

Chapter 1

Introduction

Aircraft aeroelasticity deals with the mutual interaction of aerodynamic, elastic, and inertial forces for a flexible structure. The resulting aeroelastic phenomena are safety–related and have played an important role since the beginning of modern aircraft [1]. The flutter phenomenon is one of the most important examples. This violent unstable structural vibration usually originates in the coupling of two vibrational modes in the aeroelastic system causing the extraction of energy from the airstream to the structure and potentially leading to catastrophic structural failure.

Aerodynamic and/or structural nonlinearities make an aeroelastic system susceptible to bounded flutter responses which are commonly referred to as limit–cycle oscillations or limit–cycle flutter [2]. The aerodynamics in the transonic regime, featuring shock waves and shock induced separation, are a major source of nonlinearity, and a careful modelling of the flow field is required to predict aeroelastic instability accurately. However, the nonlinear transonic aerodynamics are the most difficult to model numerically and experimentally [3]. As modern aircraft operate routinely in the transonic regime, a considerable effort has been made towards the improvement of current analysis capabilities.

In this work the prediction of the linear aeroelastic stability limit assuming dynamically linear systems is the main concern. This means that the steady state flow field may exhibit nonlinear flow phenomena, such as shock waves and separation, while the dynamic response is time–linearised about the nonlinear steady state solution assuming there is a linear relationship between the structural motion and the fluid response. The structural representation is considered to be linear throughout.

This chapter reviews the features of flutter clearance and draws conclusions for the requirements of an aerodynamic/aeroelastic tool useful in a production environment. The importance of accurate and fast numerical simulations is discussed. Then, an overview of flow modelling approaches used in the prediction of aeroelastic instability, particularly in the transonic regime, is given. Here, emphasis is put on methods for reducing the involved computational cost, towards the routine analysis of an aeroelastic

configuration. As the available aerodynamic models are diverse, with different levels of complexity, accuracy and cost, the hierarchy of aerodynamic models is presented.

1.1 Application Requirements

The first formal flutter test was conducted by von Schlippe of Junkers Airplane Company in Germany in 1935 [4] to avoid undue risk from the then standard approach of flying at maximum speed to demonstrate stability. The basic procedure was to excite the components of the structure at resonant frequencies, to measure and plot the response amplitude with increasing flight speed, and to judge the test continuation from the previous results. The basic elements of flight flutter testing (excitation, data acquisition and analysis) have remained the same ever since, although the technologies used have seen remarkable improvements, most significantly with the development of digital computers for data analysis [5].

Flight flutter testing is still a time–consuming, expensive and dangerous stage in the development of an aircraft. Modern aircraft with unique designs are increasingly complex and optimised for efficiency in all details. The airframe structures are lighter and more flexible, while less damped, due to removed redundant structural mass and the use of modern composite materials. The requirement to operate at higher speeds in the transonic and supersonic regime demands advanced aerodynamic shapes. More powerful flight control systems lead to an increased interaction with the structural and aerodynamic degrees–of–freedom and the large variety of the aeroservoelastic cases adds to the complexity. Efforts are being made towards reconfigurable morphing configurations to operate efficiently in wide–ranging environments. Also, configurations are driven by new technologies such as stealth and the quest to design more environmentally friendly "green" aircraft. The accompanying nonlinear behaviour can have significant consequences due to the unforeseen, possibly dangerous, aeroelastic responses. Thus, the cost, or equivalently, the number of required flight tests has increased continuously [6–9].

Airworthiness regulations require that an aircraft is demonstrated under flight conditions to be free of aeroelastic instability, particularly flutter, within a 15 percent safety margin of the proposed flight envelope. Flutter can be prevented by proper design, and consequently the flutter analysis is carried out throughout the development process starting in the early stages to conclude with the final clearance. In this process, the analytical flutter calculations are continuously updated, corrected and validated by data from wind tunnel models, ground vibration and stiffness tests, and flight test campaigns [10]. The number of cases for a design loads analysis for a modern transport aircraft was estimated to be about five to ten thousand [11] in order not to miss any critical condition which would require redesign of the structure. Also, there is an increasing desire to avoid excess structural weight through optimised structures.

Additionally, changes to an aircraft configuration during its life cycle, including minor modifications to the structure and the flight control system, require the safe flight envelope to be established again. High–performance aircraft are equipped with external stores of different types, each combination of which has to be cleared for flutter [12–14]. For instance, the number of possible store combinations for the F/A–18E Super Hornet was estimated to be 400 thousand [15]. Thus, the number of required flight tests is typically well beyond the available financial and staff resources, and the most critical configurations must be identified numerically [16].

Adding to this complexity is the variability in mass, stiffness and damping across an aircraft fleet due to manufacturing tolerances, material differences and ageing [10]. This can cause nominally identical aircraft to exhibit different aeroelastic stability characteristics. Measurements on a small number of aircraft of the McDonnell Douglas F–4 Phantom II quantified a 5% weight variation and a 20% variation in the hinge line inertia for the horizontal stabilator and vertical tail rudder [17]. Also, the measured frequencies were subject to uncertainty depending on the experimental procedure. Changes in the mass and stiffness properties alter the dynamic characteristics of the configuration challenging deterministic approaches.

A typical flight envelope including the common 15 percent safety margin is presented in Fig. 1.1 showing the equivalent airspeed as a function of the freestream Mach number. The instability boundary corresponds to a classical bending–torsion type of instability exhibiting the distinct transonic dip phenomenon. Here, a reduced critical flutter velocity is associated with the formation of transonic shock waves. For Mach numbers below the transonic dip, aeroelastic instability of the bending–torsion type is usually not an issue. The transonic regime is not only the most critical region for flutter to occur but also the region where the predictive capabilities of production aerodynamic tools, i.e. linear aerodynamic tools such as the doublet lattice method, are least accurate. Appropriate aerodynamic modelling tools need to be nonlinear in their nature to be accurate in dealing with nonlinear flow phenomena, implying computational fluid dynamics (CFD) modelling. It has been suggested that a first application of an unsteady nonlinear code in a production environment, due to its immaturity

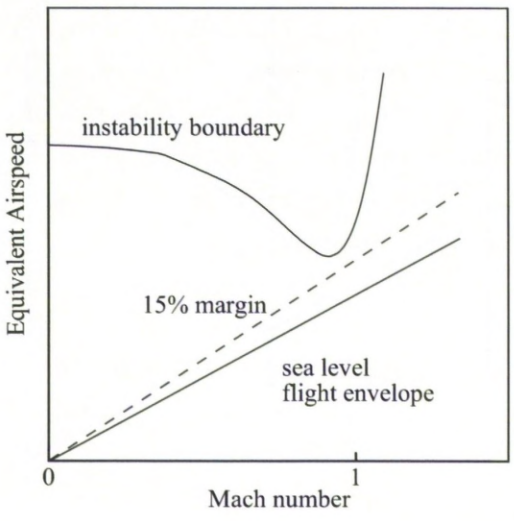

Figure 1.1: Typical flight envelope and instability boundary adapted from [15].

and cost, could be as a replacement for the (even more) expensive and time–consuming wind tunnel experiments [11, 15].

In order to reduce the cost as well as the risk involved in flight flutter testing, and to move towards certification by analysis, improvements have to take place in all experimental, analytical and numerical modelling aspects. These are discussed in detail in [7]. The state–of–the–art of aerodynamic modelling applied within production aeroelastic analyses (of high–performance aircraft) is discussed in [15] and four requirements for unsteady aerodynamic tools are identified. First, accuracy is required in the transonic regime where aeroelastic instability is likely to occur. Secondly, the analysis must be applicable to dynamic systems with the number of normal modes exceeding 100 (even though there appears to be a variation in practice in this matter). Thirdly, the modelling of nonlinear structural effects should be possible. And finally, the aerodynamic model must be fast. A similar list of requirements can be found in [11]. The first, second and fourth points are addressed directly or indirectly in this study.

The need for nonlinear aerodynamic modelling to address the first requirement of accuracy challenges the requirement for a fast method as CFD–based simulations are still expensive and time–consuming despite significant advances in algorithms and available computer power. Thus, a high fidelity nonlinear aerodynamic tool cannot be expected to be as computationally efficient as the less accurate linear aerodynamic tools currently used in a production environment. Instead, current research efforts are directed towards the development of model reduction techniques to represent the dominant system dynamics, predicted by the high fidelity tool, at reasonable cost. The application of unsteady CFD–based simulations must be defined appropriately as tens of thousands of simulations are not feasible. It will be demonstrated in this study that computational fluid dynamics can be used for instability searches over the flight envelope, as one possible application, if an appropriate sampling and reconstruction of the unsteady aerodynamic response is applied.

Following the controversial statement that all models are wrong while only a few are useful [18], a useful tool should allow the model to be updated based on available better information from more accurate simulations as well as ground and flight test data of the prototype aircraft. This capability is routinely applied in structural dynamics to update simple parameterised linear models for nonlinear effects [7, 19] and in linear aerodynamic models to correct the aerodynamic influence coefficient matrix for the well–known shortcomings of these tools in the transonic regime [15, 20]. The aerodynamic model hierarchy, presented below, naturally provides such a framework for nonlinear aerodynamic tools.

Another important aspect of the simulation requirements, which would assist the understanding of physical mechanisms, is the ability to consider the impact of sensitivity and uncertainty, as mentioned above for the F/A–18E Super Hornet. Here, parametric and model uncertainty must be distinguished. In structural dynamics, methods to

assess the impact of uncertainty in model parameters are well established [19, 21]. For instance, a probability distribution in one (or many) input parameters is propagated through the simulation and the effect on the system dynamics is investigated. Propagation tools such as interval analysis, perturbation and polynomial chaos methods, or even brute force Monte Carlo simulations, are routinely used.

In recent years these tools have started to be transferred to CFD applications. As an early example, the authors of [21] investigated several propagation methods to address parametric uncertainty for the nonlinear Burgers' equation. The feasibility of using expensive CFD–based aerodynamic modelling to investigate variability in the finite–element model of realistic aeroelastic problems was demonstrated in [22]. The propagation methods used were Monte Carlo, perturbation and interval analysis. The authors investigated the Goland wing model and a generic fighter aircraft using the Schur complement eigenvalue formulation presented in this work.

As pointed out in [9], the uncertainty associated with the aerodynamic model can be considerably larger than from the structural model. However, approaches considering uncertainty in the aerodynamic models (rather than the system parameters) are rare. This uncertainty is related to both the choice of the flow model and its spatial and temporal discretisation [23].

In [24] the influence of aerodynamic models on the amplitude of a store induced limit–cycle oscillation (LCO) was investigated for the Goland wing. It was argued that shock/boundary layer interaction in this case causes trailing edge separation and retards the shock movement (substantial in the inviscid case) thus limiting the LCO amplitude. Modelling both the inviscid/viscous interaction and the extent of the shock induced separation is therefore important in some cases.

In [25] for instance, it was demonstrated how the use of two different nonlinear CFD–based aeroelastic tools, both of which solving the Euler equations, affect the flutter predictions for two wing configurations. The presented results give a variation in the flutter onset speed.

Summarising this discussion, several capabilities are missing from the nonlinear aerodynamic tools available for production aeroelastic analyses. First, due to the involved cost using CFD–based modelling, the high fidelity tools have to be applied appropriately rather than in a brute force manner. In this thesis an approach to search for aeroelastic instability over a flight envelope will be presented. Secondly, a general method to update lower order models with better information as this becomes available is required. Such a method is discussed which allows the exploitation of a cheaper flow model to establish a general picture of the stability characteristics for the more expensive models to be focussed in presumed critical regions. Thirdly, a general approach to assess the impact of uncertainty, particularly from the flow models, in the prediction of aerodynamic phenomena like shock waves and regions of separation, and its consequences on the stability behaviour, would be important. This last point however

is not investigated in more detail in this study. Nevertheless, the issue of modelling uncertainty is considered when it comes up in the discussion of various flow models (and discretisation schemes) in order to exploit the model hierarchy.

1.2 Prediction of Transonic Aeroelastic Instability

Standard approaches in engineering applications to determine the stability of an aircraft structure immersed in an unsteady flow are the k or p–k methods [26]. These assume an inviscid linearised theory in the frequency domain for the unsteady aerodynamic response. Most notably the doublet lattice method has been the single most important tool in production flutter analyses for more than 30 years [27].

However, for the important transonic regime with its mixed sub- and supersonic regions, a linear aerodynamic theory fails due to the presence of flow nonlinearities such as shock waves and shock induced flow separation, and the linear numerical predictions have to be corrected with data from expensive and time–consuming experimental campaigns, or higher fidelity flow simulations. For these linear aerodynamic tools in the frequency domain, various approaches, often ad hoc, have been discussed for correcting the aerodynamic influence coefficient matrix with better data [15, 20].

The transonic aerodynamics have to be modelled by nonlinear methods for satisfactory and accurate results [28]. The use of computational aeroelasticity employing high fidelity aerodynamics based on nonlinear computational fluid dynamics (CFD) has matured from a research exercise to a powerful tool in engineering applications due to advances in flow modelling and computer power over the last four decades [29]. As a first step towards a virtual production flutter analysis, a suggestion is to use CFD–based simulations as a replacement for wind tunnel testing provided the accuracy and reliablity of these tools reaches the required maturity [11, 15]. The ultimate goal should be to move towards complete virtual design and certification.

The stability of an aeroelastic system can be inferred from time–marching simulations following an initial excitation. Calculations of complete aircraft configurations have been reported [30–32]. The time–accurate approach is very capable due to its generality in simulating dynamically nonlinear processes. However, it carries significant computational cost increasing with the modelling fidelity, in particular to solve for the unsteady nonlinear transonic aerodynamics. A requirement to search a space of system parameters and flight conditions for critical conditions makes this situation worse. The issue of cost limits the analysis to a few carefully chosen cases. Also, the integration of such CFD–based simulations into a multidisciplinary design environment is cumbersome.

To obviate the cost involved in solving complex systems with millions of degrees–of–freedom, and to permit routine calculations over the flight envelope, alternative approaches have been investigated over the last decade. There are two distinct direc-

tions. One, referred to as reduced order modelling (ROM), extracts the essence of the dynamic aeroelastic system to form a low dimensional problem while trying to keep the accuracy of the full order formulation. The second direction keeps the order of the full system while manipulating its solution procedure to reduce the cost. In the following an overview of these research directions is presented while more detailed discussions are given, for instance, in [10, 33].

The structural system in an aeroelastic investigation is routinely represented in a low dimensional modal form. Recent efforts in model reduction have concentrated on reducing the unsteady aerodynamic response [34]. One category of model reduction is based on an analogy with classical unsteady aerodynamics (such as Theodorsen's theory) in defining a transfer function in either the time or frequency domain to model the input–output relationship of the dynamic system under consideration. For instance, the linear or nonlinear response of a high dimensional CFD system, following a defined excitation, is identified as a Volterra series to form a ROM of the aerodynamics which is then coupled with a structural state–space model. Such reduced order aeroelastic representations would provide the means to interpret and to integrate the system's behaviour effectively in a multidisciplinary design environment, for active control and optimisation [33, 35].

Another category describes the unsteady aerodynamics by a relatively small number of dominant modes. Here, a mode is a characteristic distribution of system variables representing a specific behaviour. The most obvious choice are eigenmodes which are however difficult to extract for high dimensional systems [34]. Instead, one popular approach in aeroelastic applications [36], referred to as proper orthogonal decomposition or Karhunen–Loève expansion, uses discrete observations (snapshots, samples) of the system response from either the time or frequency domain. These observations need to cover the parameter space and flow phenomena of interest for a robust and reliable ROM to result.

Typically, the required number of observations, that defines the cost to evaluate a useful set of Karhunen–Loève modes, is large but significantly smaller than the number of degrees–of–freedom. Generating the system response is the main computational task in the approach, especially for high fidelity models, and takes about as much time as doing an analysis with the original model. In practice, the ROM needs to provide a pay off for its construction by multiple usage for different parameter combinations. The reliability of a ROM under parameter variations is an active topic of investigation [37, 38]. A variant of the proper orthogonal decomposition technique was applied both to deal with incomplete data in the reconstruction of aerodynamic flow fields and to provide a link in updating numerical predictions with experimental data [39].

The problem with both the Volterra approach and proper orthogonal decomposition is both the generation of the large number of system observations and the applicability for parameter variations. A more detailed discussion of the model reduction techniques,

using the Volterra system identification approach and the proper orthogonal decomposition, will be given in Section 4.4.

The harmonic balance method, as introduced in [40] for the analysis of nonlinear turbomachinery flow, manipulates the full order system, and is not a ROM in the strictest sense of reducing the number of spatial degrees–of–freedom [33]. However, a significant reduction can arise in the computational cost associated with simulating dynamically nonlinear, time–periodic, unsteady problems such as LCO. Near the vicinity of the instability the physically less important transient to develop a stable LCO can be very long and must be resolved in a time–accurate fashion. Instead the periodic response can be simulated directly in the frequency domain by expanding the flow variables in a truncated Fourier series assuming a fundamental frequency of the problem is present.

This approach is most effective when the flow can be represented accurately by a small number of harmonics which is a good assumption for many aeroelastic applications. Simulations of LCO have been reported for cases ranging from two dimensional aerofoil flow [41] to complete aircraft configurations [42, 43]. Recently, it was demonstrated in [44] that as many as 16 harmonics are required to resolve the dynamic content in the vicinity of a shock wave, which would then not be more efficient than time–accurate simulations. However, it was argued that for aeroelastic problems the generalised aerodynamic forces including lift and moment are of most interest [45], and that these commonly do not require these higher harmonics as the forces are spatially filtered due to the pressure integration.

An alternative approach, which is adapted in the current work, uses the theory of dynamic systems to predict aeroelastic instability of the Hopf type, which commonly leads to flutter or LCO. An arbitrary continuous dynamical system can be written in semidiscrete notation as

$$\dot{\boldsymbol{x}} = \boldsymbol{f}(\boldsymbol{x}, \boldsymbol{\mu}), \tag{1.1}$$

where $\boldsymbol{x} \in \mathbb{R}^n$ and $\boldsymbol{\mu} \in \mathbb{R}^m$ represent the vectors of state variables and the independent parameters, respectively [46,47], and $\boldsymbol{f} \in \mathbb{R}^n$ is a discrete functional relation. The phase portrait of the system either remains topologically equivalent or, when parameters pass through a critical value, changes its appearance. The appearance of a topologically non–equivalent phase portrait is called a bifurcation, the associated critical values of the independent parameters are bifurcation values.

An equilibrium $\boldsymbol{x}_0$ of Eq. (1.1) satisfies the expression $\boldsymbol{f}(\boldsymbol{x}_0, \mu) = 0$ for defined values of μ (here assuming a one parameter system). Then, a bifurcation with respect to μ in the stability of the equilibrium is called a Hopf bifurcation when there exists a pair of complex conjugate eigenvalues of the system Jacobian matrix $A(\boldsymbol{x}_0, \mu) = \partial \boldsymbol{f} / \partial \boldsymbol{x}$ crossing the imaginary axis. The other possible type of bifurcation for the one parameter problems are referred to as folds (turning points) having a zero eigenvalue.

These are not considered in this study. Two general approaches to locate bifurcation points are discussed [47].

Direct methods solve the system in Eq. (1.1) augmented by additional equations to characterise the bifurcation point. In [48], for instance, a method was developed which solves an augmented system of equations for the expression $\boldsymbol{f}(\boldsymbol{x}, \mu) = 0$ and the standard eigenvalue problem $(A - \lambda I)\,\boldsymbol{p} = 0$ with the eigenvalue $\lambda = i\,\omega$, defining the bifurcation, and the eigenvector $\boldsymbol{p}$. The eigenvector is normalised to be unique using the additional expression $\boldsymbol{c}^T\boldsymbol{p} = i$ with $\boldsymbol{c}$ as a real–valued constant vector. This provides a sufficient number of equations for the unknowns $\left[\boldsymbol{x}, \boldsymbol{p}, \omega, \mu\right]^T$.

The indirect approach, on the other hand, solves the system in Eq. (1.1) for changing values of the independent parameter in either the time or frequency domain to find when an eigenvalue crosses the imaginary axis. This theory can be applied in the linear stability analysis of aeroelastic systems.

The nonlinear flow field of the aeroelastic problem is described in a time–linearised (dynamically linear) fashion, i.e. the unsteadiness about a nonlinear steady state solution (equilibrium) is linearly dependent on the structural motion. The discretised aeroelastic system is formulated as a set of nonlinear ordinary differential equations in time and a stability problem for a full order steady state solution is examined instead of performing unsteady simulations. The least stable aeroelastic modes, originating in the wind–off structural modes and usually determining the dynamic response of the system, are evaluated directly for changes in the independent parameter, typically representing the dynamic pressure. In many aeroelastic problems a pair of complex conjugate eigenvalues with zero real part marks the onset of an instability leading to flutter and LCO.

Following an approach first published in [49–51], the bifurcation method was successfully tested on an aerofoil configuration free to move in pitch and plunge. Convergence problems associated with applying a direct solver to a large linear system were resolved by using an iterative sparse linear solver [52]. The method was extended to a larger problem investigating the flexible AGARD 445.6 wing using a modal structural model [53]. These techniques used the augmented system of equations following [48]. However, the CFD–based aeroelastic system is typically large making it difficult to solve the augmented system for the bifurcation point. Thus, two major development steps have taken place since this early work.

The shifted inverse power method was adapted to allow the tracing of the critical eigenvalues, typically starting their life in the wind–off structural system, with changing values of the independent system parameter to provide information about the damping and frequency of the aeroelastic modes [54]. This is the indirect approach in the frequency domain in the notation of [47]. Also, a model reduction technique based on the centre manifold theory was investigated to simulate an LCO response in the vicinity of the linear instability point [54].

An improved version of the basic (indirect) method used a Schur complement eigenvalue formulation to enhance computational performance and to avoid numerical problems associated with the shifted inverse power method [55]. It was applied to several wing structures and also complete aircraft configurations to study uncertainty in the predicted instability due to structural variability [22]. This approach views the coupled aeroelastic system as a modified structural eigenvalue problem with the interaction (correction) term, which depends on the response frequency and the parameters of both the aerodynamic and structural models, pre–computed. The evaluation of the interaction term incurs most of the involved cost as it generally requires operations on the high dimensional CFD–based system.

In this thesis the approximation of the interaction term is formulated so that the stability problem can be solved efficiently in larger parameter spaces. In addition, it allows that a hierarchy of aerodynamic models can be exploited, with cheaper models being used to evaluate possible conditions of interest for more expensive models, whose evaluation is then used to update the approximation.

1.3 Aerodynamic Model Hierarchy

A wide variety and complexity of aerodynamic models are available and used for aircraft applications. The hierarchy of flow models used in engineering problems and research has developed over the last five decades closely linked with the advances in computer power. The hierarchy is broadly categorised into four levels to reflect the basic differences in the underlying physical modelling assumptions. The mathematical models vary with increasing complexity from the Laplace equation to the three dimensional unsteady compressible Navier–Stokes equations applicable to most flows of practical interest. This is well–documented in a variety of survey papers [29, 56–58] and books [59, 60]. In the following a short review is presented.

The lowest level, developed from the late 1960s, are the linear potential methods assuming an inviscid, irrotational and linear flow. It is typically based on solutions of either the Laplace or Prandtl–Glauert equation which are linear second order partial differential equations. Here, the surface of the considered geometry is discretised into smaller elements (at the actual surface or a mean surface) and singularities, which are elementary solutions of the Laplace equation, are assigned to control points on these elements. The strengths of the singularities are determined by the tangential flow (non–penetration) boundary condition. Well–known examples are the vortex and doublet lattice methods, the latter one being the standard tool in production flutter analyses. Commonly, these methods, as well as nonlinear potential methods, are coupled with an integral boundary layer formulation to account for viscous effects [61].

The nonlinear potential methods, adding nonlinear compressible effects, solve the transonic small disturbance or full potential equations which are nonlinear partial dif-

ferential equations of second order. The major period of development was in the 1970s starting with a landmark paper introducing type–dependent differencing for the mixed elliptic/hyperbolic transonic small disturbance equation [62]. The ideas were extended to the full potential equation a few years later [63]. The major advance is the ability to deal with the nonlinear transonic flow, including shock waves, by switching from a central to an upwind differencing scheme. The added complexity of the available physics requires increased computational complexity; as a consequence discretising only the surface of the geometry is not sufficient anymore. Instead, the whole computational domain around the geometry needs to be discretised into elementary control volumes where the governing equations are applied to each control volume in turn.

Starting from the 1980s the available computer hardware allowed research efforts directed towards the development of efficient algorithms to solve the Euler equations, which form a set of five first order partial differential equations. This highest inviscid modelling level adds entropy and vorticity effects to the nonlinear potential flow. To list a few, notable developments to discretise the convective terms in the governing equations are the monotone characteristic–based upwind schemes to solve the exact [64] and approximate [65,66] local Riemann problems, total variation diminishing schemes [67], and the variants of the essentially non–oscillatory schemes [68]. All these approaches allow a discretisation of the flow field to have a sharp resolution of shock waves and contact discontinuities while avoiding unphysical oscillations. Block–structured and unstructured grid approaches are applied to solve the Euler equations over complex geometries. For computational efficiency, implicit schemes as well as several convergence acceleration techniques have been developed including residual smoothing, local time stepping, multigrid and preconditioning methods [69].

In the 1990s the Navier–Stokes equations, forming a set of five second order partial differential equations, were routinely used to include viscosity in the simulations. However, as is well known, flows of practical interest in engineering applications involve turbulence. Solving even the simplest turbulence problems, not to mention at realistic Reynolds numbers, for all spatial and temporal scales directly exceeds available computer power by orders of magnitude. In [70] the readiness of such a direct numerical simulation applied to the target flow over a whole aircraft was estimated for the year 2080. Therefore, the Navier–Stokes equations are commonly averaged, giving the Reynolds–averaged Navier–Stokes equations, and solved for the mean flow quantities. The averaging process introduces additional unknown quantities leading to the closure problem of turbulence. Additional models, commonly algebraic, one, or two equation turbulence models, are solved together with the Reynolds–averaged Navier–Stokes equations to simulate all scales of the turbulent content [71]. Such simulations are routinely applied in the aircraft design process.

In the first decade of the 21st century, the computer power allows the consideration of alternative, more advanced approaches which involves filtering the turbulent con-

tent into large and small scales. The large scales, containing most of the energy, are simulated directly, while the effects of the small scales are modelled. This is based on the underlying idea that the large turbulent structures depend on the specific problem, while the smaller scales have a more universal character. However, for a realistic aircraft these large eddy simulations will become standard in about three decades time [70]. In the meantime, the detached eddy simulation, a hybrid between the Reynolds–averaged Navier–Stokes equations, solved in the attached boundary layer, and the large eddy simulation, solved in strongly separated (detached) flow regions, can be used now even for realistic problems [72].

As mentioned before, simulations using the Reynolds–averaged Navier–Stokes equations are routinely performed for full aircraft models in the design process, while extensive wind tunnel testing is still required to validate and correlate with the simulation data due to the immaturity of CFD–based approaches in a production environment [11]. In aeroelastic applications high fidelity unsteady CFD–based approaches are less feasible due to the large number of required simulations, and therefore, these are of little practical importance. Large scale production aeroelastic analyses are still limited to the linear potential methods developed in the late 1960s, particularly using the doublet lattice method providing the aerodynamic influence coefficients to make the flutter prediction very efficient [15]. These linear tools are sufficient in both the sub- and supersonic domain. However, for the important transonic range nonlinear tools are required. This shows that efforts need to be directed to exploit the power of high fidelity simulations routinely in aeroelastic applications.

1.4 Objective of Work and Outline of Thesis

The objective of this work is to investigate the use of a hierarchy of nonlinear aerodynamic modelling tools in routine aircraft aeroelastic stability analyses, particularly in the transonic range. First, a method that is capable of searching for aeroelastic instability over the flight envelope is developed. Then, the application of this method to combine/update aerodynamic models of variable fidelity is demonstrated.

Chapters 2 and 3 introduce and validate the aerodynamic modelling tools used in this work for the CFD–based aeroelastic stability analysis. In Chapter 2 the two applied flow solvers are presented; one used for the Euler and Navier–Stokes equations and one, developed as part of this research, used for the unsteady full potential equations corrected for more physical content. The governing equations for all flow models are outlined and their discretisation is described. In Chapter 3 the aerodynamic models, with an emphasis on the new full potential code, are applied to standard test cases and the simulation results are compared with experimental data (where available) for the purpose of validation and to build confidence in the models.

Chapter 4 presents the tools used for the linear aeroelastic stability analysis. First, the Schur complement eigenvalue method, which describes a small structural eigenvalue problem corrected by the aerodynamic influence, is formulated in detail. Secondly, the generation of the aerodynamic influence, referred to as the Schur interaction matrix, is discussed in both the frequency and time domain. Also, an oscillatory phenomenon found in the transonic range is investigated. Thirdly, the approximation of the computationally expensive Schur interaction matrix is introduced using the kriging interpolation technique. And finally, the Schur complement eigenvalue method is compared with the classical flutter analysis and discussed in the light of two popular model reduction techniques, namely system identification using the Volterra approach and proper orthogonal decomposition.

Chapter 5 describes the linear aeroelastic stability analysis using the kriging approximation of the Schur interaction matrix. Here, two structural models are considered and described in detail; one for two degrees–of–freedom (pitch and plunge) aerofoil cases and one for the more general modal structural model. The aerofoil case of a NACA 0012 configuration is discussed for four aerodynamic models, including inviscid and viscous nonlinear potential, Euler and Reynolds–averaged Navier–Stokes modelling, and the differences in the stability predictions for the flow models are investigated. Also, the results of the Schur complement eigenvalue method are compared with results of the classical flutter analysis. Then, the method is extended to three dimensional aircraft structures, and two wing geometries, i.e. the Goland wing and the multidisciplinary opimisation (MDO) wing, are analysed. The MDO wing fully accounts for the effects of aerostatic deformation.

Chapter 6 introduces the search for transonic aeroelastic instability using high fidelity CFD–based aerodynamic models and attempts to exploit the established nonlinear aerodynamic hierarchy for the analysis. These two issues are important as the construction of the computationally cheap kriging model to generate the response surfaces of the Schur interaction matrix components is expensive in a multidimensional parameter space due to the number of required exact numerical samples. Several basic approaches are described to perform such a sampling of the parameter space efficiently, including latin hypercube, risk–based and expected improvement sampling. This is discussed for two aerofoil cases and the MDO wing. Then, the aerodynamic hierarchy is exploited by establishing a general picture of the stability problem using a cheaper flow model in order to place a few, carefully selected, more expensive simulations in presumed critical regions. The reconstruction of the interaction matrix corresponding to a higher fidelity model is then supported by both augmenting with lower fidelity data and using the co–kriging technique with the lower fidelity response providing the trend information for the augmented higher fidelity data. This approach is investigated for the NACA 0012 aerofoil case and the Goland wing/store configuration.

Chapter 7 concludes the thesis and offers an outlook and suggestions for future

work. Details of the full potential flow solver, including a detailed discussion of the integral boundary layer formulation, and the derivation of the aerofoil structural model are given in the appendices.

Chapter 2

Flow Models

Aeroelasticity deals with the dynamic interaction of an unsteady fluid flow and an elastic structure both of which have to be modelled appropriately. This chapter provides the background on the physical models used in describing the aerodynamics and on the numerical schemes which have been applied to solve these models. The governing equations of the fluid can be formulated with various assumptions. In [58] four main levels of aerodynamic modelling are discussed; linear and nonlinear potential, Euler and Navier–Stokes. The physics in a simulation can be built up from linear potential models which assume linear, irrotational and inviscid flow. Nonlinear potential models introduce nonlinear compressible flow effects found in the transonic regime. The Euler equations add entropy and vorticity effects, while the Navier–Stokes equations include viscous and heat–conduction effects. Flows of practical interest in engineering are often turbulent, requiring the Reynolds–averaged form of the Navier–Stokes equations to be solved together with a suitable turbulence model.

Two computational fluid dynamics solvers are used in this work. One, used to solve the Euler and Navier–Stokes equations, is an established research code. It has been applied to various aerodynamic and aeroelastic problems, from simple aerofoils to complete aircraft configurations [73]. The second one is newly developed within this work [74]. Based on an unsteady nonlinear full potential formulation, it is solved in combination with additional models to approximate the Euler and Navier–Stokes equations by correcting for the different physical effects.

2.1 Navier–Stokes and Euler Equations

Most aerodynamic flows of engineering interest (with an exception of flows at extreme thermodynamic conditions) are correctly modelled by the Navier–Stokes (NS) equations. The set of NS equations is derived from first principles of conservation of mass (continuity), momentum (Newton's second law) and energy (first law of thermodynamics) and is supplemented by constitutive relations of the fluid to close the system. As

is well known, solving the NS equations directly even for the simplest turbulent flows exceeds available computing power by orders of magnitude [70]. Therefore, appropriate simplifications must be considered. At present, the Reynolds–averaged Navier–Stokes (RANS) equations are generally used in combination with a suitable turbulence model to simulate the flow for an aircraft configuration. As an alternative, for negligible viscous and heat–conduction effects, the Euler equations are a convenient choice.

By default in the following, all variables are given in dimensionless notation obtained by applying reference freestream values of density, velocity, temperature and dynamic viscosity as well as a characteristic length scale of the problem. The subscript r expresses reference values with the asterisk (*) denoting dimensional quantities.

2.1.1 Reynolds–averaged Navier–Stokes Equations

The flow variables are defined as the sum of a time–average and a turbulent fluctuation about the mean value. Then, time–averaging the NS equations gives the RANS equations for the mean flow variables while introducing additional unknown correlations, i.e. the Reynolds stress tensor and the turbulent heat–flux vector, leading to the closure problem of turbulence. Write the system of equations for density ϱ, Cartesian velocity vector $\boldsymbol{q}$ and specific total energy e_t in dimensionless compact notation,

$$\frac{\partial \varrho}{\partial t} + \nabla \cdot (\varrho\, \boldsymbol{q}) = 0 \tag{2.1}$$

$$\frac{\partial \varrho\, \boldsymbol{q}}{\partial t} + \nabla \cdot (\varrho\, \boldsymbol{q} \otimes \boldsymbol{q}) + \nabla p = \nabla \cdot \boldsymbol{\tau} \tag{2.2}$$

$$\frac{\partial \varrho\, e_t}{\partial t} + \nabla \cdot \left((\varrho\, e_t + p)\, \boldsymbol{q}\right) = \nabla \cdot (\boldsymbol{\tau}\, \boldsymbol{q}) - \nabla \cdot \boldsymbol{h}. \tag{2.3}$$

The equation of state is written as

$$p = \frac{\varrho T}{\gamma M_r^2} \tag{2.4}$$

where

$$T = \gamma\,(\gamma - 1)\, M_r^2 \left(e_t - \frac{1}{2}(\boldsymbol{q} \cdot \boldsymbol{q})^{1/2}\right) \tag{2.5}$$

is the temperature. Respecting Stokes' hypothesis for an isotropic, Newtonian fluid while assuming a linear relationship between the Reynolds stresses and the rate of deformation (strain–rate) tensor, $\dot{\boldsymbol{\epsilon}} = \frac{1}{2}\left((\nabla \boldsymbol{q}) + (\nabla \boldsymbol{q})^T\right)$, the symmetric tensor $\boldsymbol{\tau}$ for viscous and turbulent stresses (generalised for compressible flow) is written as

$$\boldsymbol{\tau} = 2\left(\frac{\mu}{Re} + \frac{\mu_t}{Re}\right)\dot{\boldsymbol{\epsilon}} - \frac{2}{3}\left(\frac{\mu}{Re} + \frac{\mu_t}{Re}\right)(\nabla \cdot \boldsymbol{q})\, I - \frac{2}{3}\varrho\, k\, I, \tag{2.6}$$

where μ is the dynamic viscosity, μ_t is the turbulent (eddy) viscosity, k is the turbulence kinetic energy, and I is the 3×3 identity matrix.

Following Fourier's law of thermal conduction and taking the classical analogy between momentum and heat transfer, the heat–flux vector $\boldsymbol{h}$ is given by

$$\boldsymbol{h} = -\frac{1}{(\gamma-1)\,M_r^2}\left(\frac{\mu}{Re\,Pr}+\frac{\mu_t}{Re\,Pr_t}\right)\nabla T, \tag{2.7}$$

which is composed of laminar and turbulent contributions like the stress tensor [75].

The important dimensionless parameters are the Reynolds number $Re = \varrho_r^* q_r^* x_r^*/\mu_r^*$ based on the reference length scale x_r^*, the Mach number $M_r = q_r^*/\sqrt{\gamma R^* T_r^*}$ with R^* as the gas constant, the (laminar or molecular) Prandtl number $Pr = c_p^*\mu_r^*/\lambda^*$ set to 0.72 with λ^* as the thermal conductivity, the turbulent Prandtl number Pr_t chosen as 0.9, and the ratio of specific heats $\gamma = c_p^*/c_v^*$ set to 1.4. Variations of the dynamic viscosity with respect to the temperature are taken into account using Sutherland's law, $\mu = \mu(T)$.

To complete the formulation, an adiabatic no–slip boundary condition is applied at solid surfaces, while outer boundaries are set to uniform freestream values.

Overview of Turbulence Models

Numerous turbulence models have been developed trying to relate the additional unknown correlations to the mean flow. Nearly all algebraic, one and two equation linear turbulence models rely on the Boussinesq eddy viscosity approximation which is based on an analogy between turbulent and molecular mixing [71]. The closure based on the Boussinesq approximation requires methods to calculate the eddy viscosity. Popular turbulence models are the Spalart–Allmaras (SA) one equation model [76] and the k–ω shear–stress transport (SST) two equation model [77].

The SA model computes the eddy viscosity from $\mu_t = f_{v1}\,\varrho\,\widetilde{\nu}$ where f_{v1} is a near wall damping function and $\widetilde{\nu}$ is an intermediate quantity governed by a transport equation of the general form

$$\frac{\partial \widetilde{\nu}}{\partial t} + \nabla\cdot\left(\widetilde{\nu}\,\boldsymbol{q}\right) = \mathcal{P}_{\widetilde{\nu}} + \mathcal{D}_{\widetilde{\nu}} + \mathcal{W}_{\widetilde{\nu}}. \tag{2.8}$$

The terms on the right–hand side denote production, diffusion (including conservative and non–conservative contributions) and near wall destruction of eddy viscosity, respectively.

For the $k-\omega$ (SST) model the eddy viscosity is computed from $\mu_t = \varrho\,k/\omega$ where the turbulence kinetic energy k and the specific turbulence dissipation rate (turbulence frequency) ω are governed by transport equations of the general form

$$\frac{\partial \varrho\,k}{\partial t} + \nabla\cdot\left(\varrho\,k\,\boldsymbol{q}\right) = \mathcal{P}_k + \mathcal{D}_k + \mathcal{W}_k \tag{2.9}$$

$$\frac{\partial \varrho\,\omega}{\partial t} + \nabla\cdot\left(\varrho\,\omega\,\boldsymbol{q}\right) = \mathcal{P}_\omega + \mathcal{D}_\omega + \mathcal{W}_\omega + \mathcal{C}_\omega. \tag{2.10}$$

The right–hand side terms represent production, conservative diffusion and dissipation, respectively. The last term in the second equation denotes cross–diffusion.

For details of these turbulence models, the reader is referred to the literature, for instance [71].

2.1.2 Euler Equations

Setting the right–hand side terms of the RANS equations to zero gives the Euler equations which constitute the highest inviscid modelling level. In contrast to the RANS equations where a no–slip solid wall boundary condition is applied, the Euler flow is only required to be tangent to a solid surface.

2.1.3 Discretising and Solving

The governing equations are discretised using a block–structured, cell–centred, finite–volume scheme. Here, a finite number of non–overlapping control volumes (grid cells) constitutes the computational domain. A representative 3–block C–type computational grid for an aerofoil is shown in Fig. 2.1(a). The governing equations, applied to each control volume in turn, are formulated in a time–varying curvilinear coordinate system to facilitate the numerical solution. This is convenient since applications of engineering interest have rather complex geometries which require body–conforming grids of arbitrary local orientation and density.

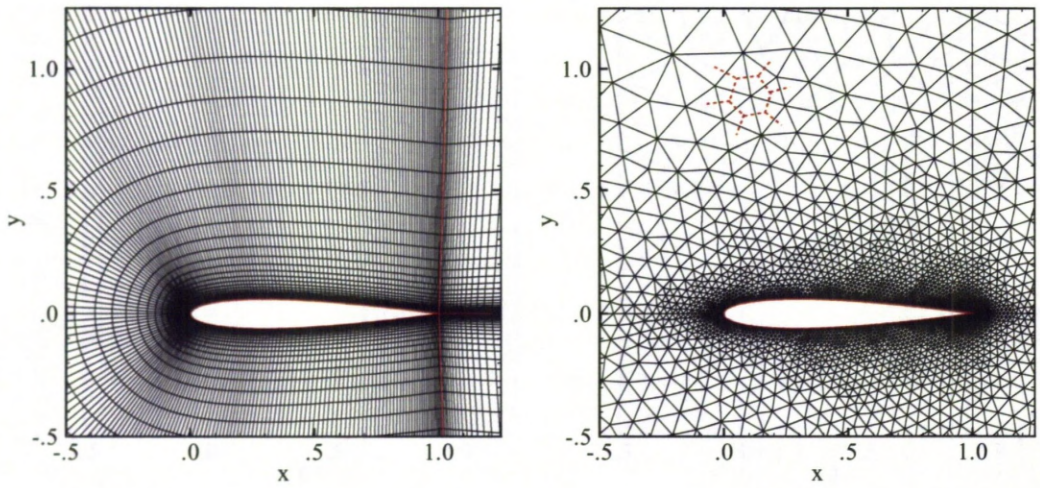

(a) 3–block C–type structured grid

(b) unstructured triangular grid

Figure 2.1: Representative structured and unstructured computational grids.

Defining a general transformation from the Cartesian space to the computational space, the NS equations can be transformed to general curvilinear coordinates and maintain their strong conservation form [78, 79]. For convenience, write the resulting

system of equations in conservative integral form using the divergence theorem,

$$\frac{d}{dt}\int\limits_{V(t)} \boldsymbol{w}_f \, dV + \int\limits_{\partial V(t)} \left(\boldsymbol{F}^i - \boldsymbol{F}^v\right) \boldsymbol{n} \, dS = 0, \tag{2.11}$$

where $\boldsymbol{w}_f = \left[\varrho, \varrho\,\boldsymbol{q}, \varrho\, e_t\right]^T$ is the vector of the conservative variables, and $\boldsymbol{F}^i$ and $\boldsymbol{F}^v$ are the inviscid and viscous fluxes, respectively. This equation is valid for any time–dependent control volume $V(t)$ with moving boundaries $\partial V(t)$ in curvilinear coordinates. Here, strong conservation is not violated by a flux over moving boundaries; the fluxes in the above integral relation are given in terms of the contravariant velocities [80] including the velocity of moving control volumes. The turbulence models are handled in a similar fashion with an additional source term including production, dissipation and non–conservative diffusion contributions.

While viscous fluxes are evaluated by second order central differences, inviscid fluxes are discretised at the faces of control volumes using the approximate Riemann solver of Osher and Chakravarthy [66]. Left and right states for the individual Riemann problems are evaluated using MUSCL (Monotonic Upstream–centered Scheme for Conservation Laws) variable extrapolation [81] to achieve essentially second order spatial accuracy, while an alternative form of the Van Albada limiter is applied to prevent spurious oscillation around steep gradients (shock waves). The source term in the turbulence models is evaluated at cell centres.

Boundary conditions are set using two layers of halo cells on the outside of the computational domain. For inviscid simulations, the halo values at solid boundaries are extrapolated from the interior values ensuring the normal velocity component relative to the wall is zero. For viscous simulations, the halo values at solid boundaries are extrapolated ensuring the velocity is equal to the solid wall velocity. At far field boundaries, halo cells take on freestream conditions.

Spatial discretisation leads to a large system of ordinary differential equations in time written in semidiscrete form as

$$\frac{d\boldsymbol{w}_f}{dt} = \boldsymbol{R}_f(\boldsymbol{w}_f) - \frac{\boldsymbol{w}_f}{V}\frac{dV}{dt} \tag{2.12}$$

where $\boldsymbol{R}_f$ is the residual vector corresponding to the unknowns. The second term on the right–hand side accounts for temporal changes of the control volumes evaluated by applying the geometric conservation law [82]. There are $n_f = 5n_{cv}$ fluid unknowns for the three dimensional Euler and the mean flow NS equations where n_{cv} is the number of control volumes. Additionally, one or two equation turbulence models, written in semidiscrete notation like the NS equations, add another n_{cv} or $2n_{cv}$ unknowns.

Following a specified number of explicit (forward Euler) iterations to smooth out the initial flow field, integration in (pseudo) time to a steady state is obtained by an

implicit time–marching scheme. The residual is linearised giving

$$\left(A_{ff} - \frac{I}{\Delta\tau}\right) \Delta \boldsymbol{w}_f = -\boldsymbol{R}_f(\boldsymbol{w}_f^\nu) \tag{2.13}$$

where ν is the discrete (pseudo) time level and $\Delta \boldsymbol{w}_f = \boldsymbol{w}_f^{\nu+1} - \boldsymbol{w}_f^\nu$. The matrix $A_{ff} = \partial \boldsymbol{R}_f / \partial \boldsymbol{w}_f$ is the fluid Jacobian matrix at time level ν. Interestingly, for large (pseudo) time steps $\Delta\tau$, Newton's method is recovered. For computational efficiency, A_{ff} is an approximate Jacobian matrix of the second order spatial scheme. Also, local time stepping is applied for quicker convergence. The turbulence model is updated in pseudo time following the NS equations in a staggered fashion. This simplifies the evaluation of the Jacobian matrix of the turbulence model since the unknowns of the NS equations are then considered as constant for the current evaluation of the turbulence residual. The resulting linear systems are solved by a preconditioned Krylov subspace iterative algorithm.

For unsteady simulations, e.g. forced periodic motions, the dual time stepping method [83] is applied. Here, the temporal derivative is approximated by a second order backward difference. The pseudo residual $\boldsymbol{P}_f$ is written as

$$\boldsymbol{P}_f = \widetilde{\boldsymbol{R}}_f(\boldsymbol{w}_f^{n+1}, V^{n+1}) - \frac{3\boldsymbol{w}_f^{n+1} - 4\boldsymbol{w}_f^n + \boldsymbol{w}_f^{n-1}}{2\Delta t} \tag{2.14}$$

where $\widetilde{\boldsymbol{R}}_f$ is the right–hand side in Eq. (2.12). The system is iterated to a steady state in pseudo time ν at each real time step n using the above implicit time–marching scheme.

Time–accurate aeroelastic simulations require the (generally) low dimensional structural model to be solved in combination with the fluid model. Therefore, the temporal derivative of the structural state–space equations is approximated accordingly. The combined equations are iterated to a steady state in pseudo time at each real time step just as for the fluid–only unsteady scheme.

2.2 Full Potential Equations and Correction Models

The Euler and RANS equations can be approximated by a nonlinear potential formulation complemented by correction models to include more physical content, e.g. viscous and strong shock wave effects. Thus, the baseline flow model applies the unsteady nonlinear full potential equations together with a wake model to convect the unsteady shedding of vorticity downstream in the usual time–accurate fashion. Viscous effects are added by an integral boundary layer formulation while an entropy and vorticity correction model offers a possible future option to deal with strong shock waves violating the assumptions of the baseline model.

By default in the following discussion, all variables are given in dimensionless notation which is obtained by applying freestream values of density, velocity and temperature as well as the characteristic length scale, i.e. the aerofoil chord length, as reference values.

2.2.1 Unsteady Full Potential Model

Following [57], the assumption of an inviscid and irrotational flow allows the introduction of a scalar velocity potential which can be given for steady or unsteady, incompressible or compressible flow. For the velocity potential to exist the vorticity of the flow field must be zero everywhere,

$$\omega = \nabla \times \nabla\Phi = 0, \tag{2.15}$$

where $\nabla\Phi = q$ are the Cartesian velocity components defined as the gradient of the velocity potential. In addition, making the isentropic assumption leads to the full potential formulation which allows the prediction of weak shock waves in the transonic regime. The conservative form of the nonlinear full potential equation is derived from the continuity equation in Eq. (2.1)

$$\frac{\partial \varrho}{\partial t} + \nabla \cdot \left(\varrho \nabla\Phi\right) = 0\,. \tag{2.16}$$

Interestingly, for an incompressible flow the latter equation reduces to the well–known linear Laplace equation $\nabla^2\Phi = \Delta\Phi = 0$. The two scalar unknowns of density and nonlinear velocity potential demand an additional relation. Therefore, consider the following formulation of the Euler momentum equation

$$\frac{\partial \boldsymbol{q}}{\partial t} + \left(\boldsymbol{q} \cdot \nabla\right) \boldsymbol{q} + \frac{\nabla p}{\varrho} = 0\,, \tag{2.17}$$

where the second term is formulated as

$$\left(\boldsymbol{q} \cdot \nabla\right) \boldsymbol{q} = \nabla\left(\frac{q^2}{2}\right) - \boldsymbol{q} \times \boldsymbol{\omega}\,, \tag{2.18}$$

with $q = \left(\boldsymbol{q} \cdot \boldsymbol{q}\right)^{1/2}$. Following a variant of the first law of thermodynamics, the last term of Eq. (2.17) is written for an isentropic fluid as

$$\frac{\nabla p}{\varrho} = \frac{1}{\gamma - 1} \frac{\nabla \varrho^{\gamma - 1}}{M_r^2} \tag{2.19}$$

where the dimensionless pressure relation for isentropic flow,

$$p = \frac{\varrho^\gamma}{\gamma M_r^2}, \tag{2.20}$$

is employed. Integrating Eq. (2.17) along an arbitrary path in the domain gives the desired unsteady Bernoulli equation

$$\frac{\partial \Phi}{\partial t} = \frac{1 - q^2}{2} - \frac{\varrho^{\gamma-1} - 1}{(\gamma - 1)\, M_r^2} \tag{2.21}$$

with the integration constant evaluated under freestream conditions assuming a time–invariant far field velocity potential. Other formulations of this system of equations can be found in the literature. The system reduces to one equation (the continuity equation) for the velocity potential in steady flow with the density obtained directly from the latter expression.

Completing the aerodynamic model requires the definition of boundary conditions for the velocity potential and density. At the outer boundaries a uniform freestream distribution is usually assumed, while at a solid surface the flow tangency condition (relative to a moving geometry) has to be ensured.

In aerodynamic applications the prediction of aerodynamic forces and moments is generally sought. According to the theorem stated by Kutta and Joukowski, the lift is proportional to the circulation Γ defined as the line integral of the velocity $\boldsymbol{q} = \nabla \Phi$ around an arbitrary closed curve $\boldsymbol{l}$. Stoke's theorem transforms this line integral into a surface integral,

$$\Gamma = \oint_{\boldsymbol{l}} \boldsymbol{q} \cdot d\boldsymbol{l} = \int_{S} (\nabla \times \boldsymbol{q}) \cdot \boldsymbol{n}\, dS\,, \tag{2.22}$$

where S is the surface bounded by the closed curve $\boldsymbol{l}$. As can be seen by comparing with the definition of vorticity in Eq. (2.15), the basic assumption of the velocity potential to exist results in zero circulation, and thus zero lift. Therefore, the Kutta condition guaranteeing a rear stagnation point at the trailing edge introduces a jump in the velocity potential at the trailing edge. This potential jump is equivalent to the circulation.

In low–frequency flows the main source of unsteady effects arises from the unsteady shedding of vorticity into the wake downstream of a lifting surface. Thus, the circulation, set at the trailing edge, needs to be convected in a time–accurate fashion. This is done by a convection equation of the general form

$$\frac{\partial \Gamma}{\partial t} + \boldsymbol{q} \cdot \nabla \Gamma = 0\,, \tag{2.23}$$

which, for convenience, is simplified by approximating the gradient operator as the streamwise derivative relating to the dividing streamline, i.e. the wake cut, and accordingly the velocity. The wake cut is considered as a sheet of vorticity in an otherwise irrotational flow field. Since the velocity potential along the wake cut is double–valued, two boundary conditions have to be imposed, i.e. the jump in the velocity potential and a continuous normal flux. The density across the wake cut is continuous.

2.2.2 Integral Boundary Layer Model

Viscous effects are modelled in the full potential solver by an integral boundary layer formulation. Practically all two equation integral models use the integral momentum equation plus either the integral kinetic energy, an entrainment or the moment–of–momentum integral equation. Methods using the integral kinetic energy equation are referred to as dissipation integral methods. A dissipation–type closure formulation was developed for both laminar and turbulent steady compressible boundary layers [84–88]. It is formulated to adequately describe mildly separated regions, and also applies to free wakes setting the skin friction to zero. A relation to predict transition was included in the formulation, while upstream history effects in nonequilibrium turbulent boundary layers are modelled by a simplified version of the shear–stress transport equation developed in [89–91]. The integral model has been coupled in a fully–simultaneous fashion to several codes [88, 92–94].

The unsteady integral equations are derived from the two dimensional, unsteady boundary layer equations. This simplified form of the Navier–Stokes equations dates back to Ludwig Prandtl in 1904 when he established the boundary layer concept [95]. Formally integrating the Prandtl boundary layer equations, a detailed derivation of which is shown in Appendix A, gives the integral relations for displacement thickness δ^* and momentum thickness θ as primary boundary layer unknowns,

$$\frac{\partial \delta^*}{\partial t} - H_{\theta_\varrho}\frac{\partial \theta}{\partial t} - \theta\frac{\partial H_{\theta_\varrho}}{\partial t} + H\frac{\theta}{u_e}\frac{\partial u_e}{\partial t} + \left(H - H_{\theta_\varrho}\right)\frac{\theta}{\varrho_e}\frac{\partial \varrho_e}{\partial t} = \mathcal{R}_{\delta^*}\,, \tag{2.24}$$

and

$$\frac{\partial \theta}{\partial t} + \left(2 + 2H^{**} - H\right)\frac{\theta}{u_e}\frac{\partial u_e}{\partial t} + \frac{\theta}{\varrho_e}\frac{\partial \varrho_e}{\partial t} = \mathcal{R}_\theta\,, \tag{2.25}$$

with the right–hand side operators written as

$$\mathcal{R}_{\delta^*} = -u_e\left(\frac{\partial \theta}{\partial \xi} + \left(H + 2 - M_e^2\right)\frac{\theta}{u_e}\frac{\partial u_e}{\partial \xi} - \frac{C_f}{2}\right) \tag{2.26}$$

and

$$\mathcal{R}_\theta = -u_e\left(\theta\frac{\partial H^*}{\partial \xi} + H^*\frac{\partial \theta}{\partial \xi} + \left(2H^{**} + H^*\left(3 - M_e^2\right)\right)\frac{\theta}{u_e}\frac{\partial u_e}{\partial \xi} - 2C_D\right) - \mathcal{R}_{\delta^*}. \tag{2.27}$$

Interestingly, the expressions inside the outer brackets in Eqs. (2.26) and (2.27) constitute the steady compressible integral relations of momentum and kinetic energy which can be found in standard literature [75, 96]. The left–hand side terms contain temporal derivatives of the inviscid solution at the edge of the boundary layer (subscript e). The inviscid edge velocity is related to the Cartesian velocity components by $u_e = \boldsymbol{q} \cdot \boldsymbol{t}$ where $\boldsymbol{t}$ is the unit tangential vector of the geometry in the streamwise direction ξ. In first order boundary layer theory the inviscid solution is taken on the solid wall.

The system in Eqs. (2.24) and (2.25) contains more unknowns than equations. The four additional unknowns in the right–hand side terms are the shape parameters of kinetic energy thickness H^* and density thickness H^{**} as well as the coefficients of local skin friction C_f and dissipation C_D. Also, the auxiliary density shape factor H_{θ_ϱ} appears on the left–hand side. To close the system, the additional unknowns are correlated with the primary unknowns based on simple analytical solutions and experimental data, for instance for the kinetic energy thickness shape parameter,

$$H^* = H^*(\delta^*, \theta, M_e, Re_\theta), \tag{2.28}$$

where the local edge Mach number M_e and the Reynolds number Re_θ based on the momentum thickness represent the inviscid solution. Upstream history effects on the Reynolds stresses, modelled as part of the dissipation coefficient C_D, are introduced via a transport equation for the shear–stress coefficient $C_\tau^{0.5}$ as a scaled representation of the Reynolds stresses.

The transport equation to correct the basic two equation model is derived from the turbulence kinetic energy equation with appropriate boundary layer assumptions, a detailed derivation of which is presented in Appendix A. Write in compact form,

$$\frac{\partial C_\tau^{0.5}}{\partial t} + \frac{C_\tau^{0.5}}{u_e}\frac{\partial u_e}{\partial t} = \mathcal{R}_{C_\tau^{0.5}}, \tag{2.29}$$

with the right–hand side operator given by

$$\mathcal{R}_{C_\tau^{0.5}} = -u_e\left(\frac{\partial C_\tau^{0.5}}{\partial \xi} - C_\tau^{0.5}\frac{K_c}{2\delta}\left(C_{\tau_{eq}}^{0.5} - a_2 C_\tau^{0.5}\right) - C_\tau^{0.5}\mathcal{Q}_{eq} - \frac{C_\tau^{0.5}}{u_e}\frac{\partial u_e}{\partial \xi}\right)\frac{u}{u_e}, \tag{2.30}$$

and the constants K_c and u_e/u set to 5.6 and 1.5, respectively. Equation (2.29) is solved in the turbulent region of the boundary layer (following fixed transition) in addition to the basic integral system.

Details about the closure relations including the additional unknowns of the third governing equation are given in Appendix A. Assuming that the unsteadiness in the boundary layer is quasi–steady, the closure correlations derived for steady flow are used in the current formulation.

The primary effect of the boundary layer and wake on the outer inviscid flow is to displace the inviscid flow by a distance equal to the displacement thickness [97]. Generally, two basic concepts can be found in the literature to model this displacing effect. One approach, referred to as the "displacement body" model, modifies the shape of the actual geometry according to the displacement thickness and applies the wall boundary condition on the thickened geometry. The second approach, the "blowing velocity" model, calculates a wall–normal velocity based on the information from the viscous solution and imposes it on the solid wall of the original geometry and the wake

centre line. The blowing velocity given by

$$v_b = \frac{1}{\varrho_e}\frac{\partial}{\partial \xi}\left[\varrho_e u_e \delta^*\right] \tag{2.31}$$

is derived from mass conservation, details of which are presented in Appendix A. For the free wake, two shear layers are calculated. Along the wake cut, used as the dividing streamline, a jump in the normal velocity component is now imposed through the blowing velocity. The conditions for density remain unchanged.

The boundary layer equations form a one dimensional model in space. Similar flow is assumed at the upstream boundary. This is that velocity profiles at different streamwise locations can be mapped onto one another when choosing an appropriate scaling reducing the number of independent variables [75, 96]. Then, the derivatives in the governing equations are set at the upstream boundary to analytical values following similar boundary layer theory [87, 98].

2.2.3 Discretising and Solving

The full potential formulation is discretised using a two dimensional, unstructured, vertex–centred, finite–volume scheme. Here, a finite number of non–overlapping dual cells (control volumes), formed around the vertices, constitute the computational domain with the unknowns of density and velocity potential stored at the vertices. A representative unstructured triangular mesh including a typical dual cell is shown in Fig. 2.1(b). The governing equations are applied to each dual cell in turn.

Write the continuity equation defined in Eq. (2.16) in conservative integral form,

$$\frac{d\varrho}{dt} + \frac{1}{V}\int_{\partial V} \varrho \nabla \Phi \cdot \boldsymbol{n}\, dS = 0\,, \tag{2.32}$$

where the latter expression is valid for any constant control volume V with non–moving boundaries ∂V. The convective fluxes $\varrho \nabla \Phi$ are evaluated by a second order spatial scheme using a linear least squares reconstruction (allowing an arbitrary number of support vertices). Here, the velocity vector is approximated from the velocity potential by a reconstruction at the dual cell edges, while the upwinded density is evaluated by a vertex–centred, slope–limited gradient scheme. This density gradient scheme was found to be essential in the current formulation to obtain a stable eigenvalue spectrum for the exact system Jacobian matrix of the spatial discretisation.

Using the vertex–based reconstruction for the velocity components, discretising the unsteady Bernoulli equation as given in Eq. (2.21) is straightforward. The circulation convection equation of the wake model in Eq. (2.23) is easily approximated using a first order upwind scheme along the ordered vertices of the wake cut starting from the first vertex off the trailing edge.

Starting from the stagnation point around the leading edge of the aerofoil two boundary layers (including the free wakes behind the aerofoil) develop, on the suction and pressure side. The integral boundary layer equations are discretised along the ordered edges of the solid surface and the wake cut forming the boundary layer system. The spatial derivatives of the boundary layer residuals in Eqs. (2.26), (2.27) and (2.30) are discretised using a first order upwind scheme. All other quantities are taken or evaluated at the current streamwise station. To form the exact Jacobian matrix terms, the closure correlations are differentiated analytically with respect to the primary unknowns of the formulation.

Boundary conditions are set using one layer of halo vertices which provide the required behaviour on the boundary itself. At far field boundaries, halo vertices simply take on freestream values assuming the flow to return to uniform conditions. At solid boundaries and the wake cut, the halo dependence of the reconstructed flow variables is isolated giving simple algebraic expressions for the halo values. A transpiration boundary condition is used to set the flow tangency condition at solid surfaces. Here, the transpiration normals of the deflected geometry are applied at the original location which remains fixed at all times. In addition, the Kutta condition is implemented by applying the solid boundary condition to the first edge off the trailing edge on both sides of the wake cut. This sets the direction of the flow so that it leaves the trailing edge smoothly. The wall normal blowing velocity v_b for the boundary layer coupling is evaluated by a first order difference along the boundary without dependence on halo values.

A detailed discussion of the applied spatial scheme to discretise the formulation of the full potential equations together with the correction models is given in Appendix B. In addition, the expressions required to form the exact Jacobian matrices of the applied spatial discretisation scheme analytically are presented.

Spatially discretising the governing equations results in a set of ordinary differential equations in time written in semidiscrete notation as

$$B_{ff}\,\frac{d\boldsymbol{w}_f}{dt} = \boldsymbol{R}_f(\boldsymbol{w}_f), \tag{2.33}$$

where $\boldsymbol{w}_f$ and $\boldsymbol{R}_f$ denote the vectors of fluid unknowns and corresponding residuals. The baseline model contains $n_f = 2n_{cv}$ unknowns where n_{cv} is the number of control volumes. The correction models only add relatively little to the costs extending the size to about $n_f \approx 2.1n_{cv}$. For convenience, write the fluid unknowns as $\boldsymbol{w}_f = \left[\boldsymbol{w}_p, \boldsymbol{w}_v\right]^T$ with p indicating the full potential model including the wake treatment and v indicating the viscous model. Accordingly, the residual is formed. The matrix B_{ff} describes the coupling in the unsteady terms between the individual models, essentially due to the integral boundary layer model, and is partitioned in blocks according to the vectors of unknowns and residuals.

A steady state solution of the fluid problem satisfies $\boldsymbol{R}_f = 0$. The roots of this nonlinear function are found using Newton's method,

$$A_{ff}\,\Delta \boldsymbol{w}_f = -\boldsymbol{R}_f(\boldsymbol{w}_f^{\nu}), \tag{2.34}$$

with $\Delta \boldsymbol{w}_f = \boldsymbol{w}_f^{\nu+1} - \boldsymbol{w}_f^{\nu}$ and the required Jacobian matrix A_{ff} given as

$$A_{ff} = \frac{\partial \boldsymbol{R}_f}{\partial \boldsymbol{w}_f} = \begin{pmatrix} A_{pp} & A_{pv} \\ A_{vp} & A_{vv} \end{pmatrix}, \tag{2.35}$$

following B_{ff} in its block structure. For the first few iterations, especially in transonic flow, the Newton updates are under–relaxed to smooth out the initial flow field and to provide a reasonable approximation to the converged solution. To achieve quadratic convergence, the matrix A_{ff}, evaluated analytically, is the exact Jacobian matrix of the applied spatial scheme. Currently, the resulting linear systems are solved by a direct solver [99].

For unsteady simulations, temporal integration is accomplished by the dual time stepping method [83] as presented earlier. Approximating the temporal derivative by a second order backward difference, the pseudo residual $\boldsymbol{P}_f$ is written as

$$\boldsymbol{P}_f = \boldsymbol{R}_f(\boldsymbol{w}_f^{n+1}) - B_{ff}\,\frac{3\boldsymbol{w}_f^{n+1} - 4\boldsymbol{w}_f^{n} + \boldsymbol{w}_f^{n-1}}{2\Delta t} \tag{2.36}$$

and solved by Newton's method with the coupled system being iterated to a steady state in pseudo time at each real time step n. For convenience, the pseudo Jacobian matrix is evaluated by assuming the matrix B_{ff} to be constant. This is justified on the grounds that the matrix has a dominant diagonal contribution close to unity, whereas off–diagonal terms (due to the boundary layer model) are small. The convergence rate is not dramatically reduced by this simplification.

Similarly, for coupled time–accurate aeroelastic simulations, the fluid system is augmented by the structural model and solved by the dual time stepping method with fluid and structural unknowns being updated simultaneously in pseudo time.

Chapter 3

Full Potential Benchmarking

Results are presented for validation purposes and to build confidence in the developed unsteady full potential flow solver which is applied to the aeroelastic stability analysis in the following chapters. Standard aerofoil test cases are shown and compared with higher fidelity flow models, such as the Euler and Reynolds–averaged Navier–Stokes equations, as well as experimental data where available.

The parallel multiblock flow solver applied in this study to solve the Euler and Navier–Stokes equations is an established research code which has been optimised and validated for more than a decade [73]. The application to aerofoil cases is presented alongside the results for the full potential flow solver. The wide variety of unsteady three dimensional flow problems, which have been simulated, includes high speed turbulent cavity flow [100], rotorcraft flow [101, 102], vortical flow of whole fighter aircraft [103, 104], and wing flutter [25, 53]. Due to this plethora of results, additional validation cases for the parallel multiblock solver are not considered herein.

3.1 LNV109A – Low Reynolds Number Aerofoil

The LNV109A aerofoil, the profile of which is included in Fig. 3.1(a), resulted from a design study [105] to constrain the pitching moment coefficient (about the quarter chord point) at about -0.05 whilst creating a maximum lift coefficient of 1.8 at a low Reynolds number of about 0.4 million. Its maximum thickness is 13% of the chord length. Experimental data (where available) were obtained from [105] and are compared with numerical simulations using the linear potential solver Xfoil [92] including the boundary layer formulation (LPv) and the viscous version of the current full potential formulation (FPv). Experimental flow conditions (specifically the angle of attack), included in Fig. 3.1(a), are adjusted for the assumed free flight conditions of the simulations to account for wall interference effects present in the wind tunnel. The chosen angle of attack for the numerical simulations follows the discussion in [88] for the same aerofoil

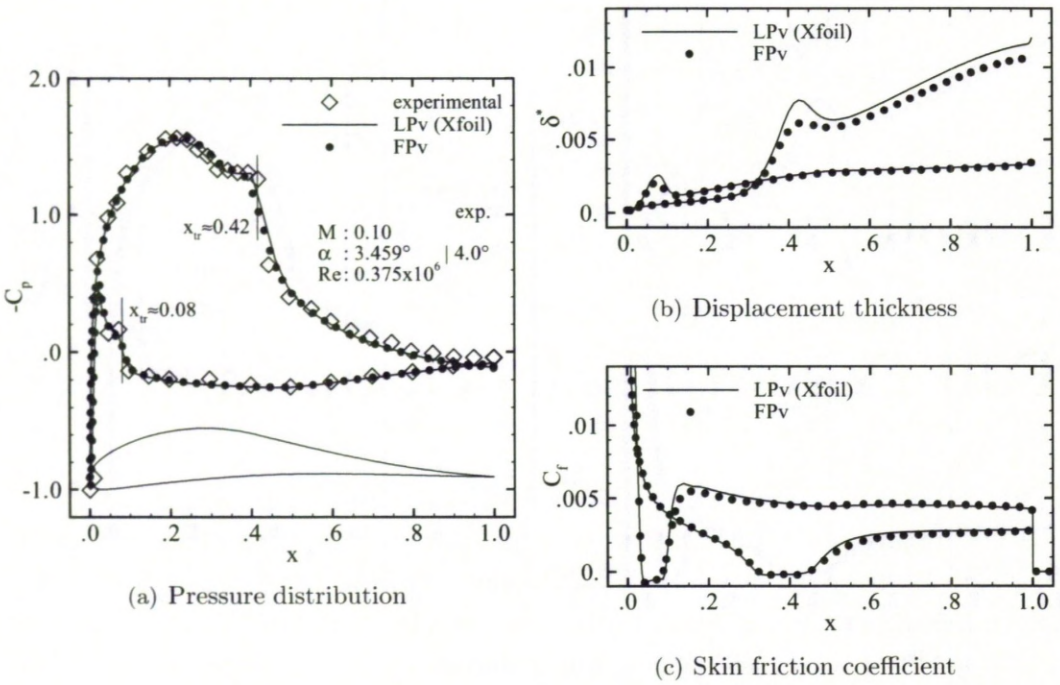

(a) Pressure distribution

(b) Displacement thickness

(c) Skin friction coefficient

Figure 3.1: Pressure distribution and boundary layer quantities of LNV109A aerofoil case showing comparisons of measurements as presented in [105] and simulations using LPv (from Xfoil [92]) and FPv flow models; results are presented for LPv simulation with 279 surface points and for FPv simulation with 420 surface points and 7,400 total points.

case. Several grid sizes were used for both the LPv and FPv simulations as indicated in Table 3.1.

Figure 3.1 presents results of steady state simulations showing the pressure distribution as well as selected boundary layer quantities. In Fig. 3.1(a) the pressure distribution shows excellent agreement between simulations and measurements. The agreement between the two simulations is not surprising since the integral boundary layer model in the FPv formulation applies the closure correlations as used in Xfoil. Laminar separation due to the adverse pressure gradient is found on the upper and lower surface with turbulent reattachment at $x_{tr} \approx 0.42$ on the upper and $x_{tr} \approx 0.08$ on the lower surface, respectively. While the transition location is predicted as part of the solution in Xfoil, it is imposed in the FPv simulation according to the results from the simulation in Xfoil. This is required as a transition model has currently not been implemented in the FPv formulation.

Interestingly, despite having slightly different values of displacement thickness in the region downstream of the transitional separation bubble on the upper surface, as is found in Fig. 3.1(b), the pressure comparison is excellent. The different development should be related to the treatment of the separation region due to the numerical imple-

	points	lift	moment	drag
experimental	/	0.791	−0.060	0.0169
LPv (Xfoil)	101	0.790	−0.0519	0.01963
	279	0.797	−0.0511	0.01815
FPv	105 (1,700)	0.792	−0.0476	0.01426
	220 (3,500)	0.784	−0.0517	0.01660
	420 (7,400)	0.785	−0.0516	0.01603

Table 3.1: Coefficients of integrated aerodynamic forces and moments for LNV109A aerofoil case; column "points" indicates number of surface points (and total number of points for FPv grids).

mentation of the model as well as the grid resolution in this particular region. However, for the coupling of the viscous model with the inviscid flow solver using the blowing velocity concept described in Eq. (2.31), the streamwise derivative of the displacement thickness (rather than the displacement thickness itself) is required in both Xfoil [92] and the FPv formulation. As can be seen in the figure, while the absolute values of the displacement thickness differ, the slope of the curves looks very similar. The agreement for the skin friction coefficient in Fig. 3.1(c) is good and shows the shallow transitional separation regions on the upper and lower surface.

A comparison of integrated aerodynamic forces and moments for the LNV109A aerofoil case is given in Table 3.1. It can be seen that the design constraint on the pitching moment coefficient is approximately satisfied (while the considered angle of attack does not correspond to the maximum lift). The FPv simulations using the different grid sizes demonstrate reasonable grid convergence.

3.2 RAE 2822 – Supercritical Aerofoil

The experimental data base of [106] provides steady measurements of pressure distributions and boundary layer quantities in the sub- and transonic flow regime for the supercritical RAE 2822 aerofoil. Results for cases 2 (subsonic) and 9 (transonic) are shown in Figs. 3.2 through 3.4 and Table 3.2. The simulations were done assuming free flight conditions. Hence, the numerical flow conditions were adjusted to match the experimental data subject to wall interference effects. The freestream Mach number and angle of attack were varied to match the integrated aerodynamic forces and moments, cf. Table 3.2. The numerical and experimental flow conditions are included in Fig. 3.2 for comparison. The Reynolds–averaged Navier–Stokes (RANS) simulations were done on a 3–block C–type structured grid with 524×78 control volumes whereas an unstructured triangular grid with sixteen thousand control volumes was used for the simulations with the FP baseline solver.

	Case 2			Case 9		
	lift	moment	drag	lift	moment	drag
experimental	−0.121	−0.028	0.0079	0.803	−0.099	0.0168
RANS (SA)	−0.112	−0.080	0.0093	0.799	−0.093	0.0195
RANS (SST)	−0.115	−0.080	0.0071	0.806	−0.093	0.0172
FPv	−0.121	−0.079	0.0083	0.809	−0.095	0.0191

Table 3.2: Coefficients of integrated aerodynamic forces and moments for RAE 2822 aerofoil cases.

Pressure distributions are presented in Fig. 3.2. The full potential simulations corrected for viscous effects (FPv) give an overall good agreement with the experiments for both cases just as the RANS results. Negligible differences can be found between the results of the two turbulence models. Here, for the RANS simulations both the Spalart–Allmaras (SA) and the k–ω (SST) turbulence models were used. A comparison of the integrated aerodynamic force and moment coefficients is presented in Table 3.2. The pitching moment is taken around the quarter chord point. Note that the value for the moment coefficient of test case 2 seems to be a typographical error in the experimental data base. The aerodynamic coefficients of lift force, pitching moment and drag force correspond in their agreement to the experimental data just as the pressure distributions. The iso–contour lines of the pressure field around the aerofoil are shown in Fig. 3.3. It can be seen that a sharp shock resolution is predicted by both the RANS and FPv flow models.

Several boundary layer quantities such as integral thicknesses and shape parameters were compared for the different numerical models and experimental data (where available). The results of displacement thickness δ^* and local skin friction coefficient C_f are shown in Fig. 3.4. The forced transition locations, specified according to the information given in the experimental data base, are clearly visible in the skin friction coefficient for the FPv results. While integral thicknesses are readily available as part of the FPv solution, the corresponding boundary layer quantities of the RANS simulations have to be extracted from the flow solutions (i.e. velocity profiles) by numerically integrating the definitions of the various quantities, such as the expression for the displacement thickness in Eq. (A.10), outward from the wall to the edge of the boundary layer defined herein by vanishing eddy viscosity.

The FPv results agree reasonably well with experimental data and also with the RANS simulations, especially for the subsonic case. In the transonic case, not surprisingly, more disagreement between the results is found. Here, the region of the shock boundary layer interaction should be emphasised where the assumptions of the first order boundary layer theory are likely to be violated. Despite the discrepancies in the

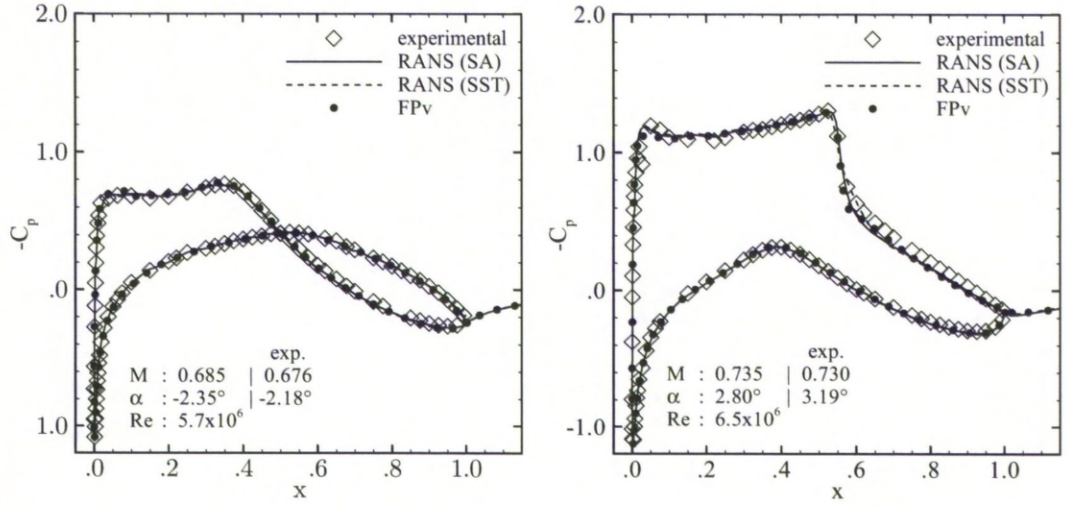

(a) Case 2 (b) Case 9

Figure 3.2: Pressure distributions of RAE 2822 aerofoil cases showing comparisons of measurements as presented in [106] and simulations using FPv and RANS flow models.

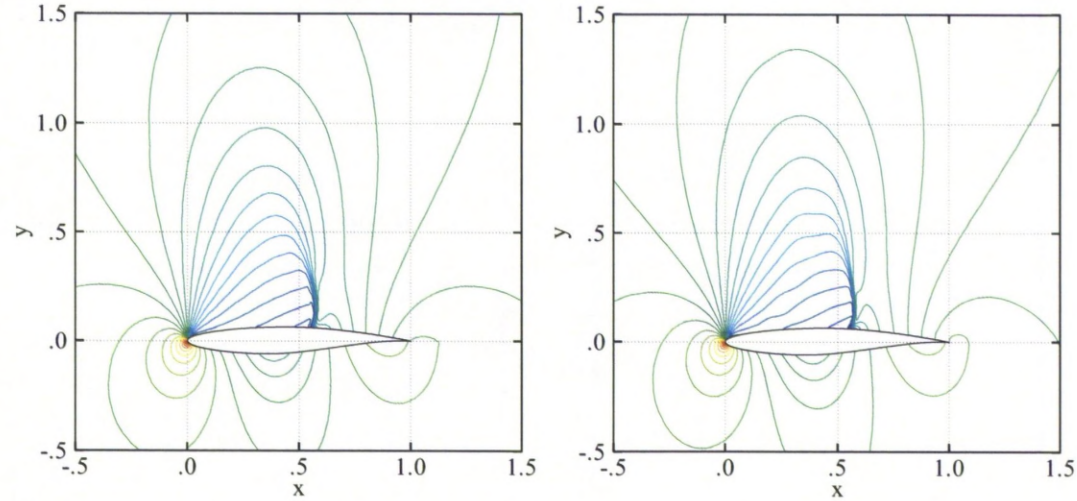

(a) Case 9 – FPv (b) Case 9 – RANS (SA)

Figure 3.3: Iso–contour lines showing pressure field of RAE 2822 aerofoil case 9; comparisons of simulations using FPv and RANS (SA) flow models.

boundary layer quantities the agreement in the pressure distributions is not significantly affected. Interestingly, measurements for the same streamwise position but at different spanwise locations show distinct spread in the experimental data suggesting three dimensional effects and also measurement uncertainty. The differences between the two turbulence models of the RANS simulations especially for the skin friction coeffi-

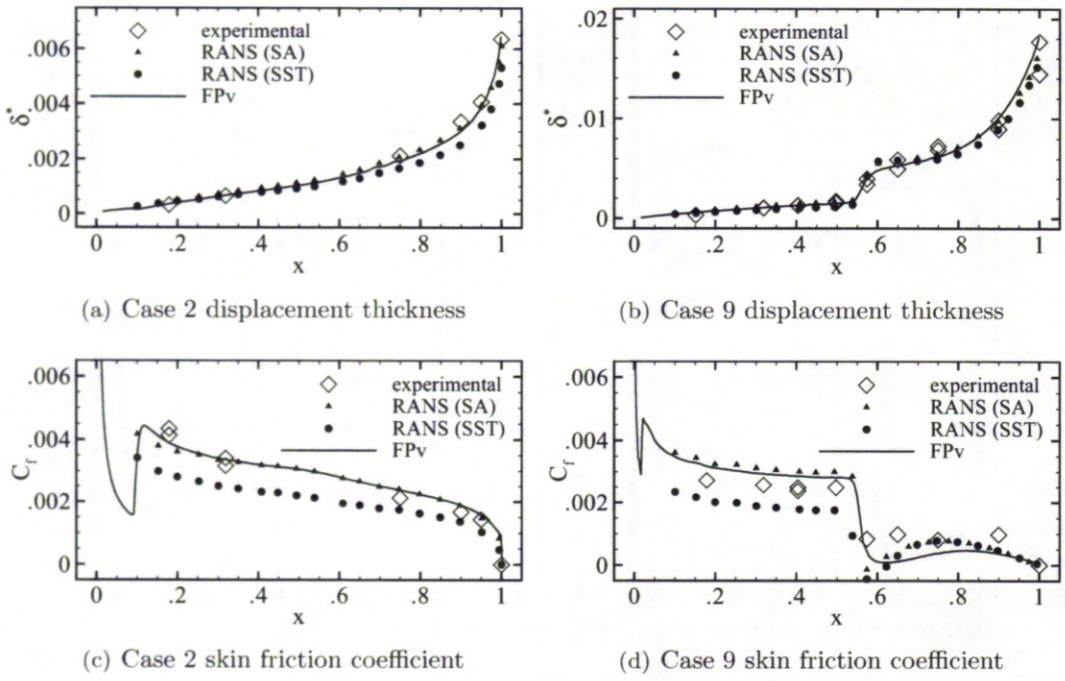

(a) Case 2 displacement thickness

(b) Case 9 displacement thickness

(c) Case 2 skin friction coefficient

(d) Case 9 skin friction coefficient

Figure 3.4: Distributions of displacement thickness and skin friction coefficient on upper surface of RAE 2822 aerofoil showing comparison of measurements from [106] and simulations using FPv and RANS flow models for cases 2 and 9.

cient illustrate a problem of turbulent closure in fluid mechanics with the applicability of a specific model depending on the flow under consideration. Also, the numerical implementation of a distinct turbulence model should be considered.

3.3 NACA 0012 – AGARD CT1

Figures 3.5 and 3.6 present results of forced pitching motion simulations using four aerodynamic models and compare with experimental data of the AGARD CT1 test case [107]. The configuration CT1 exhibits intermittent shock motion during the cycle of motion. It is defined for the NACA 0012 aerofoil at a freestream Mach number of 0.6 and a chord Reynolds number of 4.8 million. The periodic forcing about the quarter chord is prescribed by a sinusoidal motion

$$\alpha(t) = \alpha_0 + \alpha_a \sin(2\,k\,t), \tag{3.1}$$

with a reduced frequency of $k = 0.0808$, a mean incidence of $\alpha_0 = 2.89°$ and a pitch amplitude of $\alpha_a = 2.41°$. The FPv and RANS simulations are assumed to be fully turbulent. Five motion cycles with 128 steps in each were simulated. The Euler and RANS simulations were done on a 3–block C–type structured grid with 308×50 and

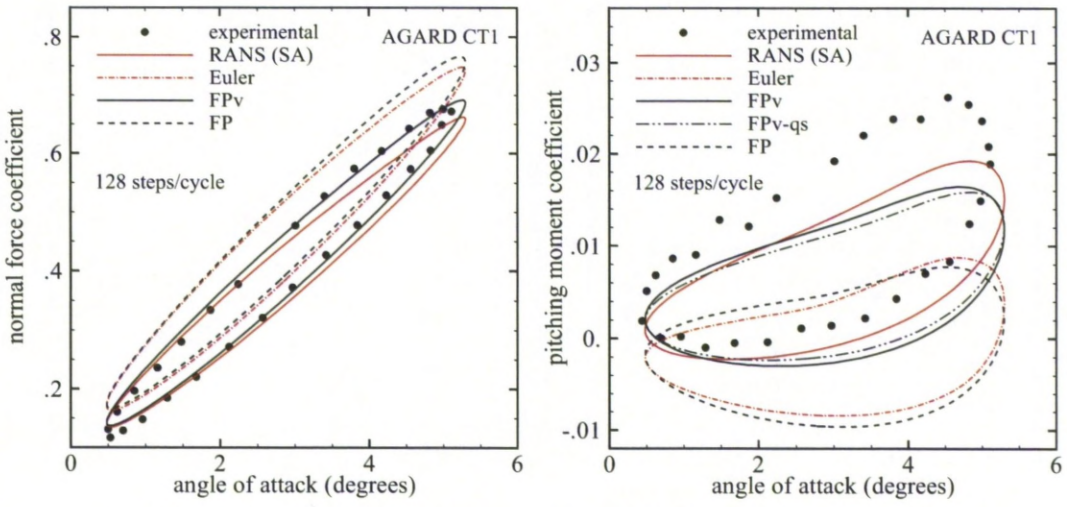

(a) Normal force coefficient

(b) Pitching moment coefficient

Figure 3.5: Normal force and pitching moment coefficient for forced pitching motion test case of AGARD CT1 [107]; comparison of different flow models with experimental data.

524×58 control volumes, respectively, while the FP simulations used an unstructured grid with twelve thousand control volumes.

Normal force and pitching moment coefficients are shown in Fig 3.5. The overall agreement of the FP model with and without boundary layer coupling compared with the results of the higher fidelity models should be considered as good, also in view of results of coupled inviscid/viscous simulations as presented in [108]. The unsteady FPv results were obtained by assuming that the matrix B_{ff} in Eq. (2.33) is the identity matrix. It was found (and these results are not presented here) that the contribution of the matrix blocks B_{vv} and B_{vp} to the unsteadiness in the FPv simulation is negligible. Also, a quasi–steady (qs) simulation is shown in Fig. 3.5(b) where all unsteady terms in the boundary layer model are omitted and a steady boundary layer is calculated at each real time step of the unsteady simulation. The results suggest indeed that a quasi–steady assumption of the boundary layer model is a sufficient simplification as it is commonly done for integral boundary layer simulations.

The inviscid results show a consistent trend compared with viscous simulation results and experiments. For the highest angles of attack during one cycle of motion the differences between results at low and high modelling fidelities, especially for the normal force coefficient, are more distinct. This might partly be attributed to the use of the transpiration boundary condition in the FP baseline solver, where the grid is not moved during the unsteady simulation and only the wall normals are orientated according to the deflection of the geometry to set the required boundary condition. This approximation, as useful and convenient as it is, obviously loses accuracy with increasing deflection angles.

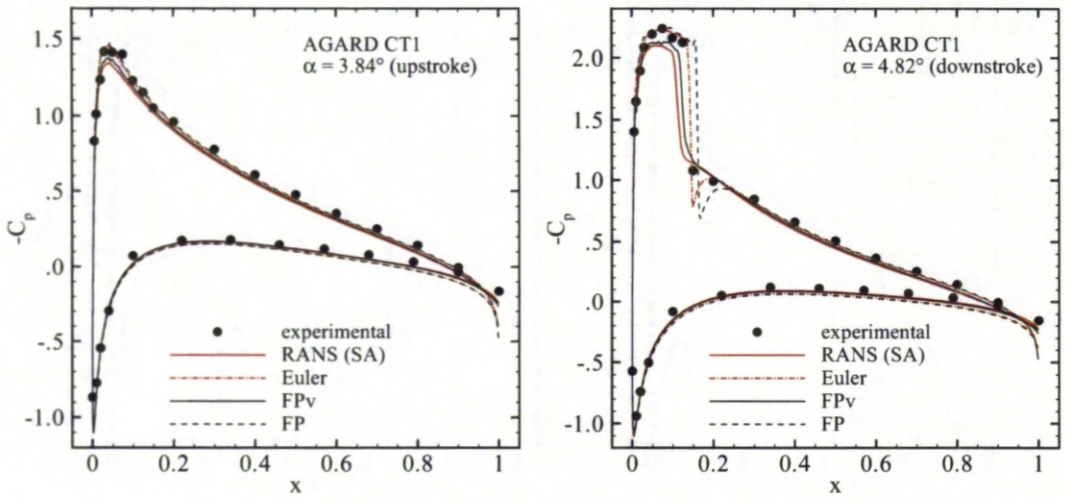

(a) $\alpha = 3.84°$ (upstroke)

(b) $\alpha = 4.82°$ (downstroke)

Figure 3.6: Unsteady pressure distributions for forced pitching motion test case of AGARD CT1 [107]; comparison of different flow models with experimental data at two angles of attack during upstroke and downstroke.

An additional explanation is the slight differences of the resolved shock wave (location and strength) formed during parts of the cycle of motion as can be seen in Fig. 3.6 for both the inviscid and viscous comparisons. The figure presents unsteady pressure distributions at two angles of attack during one cycle of motion and compares numerical results with the experimental data. Inviscid and viscous agreements between the flow models are excellent except for the aforementioned shock location. Additional simulations, using a grid partially refined in the region of the forming shock wave, were done for the FP and FPv flow models confirming that the chosen grid with twelve thousand control volumes gives reasonably grid converged solutions. This suggests that in this case the strength of the formed intermittent shock wave may violate the FP modelling assumptions.

To explain the relatively large difference for the pitching moment coefficient between the RANS results and the experimental data in Fig. 3.5, published results in [109] showed that shifting the centre for the moment calculation by a few percent of the chord length resulted in better agreement.

Chapter 4

Eigenvalue Stability Formulation

An eigenvalue–based method for aeroelastic stability analyses, referred to as the Schur complement eigenvalue method, is described in this chapter. The baseline Schur formulation has previously been applied for the stability analysis of several wing and aircraft configurations [55] to study uncertainty in the predicted instability due to structural variability [22]. A modified structural eigenvalue problem, corrected by an interaction term which depends on the response frequency and the steady state solution, describes the coupled aeroelastic system. The generation and approximation of the interaction term, representing the influence of the high dimensional computational fluid dynamics (CFD) system, is discussed. The approximation is done by reconstruction based on samples which can be generated using a frequency or time domain solver.

4.1 Schur Complement Eigenvalue Method

Write the aeroelastic system in semidiscrete state–space form as

$$\dot{\boldsymbol{w}} = \boldsymbol{R}(\boldsymbol{w}, \mu), \tag{4.1}$$

where the vector of unknowns $\boldsymbol{w} = \left[\boldsymbol{w}_f, \boldsymbol{w}_s\right]^T$ contains fluid and structural contributions, and $\boldsymbol{R}$ is the corresponding residual vector[1]. The system depends on an independent parameter μ, typically representating the dynamic pressure. An equilibrium solution $\boldsymbol{w}_0$ of the nonlinear system satisfies $\boldsymbol{R}(\boldsymbol{w}_0, \mu) = 0$. In transonic flow the importance of the equilibrium manifests itself in the observation that a shock associated nonlinearity (strength and location) is defined in the steady flow, while unsteady perturbations about this steady state can be considered to be linear [110].

The theory of dynamic systems gives criteria for an equilibrium to be stable. In particular, stability is determined by eigenvalues, $\lambda = \sigma \pm i\omega$, of the system Jacobian

[1] As discussed in the previous chapters, the matrix B on the left–hand side in the full potential formulation in Eq. (2.33) is taken to be the identity matrix because its contribution to the unsteady problem is negligible and the following discussion is simplified.

matrix $A(\boldsymbol{w}_0, \mu)$ evaluated at the steady state and chosen values of μ. A stable system has all its eigenvalues with a negative real part. The number of eigenvalues associated with the loss of stability is typically small. In many aeroelastic problems a pair of complex conjugate eigenvalues with zero real part marks the onset of an instability of the Hopf type leading to flutter and limit–cycle oscillation (LCO).

Linear stability is predicted by solving the standard eigenvalue problem

$$\left(A - \lambda I\right) \boldsymbol{p} = 0, \tag{4.2}$$

where the Jacobian matrix A is conveniently partitioned in blocks expressing the different dependencies,

$$A = \frac{\partial \boldsymbol{R}}{\partial \boldsymbol{w}} = \begin{pmatrix} A_{ff} & A_{fs} \\ A_{sf} & A_{ss} \end{pmatrix}. \tag{4.3}$$

Importantly, the matrix A is the exact Jacobian matrix of the applied spatial discretisation scheme.

In computational aeroelasticity, the structural system is commonly modelled by a small number n of normal modes while the fluid is represented by the high dimensional CFD system. Then, the Jacobian matrix has a large, but sparse, matrix block A_{ff} surrounded by thin strips for A_{fs} and A_{sf} describing the coupling between the fluid and structure. The block A_{ff} is the exact Jacobian matrix of the fluid system (herein applying a second order spatial discretisation scheme), while the structural block A_{ss} follows from the structural model (which will be discussed in Chapter 5). The block A_{fs} models the influence of the structural motion (i.e. grid location and speed) on the surrounding fluid. The block A_{sf} gives the dependence of the structural system on the fluid unknowns through the pressure forces. All matrices were tested by forming products against random vectors and comparing with the results from matrix–free evaluations. Also, having quadratic convergence in the time domain solver, using Newton's method, is an important test for the matrices. More details about the evaluation of the Jacobian matrices can be found in [52–54].

To solve the full eigenvalue problem in Eq. (4.2), the system is augmented by scaling the eigenvector $\boldsymbol{p}$ against a real–valued constant vector $\boldsymbol{c}$ to produce a unique solution. The resulting system,

$$\begin{pmatrix} \left(A - \lambda I\right) \boldsymbol{p} \\ \boldsymbol{c}^T \boldsymbol{p} - i \end{pmatrix} = 0, \tag{4.4}$$

is solved for the unknowns $\left[\boldsymbol{p}, \lambda\right]^T$ using Newton's method. The choice of $\boldsymbol{c}^T \boldsymbol{p} = i$ to augment the eigenvalue problem is arbitrary.

To achieve convergence for this augmented full eigenvalue problem using Newton's method, good initial values of the eigensolution are required. Therefore, the shifted inverse power method (IPM) is applied [111]. The IPM is an algorithm to calculate

the dominant eigensolution of a given diagonalisable $m \times m$ matrix A with distinct eigenvalues $\lambda_1, \lambda_2, \ldots, \lambda_m$ and linearly independent eigenvectors $\boldsymbol{p}_1, \boldsymbol{p}_2, \ldots, \boldsymbol{p}_m$. For any eigensolution $(\boldsymbol{p}_j, \lambda_j)$, a constant (shift) λ_0 can be chosen so that $\widehat{\lambda} = (\lambda_j - \lambda_0)^{-1}$ is the dominant eigenvalue of $(A - \lambda_0 I)^{-1}$. Iterating converges to the dominant eigensolution with $\boldsymbol{p}_j = \widehat{\boldsymbol{p}}$ and $\lambda_j = \lambda_0 + 1/\widehat{\lambda}$. The structural frequencies are conveniently chosen as the shift λ_0. An approximate Jacobian matrix, corresponding to a lower order spatial discretisation scheme, was found to be sufficient and necessary for the IPM to provide an initial guess for the augmented system at reasonable cost [52].

Solving the full eigenvalue problem in Eq. (4.4) through shift and invert methods results in an increasingly ill–conditioned system as the converged eigenvalue is approached. To avoid this, the eigenvector $\boldsymbol{p}$ is partitioned into unknowns corresponding to fluid and structural contributions [55]. Then, the Schur complement eigenvalue problem is given as

$$S(\lambda)\, \boldsymbol{p}_s = 0 \tag{4.5}$$

which is a small nonlinear eigenvalue problem of dimension n_s where $n_s = 2n$ is the number of structural unknowns (state variables). The Schur complement matrix $S(\lambda)$, obtained by block Gaussian elimination of A_{sf} from A, is explicitly written as

$$S(\lambda) = (A_{ss} - \lambda I) - A_{sf}\, (A_{ff} - \lambda I)^{-1} A_{fs}. \tag{4.6}$$

The first term on the right–hand side defines the structural eigenvalue problem and is denoted as $S^s = A_{ss} - \lambda I$, while the second part constitutes the interaction (coupling) term $S^c = -A_{sf}\, (A_{ff} - \lambda I)^{-1} A_{fs}$. Thus, the stability calculation is formulated as a modified structural eigenvalue problem corrected by the influence of the fluid system. As the interaction goes to zero, the structural eigenvalue problem is restored. The similarity to the classical linear stability analysis is discussed in Section 4.4.

Note that, having a solution $\left[\boldsymbol{p}_s, \lambda\right]^T$ for Eq. (4.5), the fluid eigenvector is obtained by one more linear solve, $(A_{ff} - \lambda I)\, \boldsymbol{p}_f = -A_{fs}\, \boldsymbol{p}_s$. This is useful when the system response after the instability onset is of interest, particularly for limit–cycles oscillations. An approach, based on the centre manifold theorem, to reduce the full order dynamics into a two degrees–of–freedom system in the critical mode has been successfully demonstrated in [54].

To solve the small complex–valued eigenvalue problem in Eq. (4.5), the system is augmented to scale the structural eigenvector $\boldsymbol{p}_s$ against an arbitrary real–valued constant vector $\boldsymbol{c}_s$, i.e. augment by the equation $\boldsymbol{c}_s^T \boldsymbol{p}_s = i$. Using the latter expression, where the right–hand side is an arbitrary (constant) choice, produces a unique solution. Then, the augmented nonlinear system is solved for the unknowns $[\boldsymbol{p}_s, \lambda]^T$. While the full eigenvalue formulation describes a problem with $n_f + n_s + 1$ unknowns, the Schur formulation only has $n_s + 1$. The number n_s of structural unknowns is generally small. There are several ways to solve the problem in Eq. (4.5).

An efficient way to solve nonlinear systems are Newton–like methods which require the formation of the residual and its Jacobian matrix. The main cost in either task is to evaluate the interaction term S^c since this involves operations on the high dimensional fluid system, whereas the cost to form the structural term S^s is negligible. Using Newton's method, the interaction term is conveniently evaluated by first forming the right–hand side as the product $A_{fs}\,\boldsymbol{p}_s$ for the current approximation to the eigenvector, and then solving one linear system against $(A_{ff} - \lambda I)$. The solution is then multiplied against the matrix A_{sf} to project the fluid response onto the structural system.

There are n relevant solutions of the nonlinear eigenvalue problem, i.e. n complex conjugate pairs of eigenvalues, and so the cost of forming the interaction term at each Newton iteration for each value of the independent parameter becomes too high. To overcome this, a series approximation [112] of the Schur complement matrix can be written for $\lambda = \lambda_0 + \lambda_\varepsilon$ as

$$S(\lambda) \approx (A_{ss} - \lambda I) - A_{sf}\left(\left(A_{ff} - \lambda_0 I\right)^{-1} + \lambda_\varepsilon \left(A_{ff} - \lambda_0 I\right)^{-1}\left(A_{ff} - \lambda_0 I\right)^{-1} \right) A_{fs} \quad (4.7)$$

where λ_ε is a small variation to the reference value λ_0, which is chosen as a structural frequency or a previously converged solution. Pre–computing the factors in the series against the columns of the matrix A_{fs} (requiring $4n$ linear solves for the first order expansion), allows the application of the expansion in the vicinity of the shift λ_0.

The quasi–Newton method evaluates the (exact) residual by the nonlinear approach given in the previous paragraph, while the series is used for the Jacobian matrix. This is convenient as only one linear solve is required per Newton iteration step once the series factors have been evaluated. The derivative of the Schur complement matrix with respect to the eigenvalue, required for the evaluation of the Jacobian matrix, is then readily available as

$$\frac{\partial S}{\partial \lambda} \approx -I - A_{sf}\left(A_{ff} - \lambda_0 I\right)^{-1}\left(A_{ff} - \lambda_0 I\right)^{-1} A_{fs}. \quad (4.8)$$

The series method also applies the series expansion to the residual which is possible for small λ_ε and for an independent parameter μ not affecting the pre–computed values. Then, the stability analysis becomes very cheap once the series factors are available. The latter condition is true for stability problems without the effects of aerostatic deformation. Including aerostatic effects however, the steady state solution changes with respect to the independent parameter, e.g. the dynamic pressure, and the series factors have to be re–evaluated as the eigenvalues are traced, making the formulation hardly affordable. This will be discussed in detail in Chapter 5.

In this work, as discussed in the next sections, a new method is introduced which avoids these difficulties. The Schur residual and the Jacobian matrix are formed by approximating the Schur interaction term S^c by a reconstruction based on samples, i.e. full order evaluations of this term, covering the parameter space of interest.

4.2 Generating Samples of the Schur Interaction Matrix

The interaction matrix can be formed in both the frequency and time domain. Solving the number of linear systems, according to the number of columns in the matrix A_{fs}, against the matrix $(A_{ff} - \lambda I)$ directly to form the Schur interaction matrix is referred to as the linear frequency domain approach. Here, two related approaches can be used, both of which are outlined in the following.

The first approach requires $n_s = 2n$ linear solves, one for each structural unknown of the state–space representation. This approach is primarily used in this study as it follows the original implementation of the eigenvalue solver [52, 52, 55]. The second approach requires n linear solves, one for each generalised coordinate (structural degree–of–freedom). This way is illustrated alongside the main discussion. Of course, the two methods give identical results for the linear stability analysis.

The fluid residual $\boldsymbol{R}_f(\boldsymbol{w}_f, \boldsymbol{x}, \dot{\boldsymbol{x}})$ depends on the fluid unknowns $\boldsymbol{w}_f$, the grid locations $\boldsymbol{x}$ and the grid velocities $\dot{\boldsymbol{x}}$ while assuming that the grid locations and velocities can be evaluated as a function of the structural unknowns $\boldsymbol{w}_s = \left[\boldsymbol{\eta}, \dot{\boldsymbol{\eta}}\right]^T$ only. The vector $\boldsymbol{\eta}$ contains the generalised coordinates of the structural model. This dependence is either evaluated analytically (as in the FP baseline solver) or by finite differences (as in the multiblock solver for the Euler and Navier–Stokes equations).

Then, using the first approach, the columns of the complex–valued interaction matrix are given as

$$S^{cj} = -A_{sf} \left(A_{ff} - \lambda I\right)^{-1} A^j_{fs} \tag{4.9}$$

where j denotes the structural unknown corresponding to the jth column of the matrices S^c and A_{fs}. Solving the $2n$ linear systems

$$\left(A_{ff} - \lambda I\right) \boldsymbol{y} = A^j_{fs} \tag{4.10}$$

follows the flow solvers with the multiblock code using a tailored preconditioned Krylov subspace iterative algorithm [52, 55] and the FP code using a direct solver [99].

It was found for the aerofoil cases, that the direct solver offers a convenient aspect in the linear frequency domain. As the first step, the direct solver factorises the coefficient matrix $(A_{ff} - \lambda I) = LU$ covering most of the cost. The second step is then to solve the linear systems by performing forward and back substitution on each of the right–hand sides which is cheap using the stored factors L and U. For the relatively small aerofoil cases with about ten thousand control volumes, the direct solver performs better with an increasing number of right–hand sides. Consequently, the evaluation of the factors for the series expansion is rather efficient. This might offer an attractive alternative to the iterative solution scheme for cases with many structural degrees–of–freedom (and thus right–hand sides), and the performance of a parallel direct solver could be considered in future studies.

In the common situation the exact steady state fluid Jacobian matrix A_{ff} of the applied spatial discretisation scheme is not available.[2] Then, the linear systems for the $2n$ columns of the matrix A_{fs} can be solved by iteration after introducing a pseudo time coordinate τ according to

$$\frac{d\boldsymbol{y}}{d\tau} = (A_{ff} - \lambda I)\,\boldsymbol{y} - A^j_{fs}. \tag{4.11}$$

Using an implicit marching scheme (equivalent to the multiblock flow solver), linearising the right–hand side about the pseudo time level ν gives after some rearranging

$$\left((\widetilde{A}_{ff} - \lambda I) - \frac{I}{\Delta\tau}\right)\Delta\boldsymbol{y} = -(A_{ff} - \lambda I)\,\boldsymbol{y}^\nu + A^j_{fs} \tag{4.12}$$

with $\Delta\boldsymbol{y} = \boldsymbol{y}^{\nu+1} - \boldsymbol{y}^\nu$. Note that the matrix $\widetilde{A}_{ff}$ on the left–hand side is an approximate fluid Jacobian matrix, while the right–hand side requires the correct expression for $A_{ff}\,\boldsymbol{y}^\nu$. Therefore, two residual evaluations are sufficient according to

$$A_{ff}\,\boldsymbol{y}^\nu = \frac{\boldsymbol{R}_f(\boldsymbol{w}_f + \varepsilon\,\boldsymbol{y}^\nu) - \boldsymbol{R}_f(\boldsymbol{w}_f - \varepsilon\,\boldsymbol{y}^\nu)}{2\,\varepsilon} \tag{4.13}$$

with the residual expanded in a first order Taylor series about the solution $\boldsymbol{w}_f$ as

$$\boldsymbol{R}_f\,(\boldsymbol{w}_f \pm \varepsilon\,\boldsymbol{y}^\nu) = \boldsymbol{R}_f\,(\boldsymbol{w}_f) \pm A_{ff}\,\varepsilon\,\boldsymbol{y}^\nu. \tag{4.14}$$

Importantly, the first term on the right–hand side is zero for a steady state flow solution. If one is desperate as neither an approximate Jacobian matrix is available nor unsteady time–marching (as described next) is desired due to the involved computational cost, using an explicit marching scheme in pseudo time is another option,

$$\boldsymbol{y}^{\nu+1} = \boldsymbol{y}^\nu + \left((A_{ff} - \lambda I)\,\boldsymbol{y}^\nu - A^j_{fs}\right)\Delta\tau, \tag{4.15}$$

where the evaluation of the right–hand side is matrix–free as for the implicit scheme. However, due to the slow convergence of explicit schemes the frequency domain solver would then not be more efficient than unsteady time–marching.

Using the second (alternative) approach, it must be emphasised that the matrix A_{fs} can be written as $A_{fs} = [A_{f\eta}, A_{f\dot{\eta}}]$ to illustrate the dependence of the fluid response on the generalised coordinates $\boldsymbol{\eta}$ and their velocities $\dot{\boldsymbol{\eta}}$ influencing the grid displacements $\boldsymbol{x}(\boldsymbol{\eta})$ and grid velocities $\dot{\boldsymbol{x}}(\dot{\boldsymbol{\eta}})$ of the fluid mesh. Then, it is convenient to write the right–hand side of the linear system in Eq. (4.10) as

$$(A_{ff} - \lambda I)\,\boldsymbol{y} = A^j_{f\eta} + \lambda\,A^j_{f\dot{\eta}}\,, \tag{4.16}$$

[2]It is assumed however, that all the other Jacobian matrix blocks in Eq. (4.3) can at least be evaluated by finite differences.

with the index j now running over the number n of generalised coordinates, thus half the number of structural unknowns n_s. This can be seen by observing that for the state–space representation the structural eigenvector is written as $\boldsymbol{p}_s = \left[\boldsymbol{p}_\eta, \lambda \boldsymbol{p}_\eta\right]^T$ using the expression $\boldsymbol{\eta} = \boldsymbol{p}_\eta \, e^{\lambda t}$ consistent with a linear stability analysis [14]. Then, n linear systems (corresponding to the first n columns of the Schur interaction matrix S^c) are solved for the complex–valued right–hand sides in Eq. (4.16).[3]

Alternatively in the time domain, the interaction matrix is evaluated from a Fourier analysis of unsteady responses forced in the structural states. Therefore, the unknowns are rearranged as the sum of a steady state solution and an unsteady perturbation, $\boldsymbol{w} = \boldsymbol{w}_0 + \delta \boldsymbol{w}$. Corresponding to the first approach in the linear frequency domain, write the fluid part of the aeroelastic system in its time–linearised form,

$$\dot{\boldsymbol{w}}_f = A_{ff} \, \delta \boldsymbol{w}_f + A_{fs} \, \delta \boldsymbol{w}_s, \tag{4.17}$$

with the Jacobian matrices blocks A_{ff} and A_{fs} evaluated at the steady state, and express the unsteady perturbation of the fluid and structure in a truncated exponential Fourier series [113],

$$\delta \boldsymbol{w}_f = \sum_{k=-K}^{K} \boldsymbol{\alpha}_k \, e^{i \, k \, \omega \, t} \qquad \text{and} \qquad \delta \boldsymbol{w}_s = \sum_{k=-K}^{K} \boldsymbol{\beta}_k \, e^{i \, k \, \omega \, t}. \tag{4.18}$$

The temporal derivative of the fluid perturbation follows accordingly,

$$\delta \dot{\boldsymbol{w}}_f = \sum_{k=-K}^{K} i \, k \, \omega \, \boldsymbol{\alpha}_k \, e^{i \, k \, \omega \, t}, \tag{4.19}$$

while the steady state is independent of temporal changes by definition. Using the latter equations substituted in Eq. (4.17), a discrete expression is derived,

$$\sum_{k=-K}^{K} \boldsymbol{\alpha}_k = - \sum_{k=-K}^{K} \left(A_{ff} - i \, k \, \omega I\right)^{-1} A_{fs} \, \boldsymbol{\beta}_k. \tag{4.20}$$

The complex–valued Fourier coefficients ($\boldsymbol{\alpha}_k$ for fluid response and $\boldsymbol{\beta}_k$ for structural forcing) are evaluated from the time signal of the unsteady forced CFD simulation over a period $T = 2\pi/\omega$, with ω as the fundamental frequency, using the standard integral

[3]Note that the same rearrangement of the matrix A_{fs} can be applied to Eqs. (4.6) and (4.7) when using the exact eigenvalue solver. However, this does not result in a cost reduction as the required number of linear solves remains unchanged. For instance, the evaluation of the alternative factors for the series method still requires $4n$ linear solves as the right–hand side would be changed according to $(A_{f\eta} + \lambda_0 A_{f\dot{\eta}}) + \lambda_\varepsilon A_{f\dot{\eta}}$. This is therefore not further pursued for the exact eigenvalue solver, while it is a very useful observation for the sample generation.

expression

$$\boldsymbol{\alpha}_k = \frac{1}{T} \int_{-T/2}^{T/2} \delta \boldsymbol{w}_f(t)\, e^{-i\,k\,\omega\,t}\, dt, \qquad k = 0, \pm 1, \pm 2, \ldots \tag{4.21}$$

and accordingly for the structural contribution $\boldsymbol{\beta}_k$. The structure is either excited at one frequency ω individually or simultaneously at integer multiples k of the fundamental frequency. Also, it can be seen that $\boldsymbol{y} = \boldsymbol{\alpha}_k / \boldsymbol{\beta}_k$ is valid for an excitation in a structural unknown corresponding to the column (of the matrix A_{fs}) and the discrete frequency $\lambda = i\,k\,\omega$ the linear system in Eq. (4.10) is solved for.

After multiplying with the Jacobian matrix block A_{sf} (evaluated analytically or by finite differences), the expression in Eq. (4.20) corresponds to the interaction term with column and magnitude set by the applied structural forcing. Evaluating the Fourier coefficients at integer multiples k of a chosen forcing frequency (provided the system was excited in all these frequencies) gives the interaction matrix components at these discrete frequencies. Specifically, the Fourier coefficients of the fluid response need to be analysed for the discrete control volumes contributing to the aerodynamic forces acting on the structure because the matrix A_{sf}, described in detail in Chapter 5, is nonzero only in the columns corresponding to these control volumes.

Solutions of the fully nonlinear time–accurate system,

$$\dot{\boldsymbol{w}}_f = \boldsymbol{R}_f(\boldsymbol{w}_f, \boldsymbol{w}_s), \tag{4.22}$$

excited in the structural states, approach the time–linearised solution of the system in Eq. (4.17) if the amplitude of the forced motion is sufficiently small, i.e. the unsteadiness in the flow is linearly dependent on the structural motion. The step of using the nonlinear system is required if the Jacobian matrices for the fluid contribution are not available explicitly in a particular CFD code (otherwise the linear frequency domain approach should be used).

Corresponding to the second approach in the linear frequency domain, write the fluid part of the aeroelastic system in its time–linearised form distinguishing between the generalised coordinates of the structure and their corresponding velocities,

$$\dot{\boldsymbol{w}}_f = A_{ff}\, \delta \boldsymbol{w}_f + \left(A_{f\eta}\, \delta \boldsymbol{\eta} + A_{f\dot{\eta}}\, \delta \dot{\boldsymbol{\eta}} \right), \tag{4.23}$$

with the Jacobian matrices blocks A_{ff}, $A_{f\eta}$ and $A_{f\dot{\eta}}$ evaluated at the steady state. The unsteady perturbation of the generalised coordinates and the temporal derivative are expressed in a truncated exponential Fourier series [113],

$$\delta \boldsymbol{\eta} = \sum_{k=-K}^{K} \boldsymbol{\beta}_k\, e^{i\,k\,\omega\,t} \qquad \text{and} \qquad \delta \dot{\boldsymbol{\eta}} = \sum_{k=-K}^{K} i\,k\,\omega\,\boldsymbol{\beta}_k\, e^{i\,k\,\omega\,t}, \tag{4.24}$$

just as the fluid perturbation, to obtain the discrete expression,

$$\sum_{k=-K}^{K} \boldsymbol{\alpha}_k = -\sum_{k=-K}^{K} \left(A_{ff} - i\,k\,\omega I\right)^{-1} \left(A_{f\eta} + i\,k\,\omega\,A_{f\dot{\eta}}\right) \boldsymbol{\beta}_k. \tag{4.25}$$

This latter expression clearly resembles Eq. (4.20), and the discussion proceeds as above. Also, the expression in Eq. (4.16) becomes evident.

The vector of structural unknowns $\boldsymbol{w}_s$ generally consists of n modal amplitudes (to scale a deformation prescribed by the mode shapes) and the corresponding deformation rates giving $2n$ vector components. It must be remarked that, using the first approach, a structural deformation must be excited independently from its deformation rate, i.e. a mathematically inconsistent relation between deflection and velocity, to fill the $2n$ relevant columns of the interaction matrix. This is not physically meaningful in the sense that the grid is moved without a grid velocity, and accordingly, a grid velocity is applied without an actual deflection. On the other hand, using the second approach, the n applied motions are physically meaningful and mathematically consistent giving the n relevant columns of the (alternative) interaction matrix S^c.

In Section 4.4 it will be shown that the interaction matrix can also be evaluated from the generalised forces following an excitation in the structural unknowns. Therefore, instead of individually forming a Fourier decomposition of the response signal in each control volume, contributing to the aerodynamic pressure forces acting on the structure, and premultiplying with the matrix A_{sf} to project the response onto the structural system, the generalised forces can be considered directly. Thus, the matrix A_{sf} can be interpreted as an integration matrix that sums the contributions from all participating control volumes.

The implications of using an undamped eigenvalue $\lambda = i\,k\,\omega$ for the extraction of the fluid response, i.e. considering a simple harmonic motion, are presented in Chapter 5. For the linear stability analysis discussed herein, this is a good enough simplification consistent with the classical flutter analysis used for decades in practical aeroelastic applications.

An example to illustrate the different generation methods, using the first approach only in both the frequency and time domain, is now presented. A NACA 0012 aerofoil configuration defined in [52] as the "heavy case" was excited in all structural states of interest simultaneously in sinusoidal motions at a fundamental (dimensionless) frequency of $\omega = 0.15$ and an amplitude of $\widehat{a} = 1.0 \times 10^{-4}$ (given in radians for the pitch motion). Following the decay of nonperiodic starting transients, one motion cycle simulated with 128 steps is used for evaluating the Fourier coefficients. Three simulations were required to obtain the interaction matrices at three frequencies ($\omega = 0.15$, 0.3, 0.45) while swapping around the factors multiplying the fundamental frequency to have distinct excitations in the structural states corresponding to plunge rate, pitch and pitch

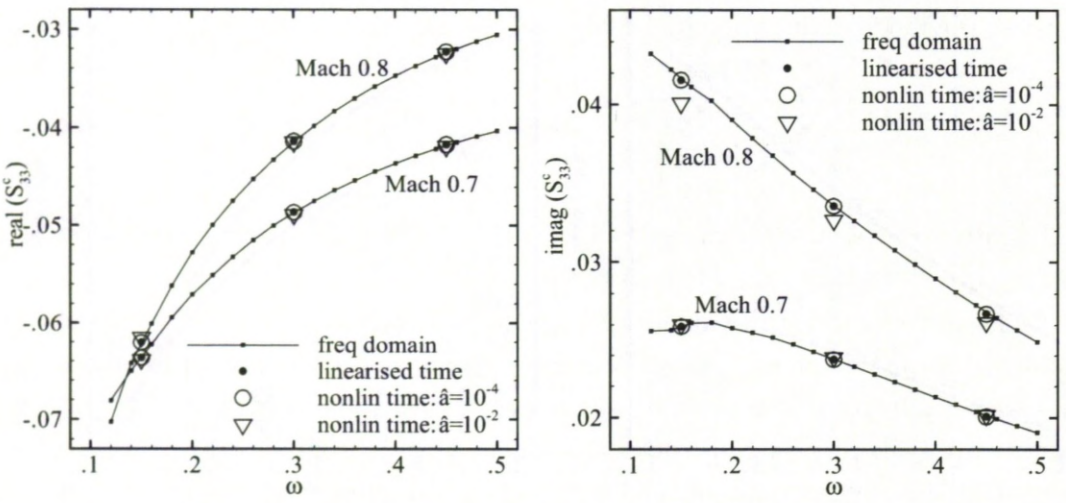

(a) Element real($S^c_{3,3}$)

(b) Element imag($S^c_{3,3}$)

Figure 4.1: Extracted element of Schur interaction matrix for Euler flow model and NACA 0012 configuration showing real and imaginary parts individually; linearised and nonlinear time domain compared with linear frequency domain.

rate. Exciting the plunge coordinate h is irrelevant. In the flow solver used for the aerofoil cases the grid is moved rigidly, and thus the problem is independent of the plunge deflection (not though of the plunge rate).

Two freestream Mach numbers are considered describing a sub- and a transonic case with a strong shock wave. Figure 4.1, showing real and imaginary parts individually, gives an excellent agreement in evaluating a representative element of the interaction matrix comparing the frequency domain results with linearised and nonlinear time domain results.

Instead of exciting all structural states simultaneously at the distinct frequencies, each structural state can be excited at each distinct frequency individually requiring more unsteady runs. It was found however, that the involved computational cost in either case was about the same to achieve equivalent errors compared with the linear frequency domain approach. This is because the time step for the forced motion has to be chosen to resolve the dynamic content of the highest frequency accurately.

Summarising the cost of the frequency and time domain extraction for the aerofoil case using the first approach, the linearised time domain simulations involve the cost of about ten steady state solves to extract the complete interaction matrix at one individual frequency, while the nonlinear version is about twice this cost. Using the linear frequency domain approach, on the other hand, evaluating the interaction matrix at one frequency (requiring $2n$ linear solves against the fluid system) takes about an equivalent cost to simulating a steady state. However, these estimated values clearly depend on the retained number n of considered normal modes.

4.2.1 Oscillatory Transonic Behaviour

Figure 4.1 includes nonlinear time domain results for a higher excitation amplitude ($\widehat{a} = 1.0 \times 10^{-2}$). The transonic results at Mach 0.8 suggest that the nonlinear approach shows discrepancies compared with the linearised frequency and time domain approaches. However, the appearance of shock waves introduces the additional aspect of an oscillatory behaviour as first presented in [114, 115]. This phenomenon is discussed in this study for its impact on the aeroelastic stability. Here, the critical flutter speed index of an aerofoil configuration shows an oscillatory trend with changes in the freestream Mach number due to the discrete numerical representation of the shock movement being restricted to the grid resolution. The oscillatory flutter speed is related to an oscillation in the elements of the Jacobian/interaction matrix.

The transonic instability boundary of the NACA 0012 "heavy case" configuration [52], based on the Euler flow model and obtained from the eigenvalue stability analysis, is presented in Fig. 4.2(a) showing the critical flutter speed index V_F. The aerofoil structural model will be presented in Chapter 5. Values of the flutter speed index above the instability boundary result in an unstable response. The critical freestream Mach number of the NACA 0012 aerofoil at zero mean angle of attack is about 0.727. Well exceeding this critical value, and thus developing a significant supersonic region including a nearly normal shock wave in the near field region of the aerofoil, leads to the observed oscillatory behaviour in the instability boundary.

A grid refinement study on a 3–block C–type family of grids, results of which are presented in the inset of Fig. 4.2(a), was conducted. While the wall normal grid resolution has little influence on the phenomenon, a dependence of the oscillatory frequency and amplitude on the streamwise grid resolution is found. Doubling the number of streamwise gridpoints approximately doubles the oscillatory frequency and increases the associated amplitude. An inspected finer grid with 513×129 points (the results of which are not shown here) continued the observed trend of increasing the frequency and amplitude. The examination of the limiting behaviour, particularly with respect to the amplitude, when reducing the streamwise grid spacing to zero is an unresolved issue. Also, it is interesting to note that a similar behaviour has not been observed for three dimensional cases which suggests the occurrence of a spatial filtering.

To support the above results from the eigenvalue stability analysis (which requires the steady state Jacobian matrix), unsteady time–accurate simulations were done on the fine grid (257×65 points) using a dimensionless time step of 0.05 which is equivalent to about 500 steps per cycle of motion. Time step refinement did not show an influence on the oscillatory effect. Starting from the same steady state solutions, unsteady responses for several values of the initial disturbance in the dimensionless plunge rate were simulated, the results of which are crossplotted with results of the eigenvalue–based approach in Fig. 4.2(b). Generally, a dependence of the simulations

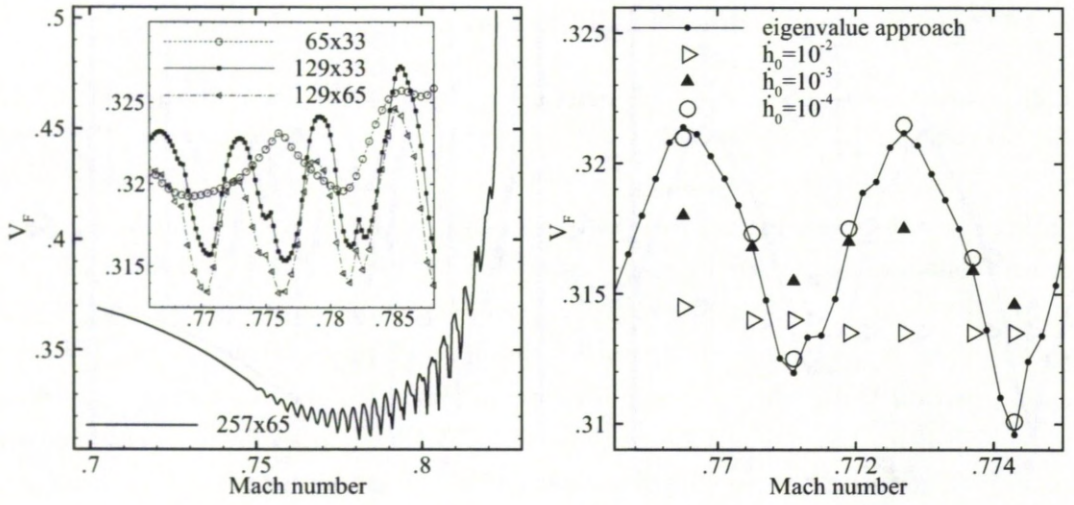

(a) Influence of grid spacing

(b) Eigenvalue–based vs time–accurate results

Figure 4.2: Oscillatory transonic instability boundaries for NACA 0012 aerofoil configuration showing (a) influence of streamwise and wall normal grid spacing and (b) comparison of eigenvalue–based and time–accurate results.

on the strength of the disturbance is observed. This means that simulations at the same combinations of freestream Mach number and flutter speed index resulted in different responses depending on the disturbance of the system. Small initial deflections give results which are very similar to the results of the eigenvalue–based approach (consistent with a linear stability analysis) revealing the same phenomenon. On the other hand, higher initial values eliminate the oscillations.

This can be explained by looking at the unsteady flow field. In an unsteady simulation the location of the shock wave changes depending on the structural motion. The variation of the pressure distribution is very weak if the system is only disturbed slightly, and hence the discrete steady state shock resolution is a strong factor throughout the unsteady response. For larger initial disturbances on the other hand, the influence of the steady state on the time–accurate simulation is dominated by dynamic effects.

Using the current eigenvalue–based approach, the Mach number increment can be decreased easily by orders of magnitude and thus approaches a continuous change, whereas the formed shock wave can not move accordingly along the aerofoil but is restricted to the discrete grid location. In Fig. 4.3 steady state pressure distributions and their gradients are shown at four distinct Mach numbers representing successive troughs and peaks using a grid with 129×33 points. The shock wave exhibits a repeating pattern which is different at trough (Mach 0.7706 and Mach 0.7765) and at peak (Mach 0.7730 and Mach 0.7790) locations. These local extrema can be considered as limiting shapes in the resolution of the shock wave. It is characteristic that the shock location moves by one grid point for successive peaks and troughs, respectively.

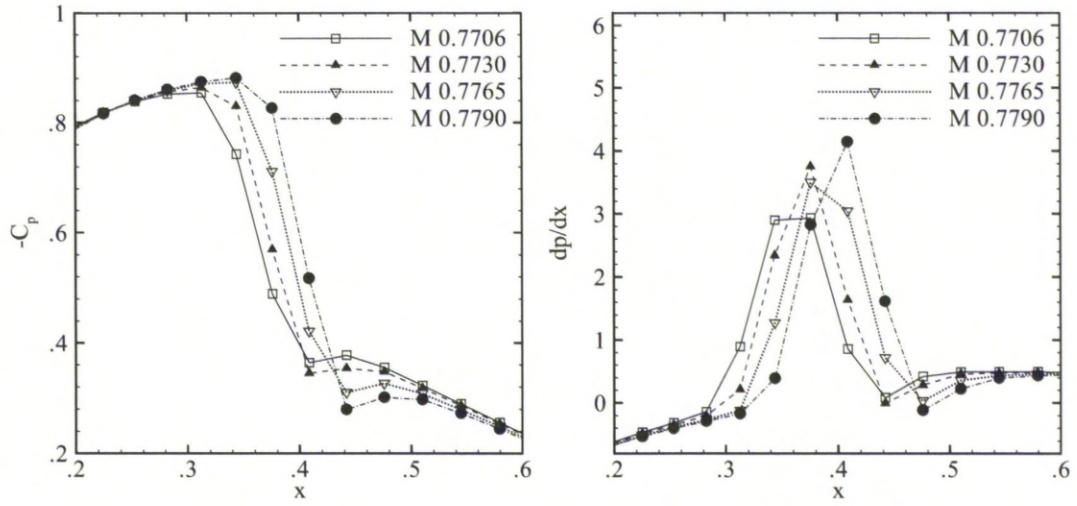

(a) Pressure coefficient

(b) Streamwise pressure gradient

Figure 4.3: Steady state pressure distribution and streamwise gradient at four distinct Mach numbers representing peaks and troughs.

The discrete steady state resolution of the shock wave is reflected, for example, in the integrated fluid forces. This is presented in Fig. 4.4(a) showing the instability boundary compared with the steady state lift–to–incidence ratio (with angles given in radians) at a small angle of attack for a range of transonic freestream Mach numbers. The lift–to-incidence ratio is a good approximation of the lift slope. Figure 4.4(a) clearly suggests a correlation between the two curves concerning the oscillations.

Importantly, in [114] for simulations of an inviscid duct flow with moving shock wave at fixed Mach number, the discrete shock resolution was found to cause an oscillatory effect. The shock capturing schemes giving the crispest shock were shown to result in the highest discrepancies between various integrated flow quantities and their exact analytical solutions. Increasing the level of artificial viscosity at the expense of losing the shock resolution reduced the associated error. Also, this one dimensional shock problem with equidistant grid points showed the oscillation to be of constant frequency and amplitude defined by the grid spacing (compare Section 4.1 in [114]).

In [115] an oscillatory behaviour was observed in inviscid steady state simulations employing a discrete adjoint method. Therein for instance, lift slopes of a NACA 0012 aerofoil obtained from linear and adjoint codes with base flows being the nonlinear steady states over a limited range of angles of attack and two fixed Mach numbers were compared with the slopes obtained by finite differencing of the nonlinear lift coefficients. For a subsonic freestream Mach number the differences between the linear/adjoint results and the nonlinear data were negligible. For the transonic freestream Mach number on the other hand, the nonlinear lift coefficient showed a lack of smoothness with varying angle of attack. A second example of a transonic diverging duct flow

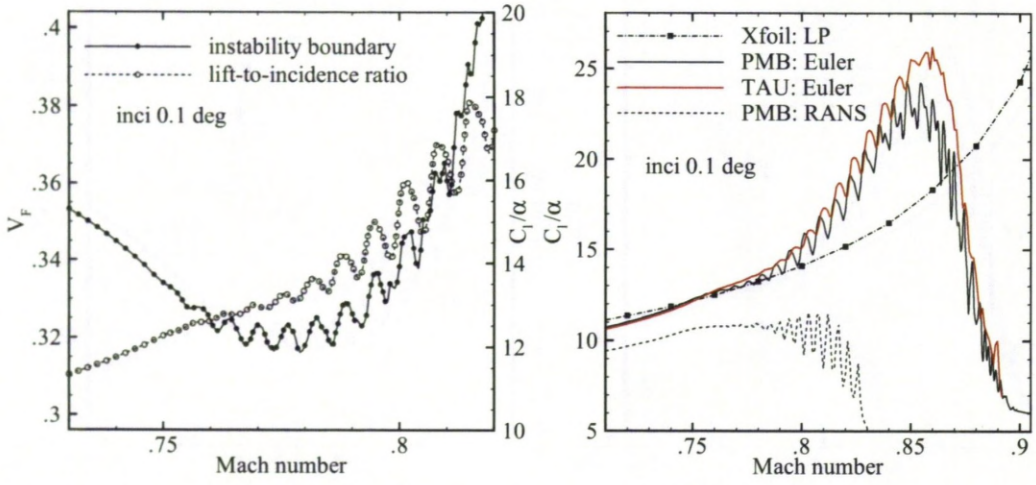

(a) Critical flutter speed index vs lift–to–incidence ratio

(b) Lift–to–incidence ratio

Figure 4.4: Crossplot of critical flutter speed index and lift–to–incidence ratio and comparison of lift–to–incidence ratio using different flow solvers and models.

illustrated a periodic behaviour of the integrated pressure with varying exit pressure. The period of the repeating pattern was determined by the grid spacing.

Figure 4.4(b) presents a comparison of the lift–to–incidence ratio between different aerodynamic models and flow solvers for the NACA 0012 aerofoil. The oscillations in Euler–based flow solutions are not unique to the parallel multiblock (PMB) solver as used in this study but were also found with the German Aerospace Center (DLR) TAU code [116]. In [114] it was discussed that viscosity (a distinction between artificial and physical viscosity is hereby irrelevant) smears out the shock wave resulting in a reduced oscillatory error. However, the curve for the lift–to–incidence ratio using the RANS modelling as shown in the figure suggests that, despite smearing out the shock wave, it is still a discrete representation.

Figure 4.5 presents one element of the Schur interaction matrix. The results obtained in the time domain with sinusoidal excitation for the sample extraction, using both the Euler and RANS equations, are given for a range of transonic freestream Mach numbers and different excitation amplitudes. In Fig. 4.5(a) the Euler time domain results are compared with the results of the linear frequency domain extraction.

As discussed for the influence of an initial disturbance on unsteady time–accurate stability simulations in Fig. 4.2(b), a dependence on the amplitude is found. Results for small forced excitation amplitudes resemble the linear frequency domain analysis including the oscillatory phenomenon, whereas higher values eliminate these. A weak variation of the pressure distribution is found for small structural motion amplitudes with a strong influence of the discrete steady state shock resolution throughout the unsteady forcing. The dynamic effects due to larger amplitudes, on the other hand,

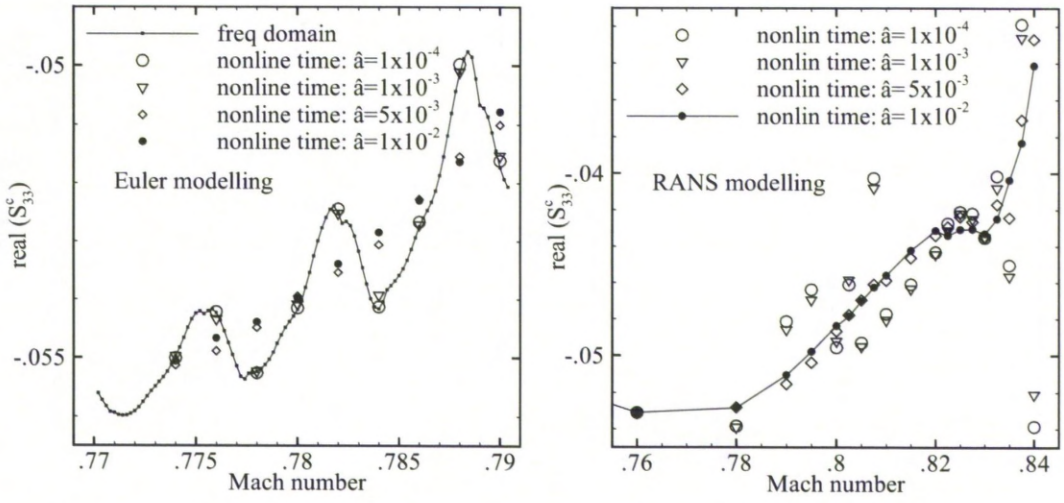

(a) Euler flow model

(b) RANS (SST) flow model

Figure 4.5: Effect of excitation amplitude on oscillatory behaviour in transonic regime for element real($S^c_{3,3}$) of the interaction matrix showing results for different flow models and a dimensionless frequency of $\omega = 0.25$.

dominate the influence of the steady state. Physically, it seems to be more meaningful to use a higher excitation amplitude since the nonsmooth behaviour, which cannot be explained with arguments of a continuous change of a system parameter, disappears.

Comparing steady state lift coefficients for Euler and RANS flow models in Fig. 4.4 suggests that the phenomenon can also be expected for RANS simulations. Figure 4.5(b) distinguishes three regions. In shock free flow at sub- and very low transonic Mach numbers, the amplitude (chosen within reason) is irrelevant. Having a distinct shock wave, the forcing amplitude becomes an important factor as for the Euler simulations. Results for smaller amplitudes scatter around a mean value, while the results for higher amplitudes, leaving the constraints of the discrete grid resolution, show a converging trend in the evaluations.

A trend for the region of distinct shock induced flow separation, starting at about Mach 0.82, is less easy to establish. While the presented matrix element describes significant oscillations, other elements have a far more gentle behaviour. To understand this, the stability at Mach 0.84 has been analysed using the kriging–based approach, described in the following chapters, as well as time–accurate simulations following a (relatively high) disturbance in the steady state solution of $\dot{h}_0 = 1.0 \times 10^{-2}$. While the time–accurate results agree better in the stability prediction with the analysis based on the higher amplitude samples, the lower amplitude samples give results deviating clearly which corresponds to the observations made in Fig. 4.2(b).

In addition, for Mach numbers exceeding 0.82 the fundamental changes in the system dynamics, particularly related to the transonic flow, must be discussed. In a well–known experimental study [117], a transonic dynamic instability of the flow, referred to as

buffeting, was investigated for the NACA 0012 aerofoil. The flow was shown to become unstable even in the absence of structural motion resulting in a self–sustained limit–cycle shock oscillation possibly including intermittent flow separation. Thus, buffeting can be considered as a limit–cycle motion of the flow field alone which generally interacts with the structural motion. The consequence is that the approach of using a linear stability analysis must be reconsidered at Mach numbers exhibiting buffeting as the assumption of a dynamically linear system is challenged [45, 118].

The buffeting phenomenon has received some attention in the literature. The shock/boundary layer interaction of the buffeting problem is computationally very demanding. A high fidelity flow model is required to be solved with a high spatial and temporal resolution to capture the unsteady effects accurately [118]. The quality of the predictions using the unsteady Reynolds–averaged Navier–Stokes equations also depends strongly on the chosen turbulence model [119]. Recently, the aeroelastic response of an aerofoil in a buffeting transonic flow was investigated, and it was concluded that a possible synchronisation between the structural frequencies and the buffeting frequency can occur providing a physical mechanism for a limit–cycle response [120]. However, buffeting is not within the scope of the presented approach and is therefore not further discussed in this study.

4.3 Approximating the Schur Interaction Matrix

The big computational challenge in solving the small nonlinear eigenvalue problem in Eq. (4.5) is the evaluation of the Schur interaction matrix S^c. This matrix depends on the eigenvalue, particularly the frequency, and the steady state solution. The steady state makes it dependent on a large number of parameters in both the flow model, e.g. Mach number, angle of attack and dynamic pressure, and the structural model due to structural parameters generally affecting the mode shapes. This means that the evaluation of the matrix S^c will become too expensive if a large space of system parameters has to be searched for aeroelastic instability.

Using Newton's method, as described in Section 4.1, requires several calculations of the interaction matrix S^c to form the residual and its Jacobian matrix at each Newton iteration. Doing this for each aeroelastic mode of interest separately, makes this approach prohibitively expensive in solving the eigenvalue problem at only one parameter combination. Using either the quasi–Newton or the series method requires less evaluations to converge the eigensolution. However, the requirement to trace a large number of normal modes at several parameter combinations still does not seem to be very attractive.

For computationally expensive simulations, such as the generation of the Schur interaction matrix using either a frequency or time domain solver, it is useful to generate a cheap approximation based on relatively few runs of the expensive full order model

to provide information about its response at untried parameter combinations. An approximation model should both predict the calculated responses precisely and adapt to the functional behaviour of the responses. Several approaches to construct response surfaces can be found in the literature. In this study the Schur interaction matrix is reconstructed using the kriging approach.

In the kriging interpolation technique a multidimensional deterministic response of a simulation is treated as a realisation of a stochastic process. This process is composed of a low order regression model and a random normally distributed signal with zero mean and a covariance depending on the variance of the input samples and the correlation between two parameter locations. Thus, the second term (the error term) is not independent at different locations but is related to the distance between points in the parameter space. The parameters of the computationally cheap kriging model are determined for a known set of (typically expensive) numerical samples of the full order formulation by an optimisation process as given, for instance, in [121, 122]. The kriging predictor gives the exact system response at a sample location. Previously, the kriging approximation was used for generating aerodynamic data applied in flight dynamics studies [123].

Consider a given set of n numerical samples, $\left[\boldsymbol{s}_1, \ldots, \boldsymbol{s}_n\right]^T$, and the corresponding system response $\boldsymbol{y}_s = \left[y(\boldsymbol{s}_1), \ldots, y(\boldsymbol{s}_n)\right]^T$. For convenience, a single scalar system response y is assumed to be a function of the m dimensional input vector $\boldsymbol{s}$. The discussion however generalises for multidimensional responses. The best linear unbiased predictor, herein referred to as the kriging predictor, minimises the error of the interpolation [121] and is given as,

$$\widehat{y}(\boldsymbol{x}) = \boldsymbol{f}(\boldsymbol{x}) \cdot \boldsymbol{\beta} + \boldsymbol{r}(\boldsymbol{x}) \cdot \left(R^{-1}(\boldsymbol{y}_s - F\boldsymbol{\beta})\right). \tag{4.26}$$

The first term is the low order regression model while the second term adjusts the prediction based on the correlation structure. The gradient of the predicted system response, required to form the Jacobian matrix in solving the Schur eigenvalue problem, is given as

$$\nabla\, \widehat{y}(\boldsymbol{x}) = \boldsymbol{f}_{\boldsymbol{x}}^T \boldsymbol{\beta} + \boldsymbol{r}_{\boldsymbol{x}}^T \left(R^{-1}(\boldsymbol{y}_s - F\boldsymbol{\beta})\right), \tag{4.27}$$

with $\boldsymbol{f}_{\boldsymbol{x}}$ and $\boldsymbol{r}_{\boldsymbol{x}}$ expressing the analytically evaluated Jacobian matrices of the vector of basis functions $\boldsymbol{f}$ and the vector of correlations $\boldsymbol{r}$ with respect to the unsampled location $\boldsymbol{x}$. The kriging predictor approximates the system response and its gradient at an unsampled location $\boldsymbol{x}$ at the expense of only two scalar products on $\boldsymbol{f}(\boldsymbol{x})$ and $\boldsymbol{r}(\boldsymbol{x})$ once the model is formed.

The root mean squared error φ is referred to as the standard error of the kriging model and is a measure of uncertainty in the prediction. It is evaluated by

$$\varphi^2(\boldsymbol{x}) = \sigma^2\Big(1 - \boldsymbol{r}(\boldsymbol{x}) \cdot R^{-1}\boldsymbol{r}(\boldsymbol{x}) + \boldsymbol{u} \cdot \left(F^T R^{-1} F\right)^{-1}\boldsymbol{u}\Big) \tag{4.28}$$

with the vector $\boldsymbol{u}(\boldsymbol{x}) = F^T R^{-1} \boldsymbol{r}(\boldsymbol{x}) - \boldsymbol{f}(\boldsymbol{x})$ and the process variance

$$\sigma^2 = \frac{1}{n}(\boldsymbol{y}_s - F\boldsymbol{\beta})^T R^{-1}(\boldsymbol{y}_s - F\boldsymbol{\beta}). \tag{4.29}$$

The second term in Eq. (4.28) reduces the prediction error since an unsampled location $\boldsymbol{x}$ is correlated with the known set of samples, whereas the third terms adjust for errors in estimating the regression model. Thus, for zero correlation between samples the square of the kriging error at an unsampled location is equal to the variance of the samples plus some correction due to the regression model. Importantly, at a sample location the error is zero [122].

The vector of regression parameters $\boldsymbol{\beta}$ is the generalised least squares estimator of the overdetermined regression problem $\boldsymbol{y}_s \approx F\boldsymbol{\beta}$ and is given by the expression

$$\boldsymbol{\beta} = \left(F^T R^{-1} F\right)^{-1} F^T R^{-1} \boldsymbol{y}_s, \tag{4.30}$$

as can be found in standard literature of statistics. Here, $F = \left[\boldsymbol{f}(\boldsymbol{s}_1), \ldots, \boldsymbol{f}(\boldsymbol{s}_n)\right]^T$ is the regression matrix with $\boldsymbol{f}$ as the basis vector. A constant regression model gives the matrix F as a $n \times 1$ column vector filled with ones, whereas in the linear case the elements of the matrix are given by $\boldsymbol{f}(\boldsymbol{s}) = \left[1, s_1, \ldots, s_m\right]^T$.

The correlation matrix R of the samples is built from the elements

$$R_{ij}(\boldsymbol{\theta}, \boldsymbol{p}, \boldsymbol{s}_i, \boldsymbol{s}_j) = \prod_{k=1}^{m} scf\left(\theta_k, p_k, s_k^{(i)} - s_k^{(j)}\right) \qquad 1 \leq i, j \leq n \tag{4.31}$$

where scf is a spatial correlation function of the arguments $\boldsymbol{\theta}$, $\boldsymbol{p}$ and the distance between samples $\boldsymbol{s}_i$ and $\boldsymbol{s}_j$. The correlation vector $\boldsymbol{r}$ written as,

$$\boldsymbol{r}(\boldsymbol{x}) = \left[R_{11}(\boldsymbol{\theta}, \boldsymbol{p}, \boldsymbol{s}_1, \boldsymbol{x}), \ldots, R_{n1}(\boldsymbol{\theta}, \boldsymbol{p}, \boldsymbol{s}_n, \boldsymbol{x})\right]^T, \tag{4.32}$$

contains the correlation between the provided set of samples and an unsampled location $\boldsymbol{x}$ in the parameter space.

The correlation parameter θ_k indicates the activity of the independent variable k, while p_k is a measure of the smoothness of the predictions in coordinate direction k. Several correlation functions have been given in the literature reflecting characteristics of the system output. In this study the applied kriging tool [124] uses exponential and spline functions. The vector of parameters $\boldsymbol{p}$ is generally predefined by a chosen correlation model (such as a Gaussian–like correlation), whereas the vector of optimal correlation coefficients $\boldsymbol{\theta}$ is given by the maximum likelihood estimate [121, 125] and minimises the expression $\det\left(R^{1/n}\sigma^2\right)$ having given the vector of regression coefficients $\boldsymbol{\beta}$ and process variance σ^2. This requires iterating to the optimum.

One important point must be discussed concerning the robustness of the kriging

approach. This issue is not well documented in the literature, but is still a well–known problem for researchers and practitioners using the kriging interpolation [116,126]. Particularly, the approach is known to show difficulty in three situations [127]; for high dimensional problems with few samples (having a lack of information), for low dimensional problems with many samples (having excessive information), and for closely located samples due to, for instance, iterative optimisation (giving a numerically unstable kriging model). The critical step of the kriging approach is to solve a multidimensional optimisation problem to have the optimal correlation parameters $\boldsymbol{\theta}$. Poor values of these parameters lead to poor predictions resulting in spurious oscillations. Attempts to resolve this issue are ongoing research efforts.

Co–kriging techniques use additional information on the functional behaviour of the response, such as gradients or co–variables. Using a spatially correlated, usually cheaper, and hence densely sampled co–variable to augment the input parameter space of a usually more expensive, sparsely sampled primary variable, allows the prediction of the primary variable accurately with very few samples. The cheaper model provides a trend of the system response with the higher fidelity data updating the prediction [122]. In this context the cheaper model is established either by a lower level aerodynamic modelling (which exploits the aerodynamic hierarchy of flow models) or by a higher level model solved on a coarse grid.

Following the above notation, a given set of n numerical samples $\left[\boldsymbol{s}_1, \ldots, \boldsymbol{s}_n\right]^T$ has a system response for the primary variable $\boldsymbol{y}_s^{\mathrm{hf}} = \left[y^{\mathrm{hf}}(\widetilde{\boldsymbol{s}}_1), \ldots, y^{\mathrm{hf}}(\widetilde{\boldsymbol{s}}_n)\right]^T$ with "hf" denoting high fidelity. Here, the input parameter space of the primary variable is extended by the response of the correlated co–variable which must be available at the primary sample locations, $\widetilde{\boldsymbol{s}}_j = \left[\boldsymbol{s}_j, y^{\mathrm{lf}}(\boldsymbol{s}_j)\right]^T$ where $j = 1, \ldots, n$ and "lf" denotes low fidelity. Then, the basic kriging formulation as outlined above can be applied. Note, that the response of the co–variable is required at all unsampled locations, as demanded by the primary variable. This can be achieved by simply forming an independent kriging model for this co–variable.

Alternative co–kriging techniques are discussed in the literature, for instance [128]. Here, the different gradient–enhanced kriging methods and the use of so–called (multiplicative, additive or hybrid) bridge functions are worth mentioning. These methods are not discussed in this context but might offer advantages in future applications.

To summarise the discussion, the requirement to calculate the computationally expensive interaction matrix S^c many times necessitates the approximation of this matrix based on a few carefully selected samples. The problem is then to spread the samples appropriately across the parameter space in order to enable an accurate approximation. This will be discussed in the following chapters. The significant advantage of the approximation approach is that, once the interaction matrix can be represented by the kriging model, the eigenvalue problem can be solved as often as necessary at very low computational cost.

4.4 Classical Analysis and Model Reduction

The most basic form of the classical flutter equation is

$$\Phi^T M \Phi \, \ddot{\boldsymbol{\eta}} + \Phi^T C \Phi \, \dot{\boldsymbol{\eta}} + \Phi^T K \Phi \, \boldsymbol{\eta} = \Phi^T \boldsymbol{f} \tag{4.33}$$

where the vector $\boldsymbol{\eta}$ contains the n modal amplitudes (generalised coordinates), $\Phi^T \boldsymbol{f}$ is the vector of the generalised aerodynamic forces, and $\Phi^T M \Phi$, $\Phi^T C \Phi$ and $\Phi^T K \Phi$ are the generalised matrices of mass, damping and stiffness, respectively. The matrix Φ to obtain the generalised form is the matrix of (linearly independent) mode shape vectors. Details will be given in the presentation of the structural models used for the stability analysis in Chapter 5.

The vector of unsteady generalised aerodynamic forces is commonly decomposed as $\Phi^T \boldsymbol{f} = Q \, \boldsymbol{w}_s$, where the vector of structural unknowns $\boldsymbol{w}_s = \left[\boldsymbol{\eta}, \dot{\boldsymbol{\eta}}\right]^T = \left[\boldsymbol{\eta}, \lambda \boldsymbol{\eta}\right]^T$ contains the generalised coordinates and their corresponding velocities. The complex–valued $n \times 2n$ matrix $Q = \left[Q_1, Q_2\right]$ is commonly known as the generalised aerodynamic influence coefficient matrix [14]. According to the second approach discussed in Section 4.2, it is clear that the expression $\Phi^T \boldsymbol{f} = Q \, \boldsymbol{\eta}$ (with the complex–valued $n \times n$ matrix $Q = Q_1 + \lambda Q_2$) can be used alternatively, which is not discussed further at this point for reasons of brevity.

Equation (4.33) is augmented by the trivial expression $I \dot{\boldsymbol{\eta}} = I \dot{\boldsymbol{\eta}}$ giving the standard state–space form,

$$\dot{\boldsymbol{w}}_s = (D + Q^c) \, \boldsymbol{w}_s \tag{4.34}$$

with the matrix expressions

$$D = \begin{pmatrix} 0 & I \\ -\Phi^T K \Phi & -\Phi^T C \Phi \end{pmatrix} \quad \text{and} \quad Q^c = \begin{pmatrix} 0 & 0 \\ Q_1 & Q_2 \end{pmatrix} \tag{4.35}$$

which can be seen easily. Here, the generalised mass matrix, $\Phi^T M \Phi = I$, is conveniently scaled to become the identity matrix, cf. Section 5.2.1. Thus, using this notation the (complex–valued) coefficient matrices Q_1 and Q_2 can be interpreted as a representation of aerodynamic stiffness and damping, respectively. The notation is chosen on purpose to illustrate the equivalence to the Schur complement eigenvalue method.

Using the expression $\boldsymbol{w}_s = \boldsymbol{p}_s \, e^{\lambda t}$, the eigenvalue problem follows

$$\left(D - \lambda I + Q^c(\lambda)\right) \boldsymbol{p}_s = 0, \tag{4.36}$$

which resembles the basic equation of the Schur complement formulation in Eq. (4.5) and more importantly,

$$Q^c(\lambda) = S^c(\lambda), \tag{4.37}$$

illustrating the nature of the interaction matrix S^c to describe the aerodynamic influence.[4] This discussion will continue in detail in Section 5.1.5 for an aerofoil case.

Like the interaction term in the Schur complement eigenvalue method, the complex–valued matrix components of Q^c can be evaluated in both the frequency and time domain from the generalised aerodynamic forces following an excitation in the generalised coordinates. Also, the matrix Q^c is commonly assumed to be dependent on the response frequency ω only rather than the full eigenvalue, $\lambda = \sigma \pm i\omega$. The small nonlinear eigenvalue problem in Eq. (4.36) can be solved, for instance, using Newton's method as outlined in Section 4.1 for the Schur complement eigenvalue method by augmenting with the arbitrary expression $\boldsymbol{c}_s^T \boldsymbol{p}_s = i$ to normalise the eigenvector.

Essentially all standard model reduction techniques applied to aeroelasticity evolve around the approximation of the linearised aerodynamics (linearised about the nonlinear steady state solution). In the following a short discussion about popular model reduction techniques is presented in order to establish their relationship to the Schur complement eigenvalue method. Particularly, system identification based on the Volterra theory and proper orthogonal decomposition are considered.

Volterra system identification generally focuses on building a "black box" model of the expensive unsteady CFD solver to represent the dynamic response due to a number of defined structural excitations. Essentially, in the above notation, it is attempted to model the aerodynamic influence coefficient matrix Q. In this sense it is an analogy to, for instance, the classical incompressible two dimensional aerofoil theory using Theodorsen's function to model the response to a sinusoidal motion in the frequency domain [33]. The kriging–based Schur complement eigenvalue method is equivalent to this by projecting the exact aerodynamic response onto the structural unknowns to form a low dimensional modified structural eigenvalue problem. Also, as was shown in Section 4.2, the columns of the matrix S^c are equivalent to the projected flow response scaled by the structural excitation (corresponding to the columns of S^c).

Several system identification approaches using different types of structural excitation have been discussed in the literature. In this study when extracting the interaction matrix in the time domain, the system dynamics are identified using a sinusoidal forcing at discrete frequencies. Surely, there are more elegant and efficient methods to do the identification over a range of frequencies at once, such as using an exponentially–shaped pulse [129] or a unit step/impulse [35] for each modal excitation individually. Also, in [130] all modes of the dynamic system were excited simultaneously over the entire frequency range using orthogonal step functions to get the entire system identification done in one unsteady CFD execution (per steady state solution). This indeed

[4]Note that the expression in Eq. (4.37) is only precise if the dependence of the structural residual $\boldsymbol{R}_s$ on the structural unknowns $\boldsymbol{w}_s$ through the generalised aerodynamic forces $\boldsymbol{f}$ is negligible in the Schur complement eigenvalue method, while only keeping the stiffness and damping terms for the matrix $A_{ss} = D$. As will be discussed in Chapters 5 and 6, this is often an accurate simplification.

makes the approach very attractive for realistic cases. However, no such system identification model reduction was found in the available literature describing the application to larger parameter spaces and changes in system parameters.

In the light of the current approach using an interpolation algorithm based on exact numerical samples, these advanced approaches to cover a whole range of frequencies at once are not considered to be necessary. Besides this observation, an interesting discussion concerning the cost of an unsteady CFD simulation can be found in [35, 131]. It is well known, that signals with a frequency content of up to half the sampling frequency can be reconstructed [113]. For a dimensionless time step of 0.05 this maximum dimensionless frequency is about $\omega = 60$ which covers the typical region of interest for aeroelastic applications well. On the other hand for the small frequency range, small time steps (to reduce the numerical error in the CFD simulation) require a large number of total unsteady steps N to resolve the frequency content according to $\Delta\omega = 2\pi/(N\Delta t)$. For instance, in [35] a total number of 3500 steps was used for a system with four normal modes including a number of initial time steps (after the steady state solution) to prevent the pollution of the response due to the startup transients.

In aeroelasticity it is common to represent the structural motion by a small number of linearly combined basis vectors referred to as mode shapes. Similarly in aerodynamics, the unsteady flow field can be described as a linear combination of complex–valued dominant modes. The most obvious choice would be the eigenmodes of the spatially discretised CFD model which however is not feasible due to the generally high dimensional systems. Using proper orthogonal decomposition instead, the basis for the reconstruction is calculated from a number of samples representing the dynamic response of the system where the number of samples is significantly smaller than the dimension of the system [34].

Denote S as the sample matrix containing the discrete system observations as columns. Then, the matrix Φ of basis vectors is calculated as $\Phi = SV$, where V is the transformation matrix satisfying the eigenvalue problem $S^H SV = VX$. Here, the diagonal matrix X contains the eigenvalues and S^H denotes the Hermitian matrix (conjugate transpose) of the matrix S [33]. An aeroelastic reduced order model based on the proper orthogonal decomposition was constructed in [132, 133]. Translated to the notation used in the current study, it can be written as,

$$\left(\begin{bmatrix} \Phi^H A_{ff} \Phi & \Phi^H A_{fs} \\ A_{sf} \Phi & A_{ss} \end{bmatrix} - \lambda I \right) \begin{pmatrix} \boldsymbol{q}_f \\ \boldsymbol{p}_s \end{pmatrix} = 0, \tag{4.38}$$

with $\boldsymbol{p}_f = \Phi \boldsymbol{q}_f$. The eigenvector $\boldsymbol{q}_f$ corresponds to the generalised coordinates of the fluid system, sometimes referred to as augmented aerodynamic state variables. In practice, the number of modes retained (and required) to describe the system behaviour is smaller than the number of samples.

From Eq. (4.38) it can be seen that this reduced order model is equivalent to the full eigenvalue problem, as discussed in Eq. (4.4), with the dimension of the fluid system reduced, depending on the required number of basis vectors to represent the dynamic process accurately. The step towards the Schur formulation, using the reduced fluid system, to solve this relatively small eigenvalue problem can be seen easily,

$$\left((A_{ss} - \lambda I) - A_{sf}\,\Phi\left(\Phi^H\,A_{ff}\,\Phi - \lambda I\right)^{-1}\Phi^H\,A_{fs}\right)\boldsymbol{p}_s = 0. \tag{4.39}$$

In contrast to the approach of proper orthogonal decomposition, the Schur complement eigenvalue method using the kriging interpolation (as model reduction) does not need to boil down the aerodynamic representation. It takes the full order aerodynamic response (limited to the linear stability analysis) and projects this response onto the structural system. Thus, the kriging interpolation is applied to the exact response of the dynamic system.

The required number of samples for the model reduction using proper orthogonal decomposition is difficult to estimate. For instance, in [132] it was concluded that about 20 basis vectors (per steady state flow field) are required to form an accurate model basis for a dynamic aerofoil case while the number for a wing case is about 50 [133] increasing with the complexity of the configuration [134]. This corresponds to the required number of samples in the presented approach herein to cover the stability prediction over an entire range of freestream Mach numbers (and altitudes for the case with aerostatic deflection). Details will be given in Chapter 6.

The robustness of proper orthogonal decomposition under changes in the parameters of the fluid system is a well–discussed topic [37, 38]. Several approaches have been investigated including a global model basis [135], with the sample matrix enriched at different parameter combinations, and an interpolation applied directly between sets of the basis vectors [136], both of which gave poor results in the transonic regime. Another approach is referred to as the subspace angle interpolation [37] between two sets of system parameters and its higher order extension is an interpolation of the data in a tangent space to the Grassmann manifold [38], details of these can be found in the given literature. The latter two approaches have been demonstrated for two fighter aircraft configurations for changes in the freestream Mach number and angle of attack. The application to higher dimensional (structural) parameter spaces has been demonstrated in [137]. The current kriging–based approach is from design applicable to larger parameter spaces.

To summarise this discussion, the basic Schur complement eigenvalue method is not a model reduction technique in itself as operations on the full order CFD–based aerodynamics are constantly done during the simulation to form the interaction term. However, the kriging–based Schur formulation is a model reduction technique based on interpolation. The interpolation is straightforward, and no unnecessary complicated

discussion of sub- or tangent spaces is required. Like any other reduced order model, a number of "snapshots" of the exact system response is required to build the reduced basis or to identify the dynamic process. In the current approach these are the samples required to adjust the parameters of the kriging model.

As a remark and idea for possible future studies, an important characteristic of model reduction, compared with unsteady CFD–based simulations (besides the involved cost), lies in the applicability in a preliminary multidisciplinary design environment. A frequency domain reduced order model can be transformed into a time domain state–space model, using rational function approximation techniques, which would allow its use in modern control theory for aeroservoelastic problems [35, 138, 139]. It would be interesting to investigate the transformation of the current Schur frequency domain representation into the time domain to accommodate the approach for aeroservoelastic problems.

Chapter 5

Stability Calculations

The aeroelastic stability analysis based on the Schur complement eigenvalue method is presented in this chapter. Here, the characteristics for different structural models are described and the application of the approximation model for the interaction term is discussed in detail.

5.1 Aerofoil Cases

5.1.1 Governing Equations of the Aerofoil Structural Model

The "typical section" aerofoil model, with oscillating pitching and plunging motions, represents the torsional and bending behaviour of a wing structure. It is a realistic model for a wing with a high aspect ratio and low sweep angle [30]. The two degrees–of–freedom model is idealised as a point mass located at the centre of gravity (cg), as well as a torsional and translational spring attached to the elastic centre (ec) located a dimensionless distance $x_\alpha/2$ from the centre of gravity, where x_α is measured in semichords and negative for an elastic centre ahead of the centre of gravity. The aerofoil model is depicted in Fig. 5.1.

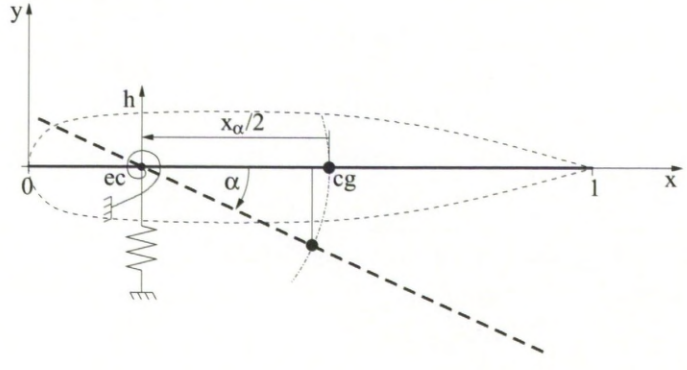

Figure 5.1: Depiction of two degrees–of–freedom aerofoil.

The equations of motion, a coupled nonlinear system of second order ordinary differential equations in time, are conveniently derived through Lagrange's equation, a detailed derivation of which is given in Appendix C. Assuming small deflection angles, the system linearises and can be written in standard state–space representation as

$$\dot{\boldsymbol{w}}_s = \boldsymbol{R}_s(\boldsymbol{w})\,, \tag{5.1}$$

with $\boldsymbol{w}_s = \left[\boldsymbol{\eta}, \dot{\boldsymbol{\eta}}\right]^T$ and $\boldsymbol{w} = \left[\boldsymbol{w}_f, \boldsymbol{w}_s\right]^T$. The vector $\boldsymbol{\eta} = \left[h, \alpha\right]^T$ contains the generalised coordinates of plunge and pitch, respectively. The residual vector $\boldsymbol{R}_s$ is,

$$\boldsymbol{R}_s = D\,\boldsymbol{w}_s + E\,\boldsymbol{f}(\boldsymbol{w}) \tag{5.2}$$

with the matrices D and E given by

$$D = \begin{pmatrix} 0 & I \\ -M^{-1}K & -M^{-1}C \end{pmatrix} \quad \text{and} \quad E = \begin{pmatrix} 0 \\ M^{-1} \end{pmatrix}, \tag{5.3}$$

where I is the 2×2 identity matrix. The vector of generalised forces

$$\boldsymbol{f} = \frac{1}{\mu_s\,\pi}\left[2\,C_l,\ 4\,C_m\right]^T \tag{5.4}$$

contains the integrated aerodynamic loads of lift C_l and pitching moment C_m about the elastic centre. The matrices of mass, damping and stiffness are given by

$$M = \begin{pmatrix} 1 & \frac{x_\alpha}{2} \\ x_\alpha & \frac{r_\alpha^2}{2} \end{pmatrix}, \quad C = \begin{pmatrix} 2\,\zeta_h \frac{2\,\omega_r}{\bar{u}} & 0 \\ 0 & 2\,\zeta_\alpha \frac{r_\alpha^2}{\bar{u}} \end{pmatrix} \quad \text{and} \quad K = \begin{pmatrix} \frac{4\,\omega_r^2}{\bar{u}^2} & 0 \\ 0 & \frac{2\,r_\alpha^2}{\bar{u}^2} \end{pmatrix}. \tag{5.5}$$

The additional dimensionless structural parameters are the radius of gyration about the elastic centre r_α, the ratio of uncoupled natural frequencies $\omega_r = \omega_h/\omega_\alpha$, and the aerofoil–to–fluid mass ratio μ_s. The structural damping ratios are denoted as ζ_h and ζ_α. The parameter $\bar{u}$ is a dimensionless representation of the freestream velocity and used as the independent parameter for aeroelastic simulations. It is interesting to note that the wind–off system decouples, i.e. independent pitching and plunging motions, by setting the static unbalance x_α to zero.

Recall the similarity to the classical formulation in Section 4.4. Besides the matrix of mode shape vectors being the identity matrix for the aerofoil structural model, the only difference to the classical approach is that it is not attempted with the Schur method to recast the aerodynamic force vector $\boldsymbol{f}$ in order to obtain a set of homogeneous ordinary differential equations for the structural dynamics. In the Schur framework the influence of the flow field is modelled via operations on the full CFD system.

Evaluating the structural Jacobian matrix A_{ss}, and the coupling block A_{sf}, is straightforward. The matrix block A_{ss} simply becomes $A_{ss} = D$. In this latter ex-

	Ref.	Aerofoil	x_{cg}	x_α	r_α	ω_r	μ_s	ζ_h	ζ_α
Heavy case	[52]	NACA 0012	0.5	−0.2	0.539	0.343	100	0	0
Isogai case	[140]	NACA 64A010	0.4	−1.8	1.865	1	60	0	0

Table 5.1: Parameters of aeroelastic aerofoil configurations.

pression the dependence of the structural residual on the structural unknowns through the integrated aerodynamic loads, i.e. $E\,\partial \boldsymbol{f}/\partial \boldsymbol{w}_s$, is ignored. This contribution, which is due to changes in the surface normal vectors with changes in the structural unknowns at fixed flow solution, was found to be very small. The matrix block A_{sf} requires the dependence of the integrated loads on the fluid unknowns, $A_{sf} = E\,\partial \boldsymbol{f}/\partial \boldsymbol{w}_f$, which is easily done analytically, as in the full potential (FP) baseline solver, or by finite differences, as in the multiblock solver for the Euler and Navier–Stokes equations.

Interestingly, the matrix A_{sf}, and consequently the Schur interaction matrix S^c, can be made independent of the applied structural model parameters. Thus, for defined flow conditions and aerofoil geometry, the dependence of the integrated forces on the pressure can be evaluated initially and scaled for the applied structural configuration once needed. This observation is not pursued further as the achieved simplification is not applicable to more realistic aircraft configurations using the modal structural model. Even though the matrix A_{sf} for the modal structural model can be rearranged to simplify its evaluation, the mode shapes depend on the structural parameters and directly influence the term $(A_{ff} - \lambda I)^{-1} A_{fs}$ through the deflection of the structure needed for the evaluation of the matrix A_{fs}.

5.1.2 Characteristic Eigenvalue Spectra

As is well known, the calculation of complete eigenvalue spectra for CFD–based aeroelastic systems is computationally very expensive [34]. Therefore, an eigenvalue–based aeroelastic stability analysis involves tracing individual eigenvalues with changing values of an independent parameter. Particularly, the wind–off structural eigenvalues are of interest. A complex conjugate pair of eigenvalues, $\lambda = \sigma \pm i\omega$, with a positive real part describe an unstable condition as an initial disturbance will be amplified rather than being damped out. This can be seen from the simple expression for a damped harmonic oscillator,

$$x = \widehat{x}\, e^{\lambda t} = \widehat{x}\, e^{\sigma t}\big(\cos(\omega t) \pm i\, \sin(\omega t)\big), \tag{5.6}$$

where x is an arbitrary system output with the complex–valued amplitude $\widehat{x}$. This latter expression follows from Euler's formula. A positive real part σ results in an exponential growth, while the stability limit is found for a zero real part.

Characteristic eigenvalue spectra of the system Jacobian matrix corresponding to the discretisation schemes of the Euler and FP/FPv equations, both of which are coupled with the aerofoil structural model, are presented in Fig. 5.2 for a transonic freestream Mach number of 0.75 and a flutter speed index $V = \bar{u}/\sqrt{\mu_s}$ of 0.25. The eigenvalues are given in dimensionless form. The spectra are calculated from the steady state Jacobian matrix A using the function *eig* in Matlab to solve the eigenvalue problem $(A - \lambda I)\,\boldsymbol{p} = 0$. Due to the involved cost and memory requirements, only coarse grids are used. The two aeroelastic eigenvalues originating in the wind–off structural modes are highlighted by larger symbols in Figs. 5.2(a) and 5.2(b). In addition, the migration of these two dominant aeroelastic modes as the independent parameter $\bar{u}$ is increased from zero is included in these figures.

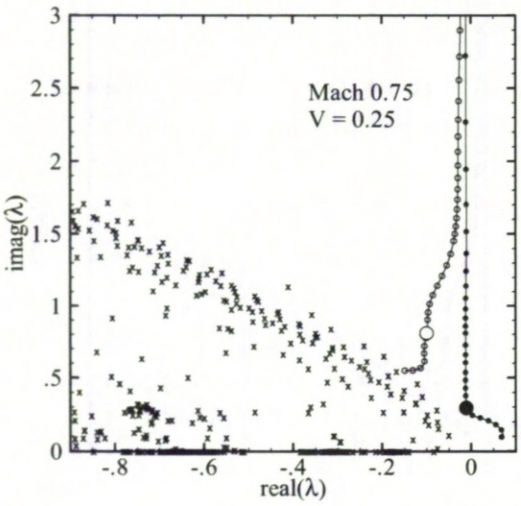

(a) Euler scheme with 2,000 control volumes

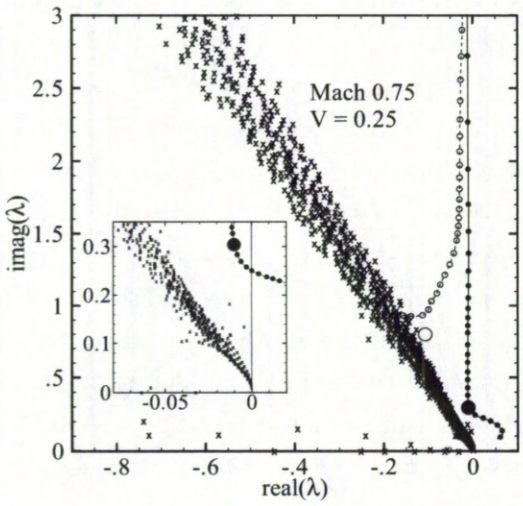

(b) FP scheme with 4,000 control volumes

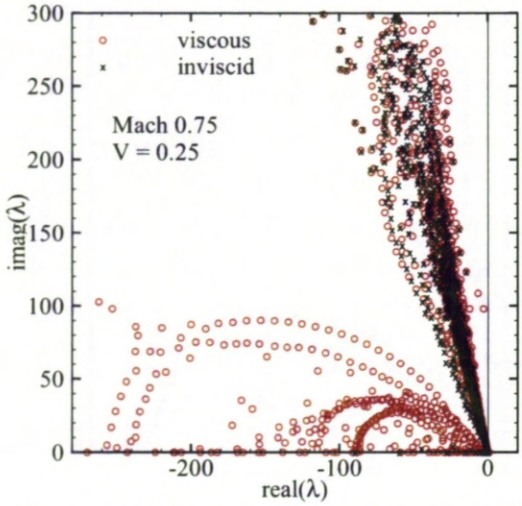

(c) FP/FPv schemes with 1,500 control volumes

Figure 5.2: Characteristic eigenvalue spectra of discretisation schemes for Euler and FP/FPv formulations at Mach 0.75 and $V = 0.25$ including root loci of the wind–off structural eigenvalues.

Figures 5.2(a) and 5.2(b) show the region close to the origin being populated by fluid eigenvalues for both aerodynamic models. In contrast to the Euler scheme, the eigenvalue spectrum of the FP model exhibits a very dense band of eigenvalues. This dense band and its proximity to the origin is clarified in the inlay of Fig. 5.2(b). An important consequence is that the mode tracing of the (wind–off) structural eigenvalues to identify the instability point can fail at certain flow conditions and structural model parameters due to the ill–conditioning of the matrix $(A_{ff} - \lambda I)$ in Eq. (4.6). Such a situation is found for the second mode using both the Euler and FP formulation shown in Figs. 5.2(a) and 5.2(b). However, in this case the second mode is increasingly damped before the ill–conditioning occurs, while the first mode goes unstable unaffected by the pack of wind–off fluid eigenvalues.

In Fig. 5.2(c) the inviscid and viscous eigenvalue spectra are compared. The majority of eigenvalues corresponding to the boundary layer system can clearly be identified by characteristic lines. Figure 5.3(a) illustrates the influence of shock induced separation on the FPv spectrum. As discussed in [94], eigenvalues emerging from the boundary layer system change sign in the vicinity of separation reflecting mathematically the separating and reverse nature of the flow. In the figure two pairs of complex conjugate eigenvalues, with imag(λ) of about 100, are on the positive half plane when approaching separation. Once separation is actually encountered at Mach 0.83 some additional unstable eigenvalues can be found at higher frequencies. Also, as mentioned in [141], frequencies related to the viscous system are normally higher than those related to the inviscid system due to differences in the characteristic length scales, e.g. the boundary layer thickness vs chord length. In the figure the unstable boundary layer modes are well outside the relevant region for the fluid/structure interaction.

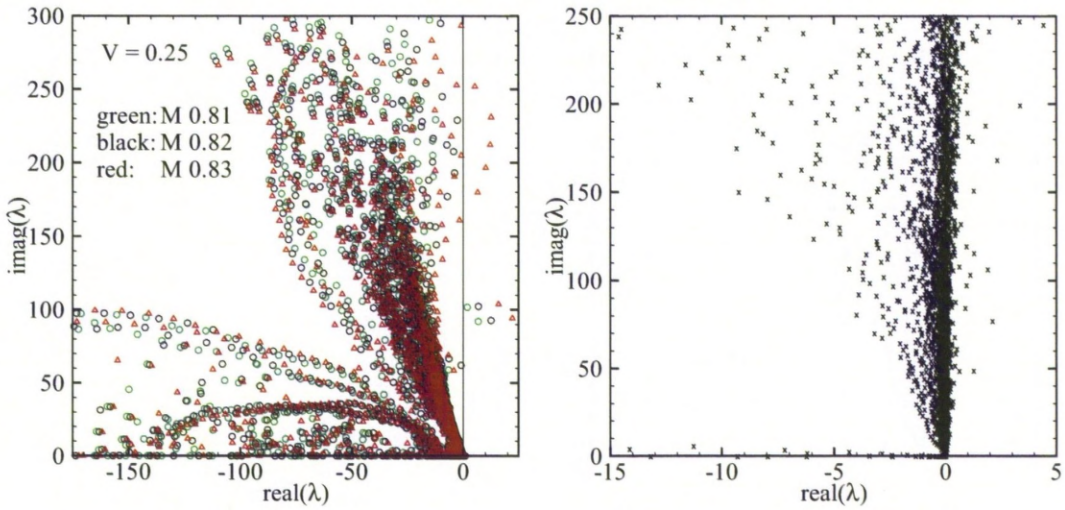

(a) Influence of separation

(b) Unstable spatial discretisation

Figure 5.3: Characteristic eigenvalue spectra of FP/FPv discretisation schemes.

Another very important observation is presented in Fig. 5.3(b). The calculation of the eigenvalue spectra was essential in constructing a stable spatial discretisation scheme for the aerodynamic model of the full potential equations. During the development of the FP flow solver several unstable discretisation schemes were encountered which made the solver simply unusable for the aeroelastic stability analysis. For instance, the eigenvalue spectrum in Fig. 5.3(b) is based on a spatial discretisation which, for the flux calculations in the continuity equation in Eq. (2.32), reconstructs the density (like the velocity vector) directly at the dual cell edges. To accommodate supersonic pockets the artificial compressibility scheme following [142] was applied. Other (unstable) discretisation schemes, e.g. a cell centred scheme with an artificial density term following [143], were found. The current (stable) density upwind scheme is described in detail in Appendix B. Interestingly, using Newton's method (rather than time–marching) to solve the discretised equations, all spatial schemes tested in this study produced accurate solutions of the flow field in the sub- and transonic regime.

5.1.3 Aerofoil Stability Results

Evaluating the Schur interaction matrix S^c based on the exact eigenvalue solver accounts for the highest cost in the stability analysis because it requires operations against the large CFD–based fluid system. As discussed in Chapter 4 the interaction term depends on the frequency/damping and the parameters defining the steady state solution, including freestream Mach number, incidence, and altitude, and the structural parameters affecting the structural mode shapes. Evaluating this matrix directly for each solve of the small nonlinear eigenvalue problem in Eq. (4.5) can become prohibitively expensive to be applied in routine calculations to search a large parameter space for instability. Once the (kriging) approximation model based on full order samples, which cover the parameter space of interest, is evaluated, the stability problem is solved without relying on the exact solver, and thus becomes very cheap. Then, any Newton–like method, discussed in Section 4.1, is a convenient choice to solve the small nonlinear eigenvalue problem (as many times as needed) with the interaction term and its Jacobian matrix readily available through the kriging predictor.

In the current formulation the approximation of the interaction term is based on a purely imaginary eigenvalue with zero damping $\lambda = i\,\omega$, whereas the structural part uses the complete eigenvalue including nonzero real part.[1] In this sense it is an analogy to the classical p–k method [26] as the aerodynamic response is based on a simple harmonic structural motion. The approximate Schur complement matrix used for the

[1] As mentioned before, one contribution is missing in this formulation compared with the exact solver. The structural part S^s contains the dependence of the structural residual $\boldsymbol{R}_s$ on the structural unknowns $\boldsymbol{w}_s$ through the integrated aerodynamic forces $\boldsymbol{f}$. These missing contributions are very small as shown by the comparisons below. The uncertainty due to the interpolation algorithm is considered to be far more significant.

stability analysis is written as

$$S \approx S^s(\lambda, \bar{u}) + \widehat{S}^c(\omega, M_r) \tag{5.7}$$

where $S^s = A_{ss} - \lambda I$ and $\widehat{S}^c$ is the kriging prediction of S^c and M_r denotes the freestream Mach number. For the two degrees–of–freedom aerofoil, as presented in the current study, the correction term S^c is independent of the bifurcation parameter, given by the reduced velocity $\bar{u}$, thus simplifying the discussion. At the critical eigenvalue, $\lambda_F = i\,\omega_F$, the approximation is exact within the limits of the interpolation algorithm. The critical eigenvalue with zero damping is easily detected using the bisection method applied to the independent (bifurcation) parameter at fixed Mach number.

The implications of the approximation $\widehat{S}^c(\omega, M_r)$ are presented in Fig. 5.4. The figure shows the tracing of the least stable aeroelastic mode with respect to the reduced velocity for the NACA 0012 "heavy case" configuration, summarised in Table 5.1, using the Euler flow model. Eigenvalues are given in nondimensional form. The calculation of 60 points on the root locus took less than a second of CPU time with the kriging model applied to the interaction term, whereas the exact Schur eigenvalue solver having a grid with 15 thousand control volumes took more than one hour (about one minute per point) on a modern desktop personal computer using the quasi–Newton method. Unsteady time marching at an individual reduced velocity using a dimensionless time step of 0.05 for temporal accuracy takes about 10 minutes per motion cycle (comprising about 500 steps). Typically five to ten cycles are required to establish a periodic oscillatory motion with negligible nonperiodic transients due to the initial disturbance.

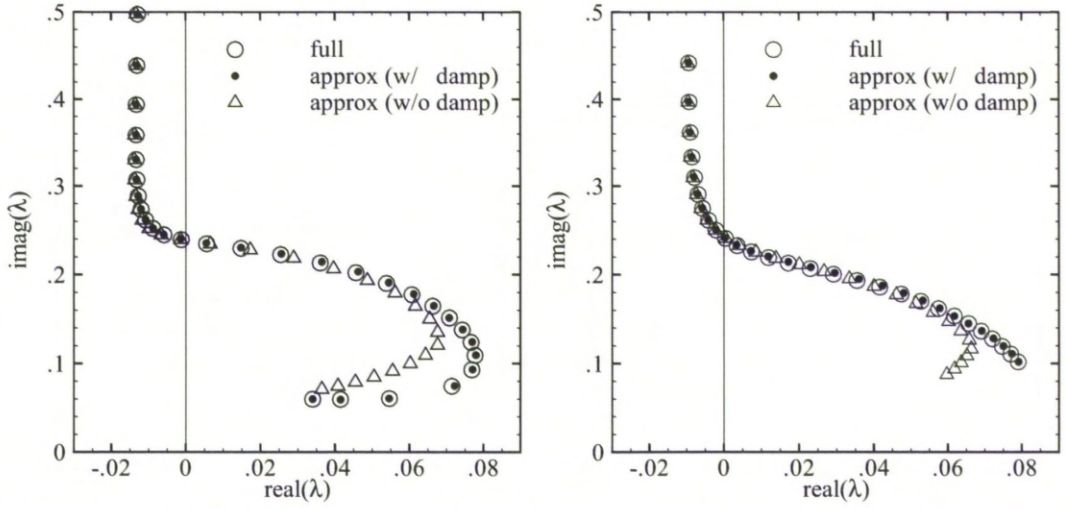

(a) Mode tracing at Mach 0.7

(b) Mode tracing at Mach 0.8

Figure 5.4: Mode tracing of least stable mode for NACA 0012 configuration using Euler flow model; comparison of full order and approximation models with damping terms $\widehat{S}^c(\lambda)$ and without damping terms $\widehat{S}^c(\omega)$.

Two approximation models are shown with the samples extracted using the linear frequency domain approach. One, denoted as "approx (w/o damping)", used full order samples with zero damping and varying frequency, whereas the second one was constructed at fixed Mach numbers for both varying damping and frequency. Using the approximation model based on nonzero damping, the trace of the relevant eigenvalue follows the full order prediction precisely.[2] However, the eigenvalue can be traced quite accurately even away from the imaginary axis without including damping in the kriging predictor. In this case the error introduced by the approximation $\widehat{S}^c(\omega, M_r)$ is very small in the relevant region close to the imaginary axis suggesting that the variation of the interaction elements with damping (or at least that the influence of this variation on the eigenvalue problem) is small compared with the structural part $S^s(\lambda, \bar{u})$.

This observation is supported in Fig. 5.5 showing the real and imaginary part of one element of the interaction matrix as a function of dimensionless damping and frequency at a fixed Mach number of 0.7. The black dots in the figure indicate sample locations while the coloured surfaces represent the kriging predictions used for the mode tracing in Fig. 5.4(a). Also, the eigenvalue trace from Fig. 5.4(a) is included in Fig. 5.5, shown as red dots, with the eigenvalue locations projected onto the response surfaces. The variation with respect to the eigenvalue's real part is indeed small.

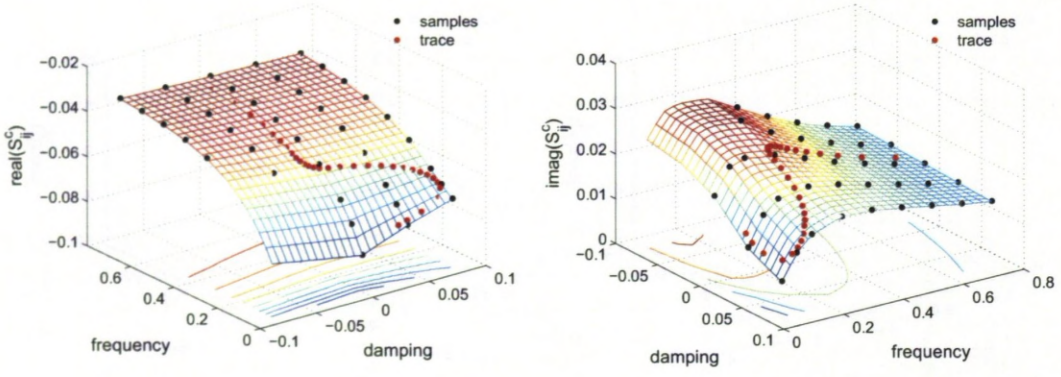

(a) real part (b) imaginary part

Figure 5.5: Extracted and interpolated element $S^c_{3,3}(\lambda)$ of Schur interaction matrix including projected trace of wind–off structural eigenvalue for Euler flow model at Mach 0.7.

For the kriging model shown in the figure, it was necessary to remove samples at low values of both damping and frequency as these samples adversely affected the construction of the approximation model. These samples interfered with eigenvalues originating in the fluid system causing an ill–conditioning of the problem in Eq. (4.6).

[2]It is a general characteristic of the kriging interpolation technique to approach the exact system response with increasing sample density as sample locations are interpolated precisely.

This ill–conditioning issue is associated with the discussion in Section 5.1.2 on the fluid eigenvalues affecting the mode tracing using the exact eigenvalue solver. Fortunately, for the cases analysed in this work (and possibly more generally) this eigenvalue interference does not corrupt the approach. If a problem is encountered for the relevant eigenvalues close to the imaginary axis, then it is a very good approximation to evaluate the interaction matrix with zero damping. This point is demonstrated in this study using a kriging reconstruction which is consistently based on samples with zero damping. Besides this, it should be remarked that any eigenvalue–based approach, working directly or indirectly with the fluid eigenvalue spectrum, would encounter this problem in a similar way.

Figure 5.6 presents the sub- and transonic instability boundary[3] as critical values of the flutter speed index V_F and dimensionless frequency ω_F for the NACA 0012 configuration. A comparison of results from the full order and the approximation models is given for four aerodynamic models. Also, since currently an exact eigenvalue solver for the RANS equations is not available, results of time–accurate simulations are included to confirm the predictions (using a chord Reynolds number of 5 million) with the plus (tilde) sign indicating a stable (unstable) response due to an initial disturbance. The agreement is excellent as expected since the sample resolution is high. Interestingly, the instability results using the FP baseline solver are conservative compared with the Euler and RANS results.

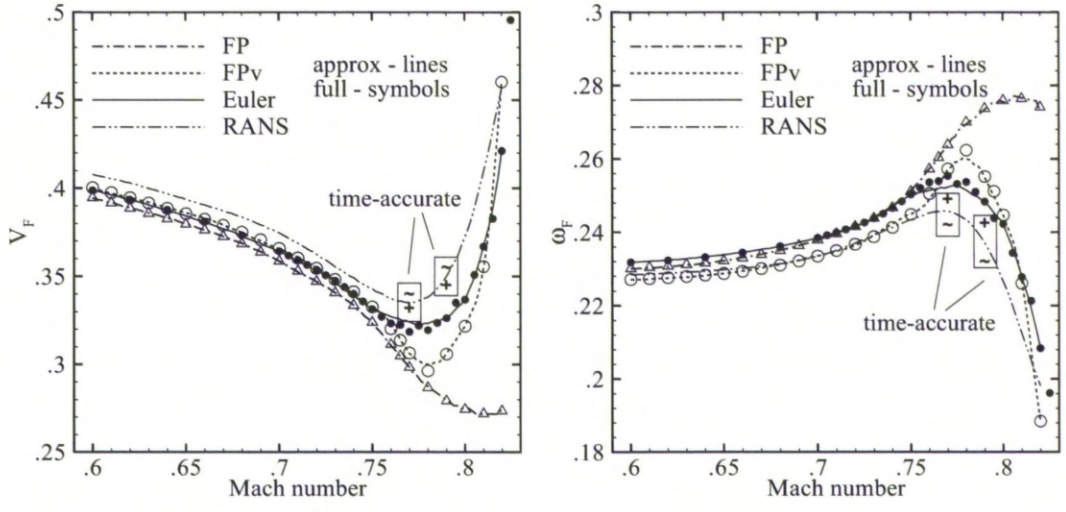

(a) Critical flutter speed index

(b) Critical frequency

Figure 5.6: Instability boundary for NACA 0012 configuration for four aerodynamic models showing comparison of full order (full) and approximation models (approx).

[3]The upper limit of the freestream Mach number is defined by the buffeting boundary for the NACA 0012 aerofoil according to [117].

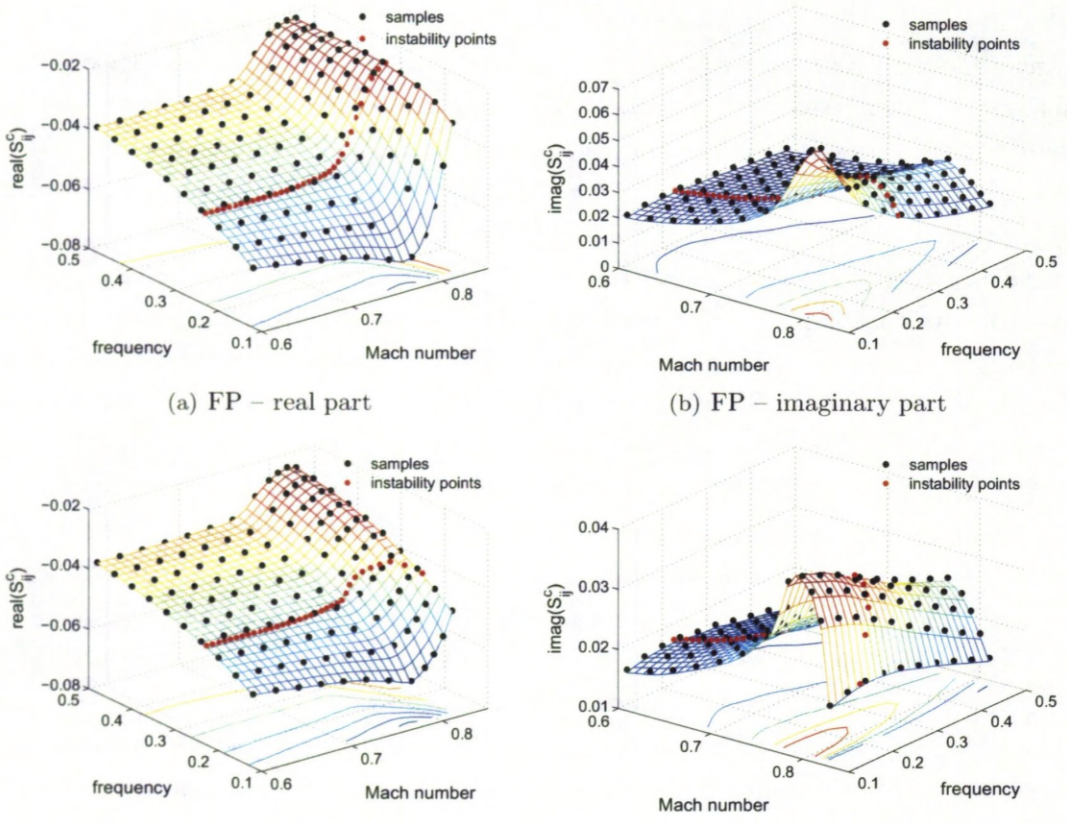

(a) FP – real part

(b) FP – imaginary part

(c) FPv – real part

(d) FPv – imaginary part

Figure 5.7: Extracted and interpolated element $S^c_{3,3}$ of Schur interaction matrix for NACA 0012 configuration including real and imaginary parts and using four aerodynamic models.

The samples for a range of freestream Mach numbers and dimensionless frequencies (with zero damping) and the corresponding kriging evaluation are shown in Fig. 5.7 for one representative element of the interaction matrix, corresponding to the extraction using the first approach of the discussion in Section 4.2. The trace of the instability is included as combinations of Mach number and critical frequency to illustrate the important regions of the response surface. The samples were extracted using either the linear frequency domain or, for the RANS simulations, the nonlinear time domain approach with an excitation amplitude of 7.25×10^{-3} applied.

Interestingly, for the flutter analysis using MSC.Nastran the aerodynamic influence coefficient matrix is evaluated at a limited number of points in the parameter space defined by the reduced frequency and Mach number. This is necessary as this evaluation significantly contributes to the computational cost. Then, an interpolation is applied to find the values between these discrete points [144]. Thus, the approach taken in this study is similar with two important differences. First, nonlinear CFD–based aerodynamic modelling is applied. Secondly, the parameter space in the current approach can

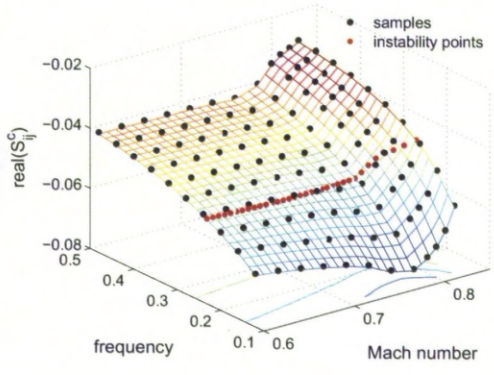

(e) Euler – real part

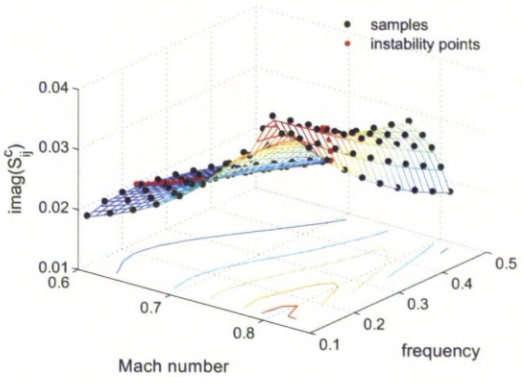

(f) Euler – imaginary part

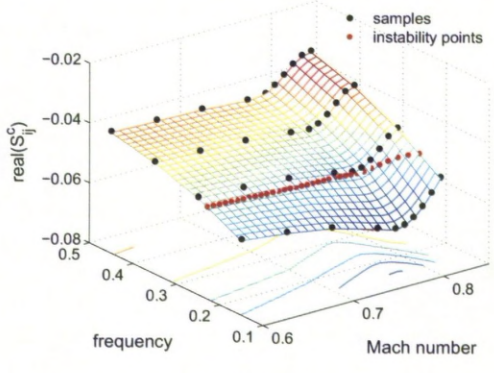

(g) RANS – real part

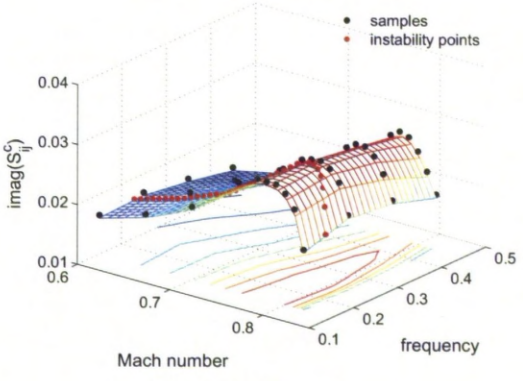

(h) RANS – imaginary part

Figure 5.7: (con't)

easily be extended to include more parameter dependencies.

Recall that the steady state solution, and consequently the interaction matrix, can depend on a large number of parameters. At this point of the current study, for the demonstration using the simple aerofoil model problem only the dependence on the frequency and freestream Mach number is considered, while later on for the wing cases the input parameter space will be extended.

An interesting point was observed for the aerofoil cases using the first extraction approach as discussed in Section 4.2 . The interaction elements of the matrix column corresponding to the plunge rate $\dot{h}$ (defined positive upwards) have very similar values of the elements corresponding to the pitch angle α (with opposite sign). An explanation for this can be found, for instance, by looking at the classical aerodynamic theory of Theodorsen [145]. Here, an increment in the pitch angle, $+\delta\alpha$, produces a contribution to the lift force equal to a negative increment in the plunge rate, $-\delta\dot{h}$.

Figure 5.8 presents one element of the Schur interaction matrix extracted for the Euler flow model using the second approach as discussed in Section 4.2, thus solving two linear systems of the form $(A_{ff} - \lambda I)\,\boldsymbol{y} = \left(A_{f\eta} + \lambda A_{f\dot{\eta}}\right)$, one for each right–hand side corresponding to the two aerofoil degrees–of–freedom. While the results discussed so far

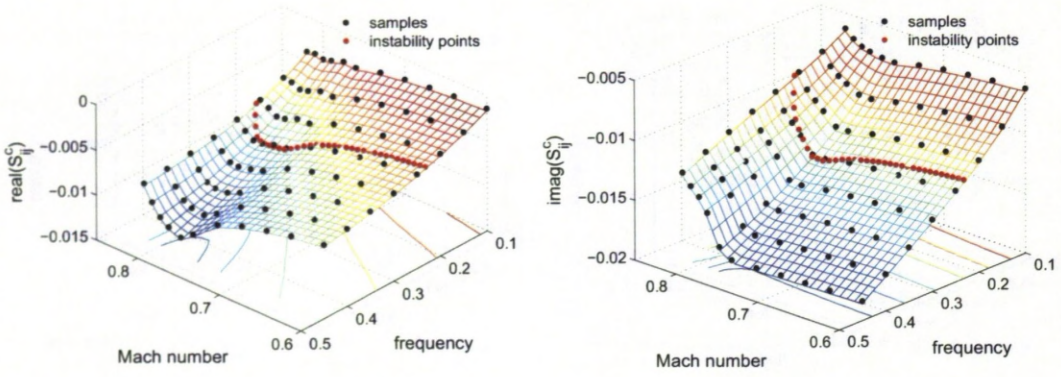

(a) Euler – real part

(b) Euler – imaginary part

Figure 5.8: Extracted and interpolated element $S^c_{3,1}$ of Schur interaction matrix for NACA 0012 configuration and Euler flow model using the alternative extraction approach.

for the aerofoil case have six nonzero complex–valued elements in the interaction matrix S^c (as the column corresponding to the plunge state h is zero in this discussion), the second approach produces only four nonzero complex–valued elements. The response surface in the figure shows a similar behaviour compared with the results in Fig. 5.7, as expected. Also, the projected trace of the instability boundary is included. The instability boundary as critical values of reduced velocity and frequency is not presented explicitly as these results are, of course, identical to the results in Fig. 5.6.

5.1.4 Interpreting the Results for the Hierarchy of Flow Models

In Fig. 5.6 there is a constant offset between Euler and RANS results as well as (at least for lower Mach numbers) between FP and FPv results, suggesting that the boundary layer as predicted by viscous modelling levels has a stabilising effect. Furthermore, it seems that the shock dynamics, which are correctly predicted by the Euler flow model, are more dominant for the aeroelastic stability compared with the viscous effects (in this configuration and at the shown range of Mach numbers). Indeed, comparing flow solutions it can be seen that shallow separation due to shock/boundary layer interaction is first encountered at about Mach 0.82.

The response surfaces of the interaction matrix element shown in Fig. 5.7 for the different flow models are now interpreted. To start with, it is important to say that the remaining five nonzero complex–valued elements of the aerofoil interaction matrix all show a similar behaviour compared with the presented matrix component. Also, it is found that among the flow models similar response features are consistently produced. This is expected because the shock dominated physics are included in all flow descriptions while the effects of separation are not yet an important factor in the considered Mach number range.

In the subsonic range the flow response (as expressed by the matrix elements) has small changes with varying system parameters, while in the transonic range clear variations, in particular with respect to the Mach number, are present. One distinct difference is found for the FP flow model at the higher Mach numbers and lower frequencies. Here, the imaginary part of the shown element takes on values almost double the corresponding element of the other models which is likely due to the shock dynamics (including location and strengths) being incorrectly predicted. Besides this, the agreement in the response surfaces suggests that, once the correct response features are simulated reasonably well by models with different fidelity, a hierarchy of flow models can be exploited in the stability analysis by combining cheaper response evaluations with available better (more expensive) information. The trend of a response, representing the physics and given by a cheaper model, can be used to support the prediction with a few, carefully selected, expensive evaluations.

Differences in the stability prediction using the different flow models require further consideration. Even for subsonic Mach numbers an offset between both the inviscid (Euler vs FP) and the viscous (RANS vs FPv) predictions of the critical flutter speed index can be found (even though the approximated error of one percent should not be of too much concern). The reason for disagreement is not found to be the grid resolution since the results presented herein are grid–converged meaning that inspected finer grids (results of which are not shown) did not change the results notably. An important factor distinguishing the solvers used for the Euler/RANS and FP/FPv flow models are the distinct spatial discretisation schemes including the treatment of boundary conditions. For instance, the FP baseline solver using a time–invariant computational domain applies a transpiration boundary condition on solid surfaces, whereas in the multiblock solver for the Euler/RANS equations the geometry is explicitly moved. These distinct boundary treatments are considered next.

Since a FP formulation with moving grids is currently not available, a transpiration boundary condition was implemented in the Euler formulation. The transpiration boundary condition only affects the Jacobian matrix block A_{fs} in Eq. (4.3) and implementing this (using finite differences) is easily done. The results shown in Fig. 5.9(a) indicate that the modified boundary condition has a slight influence on the aeroelastic stability prediction. Compared to the original results the critical flutter speed index of the Euler scheme approaches the FP prediction.

The critical flutter speed index of the FP formulation is closely followed until about Mach 0.75. Intuitively, starting from this point one would point at the underlying FP modelling assumptions being violated by the formation of strong shock waves causing an underprediction of the transonic dip. (The critical Mach number of the NACA 0012 aerofoil is at about 0.73.) However, the steady state pressure distributions at Mach 0.78 shown in Figs. 5.10(a) and 5.10(b) give excellent agreement for both the viscous and the inviscid flow solutions. These results suggest that merely an accurate simulation of

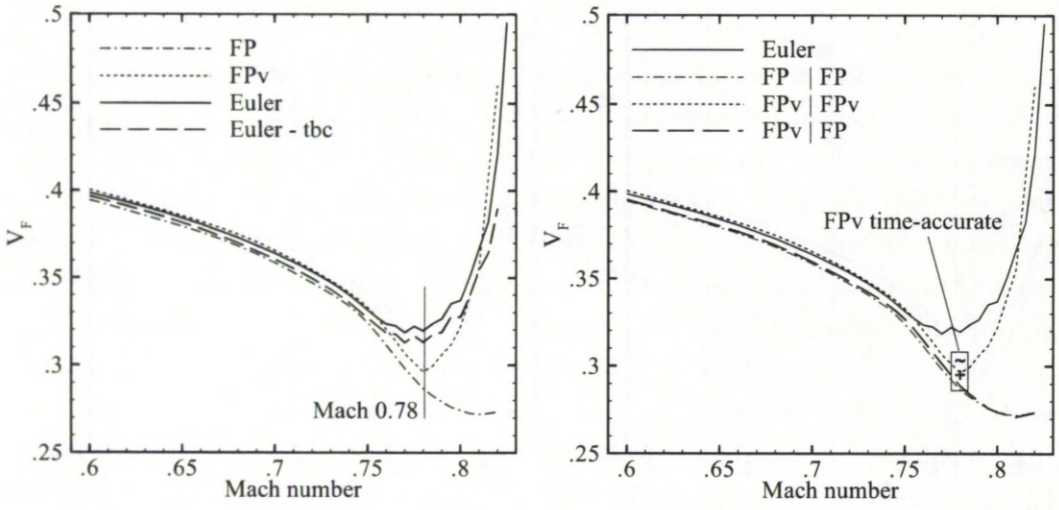

(a) Transpiration boundary condition

(b) Jacobian blocks

Figure 5.9: Influences of both the transpiration boundary condition (tbc) and the Jacobian matrix blocks for inviscid/viscous coupling on the predicted critical flutter speed index for NACA 0012 configuration.

the steady flow field is not sufficient with (unsteady) entropy and vorticity effects due to the formation of shock waves becoming more and more important.

Also, starting from about Mach 0.78 a diverging trend between FP and FPv predictions is found. At this point the predicted inviscid shock waves become too strong (now violating the FP assumptions) while viscous effects in the FPv formulation reduce their strengths (to keep having accurate steady state solutions) resulting in a correct prediction of the other side of the transonic dip with the sharp rise in the critical flutter speed index. In other words, viscous effects (included in the system Jacobian matrix) due to stronger shock/boundary layer interaction seem to become more significant than entropy and vorticity effects.

To support the observations, the inviscid/viscous coupling procedure in the FP formulation is exploited. Looking at the expression in Eq. (4.3), all matrix blocks (except A_{ss}) are split for the coupling to accommodate inviscid and viscous contributions in the fluid unknowns and their corresponding residuals, e.g. matrix block A_{ff} contains four subblocks as shown in Eq. (2.35). Then, individual subblocks are left out to estimate their importance for the stability analysis. In Fig. 5.9(b) three simulations using the FP baseline model are discussed with the first part of their labels indicating the steady state model and the second part indicating the contribution to the Jacobian matrix for the stability analysis.

The simulation using an inviscid/viscous coupling for the steady state but only the inviscid fluid subblock for the Schur complement matrix illustrates that, despite having the correct steady state, the inviscid instability boundary is predicted. Thus,

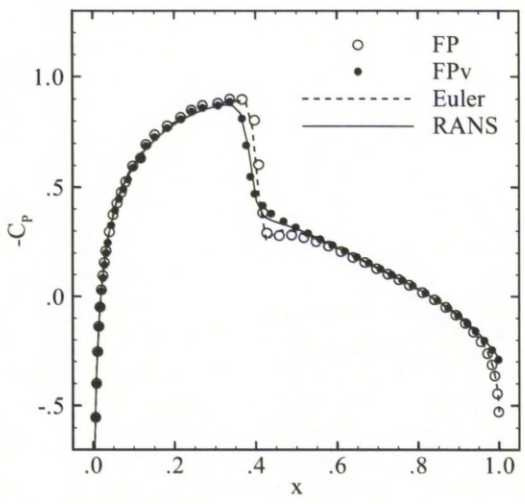

(a) Surface pressure distribution

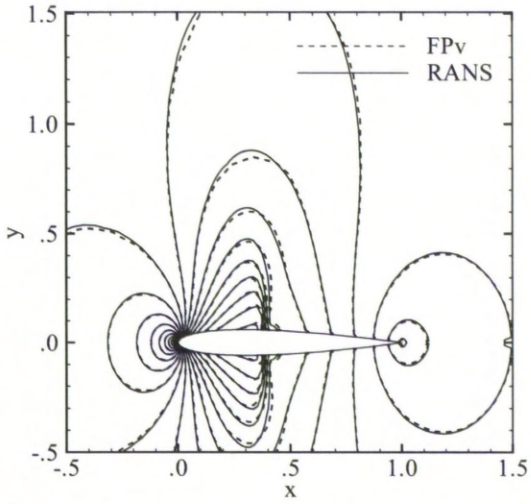

(b) Pressure field

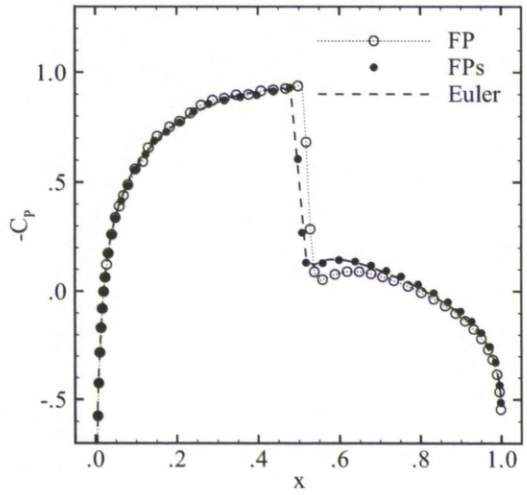

(c) Surface pressure distribution using entropy correction

Figure 5.10: Pressure distribution for NACA 0012 aerofoil showing different flow models; flow conditions for (a–b) M_r=0.78, α=0.0°, Re=5.0×10^6 and (c) M_r=0.80, α=0.0°.

the sensitivities of the important physics (in this case the viscous effects) need to be included in the matrix. Also, despite having the correct steady state compared with the Euler/RANS models, the sensitivity due to some shock effects (entropy and vorticity production) is missing in the FP formulation and may cause the underprediction in the transonic dip minimum.

In the following a simple model to correct the prediction of the shock wave in the higher transonic regime using the inviscid FP flow model is discussed. A shock correction model based on the Clebsch variable formulation [146] was presented in [147] correcting for entropy and vorticity effects. For convenience in the following discussion, the vorticity effects are ignored in this formulation limiting the application to nearly normal shock waves. The governing equation for the specific entropy ς (defined to

become zero under freestream conditions) is,

$$\frac{D\varsigma}{Dt} = \frac{\partial \varsigma}{\partial t} + \boldsymbol{q} \cdot \nabla \varsigma = 0, \tag{5.8}$$

which follows from a variant of the first law of thermodynamics, using the equation of state and a dimensionless expression for the specific enthalpy h,

$$d\varsigma = \frac{1}{(\gamma-1)M_r^2}\frac{dT}{T} - \frac{1}{\gamma M_r^2}\frac{dp}{p}. \tag{5.9}$$

applied to a moving fluid element for an inviscid adiabatic flow. The entropy equation resembles the circulation convection equation in Eq. (2.23). Thus, it is convenient to approximate the gradient operator by the streamwise derivative. As a first, very basic, approximation the equation is solved along the solid surface and the wake cut.

Also, the unsteady Bernoulli equation in Eq. (2.21) is modified to become

$$\frac{\partial \Phi}{\partial t} = \frac{1-q^2}{2} - \frac{\varrho^{\gamma-1} e^{(\gamma-1)\gamma M_r^2 \varsigma} - 1}{(\gamma-1)M_r^2}. \tag{5.10}$$

to correct the isentropic representation of the density along the boundary. Under isentropic conditions the basic full potential formulation is easily restored [147, 148]

The entropy equation for the shock correction needs to be solved behind shock waves. Therefore, an upstream boundary condition for the convective equation is defined across the shock front. The Rankine–Hugoniot shock jump relations [149] for density and pressure are,

$$\frac{\rho_d}{\rho_u} = \frac{(\gamma+1)M_u^2}{2+(\gamma-1)M_u^2} \qquad \text{and} \qquad \frac{p_d}{p_u} = 1 + \frac{2\gamma}{\gamma+1}\left(M_u^2 - 1\right), \tag{5.11}$$

with indices u and d indicating shock up- and downstream locations, respectively. Integrating Eq. (5.9) across the shock front, while using the shock jump relations and the equation of state, gives

$$\Delta\varsigma = \frac{1}{(\gamma-1)\gamma M_r^2}\left(\ln\left(1 + \frac{2\gamma}{\gamma+1}\left(M_u^2-1\right)\right) - \gamma \ln\left(\frac{(\gamma+1)M_u^2}{2+(\gamma-1)M_u^2}\right)\right), \tag{5.12}$$

where M_u expresses the normal Mach number upstream of the shock wave.

The results for the entropy correction, denoted FPs, are given in Fig. 5.10(c). Here, the surface pressure distribution for the NACA 0012 aerofoil is shown for a freestream Mach number of 0.8. The FPs agreement with the steady state Euler results is excellent in contrast to the pure FP simulation giving a wrong shock location and strength.

Interestingly, using the entropy correction on the boundary along the solid surface and the wake cut, the stability prediction is not changed considerably compared with the inviscid FP flow model, despite giving an accurate pressure distribution. These

stability results are not shown herein. To explain this, the vorticity effects do not seem to be very important. However, rather than a boundary method, a field method, i.e. solving the entropy equation in a two dimensional fashion, might be necessary to model the entropy effects behind the shock wave correctly.

Implementing the shock correction model, for both entropy and vorticity effects, as a two dimensional field method using the unstructured flow solver is not straightforward and applying this model is not very robust, as was found already using the boundary correction for the entropy. Also, the computational savings, relative to the multiblock Euler solver, achieved with such a shock correction capability do not seem to justify the complication of the FP flow solver and, at this point, the efforts required for the implementation. Hence, this is not further pursued in this work. Instead, the focus will be directed towards the application of the kriging approach to more realistic three dimensional cases.

To summarise, having a correct steady state simulation does not immediately guarantee the correct prediction of the stability limit. More effort is needed to understand to what extent either the missing physical content, such as shock effects, or the chosen discretisation of the flow models, such as the distinct upwind schemes and boundary treatments, are the main factor in this discussion. Converting the FP flow solver into an Euler solver while keeping the very basic upwind scheme might be helpful.

5.1.5 An Equivalent to the Classical p–k Method

In Section 4.4 the equivalence to the classical analysis has been established. In the following, this is demonstrated for the NACA 0012 "heavy case" aerofoil configuration. It was discussed that the generalised aerodynamic forces can be decomposed in either $f = Q_1\,\eta + Q_2\,\dot{\eta}$ or alternatively $f = Q\,\eta$ with $Q = Q_1 + \lambda Q_2$. The vector η contains the generalised coordinates, in this case the plunge and pitch coordinates.

Using the former approach, the elements of the matrix Q^c in Eq. (4.35), with one element shown in Fig. 5.11, correspond to the Schur interaction matrix elements, shown in Figs. 5.7(e) and 5.7(f). Figure 5.12 gives one element for the alternative representation corresponding to the results in Fig. 5.8. The components of the matrix Q^c are evaluated from the unsteady lift and moment coefficients following a forced sinusoidal excitation at discrete frequencies in the structural unknowns. This is very similar to the time domain approach described in Section 4.2 except that the Fourier analysis is applied directly to the integrated forces rather than the fluid response in each relevant control volume independently.

Note, that for the alternative representation two (physically meaningful) unsteady simulations, one for the plunge and one for the pitch degree–of–freedom, were done per frequency and Mach number. Here, the generalised displacements and their velocities are mathematically consistent. The representation according to Fig. 5.11, on the other

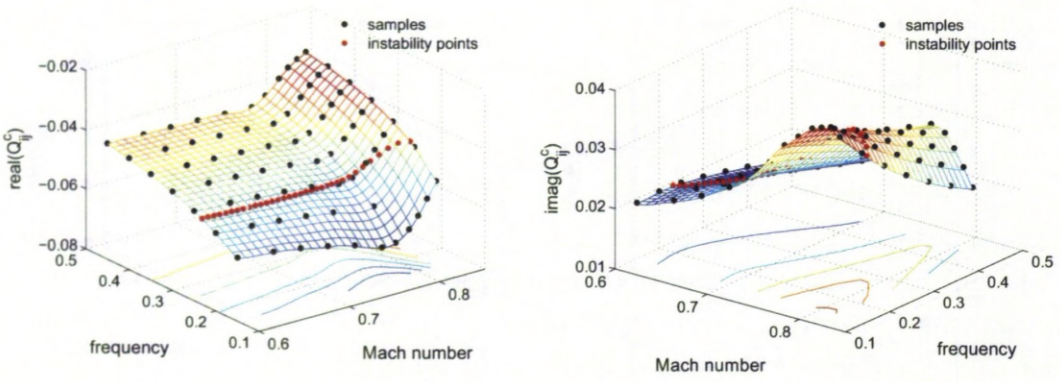

(a) real part

(b) imaginary part

Figure 5.11: Extracted and interpolated element $Q^c_{3,3}$ of the aerodynamic influence coefficient matrix for NACA 0012 configuration using Euler flow model and including projected instability points.

hand, required four unsteady runs, one for each structural unknown independently (three when ignoring the zero response due to the plunge deflection h). More elegant and efficient approaches to evaluate the aerodynamic influence from unsteady CFD simulations over a range of frequencies can be used, such as an exponentially–shaped pulse excitation [129] or unit step/impulse excitation [35,130]. However, for the current demonstration this is not intended, and actually not needed as an interpolation is applied instead.

Figure 5.13 gives the results for the stability analysis comparing the Schur and classical analyses. As should be expected, there are no significant differences between these results. The instability boundary using the alternative representation of the force vector is not included as these results are within plotting accuracy. The conclusion from this equivalence is that the methods presented in this study can directly be transferred to the classical analysis and vice versa.

5.1.6 Summary of Aerofoil Stability Calculations

Several points, concerning the objective of this work to search parameter spaces (flight envelopes) for aeroelastic instability efficiently, have been learned in the preceding main section for the aerofoil cases. Also, some insight into aerodynamic modelling uncertainty has been gained.

Most importantly, the approach using the kriging–based reconstruction of the computationally expensive Schur interaction matrix, representing the aerodynamic influence on the modified structural eigenvalue problem, gives excellent results compared with the exact (full order) eigenvalue solver. The stability calculation based on the kriging approximation is very cheap. However, the kriging model requires true samples

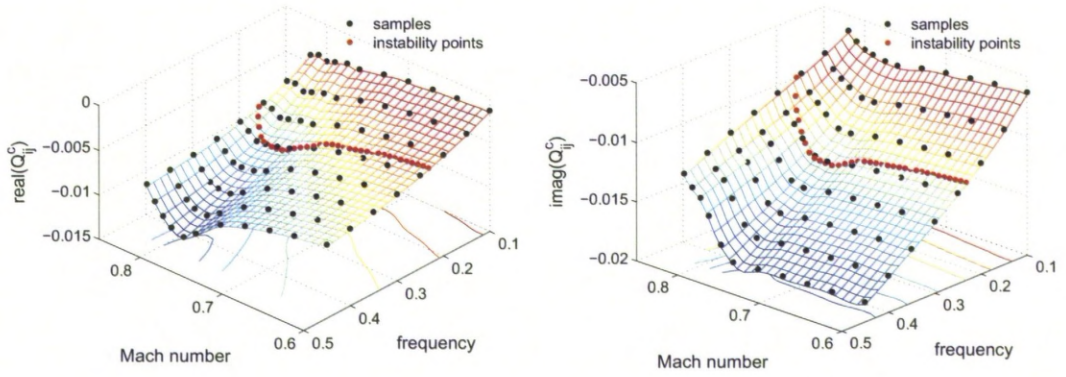

(a) real part (b) imaginary part

Figure 5.12: Extracted and interpolated element $Q^c_{3,1}$ of the alternative aerodynamic influence coefficient matrix for NACA 0012 configuration using Euler flow model and including projected instability points.

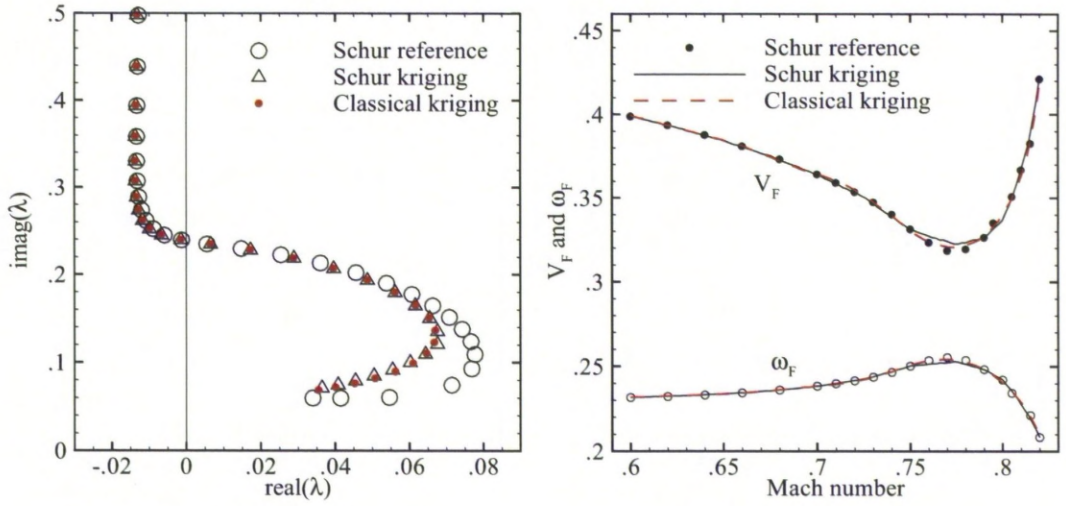

(a) Mode tracing at Mach 0.7 (b) Instability boundary

Figure 5.13: Mode tracing of least stable mode and instability boundary for NACA 0012 configuration using Euler flow model; comparison of full order and approximation models using Schur complement eigenvalue formulation and classical stability analysis.

for the Schur interaction matrix from the exact eigenvalue solver while covering the parameter space of interest. Up to this point the large number of samples, corresponding to a relatively high cost, are distributed over the parameter space using a very basic, brute force, rectangular grid sampling approach. In Chapter 6 more efficient sampling techniques, which are tailored for the purpose of this study, will be presented making the approach of sampling and reconstruction for the stability analysis very attractive in terms of cost.

The way to generate the true samples depends on the individual choice. Several approaches have been shown, all of which give identical results as they represent the same physics. The interaction matrix can be generated in the frequency and time domain, working either with the fluid response in individual control volumes projected onto the structural unknowns or with the generalised forces (making it conform with the classical flutter analysis). Importantly, for the preferred frequency domain approach the future standard implementation of the eigenvalue solver should use the second (alternative) formulation as it involves half the cost (compared with the first approach) to generate one sample.

Then, the established hierarchy of nonlinear flow models, including a full potential aerodynamic modelling corrected by viscous effects and the Euler and RANS equations, gives similar response features in the interaction term throughout the defined parameter space. This is a predictive capacity that will be exploited in Chapter 6 for the aeroelastic stability analysis by combining cheaper and more expensive flow models.

The differences between the stability predictions using the different flow models are discussed in detail based on the physics and the numerical discretisation. On the one hand, it is understood that the dominant flow physics need to be included for the stability analysis to give correct results. On the other hand, the influence, if any, of a chosen discretisation scheme (including the boundary treatment) on the stability results will require more effort to become clear. These points are related to the short discussion in Section 1.1 on the influence of aerodynamic model uncertainty.

5.2 Three Dimensional Cases

5.2.1 Governing Equations of the Modal Structural Model

As is common in computational aeroelasticity, an aircraft structure is represented by a small number of normal modes, small compared with the large dimension of the CFD system. The deflections $\delta \boldsymbol{x}_s$ of the structure are defined at a set of points $\boldsymbol{x}_s$ by,

$$\delta \boldsymbol{x}_s(t) = \Phi(\boldsymbol{x}_s)\, \boldsymbol{\eta}(t) \tag{5.13}$$

where the vector $\boldsymbol{\eta}$ contains the n generalised coordinates (modal amplitudes). The columns of the matrix Φ contain the mode shape vectors evaluated from a finite–element model of the structure using the commercial software package MSC.Nastran. As discussed in [25,53], the finite–element equations are projected onto the mode shapes and an appropriate scaling is applied to obtain generalised masses of magnitude one according to $\Phi^T M \Phi = I$. Then, a system of $2n$ scalar equations is given for the modal structural model in state–space representation, denoted here as

$$\dot{\boldsymbol{w}}_s = \boldsymbol{R}_s(\boldsymbol{w}) \tag{5.14}$$

with $\boldsymbol{w}_s = \left[\boldsymbol{\eta}, \dot{\boldsymbol{\eta}}\right]^T$ and $\boldsymbol{w} = \left[\boldsymbol{w}_f, \boldsymbol{w}_s\right]^T$. The corresponding residual vector including structural damping is written as

$$\boldsymbol{R}_s = D\,\boldsymbol{w}_s + \vartheta\, E\, \Phi^T \boldsymbol{f}(\boldsymbol{w}) \tag{5.15}$$

with the matrices D and E given by

$$D = \begin{pmatrix} 0 & I \\ -\Phi^T K \Phi & -\Phi^T C \Phi \end{pmatrix} \quad \text{and} \quad E = \begin{pmatrix} 0 \\ I \end{pmatrix}, \tag{5.16}$$

where I is the $n \times n$ identity matrix. Recall the similarity to the classical formulation in Section 4.4. The generalised stiffness matrix $\Phi^T K \Phi$ contains the n squared normal mode frequencies on the diagonal. The generalised damping matrix $\Phi^T C \Phi$ contains the n values of modal damping on the diagonal. For the test cases simulated in this study, structural damping is not considered and set to zero throughout in the following discussion. The vector $\boldsymbol{f}$ of aerodynamic (pressure) forces at the structural grid points is evaluated as the wall pressure times the area of the surface segment and the unit normal vector. It is then projected using the modes shapes to obtain the n generalised forces $\Phi^T \boldsymbol{f}$. The parameter ϑ for the mass ratio is calculated as (reference density)$\times$(reference length)^5 and follows from the nondimensionalisation of the governing equations,

$$\left(\frac{q_r^*}{x_r^*}\right)^2 \left(\ddot{\boldsymbol{\eta}} + \Phi^T C \Phi\, \dot{\boldsymbol{\eta}} + \Phi^T K \Phi\, \boldsymbol{\eta}\right) = x_r^*\, \varrho_r^* \left(q_r^* x_r^*\right)^2 \left(\Phi^T \boldsymbol{f}(\boldsymbol{w})\right), \tag{5.17}$$

where r and $(^*)$ denote reference values and dimensional quantities, respectively. Note that the generalised masses have been scaled to one. The similarity to the aerofoil structural model presented in Section 5.1.1 is evident and intended.

In the common situation, the structural grid points $\boldsymbol{x}_s$ not only do not conform with the aerodynamic surface grid, but are also defined on different surfaces. This requires the transfer of information between the fluid and structural grids. The aerodynamic (pressure) forces, defined at the surface grid, have to be transferred to the structural grid, and the modal deflections $\delta \boldsymbol{x}_s$ have to be communicated back to the CFD surface mesh. This is achieved using a method called the constant volume tetrahedron transformation [150]. Also, different to the rigid aerofoil formulation, the geometry of interest (and thus the computational mesh) deforms. This is achieved using a transfinite interpolation of the surface displacements to the internal grid points [73]. Details of these methods can be found in the given literature.

The evaluation of the Jacobian matrix blocks follows the aerofoil structural model. The matrix A_{ss} is conveniently split into two contributions; one dominated by the normal mode frequencies and one due to the aerodynamic force vector. It is given by $A_{ss} = D + \vartheta\, E\, \Phi^T \partial \boldsymbol{f} / \partial \boldsymbol{w}_s$. The second term is usually negligible. The Jacobian matrix block A_{sf} describes how the structure responds to changes in the flow field. It is

formed as $A_{sf} = \vartheta\, E\, \Phi^T \partial \boldsymbol{f} / \partial \boldsymbol{w}_f$. Currently, the evaluation of the derivatives $\partial \boldsymbol{f} / \partial \boldsymbol{w}_s$ and $\partial \boldsymbol{f} / \partial \boldsymbol{w}_f$ is done using finite differences. Conveniently, the mass ratio is set to unity for the evaluation of the Jacobian matrices and adjusted in a matched fashion once needed as discussed in the following.

5.2.2 Goland Wing – Symmetric Case without Aerostatic Effects

First, the problem without aerostatic deformation is considered. Conveniently, write the Schur complement matrix S in Eq. (4.6) as

$$S = \left(C_1 + \vartheta\, C_2 - \lambda I\right) - \vartheta\, C_3 \left(A_{ff} - \lambda I\right)^{-1} A_{fs} \tag{5.18}$$

where the matrices C_1, C_2 and C_3 follow directly from the equations of the matrices A_{ss} and A_{sf} given in the previous section. This form allows the evaluation of the matrices C_2 and C_3 independently from the parameter ϑ, representing the altitude through the reference density. The matrices A_{ff} and A_{fs} contain sensitivities of the fluid system which is, by default, made dimensionless by freestream reference values making these matrices independent of altitude effects. This formulation is possible since, at this point, aerostatic effects are not considered.

The construction of the approximation model without aerostatic effects is simplified in the sense that a matched point simulation only requires the adjustment of the mass ratio to the current value of the reference density. The other part of the computationally expensive interaction term, $\widetilde{S}^c = -C_3 \left(A_{ff} - \lambda I\right)^{-1} A_{fs}$, is sampled for different values of the eigenvalue and, as done in this study, freestream Mach number. The matrix $C_1 = D$ also needs to be matched to the current reference values as the normal mode frequencies are made dimensionless using the reference freestream velocity. However, this task is trivial. The matrix C_2, containing the sensitivities of the force vector with respect to the deformation, is neglected, similar to the aerofoil formulation, as it was found to be several (typically 3 to 5) orders of magnitude smaller than the other terms. Indeed, the reconstruction of the interaction term is considered as the most significant source of error.

Thus, the approximated Schur complement matrix used for the stability analysis is written as

$$S \approx \widetilde{S}^s(\lambda, h_r, M_r) + \vartheta(h_r)\, \widehat{S}^c(\omega, M_r) \tag{5.19}$$

where h_r indicates the dependence on the altitude in addition to the freestream Mach number. The matrix $\widetilde{S}^s = C_1 - \lambda I$ is the modified structural term and $\widehat{S}^c$ is the kriging prediction of the modified interaction term $\widetilde{S}^c$ excluding the mass ratio. Then, the roots of the approximated Schur residual are found by any Newton–like method. In the first instance, the interaction term is evaluated with zero damping, as discussed for the aerofoil case, while the structural part uses the complete eigenvalue making it

an analogy to the classical p–k method. This simplification is appropriate as will be seen in the following discussion. Using the formulation in Eq. (5.19), the approaches of sampling and kriging for the matched point simulations using a modal structural model become equivalent to the aerofoil case with only minor modifications. The approach is applied in the following.

Different types of simulations are discussed. First, an altitude can be chosen to set the reference value of the density, affecting the parameter ϑ, and then the freestream velocity, only affecting the matrix C_1 through nondimensionalisation, is varied to detect the onset of the instability. The freestream velocity becomes the bifurcation parameter. Secondly, the altitude (as bifurcation parameter) can be varied independently while adjusting the values of the density and speed of sound according to the standard atmosphere conditions. Then, the velocity follows from the current Mach number. The latter matched point analysis is mainly used herein.

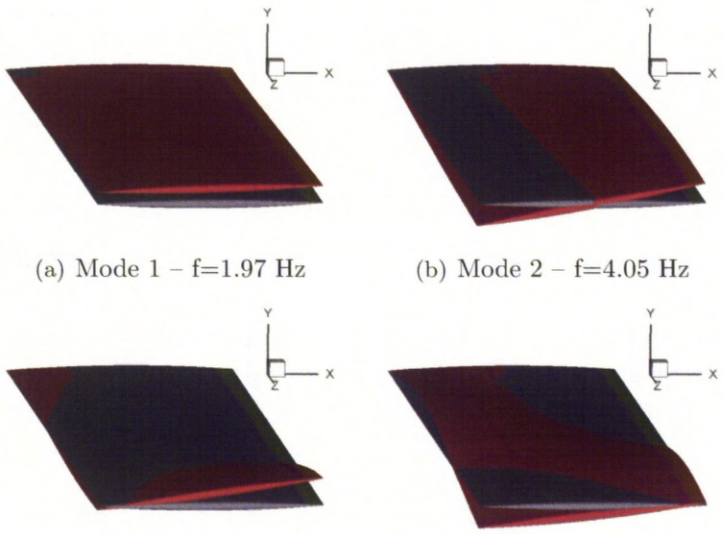

(a) Mode 1 – f=1.97 Hz (b) Mode 2 – f=4.05 Hz

(c) Mode 3 – f=9.65 Hz (d) Mode 4 – f=13.4 Hz

Figure 5.14: Mode shapes of clean Goland wing configuration.

The Goland wing is a model wing having a chord of 1.8266 m and a span of 6.096 m. It is rectangular and cantilevered with a constant cross section defined by a 4% thick parabolic–arc aerofoil. The finite–element model, used to calculate the mode shapes for the modal structural model in the CFD formulation, follows the description given in [24]. Two cases are discussed each retaining the four modes with the lowest frequencies (excluding in–plane modes) for the aeroelastic simulations. The frequencies as well as the mode shapes mapped to the CFD surface mesh for the clean wing without tip store and the wing/store configuration, respectively, are shown in Figs. 5.14 and 5.15. Here, a relatively large value of two is chosen for the modal amplitudes for illustration purposes. The considered baseline wing/store configuration has the point mass located

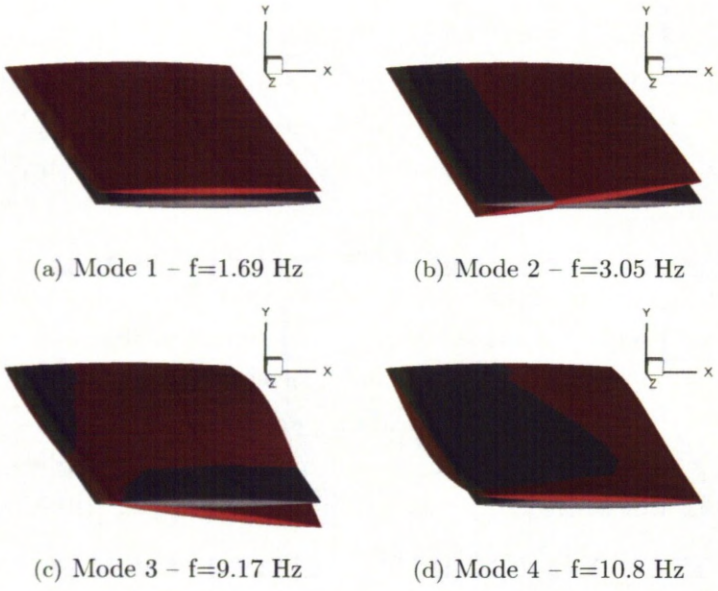

(a) Mode 1 – f=1.69 Hz

(b) Mode 2 – f=3.05 Hz

(c) Mode 3 – f=9.17 Hz

(d) Mode 4 – f=10.8 Hz

Figure 5.15: Mode shapes of Goland wing/store configuration.

at the wing tip at a streamwise location of 4.17% chord length (0.0762 m) from the leading edge [24]. A computational mesh with 200 thousand control volumes is used for the current Euler simulations while the store aerodynamics are not modelled. The wing tip is extended/rounded as a semi–circle having a radius of 2% chord length at the mid–chord location reducing towards the leading and trailing edge, respectively. The surface grid for the CFD simulations as well as a representative dimensionless pressure distribution at a freestream Mach number of 0.9 and zero degrees angle of attack, giving a transonic shock wave, are shown in Fig. 5.16. Using the Schur complement eigenvalue method, the Goland wing case with and without store has previously been discussed [22, 55] for the study of structural sensitivity.

Figures 5.17 and 5.18 give one representative element of the Schur interaction matrix with the mass ratio set to unity for the clean wing and wing/store configurations, respectively, showing real and imaginary parts individually. Herein, the reconstruction is based on 40 samples covering a Mach number range between 0.7 and 0.95 and a dimensionless frequency range between 0.05 and 0.35. The sample frequencies were chosen according to the normal mode frequencies of the first two modes, thus not covering the third and fourth mode. The consequences of this are presented below. For a defined number n of considered normal modes, a $2n \times 2n$ Schur complement matrix is formed. Using the first approach of the discussion in Section 4.2 to extract the elements of the Schur interaction matrix, there are $2n^2$ nonzero complex–valued elements (corresponding to an output dimension of $4n^2$ for the interpolation model) due to the matrix A_{sf} projecting the fluid response term $(A_{ff} - \lambda I)^{-1} A_{fs}$ onto the modal structural system.

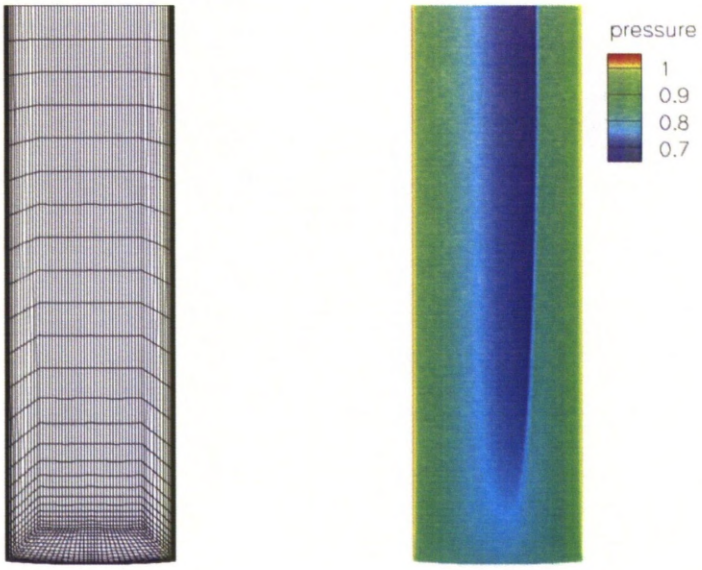

(a) Surface grid (b) Surface pressure

Figure 5.16: Surface grid and dimensionless surface pressure distribution at Mach 0.9 and zero degrees angle of attack for the Goland wing.

The presented matrix element shows a similar behaviour (with different absolute values) for the clean wing and wing/store configurations. In the subsonic region, small changes can be found in the response surfaces with respect to the input dimensions of Mach number and frequency, while there are significant variations in the transonic range. Thus, the response surfaces show a similar behaviour as for the aerofoil case. For freestream Mach numbers just below 0.9 setting the onset of the transonic range with distinct shock waves, the applied interpolation technique predicts a wave–like oscillation in the interaction elements, particularly in the imaginary parts, while capturing the main changes in element values. This artefact is due to the (physically meaningful) strong changes in the response surfaces between Mach numbers of 0.9 and 0.95.

The distinct changes in the response surfaces above a freestream Mach number of 0.9 are related to significant changes in the instability boundary, leading to shock induced limit–cycle oscillation (LCO) in the wing/store case as discussed in [24,55]. The instability boundaries for the clean wing and wing/store configurations are presented in Fig. 5.19. Here, the boundaries are shown for the two types of simulations. The results for the instability onset with increasing velocity at fixed sea level conditions are compared with the numerical predictions in [24]. The results using the sampling and reconstruction approach are included where the kriging approximation of the interaction term is shown in Figs. 5.17 and 5.18. Importantly, the kriging approach gives excellent agreement with the full order predictions based on the series method. The simulation results using the quasi–Newton approach are not shown herein as they were found to be indistinguishable.

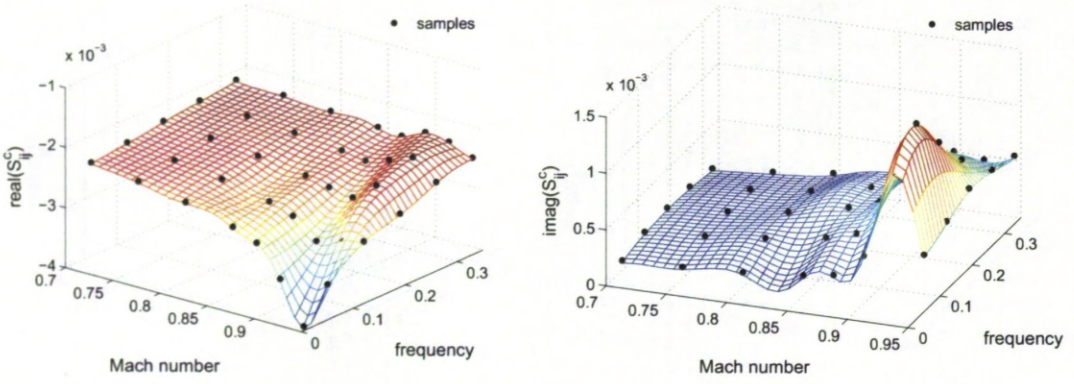

(a) real part (b) imaginary part

Figure 5.17: Extracted and interpolated element $S^c_{5,3}$ of Schur interaction matrix for clean Goland wing configuration using Euler flow model.

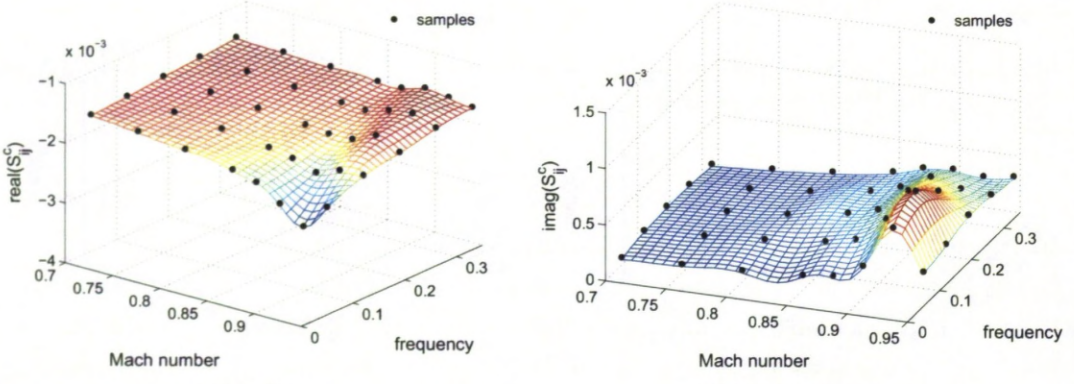

(a) real part (b) imaginary part

Figure 5.18: Extracted and interpolated element $S^c_{5,3}$ of Schur interaction matrix for Goland wing/store configuration using Euler flow model.

In Fig. 5.19(a) the clean wing configuration develops a clear transonic dip with a minimum critical velocity of about 110 m/s. Similarly, a somewhat flatter transonic dip is obtained for the wing/store configuration with a minimum velocity of about 180 m/s (stabilising the system). The basic features of the instability boundary, as discussed in [24], are found. At a freestream Mach number of about 0.9 the boundaries rapidly increase in both cases which is related to the forming of a strong shock wave. For the wing/store case, it is followed by a bucket of shock induced LCO at about Mach 0.92. Here, the dominant aeroelastic response changes from the (until then) first bending mode to the first torsion mode, which was confirmed in the present study through the critical eigenvalues. Note, that the peak before the LCO bucket is characterised by the third mode [24]. The results of time–accurate simulations, included in the figure at two freestream Mach numbers, support the eigenvalue–based results with the plus (tilde)

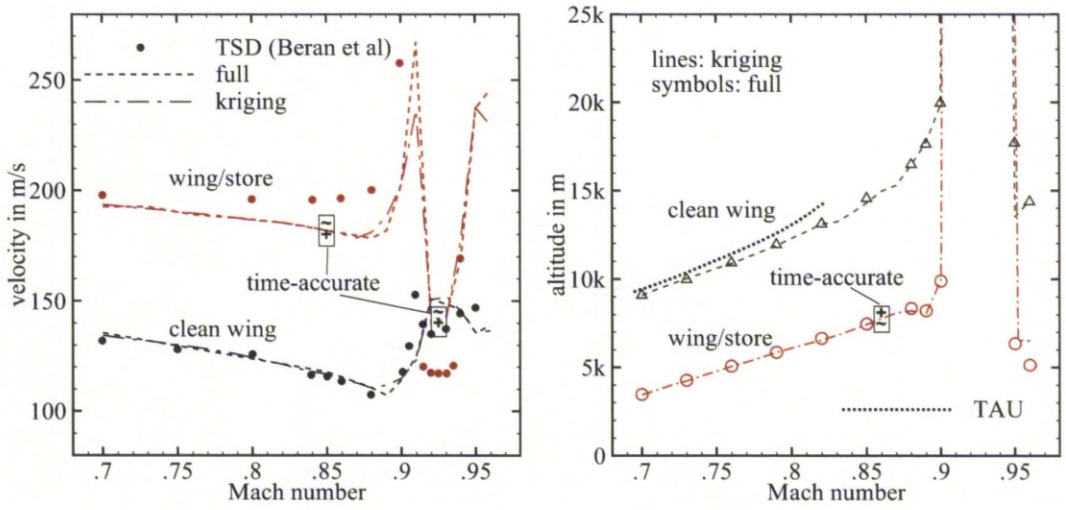

(a) Critical velocity at sea level conditions

(b) Critical altitude

Figure 5.19: Instability boundaries of Goland wing configurations showing critical values of velocity and altitude compared with numerical results (where available) in [24]; TSD – transonic small disturbance.

sign indicating a stable (unstable) response. In contrast to the lower Mach number at 0.85, the response signals of the generalised coordinates describe an instability stronger dominated by the second mode at Mach 0.925.

The reasons for the discrepancy in the results with [24], particularly for the wing/store case, are not discussed further though as the most important target in this study, i.e. the agreement between the full order and approximation models, is achieved. However, the reasons could be due to differences in the finite–element model causing variations in the normal mode shapes. Also, in [24] the results are based on a model assuming transonic small disturbance (TSD) potential flow in contrast to the current Euler flow.

Similarly in Fig. 5.19(b), showing the instability boundaries with respect to altitude changes, the wing/store configuration gives a more benign response allowing flight operations at lower altitudes compared with the clean wing. Between freestream Mach numbers of 0.91 and 0.94 the aeroelastic system is unstable (dominated by the second mode) right from the start of the considered altitude range at 30 km. Note that structural damping is not considered in the current simulations while small values of structural damping can stabilise the unrealistically high altitudes for the instability onset [151]. As in the previous paragraphs, the agreement between the full order results and the kriging approach is excellent. Also, the time–accurate results match the eigenvalue–based predictions.

Figure 5.19(b) includes an additional set of results denoted "TAU". These are results taken from a preliminary study aimed at implementing the Schur complement eigen-

value formulation, using the approach based on sampling and reconstruction, in the DLR TAU code [152]. These results for the clean Goland wing as well as NACA 0012 aerofoil results will be discussed further in Section 5.3.

Figures 5.20 and 5.21 show the tracing of the four normal modes with respect to altitude changes and compare the full order predictions with results from the kriging–approximated interaction term following Figs. 5.17 and 5.18. The full order predictions were obtained by applying the series method with a second order expansion. The agreement in both the onset of the instability and the mode tracing should be considered as excellent. The results show a classical binary instability mechanism with an instability occurring alongside the interaction of two aeroelastic modes involving the first bending and first torsion mode. In addition, the wing/store case gives a second instability at lower altitudes following the interaction of the third and fourth mode.

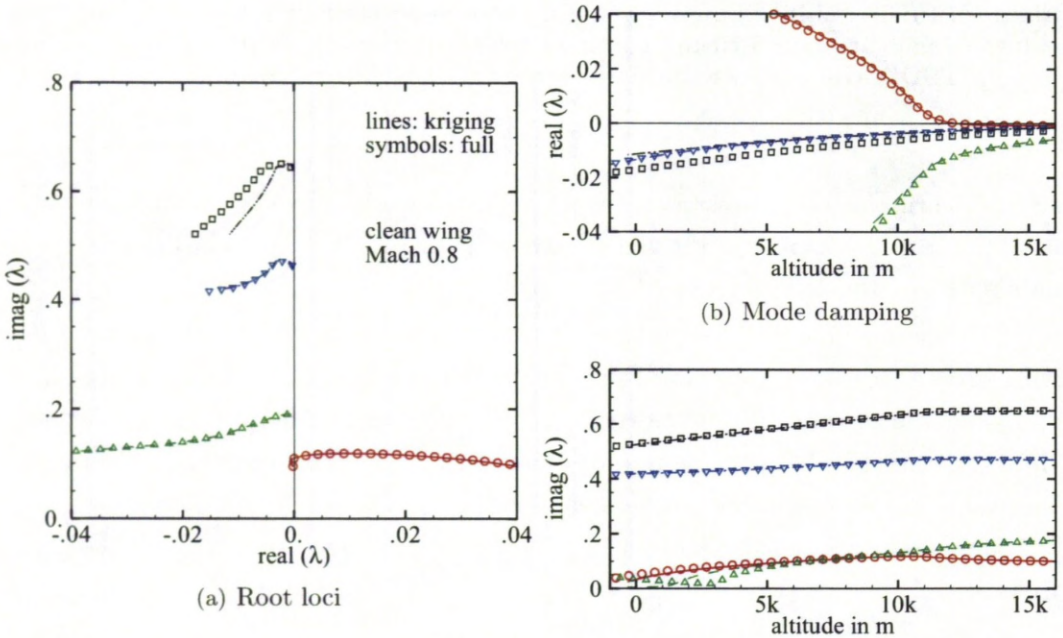

(a) Root loci

(b) Mode damping

(c) Mode frequency

Figure 5.20: Mode tracing at Mach 0.8 with respect to altitude for clean Goland wing configuration (eigenvalues in dimensionless form).

There are two interesting aspects concerning the kriging formulation. First, as for the aerofoil case, the simplification of using an approximate Schur interaction matrix based on samples with zero damping is appropriate. The modes can be traced accurately even away from the imaginary axis (where the approximation is exact within the limits of the interpolation algorithm) suggesting that the variations of the structural part, $C_1 - \lambda I$, with respect to the eigenvalue's real part are more dominant compared with the variations of the interaction part $S^c(\omega)$.

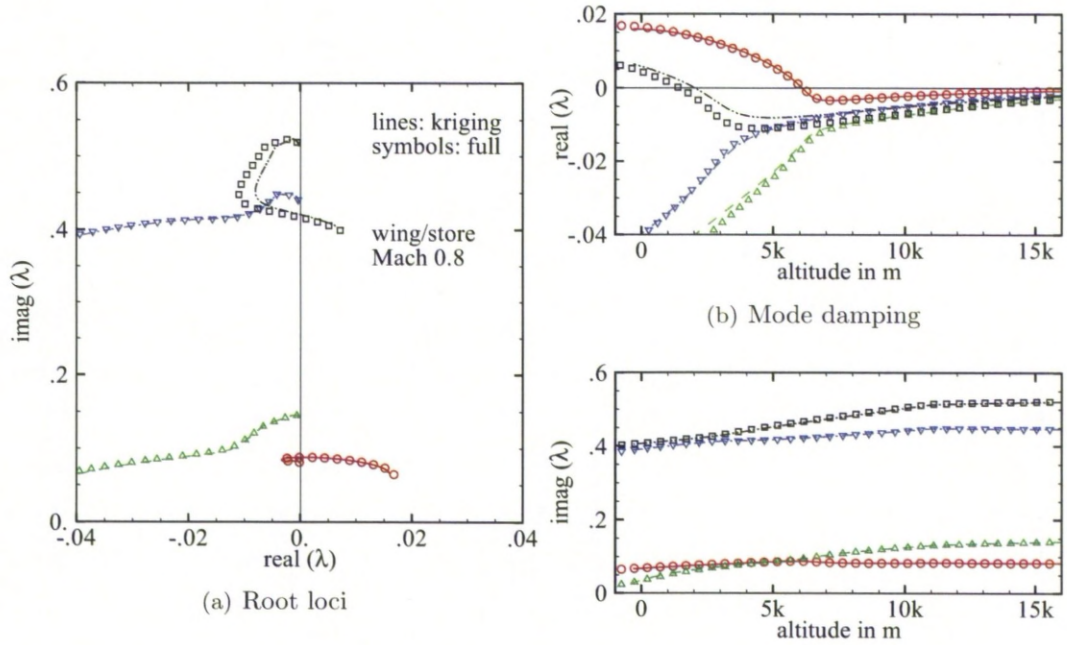

(a) Root loci

(b) Mode damping

(c) Mode frequency

Figure 5.21: Mode tracing at Mach 0.8 with respect to altitude for Goland wing/store configuration (eigenvalues in dimensionless form).

Secondly, it must be remarked that the samples, used in this study for the reconstruction of the response surfaces, cover only the frequency range of the first and second normal mode up to a dimensionless value of 0.35. Thus, the kriging model extrapolates to deal with the two higher frequency modes while doing a good job. This also suggests that the influence of the interaction term on the structural eigenvalue problem for the higher frequency modes is relatively small. The sensitivity of the modes to changes in the components of the interaction matrix will be addressed in the discussion for the MDO wing case.

The issue of cost is now addressed. For the reconstruction of the response surfaces in Figs. 5.17 and 5.18, in each case 40 samples are used corresponding to the cost of $40 \times 2n$ linear solves against the high dimensional fluid system (using the first approach discussed in Section 4.2) once the steady state solution is available. In the following one linear solve is taken as an equivalent cost factor because the solutions of the large sparse linear systems incur most of the involved cost. These samples allow the stability analysis covering an entire range of freestream Mach numbers between 0.7 and 0.95. Using the series method with a first order expansion, the evaluation of the series factors for each of the four normal modes takes $n \times 4n$ linear solves per Mach number (while tracing the modes can then be done essentially without additional cost). Thus, with the fifth Mach number the cost invested in constructing the kriging model pays off. Also, the reconstruction approach becomes more powerful with an increasing number

of normal modes as every individual sample supports the analysis/tracing of all modes while the series factors are only valid close to the shift, e.g. the normal mode frequency, they have been evaluated for.

Once the approximation model is established, the stability analysis can be done (essentially) without additional cost no matter how large the original CFD–based system becomes. The aim of using kriging to interpolate the elements of the interaction matrix is to reduce the number of calculations for a blind search over the flight envelope, i.e. for a range of flow conditions, as will be seen in the following. However, for a single point analysis excluding aerostatic effects it seems to be more advantageous to use the series method as the kriging model requires a minimum number of samples.

Another interesting aspect of constructing a response surface could be the gained insight into the involved physics through visualising the characteristics of the input–output dependencies. It could help in developing an understanding about the dominant mechanisms of the applied model [122].

5.2.3 MDO Wing – Nonsymmetric Case with Aerostatic Effects

To include the effects of aerostatic deformation, the approximate Schur complement matrix used for the stability analysis is written in a fashion similar to Eq. (5.19),

$$S \approx \widetilde{S}^s(\lambda, h_r, M_r) + \vartheta(h_r)\, \widehat{S}^c(\omega, h_r, M_r), \tag{5.20}$$

with the difference that the modified interaction term now depends on the altitude. As a consequence, the sampling has to cover the altitude range of interest. This however is equivalent to the requirements of the exact (full order) eigenvalue solver. Using the series method, the factors have to be re–evaluated constantly as the modes are traced with changing altitude. Here, the altitude change before re–evaluation depends on the demanded accuracy. As will be seen below, the reconstruction of the (modified) interaction term using interpolation becomes very attractive concerning the cost.

The multidisciplinary optimisation (MDO) wing is a highly flexible, commercial transport wing designed to operate in the transonic range. It has a span of 36 m and a thick supercritical section. The nonsymmetric section, given in Fig. 5.22, makes the steady state solution dependent on the altitude, which is attractive for the current discussion. The planform of the wing, including the surface grid for the CFD simulations, is also shown in Fig. 5.22. A computational mesh with 65 thousand control volumes is used for the discussed Euler simulations. The finite–element model is given by a wing box along the central portion of the wing [55]. For the aeroelastic stability analysis a total number of eight normal modes is considered with the (amplified) mode shapes, mapped to the CFD surface grid, and the normal mode frequencies given in Fig. 5.23. Modal damping is not considered. This case is chosen to demonstrate the applicability of the presented sampling and reconstruction approach to a higher number

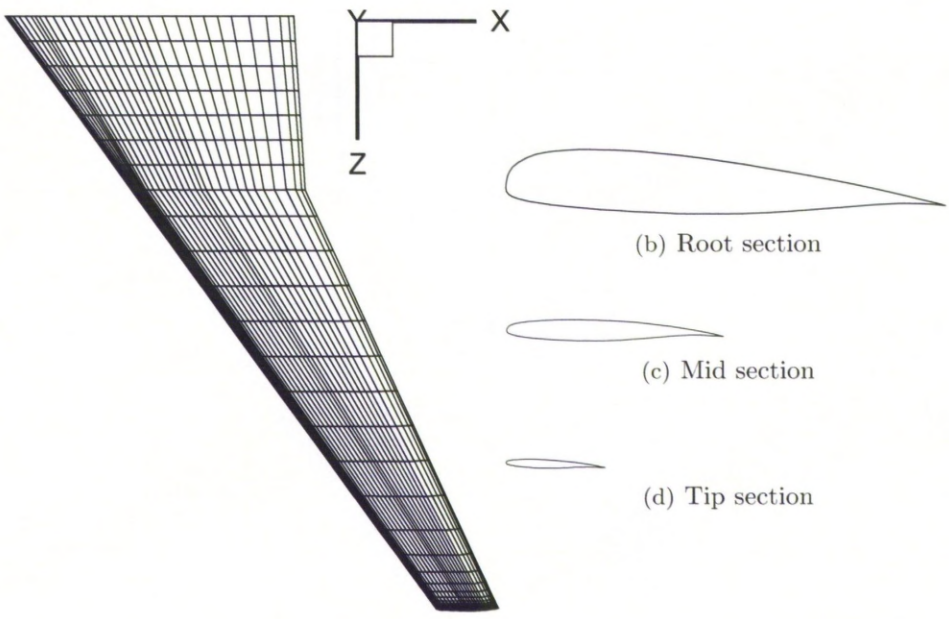

(b) Root section

(c) Mid section

(d) Tip section

(a) MDO wing planform

Figure 5.22: MDO wing planform and cross sections.

of normal modes. Due to the virtual design of the MDO wing, experimental data are not available [10].

The influence of the aerostatic deformation on the steady state solution with varying altitude is presented in Fig. 5.24 and compared with the results of a rigid wing simulation. The flow is simulated at a fixed transonic freestream Mach number of 0.85 and zero degrees angle of attack. It can be seen that a decreasing altitude, corresponding to an increase in the dynamic pressure, causes the wing to bend up and to twist the nose down slightly at the wing tip reducing the effective angle of attack [153]. The aerostatic deformation results in a weakened shock wave, present on the upper surface of the wing. Note the differences in the colour legends for the (dimensionless) pressure between the rigid and deformed wing.

Figure 5.25 gives one representative element of the Schur interaction matrix in the frequency/altitude parameter space for the Euler flow model with a freestream Mach number of 0.85 and zero degrees angle of attack corresponding to the conditions shown in Fig. 5.24. The matrix element describing a relatively simple response surface is shown with the actual value of the mass ratio matched to the altitude. The reconstruction is based on 32 samples covering dimensionless frequencies of up to 2.2 and an altitude range of up to 15 km covering the normal operational flight conditions. This kriging approximation is then applied to the aeroelastic stability analysis. The cost of the kriging prediction, having an output dimension of $4 \times n^2$ for the complex–valued elements of the interaction matrix (using the first extraction approach from Section 4.2), does not

(a) Mode 1 – f=0.84 Hz

(b) Mode 2 – f=2.16 Hz

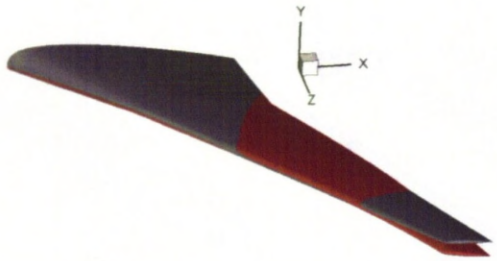

(c) Mode 3 – f=3.56 Hz

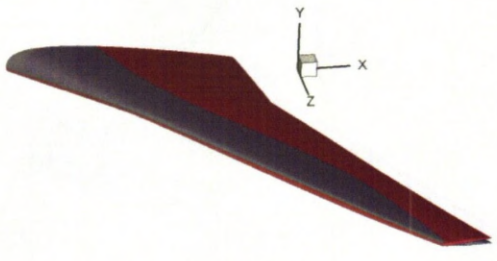

(d) Mode 4 – f=3.99 Hz

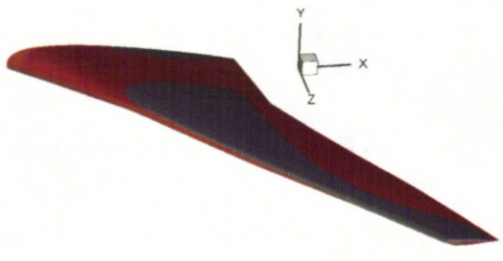

(e) Mode 5 – f=5.01 Hz

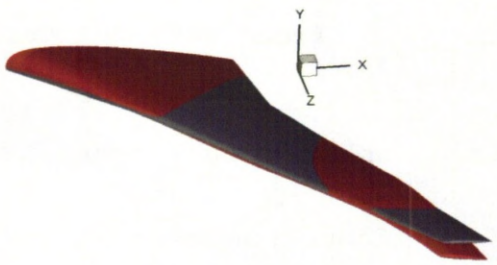

(f) Mode 6 – f=5.37 Hz

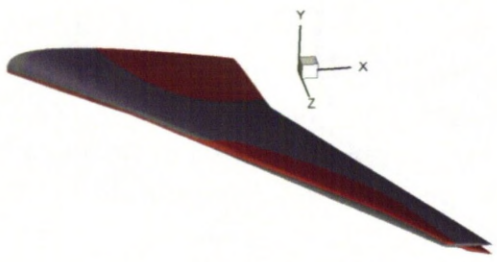

(g) Mode 7 – f=6.57 Hz

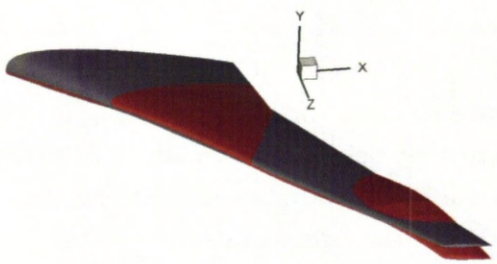

(h) Mode 8 – f=7.30 Hz

Figure 5.23: Mode shapes of MDO wing configuration.

increase significantly compared with the aerofoil formulation once the kriging model has been evaluated. Recall that the kriging model approximates the system response at the expense of only two scalar products.

The results of such a stability analysis including aerostatic effects are presented in Fig. 5.26. The figure gives an accurate tracing of all considered modes compared

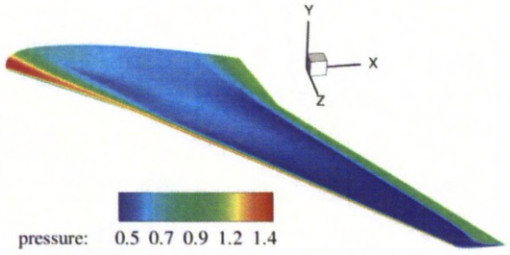

(a) Pressure distribution: rigid wing

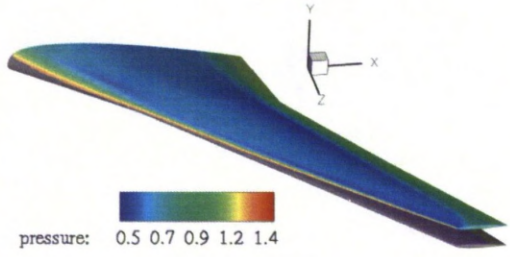

(b) Pressure distribution: flexible wing 15 km

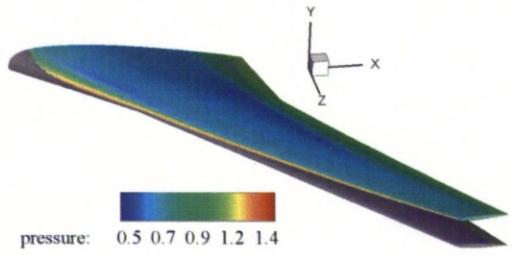

(c) Pressure distribution: flexible wing 9 km

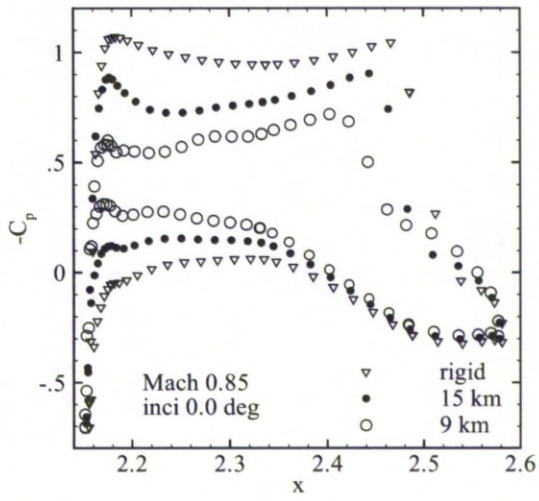

(d) Pressure coefficient at $z/z_{\text{tip}} = 0.62$

Figure 5.24: Effect of aerostatic deformation on surface pressure distribution at Mach 0.85 and zero degrees angle of attack for MDO wing.

with the full order results using the series method. Here, the series factors (just as the steady states) were re–evaluated at each new altitude for reasons of accuracy for the comparisons with an applied decrement of 500 m. The first mode goes unstable at an altitude of about 4.5 km, closely followed by the second mode crossing the imaginary axis at about 3.8 km. The differences in the frequency at lower altitudes for the fourth mode are due to the strongly damped character of this mode. The assumption of a simple harmonic aerodynamic response, i.e. $S^c(\omega)$ instead of $S^c(\lambda)$, does not hold in this case. However, this behaviour is irrelevant for the stability prediction.[4]

[4]The structural model applied in the current formulation is linear. In [153] however it was argued that for the class of flexible high aspect ratio swept wings (such as the MDO wing) the nonlinear aerostatic deformation plays a fundamental role in the instability mechanism causing a low amplitude limit cycle oscillation which may persist at high altitudes. Importantly, in [153] a nonlinear structural model (involving a larger number of degrees–of–freedom) was required to capture the described phe-

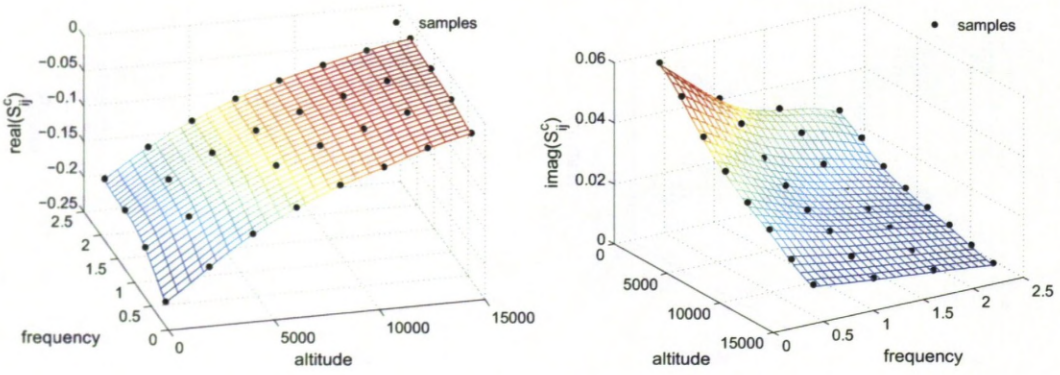

(a) real part

(b) imaginary part

Figure 5.25: Extracted and interpolated element $S^c_{9,1}$ of Schur interaction matrix for MDO wing configuration depending on altitude and dimensionless frequency at Mach 0.85 and zero degrees angle of attack.

For the sake of completeness, the influence of the small second term ϑC_2 in the structural part of Eq. (5.18) is considered. Therefore, a second kriging model was formed based on full order samples which are routinely evaluated alongside the samples of the interaction term. These samples allow the reconstruction of the corresponding response surfaces which, in this discussion, only depend on the altitude but not the frequency. This dependence is then included in the stability analysis. However, these "improved" predictions are within plotting accuracy compared with the results given in Fig. 5.26, and are therefore neither shown nor further discussed.

The issue of cost is analysed for the case with aerostatic deflection. For the reconstruction of the response surfaces in Fig. 5.25, 32 samples are used which is equivalent to the cost of $32 \times 2n$ linear solves (using the first approach discussed in Section 4.2) plus the evaluation of the steady state at each altitude. Evaluating one steady state corresponds to solving $2n$ linear systems in this case. The achieved resolution of the reconstructed response surfaces is sufficient to trace the eight normal modes accurately compared with the full order results. Using the series approach in the full order formulation on the other hand, the series factors (just as the steady states) have to be re–calculated several times as the altitude is decreased due to the included aerostatic deformation. One evaluation of the factors (for an expansion up to first order) for all eight modes takes $n \times 4n$ linear solves. Thus, the cost of forming the approximation model pays off after only the second re–evaluation of the series factors. Note, as mentioned before, for the demonstration shown in Fig. 5.26, the series factors were calculated at each new altitude (which makes it quasi–Newton) for reasons of accuracy.

nomenon, whereas a linear structure resulted in a critical dynamic pressure overpredicted by a factor of three. This is an important observation. In terms of the applicability of the approach discussed in this thesis, it must be remarked that the kriging model is constructed to approximate the results of the exact eigenvalue solver no matter if a linear or nonlinear structural model is used, and its cost must be judged relative to the exact eigenvalue solver.

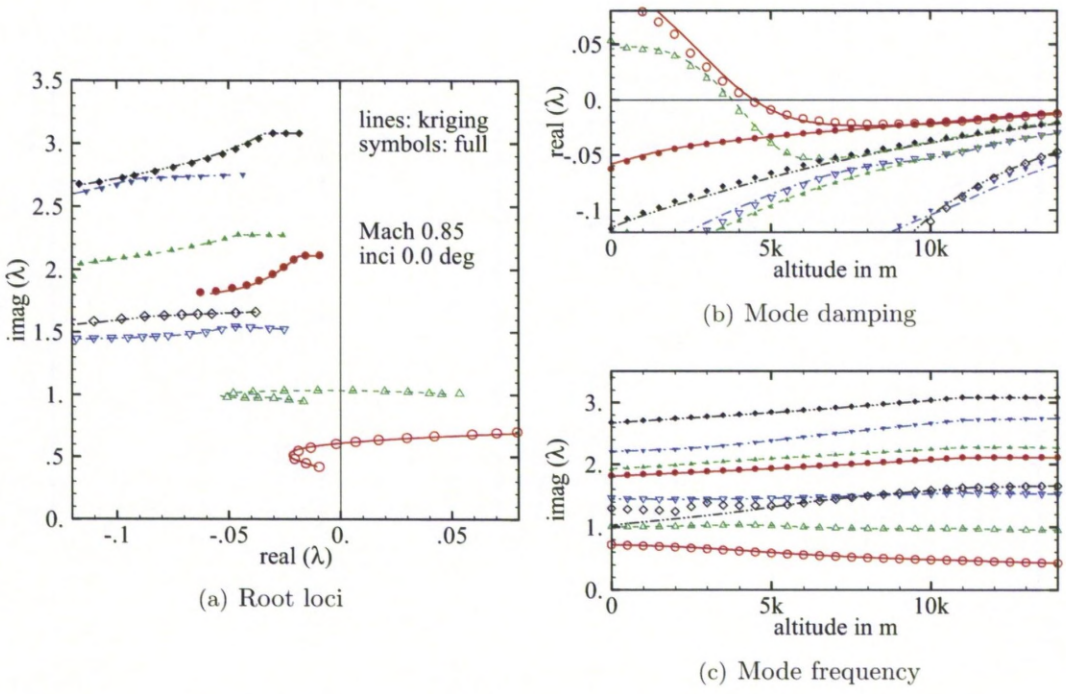

(a) Root loci

(b) Mode damping

(c) Mode frequency

Figure 5.26: Mode tracing for MDO wing configuration with respect to altitude at Mach 0.85 and zero degrees angle of attack (eigenvalues in dimensionless form).

The challenge for the kriging approach as discussed up to this point is not the inclusion of aerostatic effects at fixed freestream Mach number but the search for aeroelastic instability over the flight envelope, i.e. a range of freestream Mach numbers. Figure 5.27 shows the distribution of 140 samples for the reconstruction of the interaction matrix depending on altitude, frequency and Mach number. The contour slices for one representative interaction element at the freestream Mach number of 0.85 clearly resembles the response surfaces given in Fig. 5.25. Also, the traces of the first and second instability with changing Mach number are included in the figure to illustrate the important part of the parameter space.

The stability limit of the MDO wing configuration over a range of freestream Mach numbers between 0.7 and 0.9 is presented in Fig. 5.28 as critical values of altitude and dimensionless frequency. The results of the approximation approach are compared with full order evaluations. As can be seen in the figure, a reasonable agreement between the kriging and full order results is found. For freestream Mach numbers below 0.75, the configuration only encounters aeroelastic instability below sea level while at common cruise conditions the critical region starts at about 5 km. In addition, the first mode exhibits a second bifurcation at the highest Mach numbers which is below the second mode instability, and therefore not of immediate interest.

To support the eigenvalue based predictions, time–accurate simulations were done at Mach 0.85 with the plus (tilde) sign in the figure indicating a stable (unstable) response.

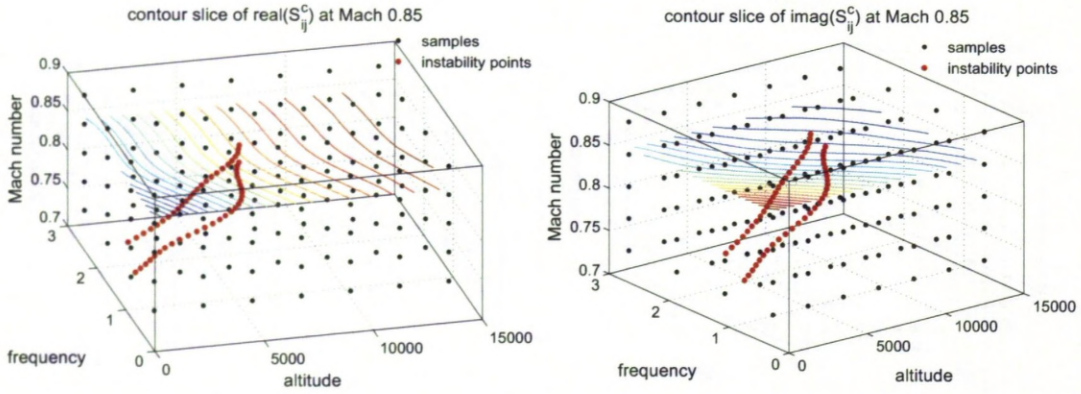

(a) real part

(b) imaginary part

Figure 5.27: Extracted and interpolated element $S^c_{9,1}$ of Schur interaction matrix for MDO wing configuration depending on altitude, frequency and Mach number at zero degrees angle of attack using Euler flow model.

The agreement is, as expected, excellent and the time–accurate system responses are dominated by the first unstable mode. The time–accurate simulations run with a dimensionless time step of 0.05 for temporal accuracy given 210 steps per cycle of motion for a dimensionless frequency of about 0.6. Then, one motion cycle corresponds to two steady state simulations (or to the extraction of two samples). Close to the instability point the time–accurate transient covers several motion cycles. Also, several time domain runs are required per Mach number to bracket the instability point.

Assume that four Mach numbers along a flight envelope are to be investigated while considering aerostatic effects. Generously, for an altitude search range of 15 km the series factors are re–evaluated only four times creating an equivalent cost of $4\times4\times n\times4n$ linear solves for the eight normal modes. Thus, the 140 samples, requiring $140 \times 2n$ linear solves (using the first approach in Section 4.2), generate about half the cost while giving competitive results. In the next chapter, the powerful approach of coordinated sampling shows how the prediction is improved with less samples.

At this point, the accuracy of the results based on the three dimensional uniform grid sampling, as shown in Fig. 5.27, is further analysed. In the aerofoil study it was found that changes in the interaction matrix with respect to the freestream Mach number are often more significant compared with frequency changes which would require more samples in the dimension of the Mach number to resolve the changes. In the current case for the MDO wing configuration, samples are calculated at five Mach numbers between 0.7 and 0.9 posing a challenge to the interpolation as this parameter dimension may be undersampled.

Also, to form the kriging model as discussed in Section 4.3, an optimisation problem has to be solved to determine the correlation parameters. Solving such an optimisation problem becomes increasingly difficult and unreliable with an increasing number of

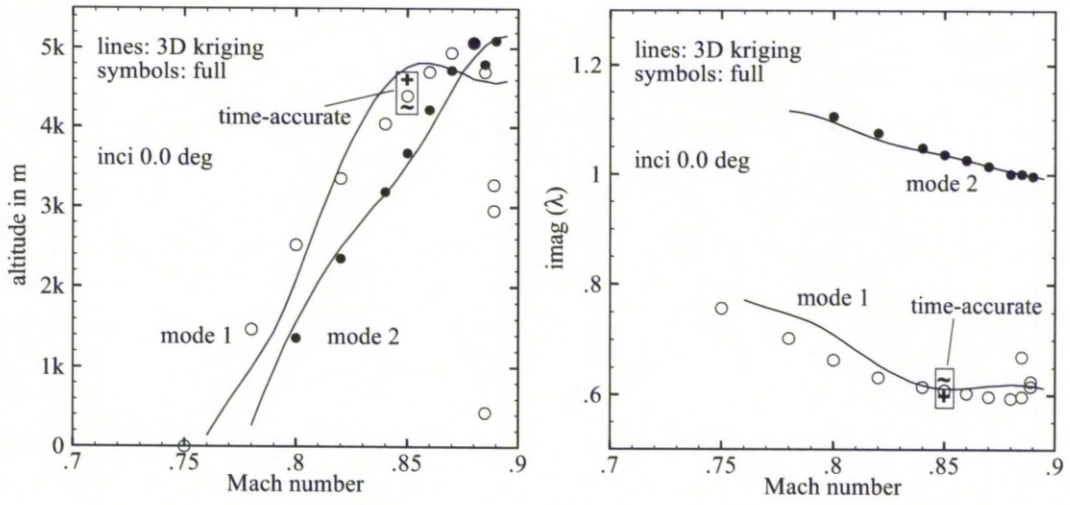

(a) Critical altitude

(b) Critical frequency

Figure 5.28: Stability results for MDO wing configuration using three dimensional grid sampling showing critical values of altitude and dimensionless frequency.

input parameter dimensions [116]. Poor predictions of the correlation parameters result in spurious oscillations, as already indicated in Figs. 5.17 and 5.18 for the Goland wing configurations, while visual inspection for more than two input dimensions is difficult. However, the basic methodology, that is outlined in this work, to address the prediction of aeroelastic instability is not limited to the kriging interpolation approach per se. Thus, despite giving good results in this study, more robust interpolation tools could be used in future applications. Currently, alternative techniques for the reconstruction such as artificial neural networks are under consideration.

Importantly, in Fig. 5.29 the stability limit is presented for the rigid MDO wing (i.e. without aerostatic deformation). Note that, strictly speaking, the structural residual in Eq. (5.15) does not describe a steady state solution as the nonsymmetric cross section of the wing will always result in a nonzero force vector. Without deformation this nonzero force vector is not balanced by the stiffness terms. However, for the evaluation of the Jacobian matrix blocks, finite differences are applied which only consider a variation about the mean solution of the force vector.

The results demonstrate the importance of including the effects of aerostatic deformation in the transonic aeroelastic stability analysis. The stability characteristics are significantly changed as can be seen in the figure. Here, the typical transonic dip, related to the first bending mode going unstable, is formed and shifted to lower Mach numbers compared with the results including aerostatic deformation in Fig. 5.28. This should be attributed to the formation of the transonic shock waves. The shock strengths are reduced by the aerostatic deformation compared with the rigid case as can be seen in the pressure distribution given in Fig. 5.24.

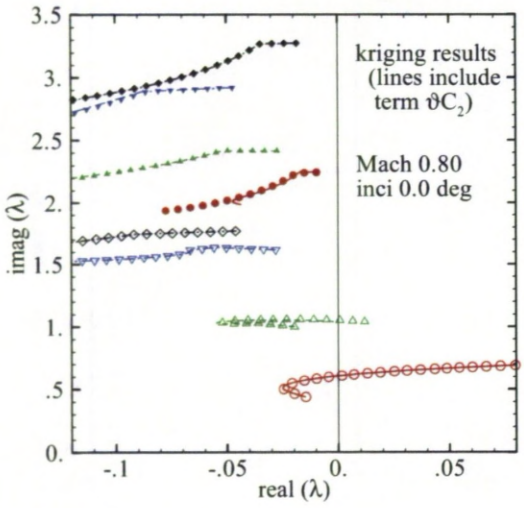

(a) Root loci

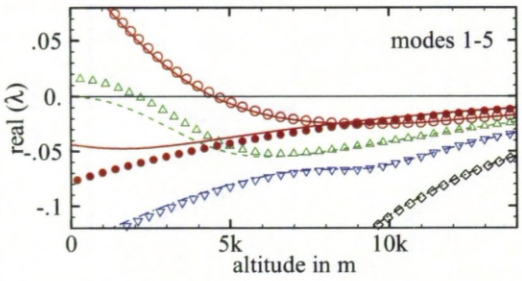

(b) Mode damping

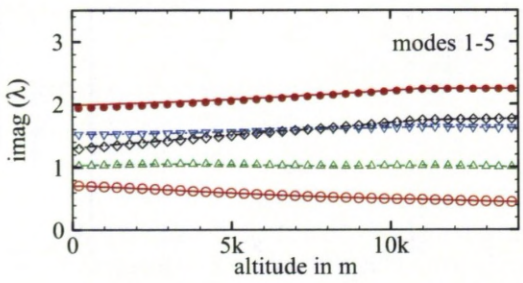

(c) Mode frequency

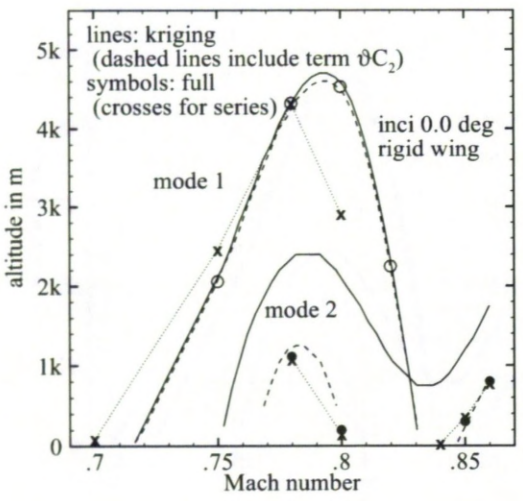

(d) Critical altitude

Figure 5.29: Stability results for rigid MDO wing configuration using two dimensional grid sampling showing (a–c) mode tracing at Mach 0.80 with respect to altitude using kriging–based analysis and (d) critical values of altitude.

Several observations concerning the presented eigenvalue–based stability analysis can be discussed. First, note the differences in the results of the exact eigenvalue solver using the series method (with a second order series expansion) and the quasi–Newton approach. Here, distinct differences are found, particularly for the instability associated with the first bending mode. This demonstrates the limits of the series expansion in some situations for larger variations in the response frequency (relative to a chosen shift). Thus, the series approach is very useful and efficient but the robustness and accuracy should always be considered.

Secondly, the agreement of the kriging–based simulations with the quasi–Newton results is excellent as expected since the kriging approximation is based on exact samples. Thirdly, a second kriging simulation is shown. These additional results consider the effect of the second term ϑC_2 in the structural part of the Schur complement matrix in Eq. (5.18) on the stability analysis. The influence on the first mode is negligible while, surprisingly, the second mode instability is significantly changed correcting the prediction towards the full order eigenvalue solver results. In this case, the variation of the force vector with respect to the structural unknowns cannot be neglected.

In Fig. 5.30 the distribution of the samples in the frequency/Mach number parameter space is presented including the trace of the first and second mode instabilities projected onto the response surface for one element of the interaction matrix. Here, as for the Goland wing case, the influence of the formation of the shock wave on the response surfaces can be identified by the significant changes. In the figure, the magnitude of the interaction term should not be misinterpreted. The results are plotted for the mass ratio set to unity. Multiplication with the actual value of this parameter introduces a factor of the order 10^6 in the region of the instability.

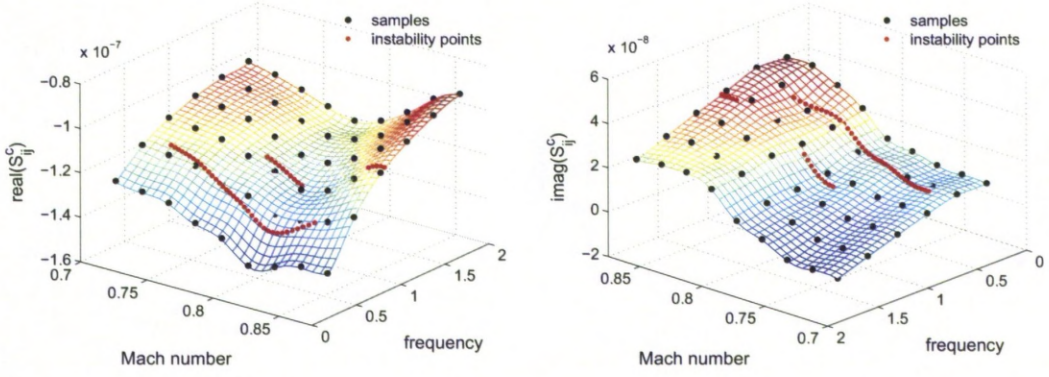

(a) real part

(b) imaginary part

Figure 5.30: Extracted and interpolated element $S^c_{9,1}$ of Schur interaction matrix for rigid MDO wing configuration at zero degrees angle of attack.

Interestingly as an additional remark, in [154,155] a model reduction technique was described to identify the system dynamics, including aerostatic effects, directly from the restart of a rigid steady state solution to avoid the re–computation of an aerostatically deflected steady state solution for each new value of the dynamic pressure. Such a capability is demonstrated in a similar fashion in this study as the influence of the aerostatic deformation is pre–computed.

Now it is assumed that the kriging model does a good job to precisely reconstruct the response surfaces of the interaction matrix elements giving an exact representation

of the full order model output. Further, it is assumed that the uncertainty in the aerodynamic modelling is reflected in the response surfaces (which is actually true but still needs to be understood in detail of how, for instance, changes in the shock location affect the interaction term). Then, the cheap approximation model can be exploited to analyse the sensitivity of the eigenvalue problem on the interaction elements.

Figure 5.31 shows the sensitivity of the mode tracing with respect to a 20% variation randomly distributed over the $2n^2$ nonzero elements. In the figure the sensitivity is expressed by one standard deviation about the mean. Theoretically, it is possible to find the sensitivity of the system response with respect to each element individually. However, this is not attempted at this point because of two arguments. First, it should always be possible to evaluate one complete sample (i.e. one complete interaction matrix). Secondly, it seems to be more important to place complete samples in the right spot in the parameter space, the information of which can be derived from the sensitivity of the traces.

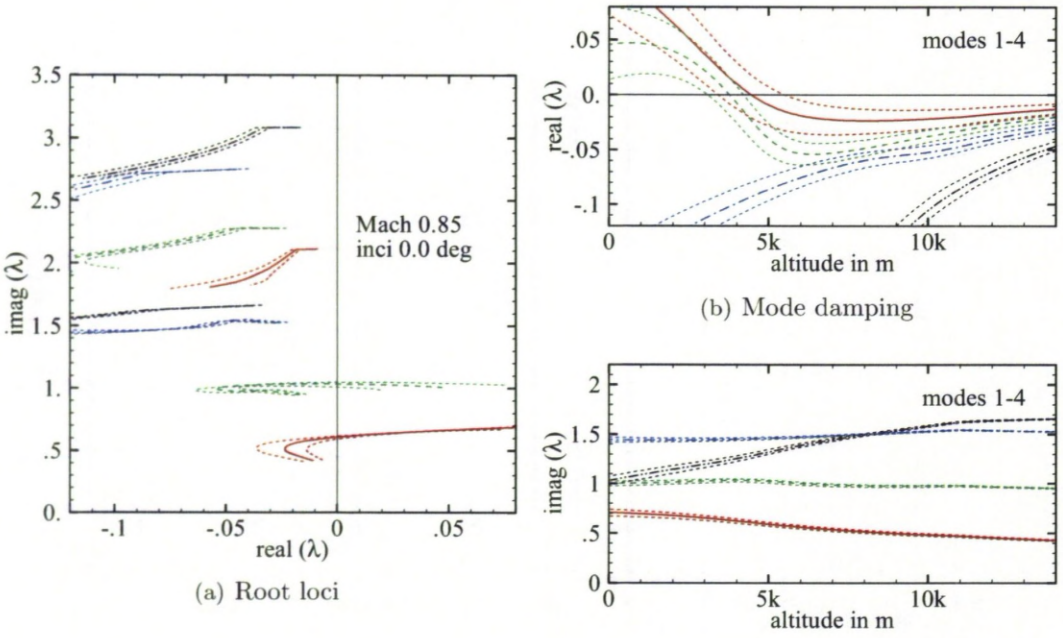

(a) Root loci

(b) Mode damping

(c) Mode frequency

Figure 5.31: Sensitivity of mode tracing for MDO wing configuration at Mach 0.85 and zero degrees angle of attack showing one standard deviation due to 20% variation.

In this case the results demonstrate that the relatively large variation does not give any tendency of the six higher frequency modes to go unstable while the first and second mode give rise to some uncertainty about the onset of the instability. The predicted frequencies are basically unaffected. In addition, this information would allow

the estimation of the importance of using higher fidelity (more expensive) aerodynamic models, and, if considered to be important, the relevant locations to place the better samples.

5.2.4 Summary of Three Dimensional Stability Calculations

The discussion on the three dimensional test cases, including the Goland wing and the MDO wing, has resulted in interesting conclusions for the purpose of this work to search flight envelopes for aeroelastic instability.

Most importantly, the discussed approach using the kriging–based reconstruction of the computationally expensive Schur interaction matrix, as established for the aerofoil cases, is applied to general three dimensional cases and higher dimensional input parameter spaces representing flight envelopes. The use of a modal structural model requires only minor modifications to the formulation. Excellent results compared with the solution of the exact (full order) eigenvalue solver are found at lower, very competitive cost.

It has been demonstrated that the application of the approach to problems including the effects of aerostatic deformation, as for the MDO wing, becomes very powerful. This important point will be emphasised in Chapter 6 by a further cost reduction using coordinated sampling.

5.3 Results of the Implementation in the TAU Code

During the course of this work, the presented eigenvalue–based stability approach, including the sampling and reconstruction method, was implemented in the DLR TAU code using its linear frequency domain solver [152]. The preliminary results from this study are presented next to supplement the discussion. Results are shown for the earlier discussed cases of the NACA 0012 "heavy case" configuration and the clean Goland wing configuration. The approach was also successfully applied to the design study of a realistic Airbus passenger jet including 15 normal modes, the results of which cannot be presented herein.

5.3.1 NACA 0012 Aerofoil Configuration

Figure 5.32 presents the sub- and transonic instability boundary, using Euler flow modelling, as critical values of the flutter speed index V_F and dimensionless frequency ω_F for the NACA 0012 "heavy case" configuration. Details about the parameters of the aerofoil structural model are summarised in Table 5.1. A comparison with results of the exact Schur complement eigenvalue solver, referred to as BIFOR, is included. The agreement between the BIFOR results based on the exact formulation and the kriging approximation is excellent, as expected, due to the high sample resolution.

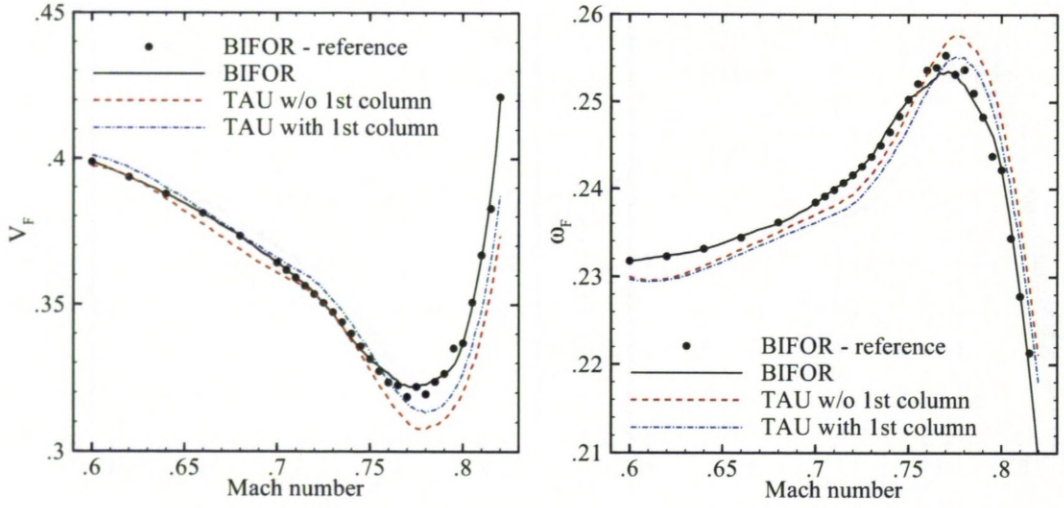

(a) Critical flutter speed index

(b) Critical frequency

Figure 5.32: Instability boundary for NACA 0012 configuration comparing BIFOR and TAU kriging–based results including BIFOR full order reference solution.

Also, the comparison to TAU is good considering the different numerical schemes for the discretisation of the governing equations and very different grid resolutions used for the two flow solvers. While a block–structured grid with 15 thousand control volumes is used for the BIFOR simulations, the unstructured triangular grid used for TAU only has two thousand.

The TAU results in Fig. 5.32 show two graphs. The numerical scheme in BIFOR rigidly moves the grid to simulate the pitching and plunging motion, whereas TAU reshapes the grid with a fixed far field boundary. The BIFOR results show an independence of the fluid response on the plunge state h in the matrix A_{fs}, i.e. the column corresponding to the plunge state is zero. The TAU results, on the other hand, do not predict this column to be zero but to have small values compared with the other structural states. As a consequence the TAU results presented in Fig. 5.32 show the stability analysis with and without this column in A_{fs} corresponding to the plunge state. The difference is relatively small but might need further consideration. Herein, for the purpose of the demonstration study this is not attempted.

The samples for a range of freestream Mach numbers and dimensionless frequencies and the corresponding kriging evaluations of the response surfaces are shown in Fig. 5.33 for one element of the interaction matrix. The trace of the instability is included as combinations of Mach number and critical frequency to illustrate the important regions of the parameter space. In both cases, the samples were extracted using the linear frequency domain solver. It can be seen that the response surfaces for the interaction matrix, as predicted by TAU and BIFOR, are very similar which is consistent with the earlier discussion in Section 5.1 where different flow solvers applying different nonlinear

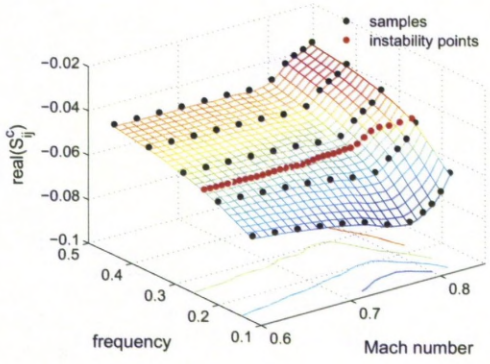

(a) BIFOR – real part

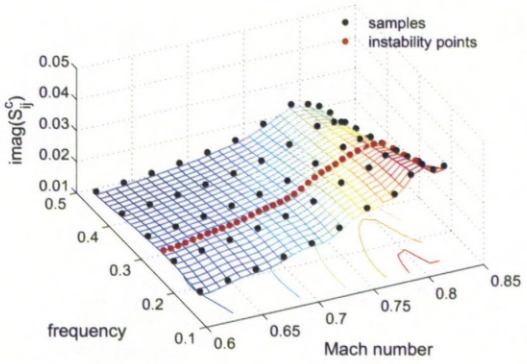

(b) BIFOR – imaginary part

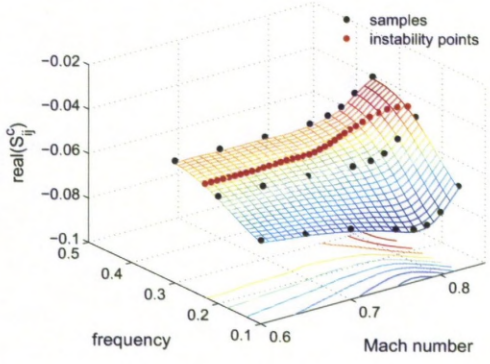

(c) TAU – real part

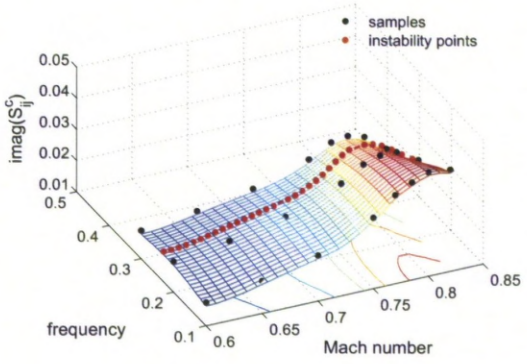

(d) TAU – imaginary part

Figure 5.33: Extracted and interpolated element $S_{3,3}^c$ of Schur interaction matrix for NACA 0012 configuration including real and imaginary parts and comparing the Euler flow models in BIFOR and TAU.

aerodynamic flow models showed the same behaviour. Thus, the shape of a response surface is dependent on the represented physics and should be (relatively) independent of the different numerical schemes.

5.3.2 Goland Wing Configuration

The results for the clean Goland wing configuration [24] using Euler flow modelling are presented in Figs. 5.34 through 5.36. The coarse computational mesh used for BIFOR has about 30 thousand control volumes while the mesh for the TAU solver has about 200 thousand. Four normal modes are included corresponding to the discussion in Section 5.2.2.

Figure 5.34 shows a comparison between BIFOR and TAU response surfaces reconstructed from a number of samples which were extracted using the first approach in the frequency domain discussed in Section 4.2. The trace of the predicted instability, projected onto the surface, is included to illustrate the important region of the

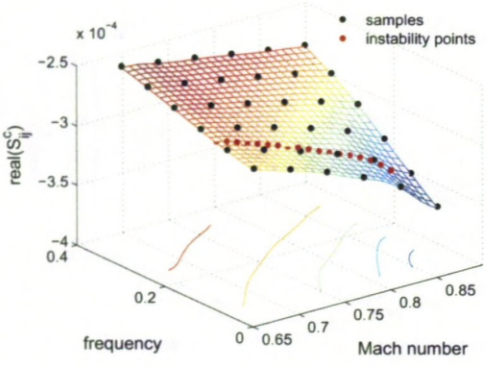

(a) BIFOR – real part

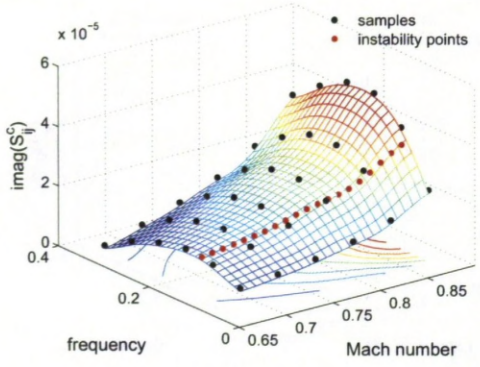

(b) BIFOR – imaginary part

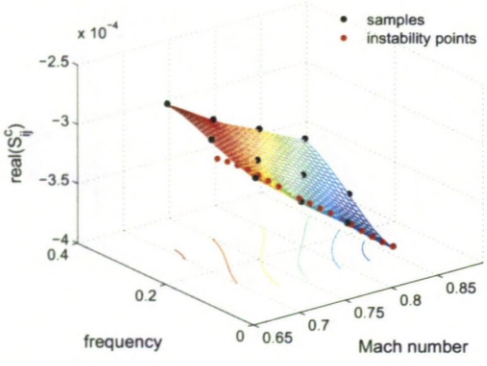

(c) TAU – real part

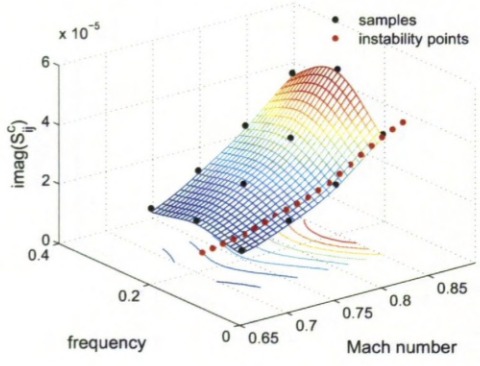

(d) TAU – imaginary part

Figure 5.34: Extracted and interpolated element $S^c_{5,1}$ of Schur interaction matrix for clean Goland wing configuration including real and imaginary parts and comparing the Euler flow models in BIFOR and TAU.

parameter space. Note that the limits of the sample space, i.e. the upper and lower limits of the dimensionless frequency and freestream Mach number, are smaller for the TAU evaluations compared with the BIFOR evaluations. Shown is one representative element of the interaction matrix with real and imaginary parts given individually. A qualitatively good agreement can be seen and this is confirmed by the corresponding stability predictions given below.

Figure 5.35 shows the tracing of the four aeroelastic modes at a freestream Mach number of 0.7. The simulations start from high altitudes (low dynamic pressures) using the normal mode frequencies as initial guess (shift) for the mode tracing. The results from the exact eigenvalue solver are obtained by applying the series method with a first order expansion. The approximation results using the samples from BIFOR give excellent agreement to the results from the exact eigenvalue solver. Also, the TAU results are in good agreement throughout. Note the extrapolation required for the higher frequency modes using the kriging approximation.

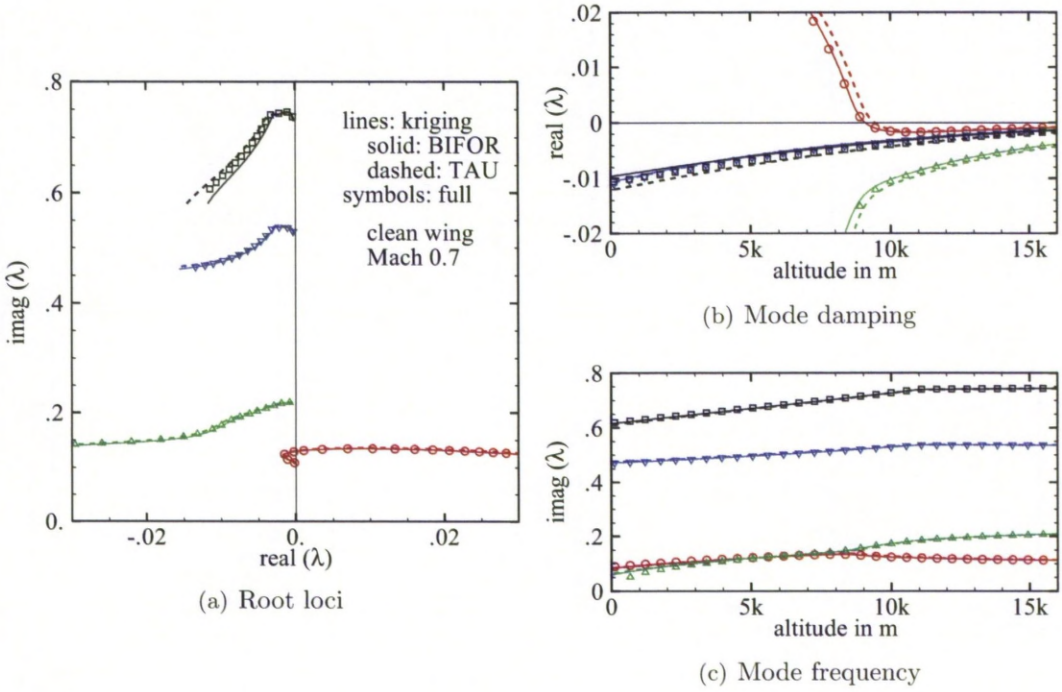

(a) Root loci

(b) Mode damping

(c) Mode frequency

Figure 5.35: Mode tracing at Mach 0.7 for clean Goland wing configuration comparing the Euler flow models in BIFOR and TAU (eigenvalues given in dimensionless form).

Figure 5.36 shows the aeroelastic instability boundary as critical values of altitude and dimensionless frequency for a range of freestream Mach numbers based on the samples and reconstruction in Fig. 5.34 and compares with the exact (full order) evaluations. The agreement is good considering the different numerical schemes. Note that in the considered Mach number range the influence of the different computational grids was found to be rather small using the BIFOR solver. The results for the coarser computational grid with about 30 thousand control volumes agree closely with the results for the finer grid with about 200 thousand control volumes, which are presented in Section 5.2.2. Particularly, this can be seen in Fig. 5.19(b) comparing the TAU and BIFOR results using the same finer grid.

A more detailed study will be required to understand the difference in the critical altitude for the higher freestream Mach numbers. There are several important aspects to this discussion like the influence of the numerical schemes used to solve the governing equations and the chosen parameters required for the sample extraction. For instance, a sensitivity study with respect to the modal amplitude factor needs to be done. This factor is defined to evaluate the columns of the matrix A_{fs} used as the right–hand side vectors for the linear frequency domain solver in TAU [152]. Also, the influence of the convergence of the linear frequency domain solver needs to be discussed. Further

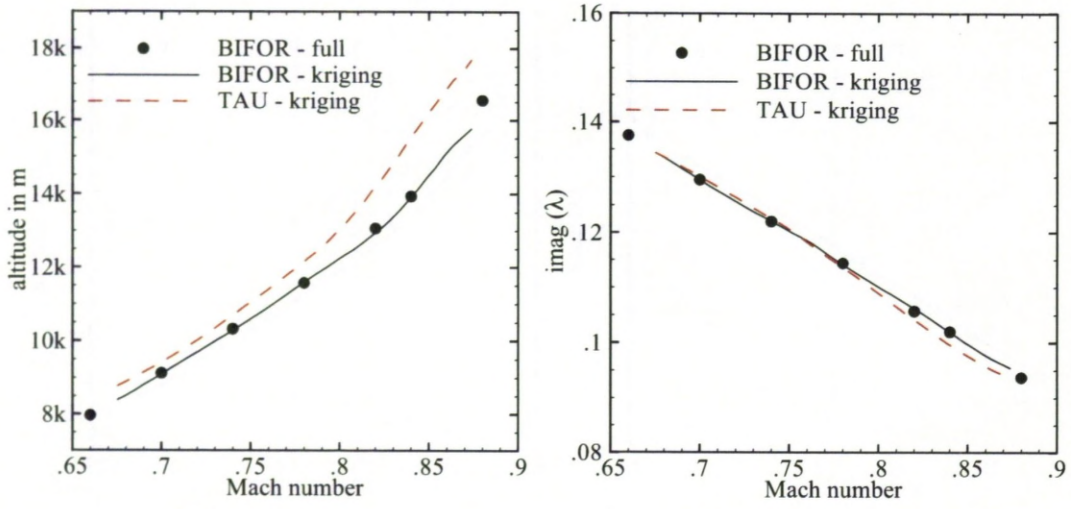

(a) Critical altitude

(b) Critical frequency

Figure 5.36: Instability boundary for clean Goland wing configuration comparing the Euler flow models in BIFOR and TAU.

interaction with DLR will allow the method to be consolidated into the production release of the TAU code, which is used by Airbus.

Chapter 6

Coordinated Sampling and Model Hierarchy

The computational task for the Schur complement eigenvalue method is to approximate the interaction matrix, as described in the preceding chapters. The goal of the research is to enable stability searches over the flight envelope, and in this chapter it is achieved by introducing searches for the approximation of the interaction matrix. The stability analysis is demonstrated using aerodynamic models of variable fidelity.

6.1 Coordinated Sampling

6.1.1 Overview of Sampling Methods

The cost to create the approximation model, i.e. the required number of samples[1] to adequately represent the variation of the interaction matrix in the parameter space, is an important factor in the aeroelastic stability analysis especially for an expensive high fidelity aerodynamic model. It is a standard practice to replace a computationally expensive multidimensional model by an inexpensive surrogate using radial basis function models, artificial neural networks or kriging tools. Then, the two main tasks of the analysis are to distribute a few true evaluations of the expensive function over the parameter space in order to allow an accurate representation of the important physics, and to use the surrogate to reconstruct/approximate the functional behaviour efficiently, robustly and precisely. In this study, the chosen approximation approach is based on the kriging formulation presented in Section 4.3. The second, often more important task of sampling is analysed in the following.

In Chapter 5 the parameter space has been sampled by using brute force rectangular grid sampling. This has led to an unnecessary large number of exact evaluations for the

[1]One sample here refers to the values of a complete interaction matrix at one combination of the independent parameters.

interaction matrix to cover the space. It is clear that the number of required samples, involving operations on the large CFD–based system, defines the involved cost of the approach as the kriging model evaluates the fluid response at the expense of only two scalar products.

An alternative, a priori, space–filling algorithm is referred to as latin hypercube sampling [156]. Here, the samples are distributed randomly (using a specified number of non–overlapping bins of equal probability) to cover the parameter space of interest evenly. Commonly, latin hypercube sampling is the preferred choice compared with the grid sampling approach. Also, latin hypercube sampling is often used for the task of an initial sampling. The recommended number of initial samples depends on the number of independent parameters. In [122], as a rule of thumb, this is $10m$ where m is the number of independent parameter dimensions, while in [157] a number of $(m+1)(m+2)/2$ is suggested as an initial selection (which allows the definition of a quadratic polynomial).

Yet another space–filling approach, which is discussed in this study, is referred to as mean squared error sampling. It exploits the kriging model to improve the response surface globally. Using the standard error of the kriging prediction, readily available in Eq. (4.28), allows the allocation of samples a posteriori to improve the kriging model (and the response evaluation) where it is needed most. The kriging error depends on the correlation between sample points which itself is evaluated as a function of the distance between the samples. As a consequence, a new sample location is likely to be found near the point maximising the distance to all surrounding samples.

All space–filling algorithms, a priori or a posteriori, tend to require an excessive number of samples to achieve the demanded accuracy. Studying the aeroelastic stability analysis using the Schur complement eigenvalue method, it was found that it is neither necessary to accurately approximate the response surfaces of the interaction matrix components globally, nor useful to apply an optimisation algorithm, such as the efficient global optimization (EGO) algorithm[2] introduced in [122], to locate a global extremum in the expensive "black box" function. In this context, the expression "global" refers to covering the entire parameter space within its bounds.

A globally accurate approximation of the interaction matrix is not required for the aeroelastic stability problem because the interest focusses on detecting the most critical conditions. Particularly, analysing both the structural governing equations and the modified structural eigenvalue problem of the Schur method, it is clear that the influence of the computationally expensive interaction term on the eigenvalue problem can be quite different. Low values of the dynamic pressure (represented in this study by the reduced velocity or the altitude) cause the influence of the fluid interaction to

[2]The efficient global optimization algorithm uses a kriging surrogate model and places new sample points according to the maximum of the expected improvement function. The idea of expected improvement is discussed at a later point in this thesis.

be low. As a consequence an inaccurate approximation of the interaction matrix can still give precise eigenvalue results. High dynamic pressures, on the other hand, result in a strong fluid/structure interaction. However, high dynamic pressures often means that the stability analysis has advanced well within the unstable region where accurate results are rather irrelevant for the linear stability limit. Also, individual aeroelastic modes can be rather insensitive to the fluid response.

A global optimisation, on the other hand, is not useful because an extremum in the Schur interaction matrix elements not only does not necessarily correspond to the point of instability but also the functional extrema of the interaction term are commonly outside the relevant region (and outside the specified parameter bounds) as can be seen in the example results given in Chapter 5. In addition, for the intended instability search over the flight envelope multiple instability points are to be expected.

Thus, the sample distribution should be tailored to the aeroelastic problem. The major approach chosen in this study, referred to as risk–based sampling, exploits the kriging formulation to focus new sample locations in the vicinity of the converged instability boundary. This is similar to the previously described mean squared error sampling in the sense that samples are always placed a posteriori at the location of the highest kriging error. However, as additional important information, only the error evaluations along the current approximation to the instability boundary are considered. Here, starting from the corner points of the parameter space giving 2^m initial samples, a kriging model is always formed with the current set of samples which is then used to run the complete instability search. As will be seen in the following, the approach converges rapidly to satisfy predefined stopping criteria.

Similarly an approach, based on the EGO algorithm and called the efficient global reliability analysis (EGRA), was introduced in [157]. This approach evaluates a kriging model (therein referred to as a Gaussian process model) based on the current set of samples and places a new sample where the so–called expected feasibility function takes its highest value. The expected feasibility function indicates the expectation that the true (exact) function evaluation exhibits an instability or satisfies a specified condition. It is based on the cumulative distribution and probability density functions using the kriging–approximated response and its standard error.

This latter approach is not chosen in the current study. It has to be understood that the solution of the small nonlinear eigenvalue problem in Eq. (4.5) is of interest, while the expected feasibility function would be directly applied to the interaction matrix. To use the EGRA approach for the solution of the eigenvalue problem (essentially the instability boundary defined as critical values of the dynamic pressure and frequency), the kriging error, which defines an assumed normal distribution, must be propagated from the interaction matrix to the solution of the eigenvalue problem. This unnecessarily complicates the approach for a basic instability search. And for this reason, simple and straightforward approaches, such as the risk–based sampling, are preferred.

The expected improvement function following [122] is used instead in the final sampling approach to evaluate the minimum of the instability boundary, which typically corresponds to the transonic dip, and thus to the most critical condition. This is related to the EGO algorithm. In this (risk–based) sampling approach the normal distribution prescribed to the components of the Schur interaction matrix is propagated through the simulation to evaluate the expected improvement function for the resulting normal distribution in the instability boundary given by a representation of the dynamic pressure and the response frequency, and to locate the best new sample location.

In the following section these approaches to sampling are described step by step in detail for an aerofoil case. Then, in Section 6.1.3 the basic, yet very effective, risk–based sampling will be demonstrated for the earlier discussed MDO wing case. Here, the input parameter space (related to the flow model) is extended to three and four dimensions by considering the effects of altitude and angle of attack in addition to the response frequency and freestream Mach number.

6.1.2 Aerofoil Cases

The large number of samples used, for instance, in Fig. 5.7 is not required to accurately predict the response surfaces near the instability. Sampling techniques can be exploited instead. Latin hypercube (LH) sampling is considered as an improved version of random (Monte Carlo) sampling [156]. While random sampling creates parameter combinations independently (and possibly without providing additional information as new samples could be identical to previous samples), LH sampling ensures that all parts of the parameter space are evenly represented. Therefore, each parameter dimension is divided into a specified number of non–overlapping bins of equal probability. One sample per dimension is randomly chosen from each bin and then randomly combined with the other parameter dimensions, thus filling the parameter space.

This approach, based on eight and 32 samples, is presented in Fig. 6.1 for the full potential (FP) flow model using the NACA 0012 "heavy case" aerofoil configuration, with the structural parameters defined in Tab. 5.1, and an unstructured grid with five thousand control volumes. Initially, four samples were placed at the corners of the parameter space in each case to avoid extrapolation with the kriging model while the remaining samples were generated (a priori) by LH sampling.

Importantly, the dimensions of the parameter space are defined to provide a good range for an initial blind search. Here, the frequency range is based on typical flutter frequencies which are chosen from the normal mode frequencies, as an instability often follows the interaction of (wind–off) structural modes. The Mach number range covers the region of interest (up to mild separation). Exceeding the freestream Mach number of 0.82, it was shown in an experimental study of the NACA 0012 [117] that the flow field itself becomes unstable (known as buffeting). This is beyond the scope of the current

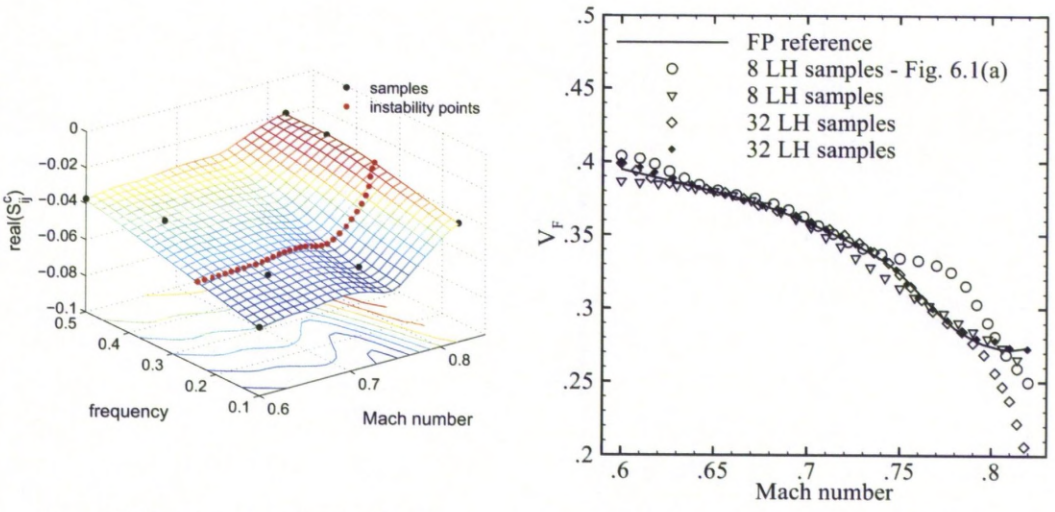

(a) real($S_{3,3}^c$) for one set of LH samples

(b) Critical flutter speed index

Figure 6.1: Latin hypercube (LH) sampling, using the FP flow model for NACA 0012 configuration, showing (a) approximated element real($S_{3,3}^c$) of Schur interaction matrix including projected trace of instability, and (b) critical flutter speed index compared with a reference solution.

study. Additional parameter dimensions such as the altitude or angle of attack, as described in Section 6.1.3 for the MDO wing, are chosen accordingly to limit the range of relevance and interest.

Looking at Fig. 6.1(a), even a few samples can approximate the interaction matrix reasonably precisely. This observation is supported in Fig. 6.1(b) showing the critical flutter speed index (the true measure for the quality of the approximations) compared with the exact (full order) reference solution which was presented in Section 5.1.3. Using eight samples a good starting point is established for a more detailed stability analysis. For instance, having a general picture of the stability limit for a configuration allows the concentration of a more detailed investigation in critical regions. Predictions based on 32 samples usually give better agreement compared with eight samples (because the parameter space is covered by more samples), although one set of samples gives results deviating considerably starting from about Mach 0.8.

Instead of relying on basic space–filling sampling algorithms, which leave the risk of missing important regions in the parameter space, information on the functional behaviour can be included to choose new sample locations a posteriori. The located maximum of the standard error for the kriging prediction, readily available, defines a natural choice for a new sample location. Iteration continues until a convergence criterion is satisfied.

The standard error of the kriging prediction, defined in Eq. (4.28), is a measure of uncertainty in the prediction. It makes immediate sense that the kriging model gives a relatively certain evaluation of the system response close to a sampled location due to

the correlation with one another. Indeed, the kriging prediction agrees with the exact system response at a sampled location. Thus, the kriging error is based on the sample variance reduced by a measure of the correlation between samples and adjusted for errors due to the estimation of the regression model from the samples.

Results from the technique, referred to as mean squared error (MSE) sampling, are shown in Fig. 6.2. Initially, a number of LH samples is created to allow a first evaluation of the kriging model and to provide an initial view of the parameter space. In the figure it is found that the response surface is well predicted with less irregularities compared with pure LH sampling with the same number of samples. It is remarked that MSE sampling is improved (a posteriori) space–filling since the kriging error depends on the chosen correlation weighted by a function of the distance between samples. Thus, a new sample location is likely to be found near the point maximising the distance to all surrounding samples while also adjusting to the level of correlation between the samples. The predicted critical flutter speed index, presented in Fig. 6.2(b) for 32 samples, gives very good agreement to the reference solution.

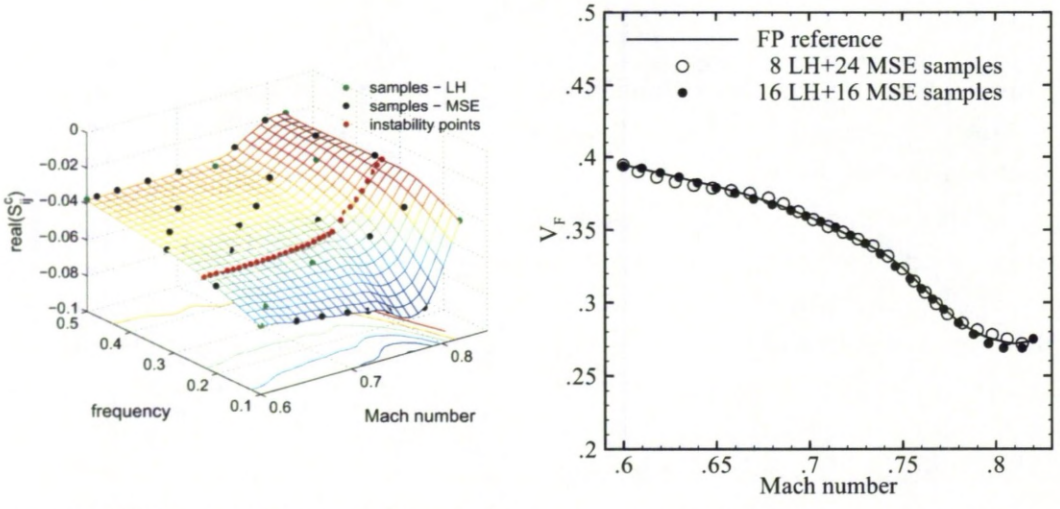

(a) real($S^c_{3,3}$) for 8 LH plus 24 MSE samples

(b) Critical flutter speed index

Figure 6.2: Mean squared error (MSE) sampling, using the FP flow model for NACA 0012 configuration, showing (a) approximated element real($S^c_{3,3}$) of Schur interaction matrix including projected trace of instability, and (b) critical flutter speed index compared with a reference solution.

Latin hypercube sampling tries to fill the complete parameter space evenly, while with MSE sampling it is attempted to minimise the kriging error globally. Thus, looking at Figs. 6.1 and 6.2, it is found that many samples are redundant for the stability analysis. As the cost of running the Schur Newton solver using the approximation model is very low, it is useful to perform a complete stability analysis based on the current set of samples, and to use the results to guide the sample placement.

Such a sampling approach proceeds by first defining the initial search space. This is done, in this example, using the four corner samples as described above. Then, the complete stability analysis is run with the cheap approximation model to detect the instability boundary giving the critical values of the flutter speed index and the response frequency. Locating the maximum of the kriging error along the current approximation to the instability boundary gives the new sample location in terms of Mach number and response frequency. In this sense it is a coordinated space–filling algorithm for the important regions of the parameter space. Iterating converges the solution to satisfy predefined stopping criteria, for instance, on the $\mathcal{L}_2$ norm of changes in successive flutter solutions and on the standard kriging error. This gives some measure of confidence in the prediction based on a distinct model in combination with the cost.

The approach, referred to as risk–based MSE sampling (or simply risk–based sampling), is illustrated in Fig. 6.3 for the Euler flow model using a grid with 15 thousand control volumes for the NACA 0012 "heavy case" configuration. It can be seen that new samples are concentrated in the region where they strongly support the prediction, i.e. close to the converged instability boundary. Also, the samples are always placed in the region where they improve the kriging model most, i.e. at the location of the highest error. An accurate detection of the instability boundary is quickly obtained. The agreement with the reference solution, given in Section 5.1.3, is excellent.

Having the steady state solutions, the twelve samples, sufficient in this example to cover a complete sub- and transonic regime, correspond to the cost of about twelve steady state solves, using the first linear frequency domain approach for the sample extraction described in Section 4.2. The cost to evaluate the samples is equivalent to form the terms in the series expansion in Eq. (4.7) for the two normal modes of the aerofoil case at three individual Mach numbers. To compare with time domain predictions, the simulation of one cycle of motion at one combination of freestream Mach number and reduced velocity corresponds to about ten to 20 steady state solves. Typically four to five values of the reduced velocity are required per Mach number to bracket the instability, and more than one cycle of motion is required to identify the system response following an initial disturbance. Thus, the stability analysis at only five Mach numbers, to trace out the instability boundary, is at least two orders of magnitude more expensive than the kriging–based eigenvalue approach.

Evaluating the entire response surface precisely within the initial search space is not attempted with the risk–based sampling approach. As a consequence, mode tracing could become inaccurate further away from the instability which, however, would be a fair trade–off compared with the cost. If this inaccuracy becomes critical, i.e. resulting in an eigenvalue with a positive real part, then the sampling criterion would automatically place a new sample in this region to correct the prediction. This is not the case for the NACA 0012 aerofoil problem discussed herein. Looking at Fig. 6.3(c), it can be said that the root locus of the critical mode is reproduced well using the

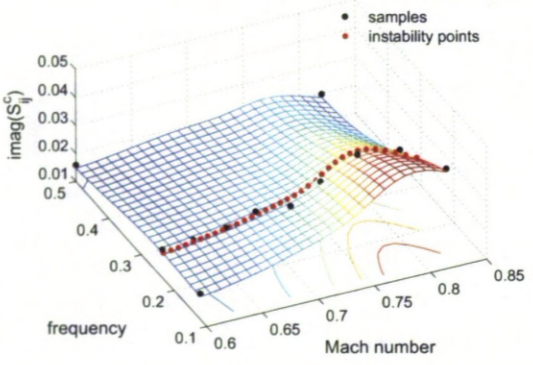

(a) Element imag($S^c_{3,3}$) based on 12 samples

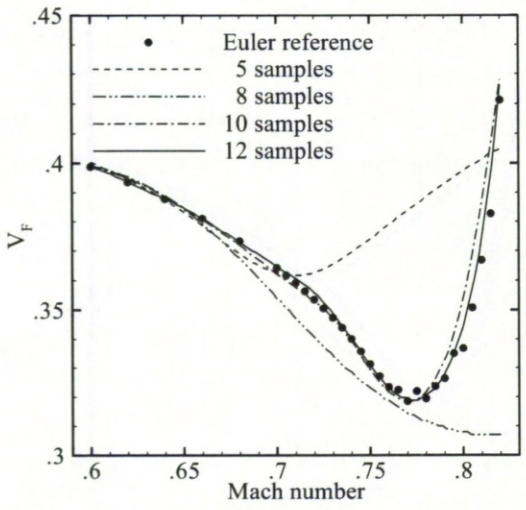

(b) Critical flutter speed index

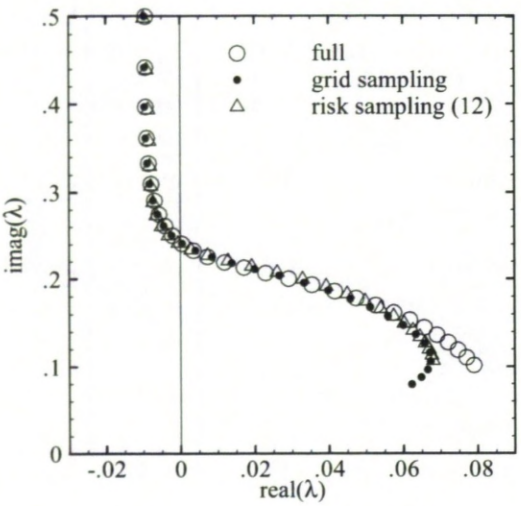

(c) Mode tracing at Mach 0.8

Figure 6.3: Risk–based MSE sampling, using the Euler flow model for NACA 0012 configuration, showing (a) approximated element imag($S^c_{3,3}$) of Schur interaction matrix including projected trace of instability, (b) critical flutter speed index compared with a reference solution, and (c) mode tracing at Mach 0.8.

twelve samples as shown in Fig. 6.3(a). Close to the imaginary axis the agreement with the results of both the exact eigenvalue solver (denoted "full") and the brute force grid sampling, shown in Fig. 5.7, is accurate.

This can be explained by interpreting the governing equations for the aerofoil structural model in Section 5.1.1. The reduced velocity $\bar{u}$, as the independent parameter, enters the eigenvalue problem by its square in the denominator of the stiffness matrix. Thus, for small values of $\bar{u}$ the influence of the structural part S^s on the eigenvalue problem is higher, while with increasing values of $\bar{u}$ the influence is reduced making the fluid interaction more important. The approximation of the interaction matrix is good enough in regions where the structural part dominates the problem. However, once the interaction term becomes more active closer to the instability, the parameter space is sufficiently covered by samples.

An alternative to the basic risk–based sampling approach is discussed next. The Isogai aerofoil model [140] is a benchmark case for predicting aeroelastic instability. Its structural parameters, chosen to represent the dynamics of an outer section of a swept–back wing, are summarised in Table 5.1. Figure 6.4(a) compares results of different aerodynamic models extracted from references [132,140,158,159]. The instability boundary, expressed as the critical flutter speed index V_F, gives an overall good agreement of the current Euler predictions compared with the numerical solutions. The complex shape of the instability boundary in the transonic regime is shown. In particular, the s–shape of the curve, giving a second stable branch for higher values of the flutter speed index, is distinct for the inviscid modelling approaches while it disappears when including viscous effects. The mode tracing for the (wind–off) structural eigenvalues is visualised in Fig. 6.4(b) describing this unusual appearance. The inset of this figure presents the development of the bending dominated mode compared with the results of [132].

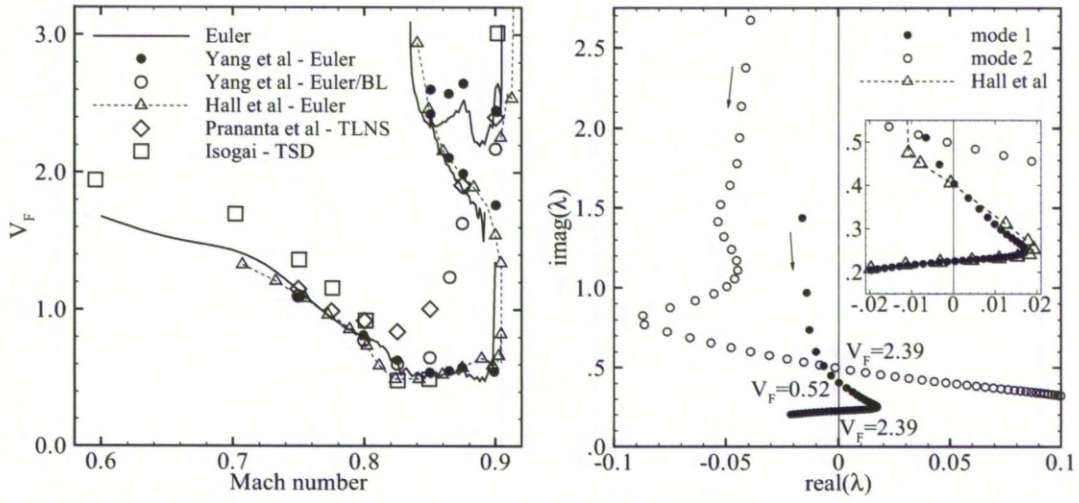

(a) Transonic instability boundary

(b) Mode tracing at Mach 0.85

Figure 6.4: Isogai [140] benchmark case comparing numerical results; BL – boundary layer, TLNS – thin layer Navier–Stokes, TSD – transonic small disturbance.

As seen, the Isogai case exhibits multiple bifurcations for inviscid flow models. Instead of using the bisection method applied to the reduced velocity $\bar{u}$ to locate the instability point at the different Mach numbers, the roots of the Schur residual, obtained at low computational cost, are evaluated at all points on a mesh defined by Mach number and reduced velocity to trace the relevant aeroelastic modes. Then, a threshold (sampling condition) is defined to place a sample to improve the approximation of the interaction matrix. In this study all mesh points at fixed Mach number having a change of sign in the eigenvalue's real part with varying reduced velocity are selected, thus allowing multiple bifurcations. Alternative sampling conditions are possible. The

selected location maximising the kriging error gives a new parameter combination in Mach number and frequency, as for the basic risk–based sampling.

In Fig. 6.5(b) it is found that as little as ten samples provide a good description of the (inviscid) transonic stability features, while about 30 samples are required to predict the upper part of the instability boundary precisely. Some outliers in Fig. 6.5(a) are due to an intermediate approximation model, during the early stages of the iteration, not giving a converged solution at individual combinations of Mach number and flutter speed index. This results in excessive frequencies, well outside the relevant region of the structural frequencies, which is then defined to place the sample at the frequency search limit for this individual Mach number.

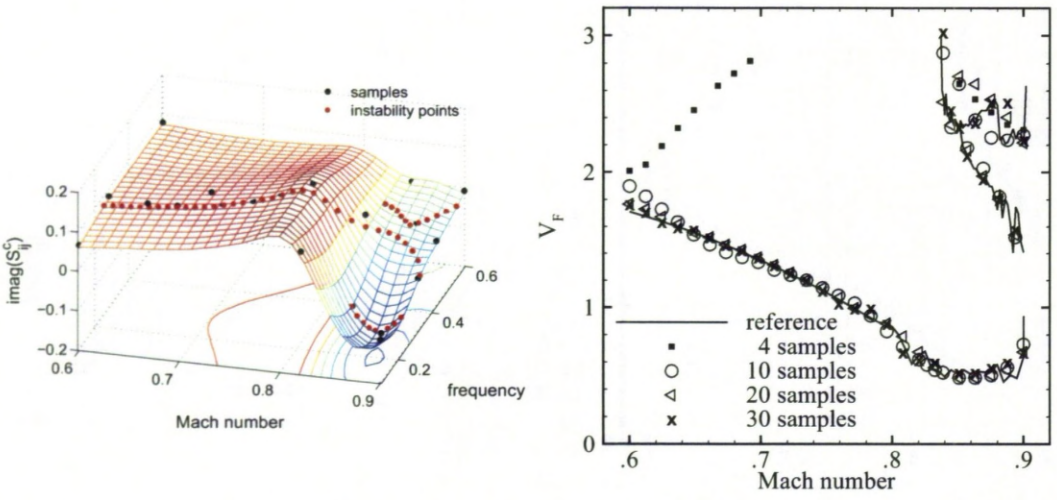

(a) Element imag($S^c_{3,3}$) based on 20 samples

(b) Critical flutter speed index

Figure 6.5: Alternative risk–based MSE sampling, using the Euler flow model for Isogai [140] configuration, showing (a) approximated element imag($S^c_{3,3}$) of Schur interaction matrix including projected trace of instability, and (b) critical flutter speed index compared with a reference solution.

There is another interesting aspect to the kriging formulation allowing the balance between local and global search for functional extrema [122]. The kriging model provides a mean (best) prediction of a response, given by Eq. (4.26), its gradient, given by Eq. (4.27), and a corresponding standard error, given by Eq. (4.28). These are all simple expressions once the kriging model is built from the samples. Also, the gradient of the standard error is available (but not used in this study). Then, a probability distribution can be given for the prediction. In Eq. (5.7) expand the interaction term of the Schur complement matrix in a first order Taylor series about the mean evaluation of the critical frequency ω_0 at fixed freestream Mach number M_r,

$$S = S^s(\lambda, \bar{u}) + \mathcal{N}\left(\widehat{S}^c(\omega_0), \varphi^2(\omega_0)\right) + \frac{\partial \widehat{S}^c(\omega_0)}{\partial \omega_0}(\omega - \omega_0), \tag{6.1}$$

with the gradient of the mean prediction $\widehat{S}^c(\omega_0)$ readily available from the kriging model. The matrix elements of the second term are assumed to be normally distributed with the mean and variance given by their kriging approximation. Here, the matrix φ contains the standard error of the kriging prediction. This latter equation is a good approximation looking at response variations in the frequency dimension. The value of ω_0 is found from a stability analysis based on mean values $\widehat{S}^c$ of the kriging prediction for S^c. Equation (6.1) models the uncertainty about the kriging approximated response $\widehat{S}^c$ at an unsampled parameter combination (*not* the uncertainty due to physical effects). Then, a Monte Carlo simulation for random realisations of the second term is done to propagate the uncertainty from the kriging model to the stability prediction.

Also, an expected improvement function [122] is given for the evaluated critical flutter speed index, assumed to be normally distributed like the kriging prediction of the interaction term, to locate the minimum value V_F^- as a function of the freestream Mach number (often related to the transonic dip). This function takes the current best approximation of the extreme value and weights a possible improved minimum value by the corresponding probability density. This can be written as,

$$E\big[I(M_r)\big] = \big(V_F^- - V_F(M_r)\big)\,\Phi\left(\frac{V_F^- - V_F(M_r)}{\sigma\big(V_F(M_r)\big)}\right) + \sigma\big(V_F(M_r)\big)\,\phi\left(\frac{V_F^- - V_F(M_r)}{\sigma\big(V_F(M_r)\big)}\right), \tag{6.2}$$

where Φ and ϕ denote the cumulative distribution function and the probability density function of the standard normal distribution, respectively, and σ is the standard deviation of the critical flutter speed index V_F at the freestream Mach number M_r. The first term in this latter equation weights the difference between the current minimum and a predicted value with the probability that the predicted value is a new minimum. The second term multiplies the standard deviation of the predicted value with the probability that it is equal to the current minimum, and is therefore high where the standard deviation is high no matter if there is a new minimun or not [160].

The approach, referred to as expected improvement (EI) sampling, is illustrated in Fig. 6.6. It is closely related to the efficient global optimization (EGO) algorithm which was mentioned earlier in Section 6.1.1. Using intermediate stability results in finding new sample points (as done for the risk–based sampling), the samples gather around the converged flutter solution as seen in Fig. 6.6(a). However, it is obvious that more samples are placed in the region of the transonic dip since detecting the minimum in the critical flutter speed index is the objective of the applied EI sampling. This is desirable because more emphasis is consequently put on the nonlinear transonic regime rather than on the subsonic range. In Fig. 6.6(b) nine samples (including the initial set) are sufficient to detect and predict the transonic dip minimum accurately.

Importantly, once the iteration results in placing samples close to each other as the transonic dip minimum is accurately detected, the iteration must stop to avoid

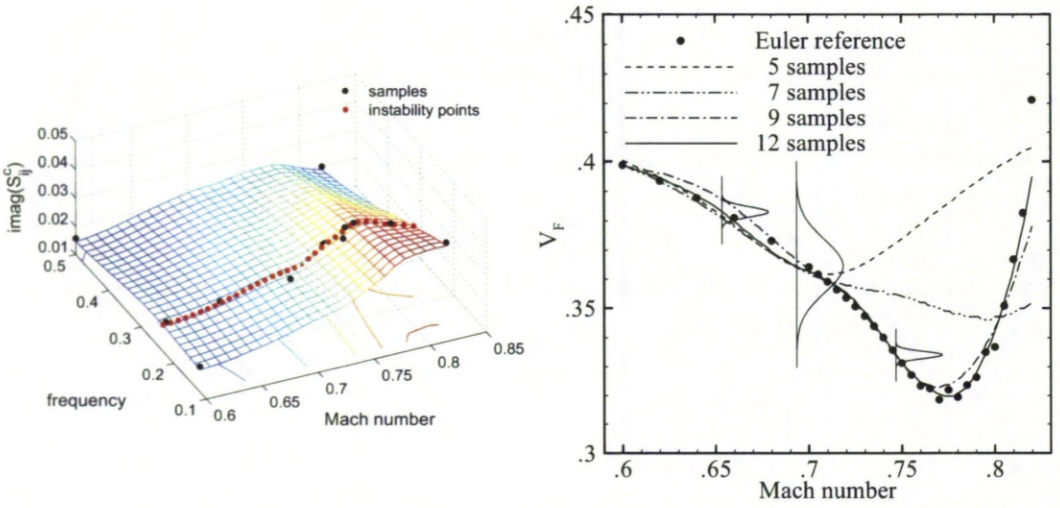

(a) Element imag($S^c_{3,3}$) based on 12 samples

(b) Critical flutter speed index

Figure 6.6: Expected improvement sampling, using the Euler flow model for NACA 0012 configuration, showing (a) approximated element imag($S^c_{3,3}$) of Schur interaction matrix including projected trace of instability, and (b) critical flutter speed index compared with a reference solution including response probability density functions.

a numerically unstable kriging model which follows from the ill–conditioning of the correlation matrix. Two closely located samples correspond to two columns in the correlation matrix R to be nearly identical giving a nearly singular matrix [122].

The figure also includes (scaled) probability density functions for the critical flutter speed index at three Mach numbers for calculations based on twelve samples. Looking at the density function with the highest standard deviation, the idea of expected improvement is well illustrated. Risk–based sampling would place a new sample where the standard deviation is highest (around Mach 0.7). Since the tail of the density function does not suggest an improvement in locating the minimum value of the critical flutter speed index (i.e. the probability to have a new minimum is very small), EI sampling ignores this location as a possible newly sampled point.

Expected improvement sampling is more expensive in finding a new sample location because a response distribution in the critical flutter speed index has to be evaluated for the range of Mach numbers using a Monte Carlo simulation. This cost remains relatively constant no matter how big the original problem becomes as the cost to run the kriging model is low. However, more advanced propagation methods such as polynomial chaos could be considered in future studies.

It is important to remark that the approach of expected improvement sampling can be generalised to locate the value along the instability boundary closest to the proposed flight envelope. This is done by replacing the function corresponding to the flutter speed index by the function corresponding to distance to the flight envelope. Such an example

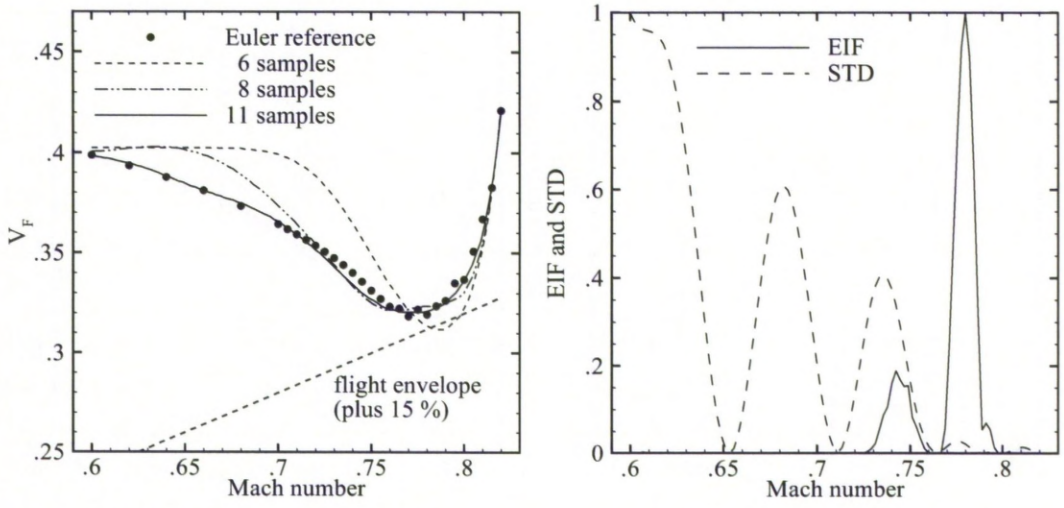

(a) Critical flutter speed index

(b) EIF vs STD (11 samples)

Figure 6.7: Expected improvement sampling on distance to flight envelope, using the Euler flow model for NACA 0012 configuration, showing (a) critical flutter speed index compared with reference solution and generic flight envelope, and (b) expected improvement function (EIF) vs standard deviation (STD) of distance to flight envelope.

is demonstrated in Fig. 6.7 using a generic flight envelope. In Fig. 6.7(a) the predicted instability boundary and the generic flight envelope are shown. The expected improvement sampling based on the minimum distance to the envelope converges rapidly. As the minimum of the transonic dip is close to the location of the minimum distance to the flight envelope in this case, the sample distribution in the frequency/Mach number parameter space is similar to the basic expected improvement sampling in Fig. 6.6(a), and is therefore not presented again.

In Fig. 6.7(b) the expected improvement function (EIF) is crossplotted with the standard deviation (STD) obtained from the normal distribution of the critical flutter speed index for eleven samples. The figure supports the discussion for Fig. 6.6(b) on the sample selection using the expected improvement. The lower Mach number region is sparsely sampled resulting in a high standard deviation. However, the minimum distance cannot be expected in that region as expressed by the EIF.

Summarising, a blind search for aeroelastic instability starts with the definition of an initial search space, in this case in the Mach number and frequency dimensions. Optionally, using latin hypercube sampling this space can then be filled evenly with more samples. To search for a complete range of the stability limit, the risk–based sampling approach is a convenient choice, whereas the expected improvement sampling technique is preferred when the most critical region (e.g. the transonic dip minimum or the smallest distance to the proposed flight envelope) is the main concern.

6.1.3 MDO Wing Case

The risk–based sampling approach, introduced for the aerofoil cases, is now examined for the MDO wing configuration using the modal structural model and including the effects of aerostatic deformation. First, the possible reduction of required samples at fixed Mach number is discussed. Then, additional input parameter dimensions are added to demonstrate the generality of the approach.

In Figs. 6.8 and 6.9, the risk–based MSE sampling (or simply risk–based sampling) is presented for the MDO wing case at Mach 0.85 and zero degrees angle of attack, corresponding to the discussion in Section 5.2.3. The effects of aerostatic deformation are fully accounted for. The sampling proceeds in a fashion similar to the aerofoil cases. First, an initial search space is spanned by the corner samples covering the altitude range of interest and the frequency range according to the normal mode frequencies. Then, the eight modes are traced with varying altitude under matched point conditions using the cheap approximation model based on the current set of samples, and the instability points are detected. Having more than one bifurcation, the location with the highest standard error in the kriging prediction gives the new sample location. Alternative sampling criteria, for example a positive gradient in the eigenvalue's real part with respect to the altitude, are possible choices. At this point, expert knowledge would need to be inserted to specify possible adaptations of the sampling criteria.

Such a risk–based sampling guarantees that samples are always placed at locations where they both support the prediction most in terms of risk, i.e. at previously evaluated instability points, and improvement, i.e. at the location of the maximum error in the kriging model. Changes in the instability prediction between two consecutive iterations define a possible convergence criterion.

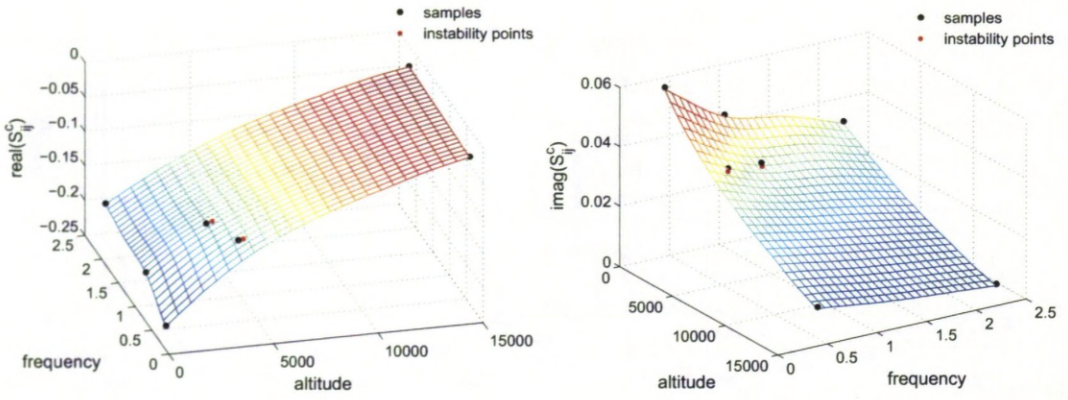

(a) real part based on 7 samples

(b) imaginary part based on 7 samples

Figure 6.8: Risk–based sampling technique, using the Euler flow model for MDO wing configuration, showing approximated element $S^c_{9,1}$ of Schur interaction matrix including projected instability points.

In this case, the sampling approach converges rapidly as can be seen in Fig. 6.8 showing one representative element of the interaction matrix (with the mass ratio corresponding to the actual values of the altitude), the sample distribution and the instability points for the first and second mode projected onto the response surface. After the third iteration, starting from the four samples of the initial search space, a new sample location matches the predicted instability points very closely. Continuing to iterate is neither necessary nor useful as the correlation matrix of the kriging model becomes increasingly ill–conditioned for sample points near previously sampled points [122]. Thus, the seven required risk–based samples mean a further cost reduction by a factor of about five compared with the uniform rectangular grid sampling shown in Fig. 5.25.

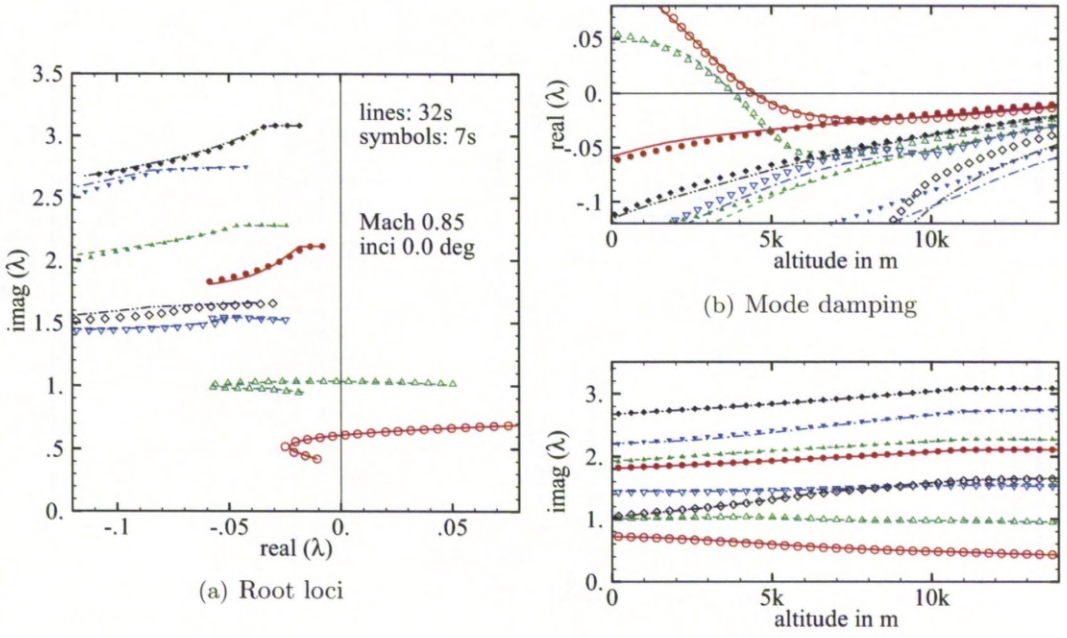

(a) Root loci

(b) Mode damping

(c) Mode frequency

Figure 6.9: Risk–based sampling technique showing mode tracing for MDO wing configuration with respect to altitude at Mach 0.85 and zero degrees angle of attack (eigenvalues given in dimensionless form).

Figure 6.9 compares the mode tracing using the kriging models based on 32 samples from the rectangular grid sampling in the previous chapter and the seven samples from the current risk–based sampling. Interestingly, the agreement is excellent also for the higher frequency modes throughout both the altitude and frequency range, even though large parts of the parameter space are essentially uncovered by samples, and consequently, accurate response surfaces are not evaluated globally. Here, looking at the presented response surface in Fig. 6.8, an almost linear behaviour can be found in these uncovered regions simplifying the search in this case.

There are two points to this observation. First, at high altitudes the influence of the interaction term is relatively small compared with the structural part as the density, defining the mass ratio, is small. Secondly, the higher frequency modes are very insensitive to changes in the interaction elements and the initial search space can give a good enough approximation. Looking at the equations of the structural model in Section 5.2.1 and the Schur complement matrix in Eq. (5.18), it is clear that the higher the normal mode frequencies are, the more dominant the structural part S^s on the eigenvalue problem becomes.

A sensitivity study for the interaction elements, as described in Section 5.2.3, both confirms the latter point and reduces the risk of missing an additional (possibly more critical) bifurcation point for the higher frequency modes. This is presented in Fig. 6.10. In this case neither of the higher frequency modes shows any tendency to go unstable, while the uncertainty in the first two modes is similar to the results in Fig. 5.31.

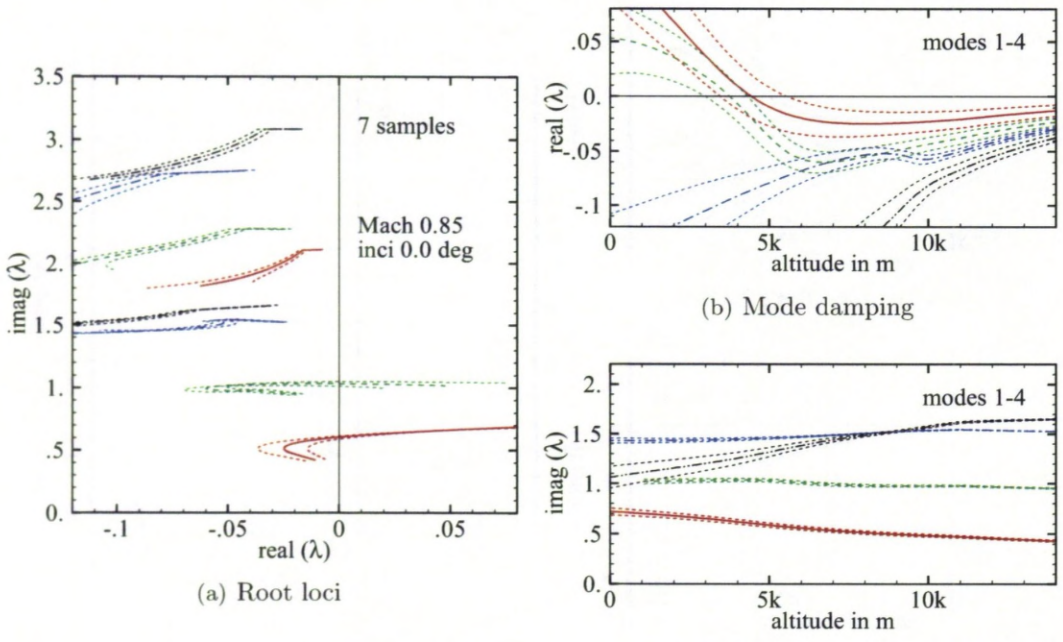

(a) Root loci

(b) Mode damping

(c) Mode frequency

Figure 6.10: Sensitivity of mode tracing for MDO wing configuration using seven samples from risk–based sampling at Mach 0.85 and zero degrees angle of attack and showing one standard deviation due to 20% variation.

In Section 5.2.3 the prediction of the transonic aeroelastic instability over a range of freestream Mach numbers has been demonstrated using three dimensional rectangular grid sampling. In addition to the altitude and frequency, the freestream Mach number has been included as a third input parameter dimension. These results are presented in Figs. 5.27 and 5.28. The agreement with full order predictions is found to be reasonable, despite the relatively coarse sample resolution in the Mach number dimension. Risk–

based sampling can be used to achieve a better distribution of samples and an improved prediction. This is presented next.

The risk–based sampling proceeds in the same fashion. First, the initial (multidimensional) search space is defined with the corner samples. Then, the instability points for the range of freestream Mach numbers and a chosen angle of attack are evaluated with the kriging model based on the current set of samples. The predicted instability point maximising the corresponding kriging error of the approximated interaction term defines the new sample location. Iteration converges the prediction.

The risk–based sampling is herein demonstrated for three and four dimensional parameter search spaces with the parameters influencing the flow condition. The initial set of samples to define the search space are as follows. The third dimension for the freestream Mach number covers a range between 0.7 and 0.89. The fourth dimension covers angles of attack between minus and plus half a degree. For the shown demonstration study, the chosen angle of attack to predict the stability limit is set to zero degrees according to the preceding discussion.

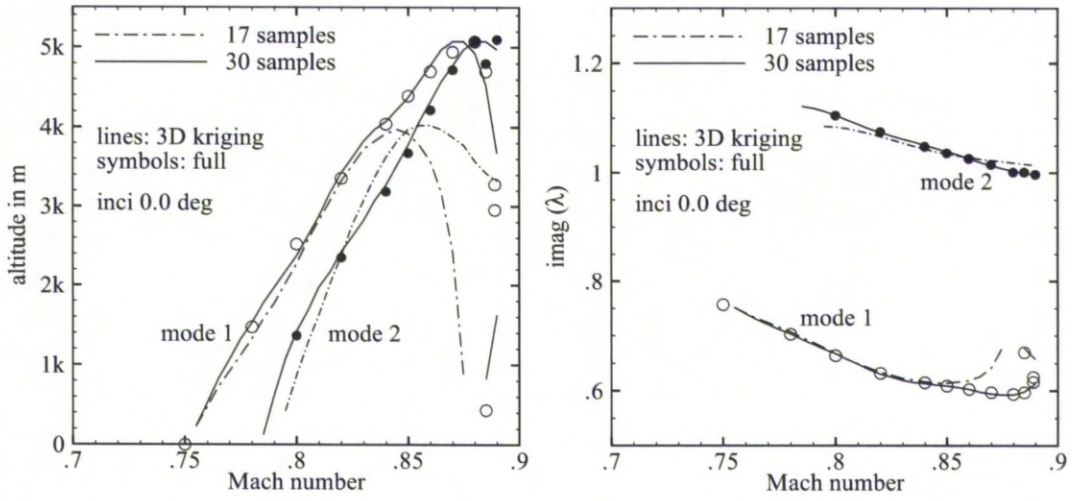

(a) Critical altitude

(b) Critical frequency

Figure 6.11: Instability boundary from three dimensional risk–based sampling for MDO wing configuration showing critical values of altitude and frequency.

Results are presented in Figs. 6.11 through 6.14. The instability boundaries as critical values of altitude and dimensionless frequency for the three and four dimensional search spaces are given in Figs. 6.11 and 6.12. The three dimensional risk–based sampling, requiring 30 samples for accurate results, gives excellent agreement with the full order predictions. The 30 samples correspond to a cost reduction by a factor of about five compared with the three dimensional grid sampling. Also the second bifurcation of the first mode is found. The four dimensional sampling is less accurate at the higher freestream Mach numbers requiring more samples to converge.

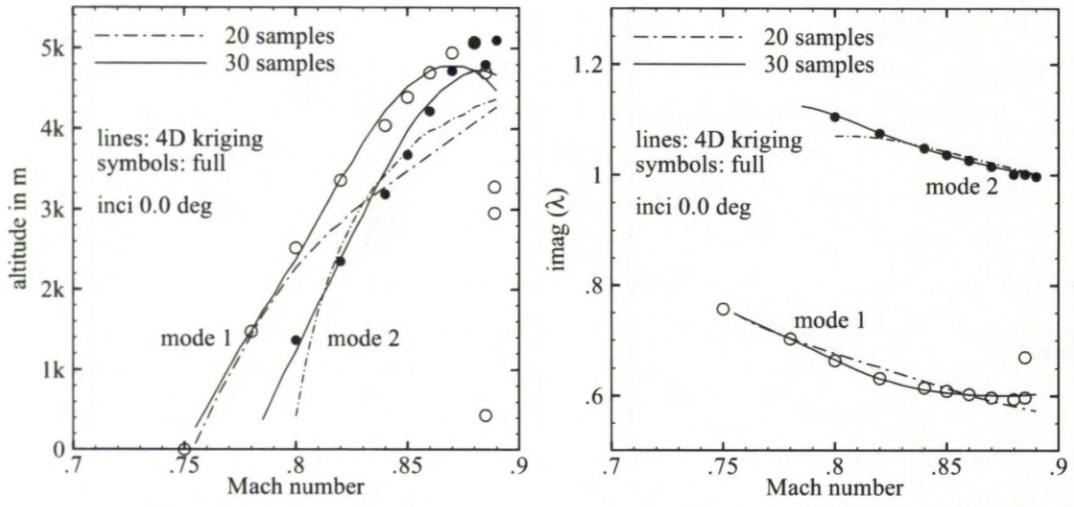

(a) Critical altitude

(b) Critical frequency

Figure 6.12: Instability boundary from four dimensional risk–based sampling for MDO wing configuration showing critical values of altitude and frequency.

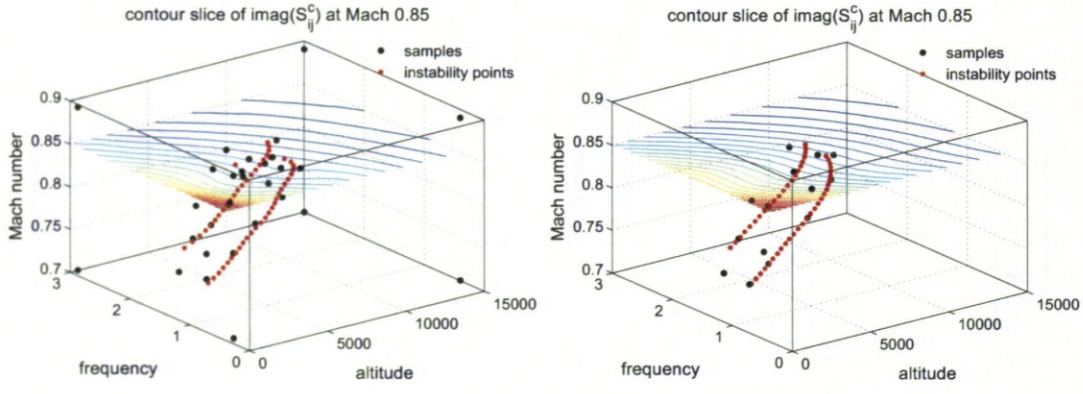

(a) Three dimensional search space

(b) Four dimensional search space

Figure 6.13: Higher dimensional risk–based sampling, using the Euler flow model for MDO wing configuration, showing approximated element imag($S_{9,1}^c$) of Schur interaction matrix including instability points.

Figure 6.13 gives an impression of both the sample distribution and the response surface at Mach 0.85. Note that in Fig. 6.13(b) only the samples at zero degrees angle of attack are shown. The response surfaces for varying angle of attack and frequency at fixed altitude and Mach number (not shown herein) gave a nearly linear dependence on the angle of attack. The corresponding traces for the eight modes are presented in Fig. 6.14. Good agreement with the full order results is found even though, in the case of the three dimensional sampling, the third and fourth mode traces cross.

Adding the fourth dimension to the sampling problem demonstrates an interesting point about the approach. The approximation model can be updated for changes in

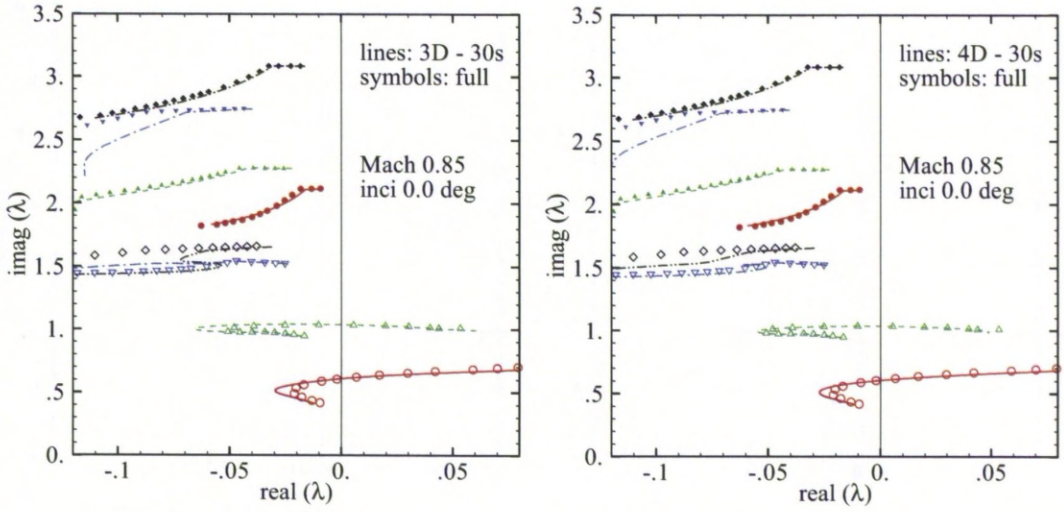

(a) Three dimensional search space

(b) Four dimensional search space

Figure 6.14: Mode tracing with respect to altitude for MDO wing configuration using three and four dimensional risk–based sampling (eigenvalues given in dimensionless form).

the system parameters by adding additional samples that account for these changes. All the previous sampled points are kept as these will support the prediction of the approximation model as it will grow gradually depending on the requirements. Thus, the re–use of samples is a major advantage of the kriging approach.

6.2 Using the Model Hierarchy

6.2.1 NACA 0012 Aerofoil Configuration

Following the preceding discussion, an appropriate sampling technique reduces the involved cost considerably in detecting the instability boundary for a case in which little prior knowledge is assumed. The approach can be taken a step further. As mentioned in Chapter 5, the flow models of different fidelity predict similar features (as described by the Schur interaction term). In this sense, for instance, a response obtained by a FPv flow model is correlated with a RANS prediction as changes in a system parameter, such as the freestream Mach number, cause similar changes in the outcomes of the different flow models, which is illustrated in Fig. 5.7. Of course, the fundamental assumptions of both the FP formulation and the integral boundary layer model would hamper an accurate prediction compared with the RANS equations. However, their correlation is a predictive capacity and can be exploited.

To start with, a blind search using the expensive high fidelity model is avoided. The initial analysis using a cheaper model delimits the search space for aeroelastic instability and creates a general picture for a configuration. Risk–based sampling can be used.

In addition, a relationship for the critical frequency of the form $\omega_F = \omega_F(M_r)$ can be given (for the analysis using frequency/Mach number parameter spaces as described in this work). This allows the placement of a few carefully selected high fidelity samples in presumed critical regions as predicted by the cheaper model.

Figures 6.15 and 6.16 present the analysis for the NACA 0012 "heavy case" aerofoil configuration exploiting the hierarchy of aerodynamic models. The lower fidelity model is established by the FPv formulation whereas the RANS equations are used for the higher fidelity model. In Fig. 6.15 the instability boundary is shown as critical values of flutter speed index and dimensionless frequency. In addition, the predictions based on three different kriging approaches are included. Correspondingly in Fig. 6.16, one element of the interaction matrix is given for two different approaches to the kriging approximation based on an augmented set of samples, details of which are discussed shortly.

A set of four RANS samples (i.e. four complete interaction matrices), selected according to the FPv prediction, is used with the sample distribution given in Figs. 6.15(b) and 6.16. Extracting all FPv samples in Fig. 5.7, using the linear frequency domain approach, is less expensive than evaluating the few RANS samples, using the time domain approach. The FPv simulations were run on a grid with five thousand control volumes, while the applied RANS grid has 20 thousand control volumes.

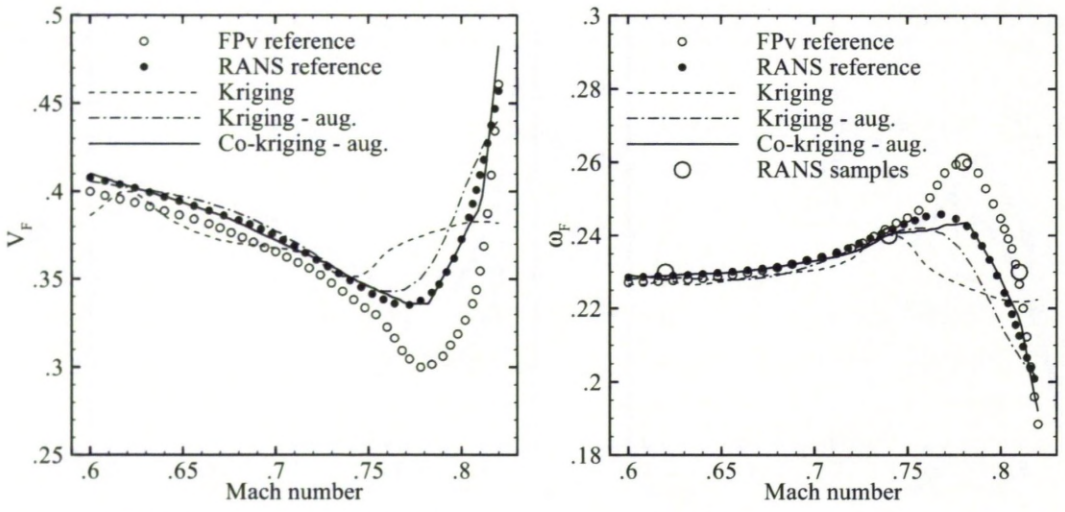

(a) Critical flutter speed index

(b) Critical frequency

Figure 6.15: Direct kriging and co–kriging techniques applied to aeroelastic stability analysis of NACA 0012 configuration showing critical values of flutter speed index and dimensionless frequency.

First, a kriging model based on these four samples was used and, as the results in Fig. 6.15 demonstrate, the small number of samples (and their distribution) is inadequate. The distribution of samples in the frequency/Mach number parameter space

along the instability boundary almost shows one dimensional dependence on the Mach number with little change in the direction of frequency. This complicates significantly the creation of a kriging model with two input parameter dimensions required for the stability analysis as discussed herein. The variation of the interaction matrix with respect to the frequency is neither well represented nor supported by the samples.

Thus, it was found to be useful to augment the set of high fidelity samples by the lower fidelity corner points defining the initial search space. This assumes that the initial search space is big enough to support the kriging model in the frequency dimension but not to adversely affect the approximation for the higher fidelity data close to the instability. Then, a second kriging model, labelled "Kriging – aug.", based on the augmented data is formed and used for the stability analysis. The resulting prediction shows a far better agreement compared with the reference solution which is based on the kriging model shown in Figs. 5.7(g) and 5.7(h).

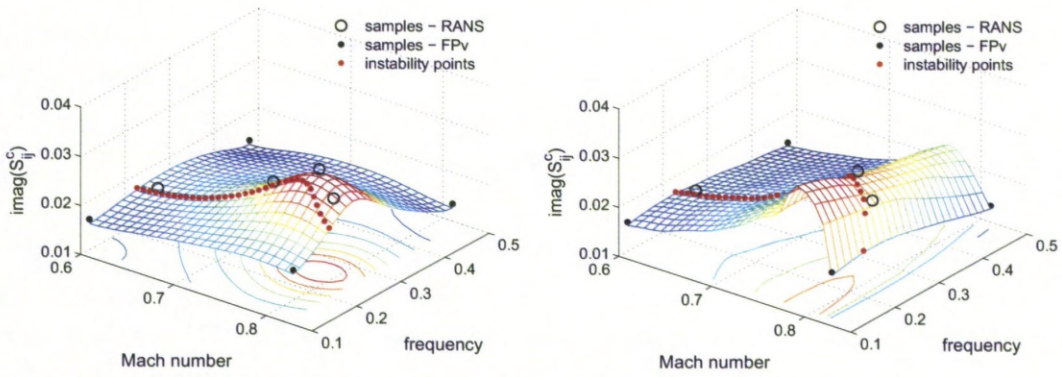

(a) Element imag($S^c_{3,3}$) based on direct kriging (b) Element imag($S^c_{3,3}$) based on co–kriging

Figure 6.16: Direct kriging and co–kriging techniques applied to aeroelastic stability analysis of NACA 0012 configuration, using augmented sample set, showing approximated element imag($S^c_{3,3}$) of Schur interaction matrix.

Thirdly, the co–kriging approach to the approximation treats the lower fidelity response as a (spatially correlated) co–variable to the higher fidelity prediction. Then, the input parameter space of the RANS samples (already augmented by the FPv corner samples) is extended by the FPv response given in Fig 5.7. This means, besides the dependence on the frequency and Mach number, the approximation of the RANS–based response surfaces also depends on the FPv response which provides the trend information. Comparing Fig. 5.7(h) with Fig. 6.16(b) it is found that the response surface of the presented interaction element is reproduced well. Correspondingly, an accurate prediction of the instability boundary is found in Fig. 6.15. However, as seen in the previous paragraph, even a direct kriging model based on the augmented data set gives good results which corresponds to the earlier observation in Section 6.1 that

the response surface close to the instability (as fairly given by the RANS samples) is essential for an accurate stability prediction.

Instead of estimating the stability limit over a range of Mach numbers, the most critical condition as found from a cheaper model can be chosen to place one expensive sample. In the vicinity of this critical location, the stability prediction continues as described using the kriging approximation based on a cheaper flow model, while the difference between the responses of higher and lower fidelity is used as constant shift added to the kriging predicted (lower fidelity) response of the interaction term.

6.2.2 Goland Wing/Store Configuration

Next the co-kriging approach is applied to the Goland wing/store configuration using the Euler and RANS equations from the model hierarchy. The Euler results follow the discussion in Section 5.2.2, while the RANS simulations are done using the two equation $k-\omega$ turbulence model and an H-type computational grid with about three million control volumes. The first wall normal grid spacing is 6×10^{-6} in dimensionless units. Also, a coarser level with about 350 thousand control volumes was extracted from the finer level grid maintaining a first grid spacing of 1.4×10^{-5}. The chord Reynolds number is specified to be 15 million following reference [24] and is not varied in this study strictly violating matched point conditions according to the freestream Mach number and altitude.

Representative surface pressure distributions are shown in Fig. 6.17 for the Goland wing at two freestream Mach numbers and two locations in the spanwise direction close to the wing root ($z/z_{\text{tip}} = 0.15$) and wing tip ($z/z_{\text{tip}} = 0.9$). The results of the Euler equations are compared with the RANS predictions. For both transonic freestream Mach numbers a strong shock wave is formed near the wing root weakening towards the tip. The differences between the two flow models are relatively small as expected considering the high reference Reynolds number. The shock location moves marginally upstream in the RANS results while the characteristic inviscid overshoot at the bottom of the shock wave is corrected by the viscous effects.

The constant volume tetrahedron (CVT) transformation [150] is applied in the multiblock flow solver to transfer information, i.e. pressure forces and deflections, between the fluid and structural grids, as mentioned in Section 5.2.1. It is a local intergrid transfer method which means that the grid locations at the boundaries of structural elements (defined by three structural grid points) are matched while the slope is not. This is indicated in Fig. 6.18(b) showing the third normal mode shape mapped to the surface mesh of the RANS grid. Within each triangular element the projection is smooth while the slope differences between these elements are slightly visible by triangular shades. One can imagine that linear extrapolation, which is required for the

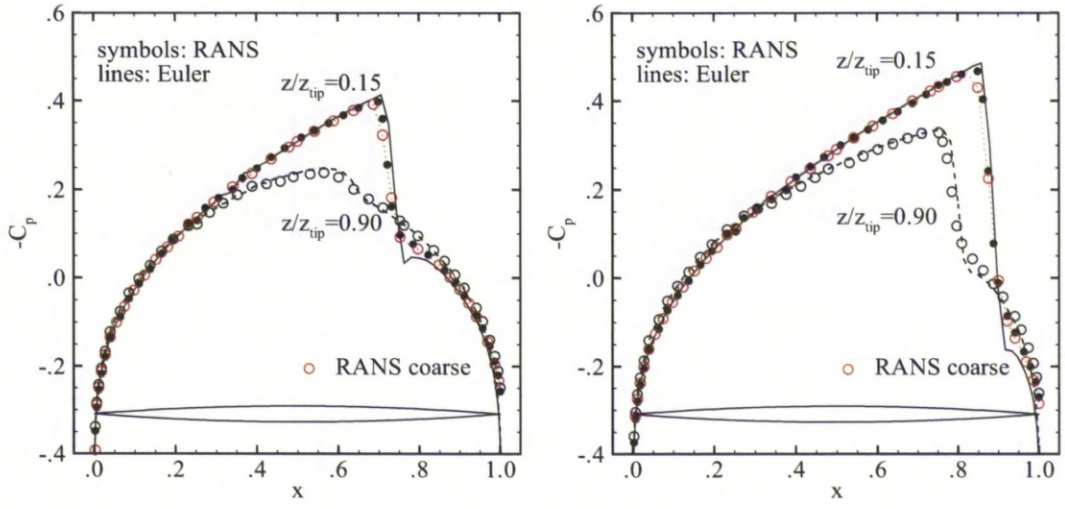

(a) M_r=0.9, α=0.0°, Re=15.0×10^6 (b) M_r=0.925, α=0.0°, Re=15.0×10^6

Figure 6.17: Surface pressure distribution for Goland wing comparing Euler and RANS flow models at two freestream Mach numbers and two spanwise locations.

Goland wing towards the trailing edge behind the two thirds chord line[3], amplifies the effects of this slope difference. The latter point is indicated in Fig. 6.18(a) for the third mode shape showing a zigzag–like trailing edge. These intergrid transfer issues were previously addressed in [161].

The problems caused by extrapolation using CVT are also found for the Euler computational grids. However, as the Euler grid resolution is coarser compared with the RANS requirements, this was not deemed as a serious obstacle in the preceding discussion. To improve the situation for the Goland RANS grid and to avoid a possible pollution of the results, the mode shapes are re–defined to avoid extrapolation using CVT. The mode shapes are linearly extrapolated to the trailing edge line at each spanwise location (rib) of the finite–element model as a preprocessing step before they are applied in the intergrid transfer formulation in the CFD solver. As can be seen in Fig. 6.18(b), the quality of the transformed mode shapes is improved.

The influence of this mode shape modification on the Euler results is analysed shortly. In Fig. 6.18(c) Euler kriging results of the Goland wing/store configuration are shown. The kriging reference solution is taken from Fig. 5.19. Results of the exact (full order) eigenvalue solver are not included at this point as excellent agreement was demonstrated in Section 5.2.2 for this case.

In the figure the results denoted "alternative samples" correspond to a kriging model based on samples which were extracted using the second approach discussed in

[3]The finite–element model of the Goland wing describes a rectangular wing box. Its skeleton is built from three spars, placed at the zero, one third and two thirds chord lines, and eleven ribs, evenly spaced along the span. A complete description of the structural model is provided in [24].

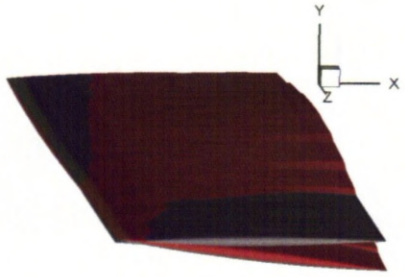

(a) Mapped mode shape

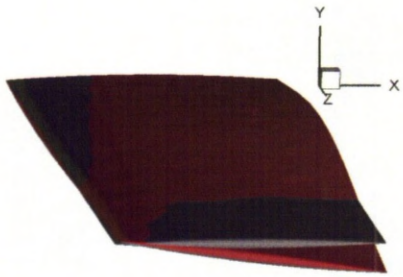

(b) Improved mapped mode shape

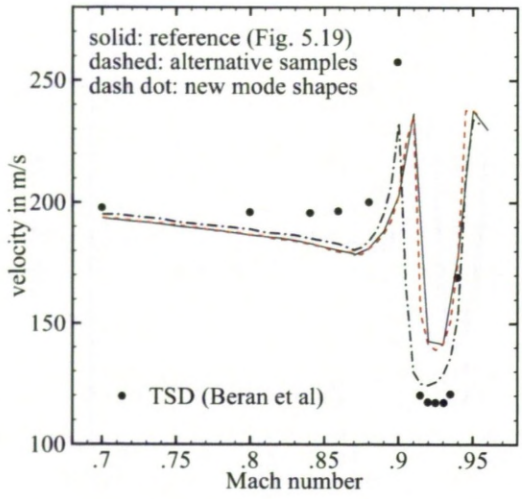

(c) Critical velocity at sea level conditions

Figure 6.18: Influence of mode shape definition for Goland wing/store configuration, showing (a–b) third mode shape mapped to RANS surface mesh and (c) kriging predicted critical velocity of Euler flow model compared with numerical results of [24]; TSD – transonic small disturbance.

Section 4.2 by solving n linear systems of the form $(A_{ff} - \lambda I)\,\boldsymbol{y} = \left(A_{f\eta} + \lambda A_{f\dot{\eta}}\right)$, one for each of the right–hand sides corresponding to the generalised coordinates. These results, as also presented for the NACA 0012 aerofoil case in Section 5.1.3, demonstrate the equivalence of the alternative approach to the first (original) approach requiring $2n$ linear solves of the form $(A_{ff} - \lambda I)\,\boldsymbol{y} = A_{fs}$, one for each unknown of the structural state–space representation, where $A_{fs} = \left[A_{f\eta}, A_{f\dot{\eta}}\right]$. Indeed, the instability boundaries are indistinguishable. The alternative approach for the sample extraction is used throughout in the following discussion as it involves half the computational cost. One element of the (alternative) interaction matrix for the Euler flow model is given in Fig. 6.19 showing the fluid response in the direction of the first generalised coordinate with respect to changes in the second generalised coordinate, i.e. element $S^c_{5,2}$.

The results denoted "new mode shapes" use the alternative extraction approach for the re–defined mode shapes. Clear differences compared with the reference results can be found around the bucket of shock induced limit–cycle oscillation (LCO) bringing the current results closer to the prediction in [24]. This can be explained by the effects of the improved mode shapes. It was found that the extrapolation using CVT does not significantly pollute the intergrid transformation for the first mode which has dominant bending behaviour. The first mode is the unstable mode in the lower Mach number

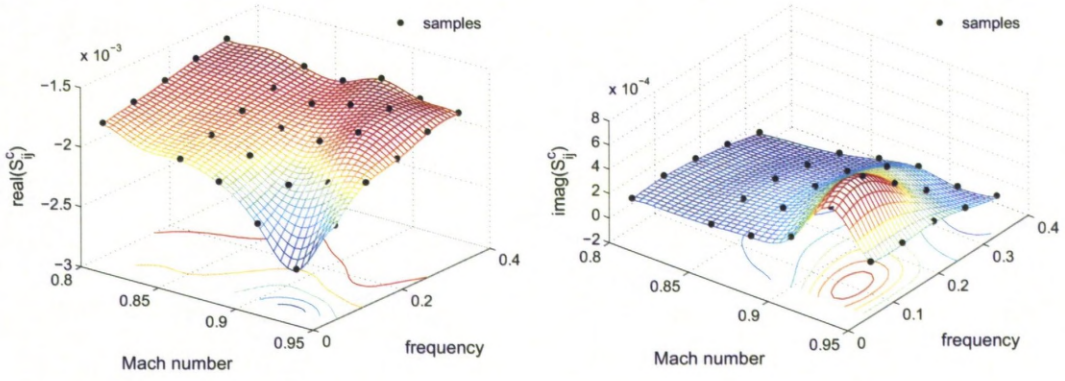

(a) real part (b) imaginary part

Figure 6.19: Extracted and interpolated element $S^c_{5,2}$ of Schur interaction matrix for Goland wing/store configuration using alternative extraction approach for Euler flow model.

range where the differences to the reference solution are small. The differences to the results in [24] are small but distinct and are not simply explained by the intergrid transformation. The three higher modes have a stronger torsional character with the CVT transformation giving poorer results when extrapolating to the trailing edge. This is indicated in Fig. 6.18 for the third mode. The dynamics in the LCO bucket are dominated by the second mode (dominant torsion) which could explain the differences to the reference solution using the original mode shapes. Also, the peak at freestream Mach numbers just below the LCO bucket is strongly influenced by the third mode.

The results indicate two points. First, the numerical implementation of an intergrid transfer method (such as CVT) is important and can result in uncertainty for the stability prediction as presented in [161]. Secondly, the mode shapes themselves are important. As these depend on the structural model, variability in the structural model parameters should be considered routinely. This latter issue was previously investigated in [22] for the Goland wing.

As a frequency domain solver to extract the samples of the Schur interaction matrix is currently not available for the RANS equations defining the highest level in the presented hierarchy, forced time domain simulations are required. Instead of evaluating the Fourier coefficients in each control volume, contributing to the generalised pressure forces, individually and then multiplying with the Jacobian matrix block A_{sf} to project the responses onto the structural degrees–of–freedom as described in Section 4.2, the response signals of the generalised forces are analysed directly to evaluate the aerodynamic influence coefficient matrix Q according to the expression $\Phi^T \boldsymbol{f} = Q\,\boldsymbol{\eta}$. This was introduced in Section 5.1.5 for an aerofoil case analysing the time signals of the lift and moment coefficients which describe the generalised forces of the plunge and pitch degrees–of–freedom.

As was shown in Section 4.4, the aerodynamic influence coefficient matrix Q^c corresponds to the Schur interaction matrix S^c plus a small correction, which is usually negligible as demonstrated in Chapter 5, thus write,

$$Q^c(\lambda) = \vartheta\, C_2 - \vartheta\, C_3 \left(A_{ff} - \lambda I\right)^{-1} \left(A_{f\eta} + \lambda A_{f\dot{\eta}}\right), \tag{6.3}$$

where $C_2 = E\,\Phi^T \partial \boldsymbol{f} / \partial \boldsymbol{w}_s$ and $C_3 = E\,\Phi^T \partial \boldsymbol{f} / \partial \boldsymbol{w}_f$ using the notation of Section 5.2. The first term on the right–hand side is the small correction whereas the second term describes the Schur interaction matrix.

To test the time domain extraction approach for the modal structural model using the generalised forces, the Euler equations are discussed first. This allows the comparison with the results of the linear frequency domain solver. Therefore, the samples to reconstruct the interaction matrix (i.e. the aerodynamic influence coefficient matrix) within the parameter space shown in Fig. 6.19 are generated by running forced periodic motion simulations. For each sample as combination of frequency and freestream Mach number to describe the dynamics of the Goland wing/store configuration with four retained normal modes, four unsteady simulations are required exciting one mode at a time with a mathematically consistent relation between deflection and deflection rate. Three cycles of motion with 50 real time steps per cycle are used which allows the decay of startup transients to use the third cycle to extract the response information from the generalised forces. The excitation amplitude of the sinusoidal motion is defined to be 1.0×10^{-3}. These values were chosen based on the experience gained with the aerofoil cases. At each real time step the pseudo residual, defined in Eq. (2.14), is converged two orders of magnitude in about 10 to 20 pseudo iterations.

Visual inspection of the response surfaces does not indicate differences compared with the results presented in Fig. 6.19, and hence these are not shown. The same applies to the predicted instability boundary, using the kriging–based approach, as the results agree closely with the previous results. Thus, confidence is established in the procedure using the Euler equations and the focus is now directed towards the RANS modelling.

The computational requirements for the RANS flow model are more demanding compared with the Euler simulations, and the need to run time domain forced motion simulations to extract the numerical samples makes this situation worse. Using the coarser RANS grid, one steady state solution is simulated by converging the residual six orders of magnitude in about half an hour running on 16 processors. To extract one sample of the interaction matrix, requiring four unsteady runs as described in the previous paragraph, corresponds to about eight steady state solves. Here, the same parameters (cycles of motion, steps per cycle, excitation amplitude and convergence in pseudo time) as specified for the Euler simulations are used for the RANS forced motion simulations. Using the finer RANS grid, the simulation of a steady state running on 32

processors takes about six hours, while the extraction of one sample then corresponds to two steady state simulations. To compare, a steady state solution for the Euler equations using a grid with 200 thousand control volumes is obtained in less than half an hour running on four processors with the extraction of one sample taking less than one third of this time using the second approach in the frequency domain requiring four linear solves.

In Figs. 6.20 and 6.21 the results for coarse grid RANS simulations are presented. The response surface of one representative element of the Schur interaction matrix is shown in Fig. 6.20. The similarity to the Euler results in Fig. 6.19 is evident and expected following the earlier discussed aerofoil results in Section 5.1. Within the considered range of freestream Mach numbers of up to 0.95, shock induced flow separation is not yet encountered in the steady state RANS simulations, leaving the shock nonlinearity as the dominant mechanism of the dynamic response. Note that the differences found in typical flow characteristics such as surface pressure distributions (indicated in Fig. 6.17) or skin friction (not shown herein) between the steady state RANS simulations using the coarser and finer grids are rather small indicating that the spatial resolution achieved by the coarser grid is acceptable.

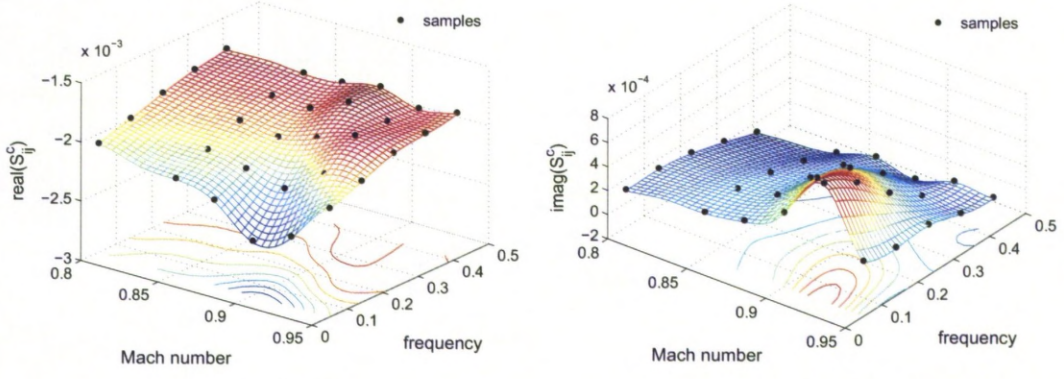

(a) real part

(b) imaginary part

Figure 6.20: Extracted and interpolated element $S^c_{5,2}$ of Schur interaction matrix for Goland wing/store configuration using alternative extraction approach for RANS flow model on coarse mesh.

Figure 6.21 presents the corresponding results of the stability analysis using the kriging approximation of the interaction matrix. The figure indicates the instability points (in dependence on the freestream Mach number) at fixed sea level conditions for all four aeroelastic modes originating in the wind–off structural modes. Critical values of the freestream velocity and the dimensionless frequency are given for the RANS simulations and compared with the Euler results. The configuration is unstable

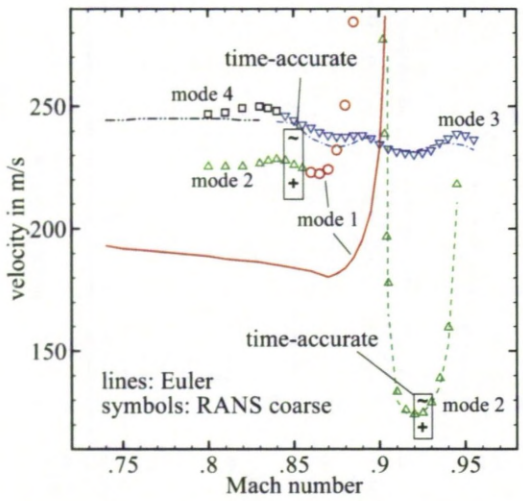

(a) Critical velocity

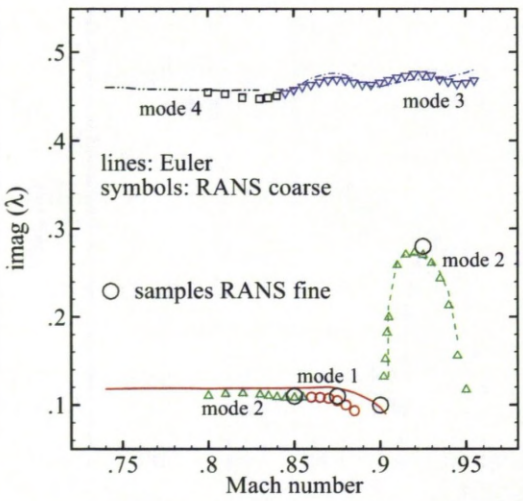

(b) Critical frequency

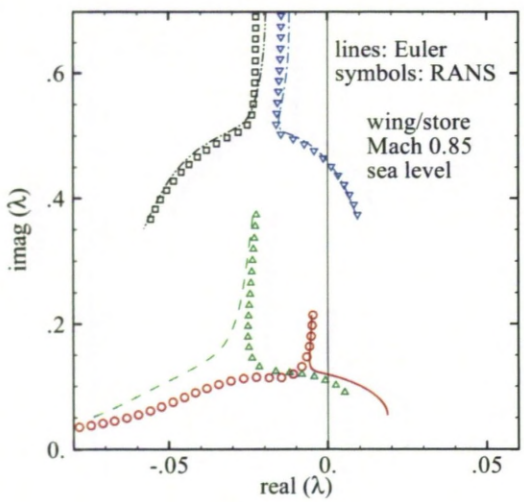

(c) Root loci

Figure 6.21: Instability behaviour of Goland wing/store configuration for Euler and RANS flow models showing (a–b) critical values of velocity and dimensionless frequency at sea level conditions including instability points for all modes and (c) mode tracing at Mach 0.85 with respect to freestream velocity.

at a given Mach number once the instability boundary is first crossed with increasing freestream velocity. Also, the mode tracing at Mach 0.85 is included.

The Euler results show the earlier discussed behaviour. At the lower freestream Mach numbers the first mode is the critical mode, developing the typical transonic dip, followed by the bucket of shock induced LCO as described in [24]. The development of the first mode instability is very similar to the aerofoil results presented in Fig. 5.6. Also visible in the figure is the third mode instability dominating the response in the peak following the transonic dip at a freestream Mach number of about 0.9.

The RANS results, using the coarser grid, show a surprising behaviour for the lower freestream Mach numbers. While the second, third and fourth mode instabilities follow closely the Euler results, the first mode behaviour (of the Euler predictions)

is significantly influenced. The RANS prediction, based on the kriging–reconstructed interaction matrix in Fig. 6.20, suggests that the second mode is critical over a larger range of Mach numbers below the transonic flow region followed by the first mode near the peak. This crossing of the first and second mode is indicated in Fig. 6.21(c). The corresponding frequencies however are not effected by this switching of modes. The difference in the critical velocity is considerable even though a significant influence of the viscous effects would only be expected in the higher Mach number range due to the stronger shock/boundary layer interaction.

To investigate this behaviour in more detail, RANS simulations on the finer grid are included in the discussion using the co–kriging approach, as introduced for the aerofoil case in Section 6.2.1, to reconstruct the interaction matrix based on very few samples. Four samples are used initially with their locations in the parameter space indicated in Fig. 6.21(b). Following the Euler and coarser grid RANS stability predictions the sample locations are chosen to cover the first and second mode instabilities. Then, as for the aerofoil case, the set of the four expensive RANS samples is augmented by the corner samples (limiting the parameter space) from a less expensive flow model. Here, cheaper samples from both the Euler and the coarser grid RANS simulations are considered. Also, for the co–kriging approach the input parameter space of the augmented set of samples is extended by the response of the lower fidelity predictions to provide the trend information.

Note that the step of using the results of RANS simulations on a coarser grid is important. The basic assumption of the co–kriging approach is the correlation in the parameter space between the responses of flow simulations having a variable fidelity. This variable fidelity can be established by using both different levels of the aerodynamic hierarchy and computational grids of different resolution. Exploiting the aerodynamic hierarchy requires that the dominant physics are captured by the chosen model, as discussed in Section 5.1.4 for the NACA 0012 aerofoil case.

In the case of the Goland wing at zero degrees angle of attack, freestream Mach numbers below 0.95, and a reference Reynolds number of 15 million, shock induced flow separation was not predicted in the steady state simulations. This suggests that the shock dynamics are the driving mechanism which would allow the use of the Euler equations. The agreement in the co–kriging results, using the interaction matrices of both the Euler and coarser grid RANS simulations as co–variable, is demonstrated next. If separation is encountered, then RANS simulations (or a lower fidelity model accounting for viscous effects) are required.

The results for the co–kriging approach are presented in Figs. 6.22 through 6.25. In Fig. 6.22 the instability boundary given by the first and second mode is shown for the co–kriging approach based on both the Euler and coarser grid RANS results acting as the correlated co–variable to provide the trend information for the few more expensive samples. There are several interesting observations.

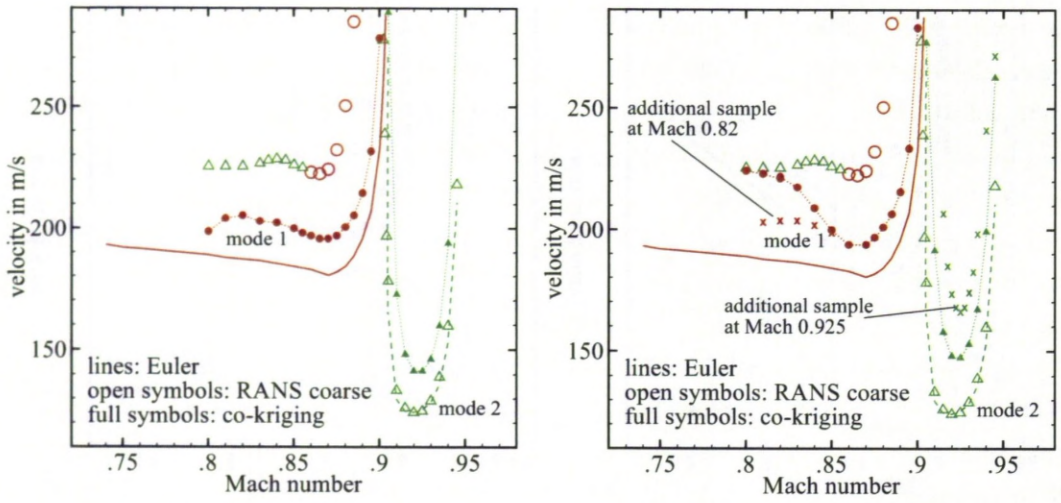

(a) Co–kriging based in Euler

(b) Co–kriging based on RANS (coarse)

Figure 6.22: Co–kriging technique applied to aeroelastic stability analysis of Goland wing/store configuration showing critical values of freestream velocity at sea level conditions and using both Euler and coarser grid RANS predictions as correlated co–variable.

First, in contrast to the misleading results of the coarser grid RANS predictions, the lower range of freestream Mach numbers is dominated by a bending–torsion type of instability, as expected, with the first mode being critical throughout.

Secondly, the differences between the finer grid RANS and Euler predictions in the region of the bending–torsion type instability, forming the typical transonic dip, are smaller giving a similar behaviour compared with the aerofoil results shown in Fig. 5.6. The viscous effects have a stabilising influence on the configuration and increase the flutter onset velocity.

Thirdly, for freestream Mach numbers below 0.85 the high fidelity predictions based on co–kriging using the Euler and coarser grid RANS results as correlated co–variables deviate considerably. This is due to the required extrapolation of the finer grid RANS response with the first initial sample being located at Mach 0.85 as shown in Fig. 6.21. Thus, below the freestream Mach number of 0.85 the predictions consequently either approach the Euler or coarser grid RANS results. Therefore, extrapolation should be avoided by a careful placement of the expensive high fidelity samples. Using an additional sample located at Mach 0.82, this latter observation is supported by the stability results as indicated in the figure.

And finally, the critical freestream velocity in the bucket of shock induced LCO is increased by the RANS predictions using the finer grid compared with the lower fidelity results. Adding a second RANS sample using the finer grid at Mach 0.925 shows a further increase in the critical velocity.

Time–accurate simulations have been done to confirm the Euler and coarser grid RANS predictions. As with all time–accurate aeroelastic simulations in this study, the system parameters have been chosen following the results of the eigenvalue–based linear stability analysis to avoid unnecessary iteration to bracket the instability. The RANS results are included in Fig. 6.21 with a plus (tilde) sign indicating a stable (unstable) response due to an initial disturbance in the structural unknowns. To give an idea of the computational cost involved for unsteady RANS flow modelling on the coarser grid, the simulation of one cycle of motion, requiring about 600 real time steps at a dimensionless response frequency of about 0.1 corresponding to a first mode instability and using a dimensionless time increment of 0.1, takes about six hours running on ten processors. Several cycles always have to be simulated following an initial excitation.

Figure 6.23 compares the response surface of one representative element of the interaction matrix using the approaches of kriging and co–kriging for the augmented set of samples of variable fidelity. These include the four initial finer grid RANS samples and the lower fidelity corner samples, which are the coarser grid RANS samples in this figure. The differences are relatively small in most parts of the parameter space, and consequently the stability analysis based on direct kriging using the eight samples, the results of which are not shown herein, predicts the bending–torsion type of instability forming the transonic dip accurately. However, using this direct kriging completely fails to predict the bucket of instability associated with shock induced LCO [24], whereas the reconstruction of the interaction matrix using the co–kriging approach is accurate enough to give the expected results as shown in Fig. 6.22.

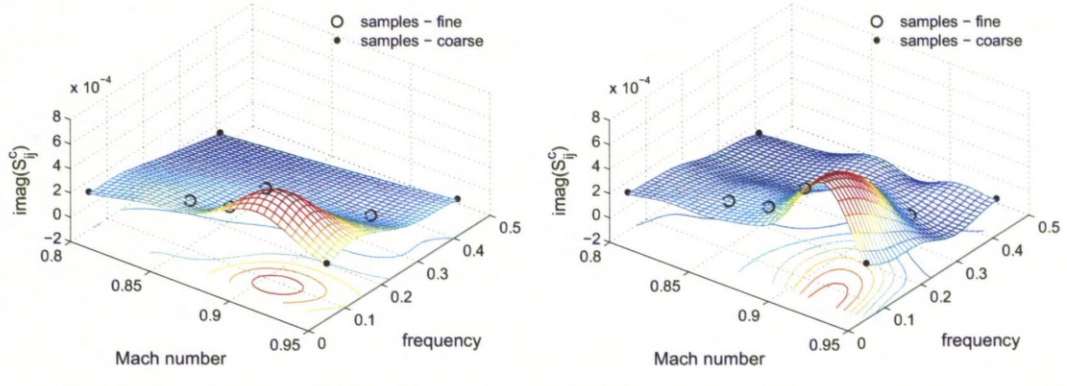

(a) Element $\text{imag}(S^c_{5,2})$ based on direct kriging (b) Element $\text{imag}(S^c_{5,2})$ based on co–kriging

Figure 6.23: Direct kriging and co–kriging techniques applied to aeroelastic stability analysis of Goland wing/store configuration, using augmented sample set and coarser grid RANS results as correlated co–variable, showing approximated element $\text{imag}(S^c_{5,2})$ of Schur interaction matrix.

Finally, the mode tracing for the stability analysis based on the kriging approximation for both the Euler and RANS simulations (using the finer grid) at freestream Mach

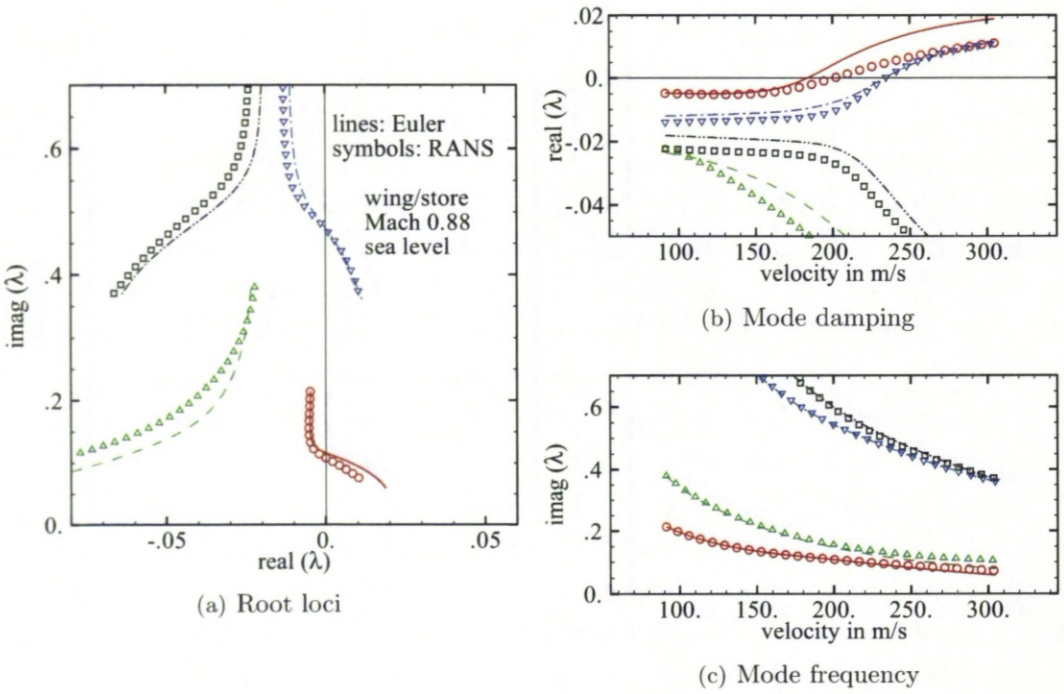

(a) Root loci

(b) Mode damping

(c) Mode frequency

Figure 6.24: Mode tracing with respect to freestream velocity at fixed sea level conditions for Goland wing/store configuration showing results for Euler and RANS flow models at Mach 0.88 (eigenvalues given in dimensionless form).

numbers of 0.88 and 0.92 is presented in Figs. 6.24 and 6.25. The RANS results use the co–kriging approach with the coarser grid RANS response as co–variable. While the differences between the Euler and RANS predictions at the lower freestream Mach number are relatively small, the change in the critical frequency associated with the second mode instability at the higher Mach number is distinct.

A detailed sensitivity study with respect to the parameters used for the forced periodic motion simulations to extract the samples would be required to be more confident in the results. Four important parameters must be varied to compromise between accuracy and cost; the number of forced cycles to have negligible startup transients, the number of real time steps per cycle of motion to have a sufficient temporal resolution and a negligible numerical error, the excitation amplitude to identify the dynamic content of the system correctly, and the convergence in pseudo time at each real time step to reduce the numerical (iterative) error. The current parameters, given earlier, are chosen according to the experience gained from the aerofoil cases to give good results. However, due to the large variation between the different modes in the modal amplitude, which was found in time–accurate responses, a more sensible approach might be to excite different modes at different amplitudes in order not to violate the principle of superposition for the linear stability analysis.

The discussion of the various simulation parameters forms part of a proper system identification process to develop a useful reduced order model [35] and is just as impor-

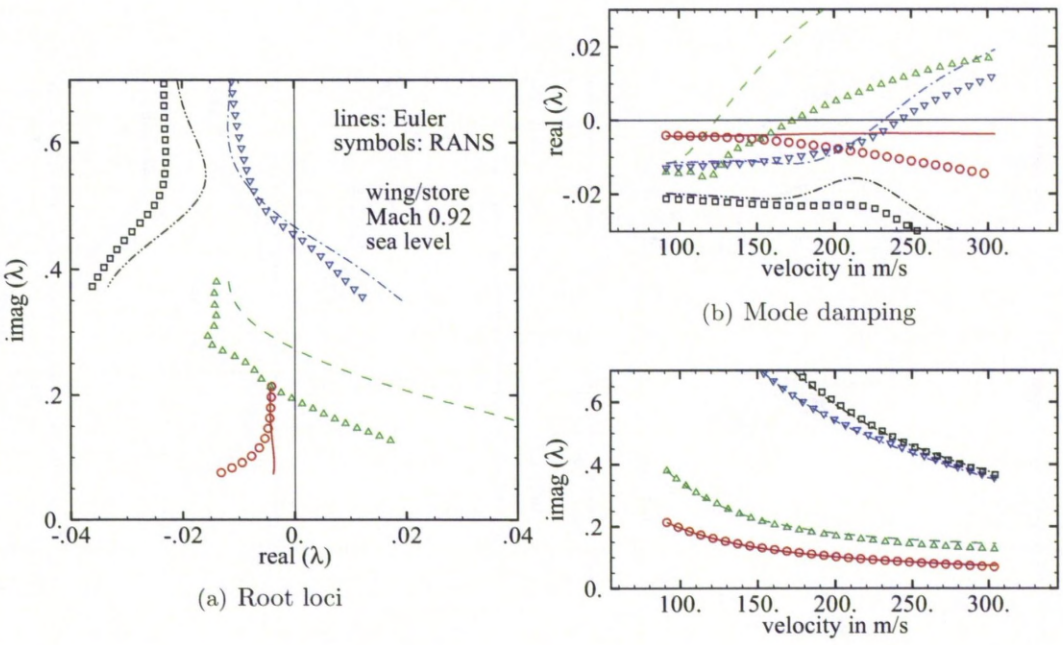

(a) Root loci

(b) Mode damping

(c) Mode frequency

Figure 6.25: Mode tracing with respect to freestream velocity at fixed sea level conditions for Goland wing/store configuration showing results for Euler and RANS flow models at Mach 0.92 (eigenvalues given in dimensionless form).

tant for temporal accuracy in unsteady CFD–based simulations. In [35], for instance, it was argued to perform linearity tests at the conditions of interest by applying input signals of various amplitudes and by testing the assumption of modal superposition. Currently, such a study has been done for the aerofoil cases but not for the modal structural model using the RANS equations (while the Euler time domain extraction agrees well with frequency domain results as indicated above). The uncertainty (and cost) associated with time domain simulations for all flow models, and particularly the RANS equations, could partly be avoided if a frequency domain solver is available. The aerofoil code for the unsteady full potential equations, for instance, evaluates all system Jacobian matrices required for the frequency domain approach analytically while solving the linear systems to machine accuracy using a direct solver. This eliminates the uncertainty associated with all the aformentioned simulation parameters. Of course, such an entirely analytical formulation is significantly more difficult to establish for realistic problems, particularly using the RANS equations.

6.3 Summary of Sampling and Using the Model Hierarchy

To summarise the discussion of this chapter, the approximation of the interaction matrix, modelling the influence of the high dimensional computational fluid dynamics

system on the aeroelastic problem, has been demonstrated using both efficient coordinated sampling approaches and flow simulations of variable fidelity.

The study of the stability simulations showed that an accurate reconstruction of the interaction matrix is not required globally in a given parameter space as the influence of this expensive term on the small nonlinear eigenvalue problem can be rather small, for instance, for low values of the bifurcation parameter or insensitive (wind–off) structural modes. Then, risk–based sampling reduces the required number of exact (full order) simulations while searching the parameter space for instability. The risk–based sampling approaches place samples iteratively according to intermediate stability results obtained by using the computationally cheap kriging approximation which is always based on the current set of samples. The sampling approaches have been discussed for aerofoil cases and the aerostatically deflected MDO wing configuration.

The stability analysis based on co–kriging using aerodynamic simulations of variable fidelity (different flow models and grid resolutions) has been demonstrated for the NACA 0012 "heavy case" aerofoil configuration and the Goland wing/store configuration. Here, the lower fidelity response can be used to provide the trend information for the higher fidelity kriging model assuming that the dominant physics are captured approximately by the lower fidelity simulation. To reduce the required number of higher fidelity samples, and hence the computational cost, an augmented set of samples proved to be very useful. A few higher fidelity samples are placed close to the instability boundary which is predicted by an initial lower fidelity simulation to explore the parameter space. These few samples are then augmented with lower fidelity samples placed at the corners of the parameter space limiting the search region and supporting the construction of the higher fidelity kriging approximation.

The instability boundary is given as critical values of the response frequency and dynamic pressure as well as various parameters of the steady state simulation like freestream Mach number and angle of attack. According to the conclusions from the coordinated sampling study, placing the higher fidelity samples close to the instability boundary usually gives a good enough approximation for the elements of the interaction matrix as these expensive evaluations are provided in the relevant regions.

The issue of parallelisation has not been discussed in the preceding discussion. Particularly, risk–based sampling creates samples iteratively (a posteriori) as intermediate information is required to choose the sample locations efficiently. However, considering realistic engineering problems with many structural degrees–of–freedom, an efficient parallel operation is achieved by splitting the task for the sample extraction. In the frequency domain, for instance, the linear systems for the n relevant right–hand sides (one for each structural degree–of–freedom) to evaluate the columns of the interaction matrix can be solved in parallel. The same applies in the time domain running each of the n forced motion simulations on a different set of processors.

Chapter 7

Conclusions and Outlook

The main objective of this thesis was to investigate the use of a hierarchy of high fidelity nonlinear computational fluid dynamics models in routine aircraft aeroelastic stability analyses, particularly in transonic flow featuring shock waves and shock induced separation. The search for linear aeroelastic instability over a proposed transonic flight envelope, while exploiting the model hierarchy, was the specific task addressed.

This was demonstrated successfully by introducing searches for the approximation of the interaction matrix, modelling the influence of the high dimensional computational fluid dynamics system on the modified structural eigenvalue problem solved for the stability analysis. The approximation used the kriging interpolation technique based on exact numerical samples describing the system response. The co–kriging approach was formulated to allow the correction of a lower fidelity prediction with higher fidelity simulations guided by the lower fidelity results.

In Chapter 2 the hierarchy of aerodynamic models was established discussing the nonlinear full potential equations, corrected for viscous effects by an integral boundary layer model, the Euler equations and the Reynolds–averaged Navier–Stokes equations. The hierarchy of aerodynamic models allows the simulation to be updated by adding more physical content from a higher level approach once this is required. In Chapter 3 the newly developed full potential flow solver was tested against available experimental data and results from higher fidelity flow models for standard aerofoil cases. The presented cases showed excellent agreement.

The applied aeroelastic tools were described in detail in Chapter 4. The aeroelastic stability problem is written as a modified structural eigenvalue problem, which is corrected by an interaction term depending on the response frequency and the high fidelity steady state solution. Solving the small nonlinear eigenvalue problem to trace the aeroelastic modes originating in the wind–off structural modes is very efficient, and the evaluation of the structural terms, considered to be linear herein, as part of this eigenvalue problem is rather simple. However, as the generation of the interaction term is the limiting factor in the analysis in terms of cost, its approximation was discussed.

The approximation was done by kriging interpolation based on true samples, which were generated in the frequency and time domain. The original implementation of the eigenvalue solver, i.e. the linear frequency domain solver, was optimised by a straightforward rearrangement of the right–hand side terms reducing the computational cost per evaluation of an exact numerical sample of the interaction matrix by a factor of two. The discussion on classical flutter analysis showed the equivalence of the herein presented Schur complement eigenvalue method and the classical analysis.

In Chapter 5 the kriging–based approach was derived and thoroughly investigated for two structural models. It was demonstrated for an aerofoil case and two wing cases that the approximation approach gives excellent agreement with the exact eigenvalue solver while being computationally more efficient if applied over a flight envelope rather than in a single point analysis. Further, the results of an aerofoil case were compared for four different flow models to discuss the influence of physical effects and numerical discretisation on the stability behaviour. Then, the kriging–based method for three dimensional cases was shown to be equivalent to the aerofoil formulation with only minor modifications required. The stability analyses for the symmetric Goland wing cases with and without tip store and the MDO wing case, fully accounting for the effects of aerostatic deformation, were discussed.

The search for aeroelastic instability using the hierarchy of flow models, while assuming little prior knowledge of the stability behaviour, was presented in Chapter 6. Therefore, several sampling techniques were considered for the aerofoil cases. Efficient risk–based sampling in combination with the kriging interpolation was found to allow accurate instability searches over a flight envelope, which describes a multidimensional parameter problem. This was then demonstrated for the aerostatically deformed MDO wing configuration using a four dimensional search space with the freestream angle of attack as an arbitrarily chosen fourth variable added to the input dimensions of the response frequency, altitude and freestream Mach number.

The stability analysis based on flow models of variable fidelity, using data fusion and co–kriging, was discussed for the NACA 0012 aerofoil case and the Goland wing/store configuration. Two steps were shown to be useful. First, the set of higher fidelity (expensive) samples was augmented by lower fidelity samples at the corners of the initial search space. Secondly, the lower fidelity, spatially correlated response was used within the co–kriging technique to provide the trend information for the few higher fidelity evaluations. These two steps support the required construction of the higher fidelity interaction matrix to give accurate stability predictions at lower computational cost. As a convenient additional aspect, a stability analysis based on the Reynolds–averaged Navier–Stokes equations has not been done before in the context of the Schur complement eigenvalue method.

There are several important directions which can be taken in future studies. To complete the hierarchy of aerodynamic models, the linear potential level must be dis-

cussed. Work has started to combine flow solvers using linear potential aerodynamic models, namely the doublet lattice method and the vortex lattice method, with the current eigenvalue stability approach.

As mentioned in Section 5.2.3, aeroelastic stability problems occur where a linear representation of the structure is insufficient giving misleading results. The extension of the presented eigenvalue stability approach using nonlinear aerodynamic modelling to accommodate nonlinear structural models is an important step. This corresponds to the third requirement put forward in [15] (as discussed in Section 1.1) and not further addressed in this thesis. A computational problem which arises for such nonlinear models is the large number of structural degrees–of–freedom corresponding to a large number of required linear solves against the high dimensional fluid system. This problem is present for the exact eigenvalue solver and accordingly for the approximation model due to the required sample generation. Here, it is necessary to discuss the possibility of forming a reduced model basis for the structure around the nonlinear steady state, e.g. using an eigenmode analysis.

In addition, updating the approximation model with available information from flight tests must be discussed. Processed response signals provide estimates for modal frequency and damping at given parameter combinations (like freestream Mach number and altitude) within the stable flight envelope [5, 7]. This information could then be used, for instance, in an inverse eigenvalue problem to update the interaction matrices obtained from a high fidelity CFD–based simulation. These updated matrices could provide the means to predict the instability onset beyond the flight test limits.

The kriging approximation can also be used to consider the influence of variability in the structural parameters on the stability prediction. In the current study the approximation model has been applied to instability searches in a multidimensional parameter space which is related to the aerodynamic model considering changes in the freestream Mach number, altitude and angle of attack. The applicability to structural parameter spaces needs to be shown. This is related to the earlier work [22] using the Schur complement eigenvalue method to investigate the variability in parameters of the finite–element model of the Goland wing configuration. Seven parameters were identified from a linear aeroelastic tool to have a significant influence on the stability characteristics. The current approach could be used by creating a kriging model for the Schur interaction matrix based on true matrix evaluations with the input parameter space including the relevant structural parameters.

The kriging approach can be combined with a model reduction technique to evaluate a limit–cycle response in the vicinity of the linear instability point. This has been demonstrated for the exact eigenvalue solver in [54]. Using the current approach, the stability limit is predicted by searching the flight envelope to identify the most critical regions of interest. Here, the influence of individual modes on the stability characteristics is investigated inexpensively. The eigensolution in the critical mode,

obtained from the kriging–based stability analysis, is then transferred back to the exact eigenvalue solver requiring one steady state solution to obtain the Jacobian matrices and one linear solve to obtain the fluid eigenvector. Based on the centre manifold theorem, this information is then reduced into a two degrees–of–freedom system in the critical mode to investigate the limit–cycle response.

An important characteristic of the kriging model applied to the stability analysis, which essentially describes an aeroelastic model reduction technique, lies in the applicability in a preliminary multidisciplinary design environment. Besides the cost, full order computational fluid dynamics simulations are not well suited for such tasks. However, a frequency domain reduced order model can be transformed into a time domain state–space model, using traditional rational function approximation techniques, to allow its use in modern aeroservoelastic analyses. It would be interesting to investigate the transformation of the current frequency domain representation into the time domain to accommodate the approach in such an analysis.

The presented methods should be incorporated into a production aeroelastic tool. As shown in this thesis in Section 5.3, the eigenvalue solver has been implemented into the DLR TAU code to extract true samples to identify the system dynamics and the kriging–based reconstruction of the interaction matrix has been used to do the stability analysis [152]. Further interaction with the German Aerospace Center will allow the method to be consolidated into the production release of the TAU code, which is the adopted computational fluid dynamics code of Airbus.

Bibliography

[1] Garrick, I. E. and Reed III, W. H., "Historical development of aircraft flutter," *Journal of Aircraft*, Vol. 18, No. 11, 1981, pp. 897–912.

[2] Bunton, R. W. and Denegri, Jr., C. M., "Limit cycle oscillation characteristics of fighter aircraft," *Journal of Aircraft*, Vol. 37, No. 5, 2000, pp. 916–918.

[3] Dowell, E. H., Edwards, J. W., and Strganac, T. W., "Nonlinear aeroelasticity," *Journal of Aircraft*, Vol. 40, No. 5, 2003, pp. 857–874.

[4] von Schlippe, B., "Zur Frage der selbsterregten Flügelschwingungen," *Luftfahrtforschung*, Vol. 13, No. 2, 1936, Translated and Reprinted in NACA–TM–806 (1936).

[5] Kehoe, M. W., "A historical overview of flight flutter testing," Tech. Rep. NASA–TM–4720, Dryden Flight Research Center, Edwards, CA, 1995.

[6] Kaynes, I. W., "Aeroelastic review," Tech. Rep. DERA/ MSS/ MSTR2/ CR010456, Defence Evaluation and Research Agency UK, 2001.

[7] Cooper, J. E., "Towards faster and safer flight flutter testing," *RTO–MP–089, AVT Symposium on Reduction of Military Vehicle Acquisition Time and Cost through Advanced Modelling and Virtual Simulation, Paris, France, 22–25 April 2002*, 2002.

[8] Livne, E. and Weisshaar, T. A., "Aeroelasticity of nonconventional airplane configurations — past and future," *Journal of Aircraft*, Vol. 40, No. 6, 2003.

[9] Pettit, C. L., "Uncertainty quantification in aeroelasticity: recent results and research challenges," *Journal of Aircraft*, Vol. 41, No. 5, 2004, pp. 1217–1229.

[10] de C. Henshaw, M. J., Badcock, K. J., Vio, G. A., Allen, C. B., Chamberlain, J., Kaynes, I., Dimitriadis, G., Cooper, J. E., Woodgate, M. A., Rampurawala, A. M., Jones, D., Fenwick, C., Gaitonde, A. L., Taylor, N. V., Amor, D. S., Eccles, T. A., and Denley, C. J., "Non–linear aeroelastic prediction for aircraft applications," *Progress in Aerospace Sciences*, Vol. 43, 2007, pp. 65–137.

[11] Bhatia, K. G., "Airplane aeroelasticity: practice and potential," *Journal of Aircraft*, Vol. 40, No. 6, 2003, pp. 1010–1018.

[12] Meijer, J. J., "Aeroelasticity," Tech. Rep. RTO–AG–300–V14 Introduction to Flight Test Engineering, 1995.

[13] Walgemoed, H., "Flight envelope," Tech. Rep. RTO–AG–300–V14 Introduction to Flight Test Engineering, 1995.

[14] Wright, J. R. and Cooper, J. E., *Introduction to aircraft aeroelasticity and loads*, John Wiley & Sons, Ltd, Chichester, England, 2007.

[15] Yurkovich, R. N., "Status of unsteady aerodynamic prediction for flutter of high–performance aircraft," *Journal of Aircraft*, Vol. 40, No. 5, 2003, pp. 832–842.

[16] Dowell, E. H., Thomas, J. P., Hall, K. C., and Denegri Jr., C. M., "Theoretical predictions of F–16 fighter limit cycle oscillations for flight flutter testing," *Journal of Aircraft*, Vol. 46, No. 5, 2009, pp. 1667–1672.

[17] Pitt, D. M., Haudrich, D. D., Thomas, M. J., and Griffin, K. E., "Probabilistic aeroelastic analysis and its implications on flutter margin requirements," *AIAA Paper 2008–2198*, 2008.

[18] Box, G. E. P. and Draper, N. R., *Empirical model–building and response surfaces*, Wiley, Chichester, England, 1987.

[19] Friswell, M. I. and Mottershead, J. E., *Finite element model updating in structural dynamics*, Kluwer Academic Press, Dorndrecht, The Netherlands, 1995.

[20] Palacios, R., Climent, H., Karlsson, A., and Winzell, B., "Assessment of strategies for correcting linear unsteady aerodynamics using CFD or experimental results," *IFASD 2001–074*, 2001.

[21] Walters, R. W. and Huyse, L., "Uncertainty analysis for fluid mechanics with applications," Tech. Rep. NASA/CR–2002–211449, NASA Langley Research Center, Hampton, VA, 2002.

[22] Marques, S., Badcock, K. J., Khodaparast, H. H., and Mottershead, J. E., "CFD based aeroelastic stability predictions under the influence of structural variability," *AIAA Paper 2009–2324*, 2009, to appear in Journal of Aircraft.

[23] Oberkampf, W. L. and Blottner, F. G., "Issues in computational fluid dynamics code verification and validation," *AIAA Journal*, Vol. 36, 1998, pp. 688–695.

[24] Beran, P. S., Khot, N. S., Eastep, F. E., Snyder, R. D., and Zweber, J. V., "Numerical analysis of store–induced limit–cycle oscillation," *Journal of Aircraft*, Vol. 41, No. 6, 2004, pp. 1315–1326.

[25] Taylor, N. V., Allen, C. B., Gaitonde, A. L., Jones, D. P., Vio, G. A., Cooper, J. E., Rampurawala, A. M., Badcock, K. J., Woodgate, M. A., and de C. Henshaw, M. J., "Aeroelastic analysis through linear and non–linear methods: a summary of flutter prediction in PUMA DARP," *The Aeronautical Journal*, Vol. 110, No. 1107, 2006, pp. 333–343.

[26] Hassig, H. J., "An approximate true damping solution of the flutter equation by determinant iteration," *Journal of Aircraft*, Vol. 8, No. 11, 1971, pp. 885–889.

[27] Albano, E. and Rodden, W. P., "A doublet–lattice method for calculating lift distributions on oscillating surfaces in subsonic flows," *AIAA Journal*, Vol. 7, No. 2, 1969, pp. 279–285.

[28] Ashley, H., "Role of shocks in the "sub–transonic" flutter phenomenon," *Journal of Aircraft*, Vol. 17, No. 3, 1980, pp. 187–197.

[29] Shang, J. S., "Three decades of accomplishments in computational fluid dynamics," *Progress in Aerospace Sciences*, Vol. 40, 2004, pp. 173–197.

[30] Farhat, C., Geuzaine, P., and Brown, G., "Application of a three–field nonlinear fluid–structure formulation to the prediction of the aeroelastic parameters of an F–16 fighter," *Computers & Fluids*, Vol. 32, No. 1, 2003, pp. 3–29.

[31] Prananta, B. B., Kok, J. C., Spekreijse, S. P., Hounjet, M. H. L., and Meijer, J. J., "Simulation of limit cycle oscillation of fighter aircraft at moderate angle of attack," Tech. Rep. NLR–TP–2003-526, National Aerospace Laboratory NLR, 2003.

[32] Woodgate, M. A., Badcock, K. J., Rampurawala, A. M., Richards, B. R., Nardini, D., and deC Henshaw, M. J., "Aeroelastic calculations for the Hawk aircraft using the Euler equations," *AIAA Journal*, Vol. 42, No. 4, 2005, pp. 1005–1012.

[33] Lucia, D. J., Beran, P. S., and Silva, W. A., "Reduced–order modeling: new approaches for computational physics," *Progress in Aerospace Sciences*, Vol. 40, 2004, pp. 51–117.

[34] Dowell, E. H. and Hall, K. C., "Modelling of fluid–structure interaction," *Ann. Rev. Fluid Mech.*, Vol. 33, 2001, pp. 445–490.

[35] Silva, W. A. and Bartels, R. E., "Development of reduced–order models for aeroelastic analysis and flutter prediction using the CFL3Dv6.0 code," *Journal of Fluids and Structures*, Vol. 19, 2004, pp. 729–745.

[36] Romanowski, M. C., "Reduced order unsteady aerodynamics and aeroelastic models using Karhunen–Loeve eigenmodes," *AIAA Paper 96–3981*, 1996.

[37] Lieu, T. and Farhat, C., "Adaptation of aeroelastic reduced–order models and application to an F–16 configuration," *AIAA Journal*, Vol. 45, No. 6, 2007, pp. 1244–1257.

[38] Amsallem, D. and Farhat, C., "Interpolation method for adapting reduced–order models and application to aeroelasticity," *AIAA Journal*, Vol. 46, No. 7, 2008, pp. 1803–1813.

[39] Bui–Thanh, T., Damodaran, M., and Willcox, K., "Proper orthogonal decomposition extensions for parametric applications in transonic aerodynamics," *AIAA Paper 2003–4213*, 2003.

[40] Hall, K. C., Thomas, J. P., and Clark, W. S., "Computation of unsteady nonlinear flows in cascades using a harmonic balance technique," *AIAA Journal*, Vol. 40, No. 5, 2002, pp. 879–886.

[41] Thomas, J. P., Dowell, E. H., and Hall, K. C., "Modeling viscous transonic limit–cycle oscillation behavior using a harmonic balance approach," *Journal of Aircraft*, Vol. 41, No. 6, 2004, pp. 1266–1274.

[42] Thomas, J. P., Dowell, E. H., and Hall, K. C., "Further investigation of modeling limit cycle oscillation behavior of the F–16 fighter using a harmonic balance approach," *AIAA Paper 2005-1917*, 2005.

[43] Thomas, J. P., Dowell, E. H., and Hall, K. C., "An investigation of the sensitivity of F–16 fighter flutter onset and limit cycle oscillations to uncertainties," *AIAA Paper 2006-1847*, 2006.

[44] Woodgate, M. A. and Badcock, K. J., "Implicit harmonic balance solver for transonic flow with forced motions," *AIAA Journal*, Vol. 47, No. 4, 2009, pp. 893–901.

[45] Dowell, E. H., "Some recent advances in nonlinear aeroelasticity: fluid–structure interaction in the 21st century," *AIAA 2010–3137*, 2010.

[46] Kuznetsov, Y. A., *Elements of applied bifurcation theory*, Springer–Verlag, Inc., New York, NY, 2nd ed., 1998.

[47] Seydel, R. U., *Practical bifurcation and stability analysis: from equilibrium to chaos*, Springer–Verlag, Inc., New York, NY, 2nd ed., 1994.

[48] Griewank, A. and Reddien, G., "The calculation of Hopf points by a direct method," *IMA Journal of Numerical Analysis*, Vol. 3, 1983, pp. 295–303.

[49] Morton, S. A. and Beran, P. S., "Hopf–bifurcation analysis of airfoil flutter at transonic speeds," *AIAA Paper 96–0060*, 1996.

[50] Morton, S. A. and Beran, P. S., "Hopf bifurcation analysis applied to deforming airfoils at transonic speeds," *AIAA Paper 97–1772*, 1997.

[51] Morton, S. A. and Beran, P. S., "Hopf–bifurcation analysis of airfoil flutter at transonic speeds," *Journal of Aircraft*, Vol. 36, No. 2, 1999, pp. 421–429.

[52] Badcock, K. J., Woodgate, M. A., and Richards, B. E., "Hopf bifurcation calculations for a symmetric airfoil in transonic flow," *AIAA Journal*, Vol. 42, No. 5, 2004, pp. 883–892.

[53] Badcock, K. J., Woodgate, M. A., and Richards, B. E., "Direct aeroelastic bifurcation analysis of a symmetric wing based on Euler equations," *Journal of Aircraft*, Vol. 42, No. 3, 2005, pp. 731–737.

[54] Woodgate, M. A. and Badcock, K. J., "Fast prediction of transonic aeroelastic stability and limit cycles," *AIAA Journal*, Vol. 45, No. 6, 2007, pp. 1370–1381.

[55] Badcock, K. J. and Woodgate, M. A., "Bifurcation prediction of large–order aeroelastic models," *AIAA Journal*, Vol. 48, No. 6, 2010, pp. 1037–1046.

[56] Agarwal, R., "Computational fluid dynamics of whole–body aircraft," *Ann. Rev. Fluid Mech.*, Vol. 31, 1999, pp. 125–169.

[57] Holst, T. L., "Transonic flow computations using nonlinear potential methods," *Progress in Aerospace Sciences*, Vol. 36, 2000, pp. 1–61.

[58] Raj, P., "Computational uncertainty: Achilles' heel of simulation based aircraft design," AVT–147 Symposium on Computational Uncertainty in Military Vehicle Design, 2007.

[59] Hirsch, C., *Numerical computation of internal and external flows, Volume 1: Fundamentals of numerical discretization*, John Wiley & Sons Ltd., Chichester, UK, 1995.

[60] Hirsch, C., *Numerical computation of internal and external flows, Volume 2: Computational methods for inviscid and viscous flows*, John Wiley & Sons Ltd., Chichester, UK, 2002.

[61] Lock, R. C. and Williams, B. R., "Viscous–inviscid interactions in external aerodynamics," *Progress in Aerospace Sciences*, Vol. 24, 1987, pp. 51–171.

[62] Murman, E. and Cole, J., "Calculation of plane steady transonic flows," *AIAA Journal*, Vol. 9, No. 1, 1971, pp. 114–121.

[63] Jameson, A., "Iterative solution of transonic flows over airfoils and wings including flows at Mach 1," *Commun Pure Appl Math*, Vol. 17, 1974, pp. 283–309.

[64] Godunov, S. K., "A finite difference method for the numerical computation of discontinuous solutions of the equations of fluid dynamics," *Math Sb*, Vol. 47, 1959, pp. 271–306.

[65] Roe, P. L., "Approximate Riemann solvers, parameter vectors and difference schemes," *Journal of Computational Physics*, Vol. 43, 1981, pp. 357–372.

[66] Osher, S. and Chakravarthy, S. R., "Upwind schemes and boundary conditions with applications to Euler equations in general geometries," *Journal of Computational Physics*, Vol. 50, 1983, pp. 447–481.

[67] Harten, A., "High resolution schemes for hyperbolic conservation laws," *Journal of Computational Physics*, Vol. 49, No. 3, 1983, pp. 357–393.

[68] Harten, A., Engquist, B., Osher, S., and Chakravarthy, S. R., "Uniformly high order accurate essentially non–oscillatory schemes, III," *Journal of Computational Physics*, Vol. 71, No. 2, 1987, pp. 231–303.

[69] Hafez, M. and Wahba, E., "Numerical simulations of transonic aerodynamic flows based on a hierarchical formulation," *Int. J. Numer. Meth. Fluids*, Vol. 47, 2005, pp. 491–516.

[70] Spalart, P. R., "Strategies for turbulence modelling and simulations," *Int. J. Heat Fluid Flow*, Vol. 21, 2000, pp. 252–263.

[71] Wilcox, D. C., *Turbulence modeling for CFD*, DCW Industries, Inc., La Cañada, CA, 3rd ed., 2006.

[72] Spalart, P. R., "Detached–eddy simulation," *Ann. Rev. Fluid Mech.*, Vol. 41, 2009, pp. 181–202.

[73] Badcock, K. J., Richards, B. E., and Woodgate, M. A., "Elements of computational fluid dynamics on block structured grids using implicit solvers," *Progress in Aerospace Sciences*, Vol. 36, 2000, pp. 351–392.

[74] Timme, S. and Badcock, K. J., "oFPfoil (v1.0) – User Guide," Tech. rep., Computational Fluid Dynamics Laboratory, University of Liverpool, Liverpool, United Kingdom, 2010, available at http://cfd4aircraft.com/4downloads.php.

[75] Schlichting, H. and Gersten, K., *Boundary–layer theory*, Springer–Verlag, Inc., Berlin, Germany, 8th ed. (rev. and enl.), 2000.

[76] Spalart, P. R. and Allmaras, S. R., "A one–equation turbulence model for aerodynamic flows," *AIAA Paper 92–0439*, 1992.

[77] Menter, F. R., "Zonal two equation $k-\omega$ turbulence models for aerodynamic flows," *AIAA Paper 93–2906*, 1993.

[78] Vinokur, M., "Conservation equations of gas dynamics in curvilinear coordinate systems," *Journal of Computational Physics*, Vol. 14, 1974, pp. 105–125.

[79] Viviand, H., "Conservative forms of gas dynamic equations," *Rech. Aerosp.*, Vol. 1, 1974, pp. 65–68.

[80] Steger, J. L., "Implicit finite–difference simulation of flow about arbitrary two–dimensional geometries," *AIAA Journal*, Vol. 16, No. 7, 1978, pp. 679–686.

[81] van Leer, B., "Towards the ultimative conservative difference scheme. V. a second–order sequel to Godunov's method," *Journal of Computational Physics*, Vol. 32, 1979, pp. 101–136.

[82] Thomas, P. D. and Lombard, C. K., "Geometric conservation law and its application to flow computations on moving grids," *AIAA Journal*, Vol. 17, No. 10, 1979, pp. 1030–1037.

[83] Jameson, A., "Time dependent calculations using multigrid with applications to unsteady flows past airfoils and wings," *AIAA Paper 91–1596*, 1991.

[84] Whitfield, D. L., "Analytical description of the complete turbulent boundary layer velocity profile," *AIAA Paper 78–1158*, 1978.

[85] Whitfield, D. L., Swafford, T. W., and Jacocks, J. L., "Calculation of turbulent boundary layers with separation and viscous–inviscid interaction," *AIAA Journal*, Vol. 19, No. 10, 1981, pp. 1315–1322.

[86] Swafford, T. W., "Analytical approximation of two–dimensional separated turbulent boundary layers," *AIAA Journal*, Vol. 21, No. 6, 1983, pp. 923–926.

[87] Drela, M., *Two–dimensional transonic aerodynamic design and analysis using the Euler equations*, Ph.D. thesis, Department of Aeronautics and Astronautics, Massachusetts Institute of Technology, 1985.

[88] Drela, M. and Giles, M. B., "Viscous–inviscid analysis of transonic and low Reynolds number airfoils," *AIAA Journal*, Vol. 25, No. 10, 1987, pp. 1347–1355.

[89] Bradshaw, P., Ferris, D. H., and Atwell, N. P., "Calculation of boundary–layer development using the turbulent energy equation," *Journal of Fluid Mechanics*, Vol. 28, No. 3, 1967, pp. 593–616.

[90] Bradshaw, P. and Ferris, D. H., "Calculation of boundary–layer development using the turbulent energy equation: compressible flow on adiabatic walls," *Journal of Fluid Mechanics*, Vol. 46, No. 1, 1971, pp. 83–110.

[91] Green, J. E., Weeks, D. J., and Brooman, J. W. F., "Prediction of turbulent boundary layers and wakes in compressible flow by a lag–entrainment method," Tech. Rep. R. & M. No. 3791, Aeronautical Research Council, 1977.

[92] Drela, M., "XFOIL: an analysis and design system for low Reynolds number airfoils," *Proceedings of the Conference on Low Reynolds Number Aerodynamics, Notre Dame, IN, USA, 5–7 June 1989*, 1989, pp. 1–12.

[93] Nishida, B. A., *Fully simultaneous coupling of the full potential equation and the integral boundary layer equations in three dimensions*, Ph.D. thesis, Department of Aeronautics and Astronautics, Massachusetts Institute of Technology, 1996.

[94] Batina, J. T., "Introduction of the ASP3D computer program for unsteady aerodynamic and aeroelastic analyses," Tech. Rep. TM–2005–213909, NASA Langley Research Center, Hampton, VA, 2005.

[95] Prandtl, L., "Über Flüssigkeitsbewegung bei sehr kleiner Reibung," *Proc. Third Intern. Math. Congr.*, 1904, Translated and Reprinted in NACA TM 452 (1928).

[96] White, F. M., *Viscous fluid flow*, McGraw–Hill, Inc., New York, NY, 3rd ed., 2006.

[97] Lighthill, M. J., "On displacement thickness," *Journal of Fluid Mechanics*, Vol. 4, 1958, pp. 383–392.

[98] Cebeci, T. and Bradshaw, P., *Momentum transfer in boundary layers*, Hemisphere Publishing Corporation, Washington, D. C., 1977.

[99] Davis, T. A., "UMFPACK Version 5.4.0 User Guide," Tech. Rep. TR–04–003 rev., Dept. of Computer and Information Science and Engineering, Univ. of Florida, Gainesville, FL, 2009.

[100] Barakos, G., Lawson, S. J., Steijl, R., and Nayyar, P., "Numerical simulations of high–speed turbulent cavity flow," *Flow Turbulence Combust*, Vol. 83, 2009, pp. 569–585.

[101] Steijl, R., Barakos, G., and Badcock, K., "A framework for CFD analysis of helicopter rotors in hover and forward flight," *Int. J. Numer. Meth. Fluids*, Vol. 51, 2006, pp. 819–847.

[102] Steijl, R. and Barakos, G., "Computational study of helicopter rotor–fuselage aerodynamic interactions," *AIAA Journal*, Vol. 47, No. 9, 2009, pp. 2143–2157.

[103] Boelens, O. J., Prananta, B. B., Soemarwoto, B. I., Allan, M. R., Badcock, K. J., and Fritz, W., "Towards an aero–servo–elastic simulation capability for high performance fighter aircraft," *RTO–MP–AVT–123, AVT Symposium on Flow–Induced Unsteady Loads and the Impact on Military Applications*, 2005.

[104] Badcock, K. J., "Evaluation of results from a Reynolds averaged multiblock code against F–16XL flight data," *AIAA Paper 2007–0490*, 2007.

[105] Liebeck, R. H. and Camacho, P. P., "Airfoil design at low Reynolds number with constrained pitching moment," *Proceedings of the Conference on Low Reynolds Number Aerodynamics, Notre Dame, IN, USA, 17–19 June 1985*, 1985, pp. 27–51.

[106] Cook, P. H., McDonald, M. A., and Firmin, M. C. P., "Aerofoil RAE 2822 – Pressure distributions, and boundary layer and wake measurements," Tech. Rep. AGARD AR 138, 1979.

[107] Landon, R. H., "NACA 0012. Oscillatory and transient pitching," Tech. Rep. AGARD–R–702, 1982.

[108] Howlett, J. T., "Calculation of unsteady transonic flows with mild separation by viscous–inviscid interaction," Tech. Rep. NASA–TP–3197, NASA Langley Research Center, Hampton, VA, 1992.

[109] Badcock, K. J. and Gaitonde, A. L., "An unfactored implicit moving mesh method for two–dimensional unsteady N–S equations," *Int. J. Numer. Meth. Fluids*, Vol. 23, 1996, pp. 607–631.

[110] Försching, H. and Hönlinger, H., "The expanding domain of aeroelastic simulation," *Euromech–Colloquium 349*, 1996, pp. 1–14.

[111] Golub, G. H. and van Loan, C. F., *Matrix computations*, John Hopkins University Press, Baltimore, MD, 3rd ed., 1996.

[112] Bekas, C. and Saad, Y., "Computation of smallest eigenvalues using spectral schur complements," *SIAM J. Sci. Comput.*, Vol. 27, No. 2, 2005, pp. 458–481.

[113] Oran Brigham, E., *The fast Fourier transform and its applications*, Prentice–Hall, Englewood Cliffs, NJ, 1988.

[114] Lindquist, D. R., *Computation of unsteady transonic flowfields using shock capturing and the linear perturbation Euler equations*, Ph.D. thesis, Department of Aeronautics and Astronautics, Massachusetts Institute of Technology, 1992.

[115] Giles, M. B., Duta, M. C., Müller, J.-D., and Pierce, N. A., "Algorithm development for discrete adjoint methods," *AIAA Journal*, Vol. 41, No. 2, 2003, pp. 198–205.

[116] Dwight, R. P. and Han, Z.-H., "Efficient uncertainty quantification using gradient–enhanced kriging," *AIAA 2009–2276*, 2009.

[117] McDevitt, J. B. and Okuno, A. F., "Static and dynamic pressure measurements on a NACA 0012 airfoil in the Ames high Reynolds number facility," Tech. Rep. NASA–TP–2485, Ames Research Center, Moffett Field, CA, 1985.

[118] Schwarz, J. B., Dowell, E. H., Thomas, J. P., Hall, K. J., Rausch, R. D., and Bartels, R. E., "Improved flutter boundary prediction for an isolated two–degree–of–freedom airfoil," *AIAA Journal*, Vol. 46, No. 6, 2009, pp. 2069–2076.

[119] Barakos, G. and Drikakis, D., "Numerical simulation of transonic buffet flows using various turbulence closures," *Int. J. Heat Fluid Flow*, Vol. 21, 2000, pp. 620–626.

[120] Raveh, D. E., "A numerical study of an oscillating airfoil in transonic buffeting flows," *AIAA Journal*, Vol. 47, No. 3, 2009, pp. 505–515.

[121] Sacks, J., Welch, W. J., Mitchell, T. J., and Wynn, H. P., "Design and analysis of computer experiments," *Statistical Science*, Vol. 4, No. 4, 1989, pp. 409–435.

[122] Jones, D. R., Schonlau, M., and Welch, W. J., "Efficient global optimization of expensive black–box functions," *Journal of Global Optimization*, Vol. 13, No. 4, 1998, pp. 455–492.

[123] Ghoreyshi, M., Badcock, K. J., and Woodgate, M. A., "Accelerating the numerical generation of aerodynamic models for flight simulation," *AIAA Journal*, Vol. 46, No. 3, 2009, pp. 972–980.

[124] Lophaven, S. N., Nielsen, H. B., and Sœndergaard, J., "DACE – A matlab kriging toolbox," Tech. Rep. IMM–TR–2002–12, Technical University of Denmark, Denmark, 2002.

[125] Welch, W. J., Buck, R. J., Sacks, J., Wynn, H. P., Mitchell, T. J., and Morris, M. D., "Screening, predicting, and computer experiments," *Technometrics*, Vol. 34, No. 1, 1992, pp. 15–25.

[126] Dwight, R. P., *Personal communication*, 2010.

[127] Martin, J. D., "Robust kriging models," *AIAA Paper 2010–2854*, 2010.

[128] Han, Z.-H., Grötz, S., and Zimmermann, R., "On improving efficiency and accuracy of variable–fidelity surrogate modeling in aero–data for loads context," *Proceedings of CEAS 2009 European Air and Space Conference*, 2009.

[129] Bakhle, M. A., Mahajan, A. J., Keith, , Jr., T. G., and Stefko, G. L., "Cascade flutter analysis with transient response aerodynamics," *Computers & Structures*, Vol. 41, No. 5, 1991, pp. 1073–1085.

[130] Silva, W. A., "Simultaneous excitation of multiple–input/multiple–output CFD–based unsteady aerodynamic systems," *Journal of Aircraft*, Vol. 45, No. 4, 2008, pp. 1267–1274.

[131] Raveh, D. E., "Identification of computational–fluid–dynamics based unsteady aerodynamic models for aeroelastic analysis," *Journal of Aircraft*, Vol. 41, No. 3, 2004, pp. 620–632.

[132] Hall, K. C., Thomas, J. P., and Dowell, E. H., "Proper orthogonal decomposition technique for transonic unsteady aerodynamic flows," *AIAA Journal*, Vol. 38, No. 10, 2000, pp. 1853–1862.

[133] Thomas, J. P., Dowell, E. H., and Hall, K. C., "Three–dimensional transonic aeroelasticity using proper orthogonal decomposition–based reduced–order models," *Journal of Aircraft*, Vol. 40, No. 3, 2003, pp. 544–551.

[134] Lieu, T., Farhat, C., and Lesoinne, M., "Reduced–order fluid/structure modeling of a complete aircraft configuration," *Comput. Methods Appl. Mech. Engrg.*, Vol. 195, 2006, pp. 5730–5742.

[135] Schmidt, R. and Glauser, M., "Improvements in low dimensional tools for flow–structure interaction problems: using global POD," *AIAA Paper 2004–0889*, 2004.

[136] Lieu, T. and Lesoinne, M., "Parameter adaptation of reduced order models for three–dimensional flutter analysis," *AIAA Paper 2004–0888*, 2004.

[137] Amsallem, D., Cortial, J., Carlberg, K., and Farhat, C., "A method for interpolating on manifolds structural dynamics reduced–order models," *Int. J. Numer. Meth. Engng.*, Vol. 80, 2009, pp. 1241–1258.

[138] Baker, M. L., Goggin, P. J., and Winther, B. A., "Aeroservoelastic modeling, analysis, and design techniques for transport aircraft," *RTO–MP–36, AVT Symposium on Structural Aspects of Flexible Aircraft Control, Ottawa, Canada, 18–20 October 1999*, 1999.

[139] Cowan, T. J., Arena, Jr., A. S., and Gupta, K. K., "Accelerating computational fluid dynamics based aeroelastic predictions using system identification," *Journal of Aircraft*, Vol. 38, No. 1, 2001, pp. 81–87.

[140] Isogai, K., "Transonic–dip mechanism of flutter of a sweptback wing: part II," *AIAA Journal*, Vol. 19, No. 9, 1981, pp. 1240–1242.

[141] Epureanu, B. I., Dowell, E. H., and Hall, K. C., "Reduced–order models of unsteady transonic viscous flows in turbomachinery," *Journal of Fluids and Structures*, Vol. 14, 2000, pp. 1215–1234.

[142] Hafez, M., South, J., and Murman, E., "Artificial compressibility methods for numerical solutions of transonic full potential equation," *Int. J. Numer. Meth. Fluids*, Vol. 17, No. 8, 1979, pp. 838–844.

[143] Holst, T. L. and Ballhaus, W. F., "Fast, conservative schemes for the full potential equation applied to transonic flows," *AIAA Journal*, Vol. 17, No. 2, 1979, pp. 145–152.

[144] Rodden, W. P. and Johnson, E. H., *MSC.Nastran aeroelastic analysis user's guide*, MSC.Software Corporation, Santa Ana, CA, 2004.

[145] Fung, Y. C., *An introduction to the theory of aeroelasticity*, John Wiley & Sons, Inc., New York, NY, 1955.

[146] Clebsch, A., "Über die Integration der hydrodynamischen Gleichungen," *J. Reine Angew. Math.*, Vol. 56, 1859, pp. 1–10.

[147] Westland, J. and Hounjet, M. H. L., "Clebsch variable model for unsteady, inviscid, transonic flow with strong shock waves," *AIAA Paper 93–3025*, 1993.

[148] Batina, J. T., "Unsteady transonic small–disturbance theory including entropy and vorticity effects," *AIAA Journal*, Vol. 26, No. 6, 1989, pp. 531–538.

[149] Wesseling, P., *Principles of computational fluid dynamics*, Springer–Verlag, Inc., Berlin, Germany, 2001.

[150] Goura, G. S. L., *Time marching analysis of flutter using computational fluid dynamics*, Ph.D. thesis, Department of Aerospace Engineering, University of Glasgow, Glasgow, United Kingdom, 2001.

[151] Beran, P. S., *Personal communication*, 2010.

[152] Badcock, K. J., Timme, S., and Marques, S., "Implementing the Schur complement eigenvalue formulation in the DLR TAU code," Tech. rep., Computational Fluid Dynamics Laboratory, University of Liverpool, Liverpool, United Kingdom, 2010.

[153] Bendiksen, O. O., "Transonic limit cycle flutter of high–aspect–ratio swept wings," *Journal of Aircraft*, Vol. 45, No. 5, 2008, pp. 1522–1533.

[154] Silva, W. A., "Recent enhancements to the development of CFD–based aeroelastic reduced–order models," *AIAA Paper 2007-2051*, 2007.

[155] Silva, W. A., Vatsa, V. N., and Biedron, R. T., "Development of unsteady aerodynamic and aeroelastic reduced–order models using the FUN3D code," *IFASD–2009–030*, 2009.

[156] McKay, M. D., Conover, W. J., and Beckman, R., "A comparison of three methods for selecting values of input variables in the analysis of output from a computer code," *Technometrics*, Vol. 21, No. 2, 1979, pp. 239–245.

[157] Bichon, B. J., Eldred, M. S., Swiler, L. P., Mahadevan, S., and McFarland, J. M., "Efficient global reliability analysis for nonlinear implicit performance functions," *AIAA Journal*, Vol. 46, No. 10, 2008, pp. 2459–2468.

[158] Prananta, B. B., Hounjet, M. H. L., and Zwaan, R. J., "Two–dimensional transonic aeroelastic analysis using thin–layer Navier–Stokes method," *Journal of Fluids and Structures*, Vol. 12, 1998, pp. 655–676.

[159] Yang, S., Zhang, Z., Liu, F., Luo, S., Tsai, H.-M., and Schuster, D. M., "Time–domain aeroelastic simulation by a coupled Euler and integral boundary–layer method," *AIAA Paper 2004–5377*, 2004.

[160] Sasena, M. J., Papalambros, P., and Goovaerts, P., "Exploration of metamodeling sampling criteria for constrained global optimization," *Engineering Optimization*, Vol. 34, No. 3, 2002, pp. 263–278.

[161] Swift, A. and Badcock, K. J., "Inter–grid transfer influence on transonic flutter predictions," *AIAA Paper 2010–3049*, 2010.

[162] Clauser, F. H., "Turbulent boundary layers in adverse pressure gradients," *Journal of Aeronautical Sciences*, Vol. 21, 1954, pp. 91–108.

[163] Swafford, T. W. and Whitfield, D. L., "Time–dependent solution of three–dimensional compressible turbulent integral boundary–layer equations," *AIAA Journal*, Vol. 23, No. 7, 1985, pp. 1005–1013.

[164] Neel, R. E., *Advances in computational fluid dynamics: turbulent separated flows and transonic potential flows*, Ph.D. thesis, Virginia Polytechnic Institute and State University, 1997.

[165] Barth, T. J. and Jespersen, D. C., "The design and application of upwind schemes on unstructured meshes," *AIAA Paper 89–0366*, 1989.

[166] Kuzmin, D., "A vertex–based hierarchical slope limiter for p–adaptive discontinuous Galerkin methods," *Journal of Computational and Applied Mathematics*, Vol. 233, No. 12, pp. 3077–3085.

[167] Veldmann, A. E. P., "Matched asymptotic expansions and the numerical treatment of viscous–inviscid interaction," *Journal of Engineering Mathematics*, Vol. 39, 2001, pp. 189–206.

[168] Goldstein, S., "On laminar boundary layer flow near a point of separation," *Quart. J. Mech. Appl. Math.*, Vol. 1, 1948, pp. 43–69.

[169] Veldman, A. E. P., "A numerical view on strong viscous–inviscid interactions," *Computational Methods in Viscous Flows*, edited by W. G. Habashi, Pineridge Press, Swansea, UK, 1984, pp. 343–363.

[170] Carter, J. E., "A new boundary–layer inviscid iteration technique for separated flow," *AIAA Paper 1979–1450*, 1979.

Appendix A

Integral Boundary Layer Model

The integral boundary layer model is presented in more detail. The unsteady integral equations governing the boundary layer flow are derived from the Prandtl boundary layer equations. Then, the closure relations for the additional unknowns of the integral model are given. Also, the blowing velocity model to apply the displacing effect of the boundary layer on the outer inviscid flow is derived from the continuity equation.

Governing Equations

In dimensionless notation, the Prandtl boundary layer equations in local streamwise and normal wall coordinates (ξ, η) are [75, 96],

$$\frac{\partial \varrho}{\partial t} + \frac{\partial \varrho u}{\partial \xi} + \frac{\partial \varrho v}{\partial \eta} = 0 \tag{A.1}$$

$$\varrho \frac{\partial u}{\partial t} + \varrho u \frac{\partial u}{\partial \xi} + \varrho v \frac{\partial u}{\partial \eta} + \frac{\partial p}{\partial \xi} = \frac{\partial \tau_{xy}}{\partial \eta} \tag{A.2}$$

where (u, v) are the streamwise and normal velocity components, and τ_{xy} is composed of laminar and turbulent contributions

$$\tau_{xy} = \frac{\mu}{Re} \frac{\partial u}{\partial \eta} - \varrho \overline{u'v'}, \tag{A.3}$$

with (u', v') as the velocity fluctuations. According to a first order approximation, the normal pressure gradient is neglected at a given streamwise location and the solid wall and wake curvature effects are omitted. The energy equation is dropped restricting the application to adiabatic flows [87].

Integral Momentum Equation

To derive the unsteady integral momentum equation, integrate the continuity equation given in Eq. (A.1) in wall normal direction η at an arbitrary streamwise location ξ and

time t assuming impermeable walls

$$\varrho v = -\int_0^\eta \frac{\partial \varrho}{\partial t}\, d\eta - \int_0^\eta \frac{\partial \varrho u}{\partial \xi}\, d\eta\,. \tag{A.4}$$

Combined with the latter expression, the streamwise momentum equation gives after integration from the wall outward to the freestream (denoted by δ as the thickness of the boundary layer), and reordered to separate the derivatives with respect to time and space,

$$\int_0^\delta \left[\varrho \frac{\partial u}{\partial t} - \varrho_e \frac{\partial u_e}{\partial t} - \frac{\partial u}{\partial \eta} \int_0^\eta \frac{\partial \varrho}{\partial t}\, d\eta + \varrho u \frac{\partial u}{\partial \xi} - \frac{\partial u}{\partial \eta} \int_0^\eta \frac{\partial \varrho u}{\partial \xi}\, d\eta - \varrho_e u_e \frac{\partial u_e}{\partial \xi} - \frac{\partial \tau_{xy}}{\partial \eta} \right] d\eta = 0\,. \tag{A.5}$$

Here, the pressure derivative is replaced by

$$-\frac{\partial p}{\partial \xi} = \varrho_e \frac{\partial u_e}{\partial t} + \varrho_e u_e \frac{\partial u_e}{\partial \xi}\,, \tag{A.6}$$

which follows from Eq. (A.2) applied at the edge of the boundary layer (denoted by the subscript e). Using the rule of integration by parts, the terms

$$\int_0^\delta \frac{\partial u}{\partial \eta} \left[\int_0^\eta \frac{\partial \varrho u}{\partial \xi}\, d\eta \right] d\eta = \int_0^\delta (u_e - u) \frac{\partial \varrho u}{\partial \xi}\, d\eta\,, \tag{A.7}$$

and

$$\int_0^\delta \frac{\partial u}{\partial \eta} \left[\int_0^\eta \frac{\partial \varrho}{\partial t}\, d\eta \right] d\eta = \int_0^\delta (u_e - u) \frac{\partial \varrho}{\partial t}\, d\eta\,, \tag{A.8}$$

are rewritten in a more convenient form simplifying Eq. (A.5). Rearranging gives,

$$\int_0^\delta \left[\frac{\partial}{\partial t}\left[\varrho_e u_e - \varrho u\right] - u_e \frac{\partial}{\partial t}\left[\varrho_e - \varrho\right] + \frac{\partial}{\partial \xi}\left[(u_e - u)\varrho u\right] + (\varrho_e u_e - \varrho u) \frac{\partial u_e}{\partial \xi} + \frac{\partial \tau_{xy}}{\partial \eta} \right] d\eta = 0. \tag{A.9}$$

Using the Leibniz integral rule for differentiation under the integral sign and introducing the compressible definitions for displacement thickness δ^*, momentum thickness θ and an auxiliary density thickness θ_ϱ,

$$\varrho_e u_e \delta^* = \int_0^\delta (\varrho_e u_e - \varrho u)\, d\eta, \qquad \varrho_e u_e^2 \theta = \int_0^\delta (u_e - u)\, \varrho u\, d\eta, \qquad \varrho_e \theta_\varrho = \int_0^\delta (\varrho_e - \varrho)\, d\eta, \tag{A.10}$$

give

$$\frac{\partial}{\partial t}\left[\varrho_e u_e \delta^*\right] - u_e \frac{\partial}{\partial t}\left[\varrho_e \theta_\varrho\right] + \frac{\partial}{\partial \xi}\left[\varrho_e u_e^2 \theta\right] + \varrho_e u_e \delta^* \frac{\partial u_e}{\partial \xi} - \tau_W = 0, \tag{A.11}$$

where τ_W is the wall shear–stress. The latter expression is rearranged and given in compact notation as

$$\frac{\partial \delta^*}{\partial t} - \frac{\partial \theta_\varrho}{\partial t} + \mathcal{T}_{\delta^*} = -u_e \mathcal{S}_{\delta^*}\,, \tag{A.12}$$

where the operators $\mathcal{S}_{\delta^*}$ and $\mathcal{T}_{\delta^*}$ are

$$\mathcal{S}_{\delta^*} = \frac{\partial \theta}{\partial \xi} + \left(H + 2 - M_e^2\right)\frac{\theta}{u_e}\frac{\partial u_e}{\partial \xi} - \frac{C_f}{2} \tag{A.13}$$

and

$$\mathcal{T}_{\delta^*} = H\frac{\theta}{u_e}\frac{\partial u_e}{\partial t} + \left(H - H_{\theta_\varrho}\right)\frac{\theta}{\varrho_e}\frac{\partial \varrho_e}{\partial t}, \tag{A.14}$$

respectively. The shape parameter H and the local skin friction coefficient C_f are defined as

$$H = \frac{\delta^*}{\theta} \tag{A.15}$$

and

$$C_f = \frac{2\tau_W}{\varrho_e u_e^2}\,. \tag{A.16}$$

In addition, in an adiabatic compressible freestream the relation

$$\frac{u_e}{\varrho_e}\frac{\partial \varrho_e}{\partial u_e} = -M_e^2 \tag{A.17}$$

is applied where M_e is the local Mach number at the edge of the boundary layer [96]. Also, $H_{\theta_\varrho} = \theta_\varrho/\theta$ is the auxiliary density shape factor. Interestingly, the operator $\mathcal{S}_{\delta^*}$ is the steady integral momentum equation in compressible notation as can be found standard literature. The operator $\mathcal{T}_{\delta^*}$ contains only derivatives of the inviscid edge solution with respect to time. Additionally, the second term in Eq. (A.12) is written as

$$\frac{\partial \theta_\varrho}{\partial t} = H_{\theta_\varrho}\frac{\partial \theta}{\partial t} + \theta\frac{\partial H_{\theta_\varrho}}{\partial t}. \tag{A.18}$$

The operator $\mathcal{T}_{\delta^*}$ as well as the last term of the latter expression can be broken down in dependencies on the primary unknowns of the boundary layer and the inviscid flow model with density and velocity potential.

Integral Mean Kinetic Energy Equation

Following the derivation of the integral momentum equation, Eqs. (A.4) and (A.6) are substituted into the streamwise momentum equation pre–multiplied by $2u$ and integrated from the wall outward to the freestream. Reordering to separate the derivatives

with respect to time and space gives

$$\int_0^\delta \left[2\varrho u \frac{\partial u}{\partial t} - 2\varrho_e u \frac{\partial u_e}{\partial t} - 2u \frac{\partial u}{\partial \eta} \int_0^\eta \frac{\partial \varrho}{\partial t}\, d\eta \right] d\eta$$
$$+ \int_0^\delta \left[2\varrho u^2 \frac{\partial u}{\partial \xi} - 2u \frac{\partial u}{\partial \eta} \int_0^\eta \frac{\partial \varrho u}{\partial \xi}\, d\eta - 2\varrho_e u_e u \frac{\partial u_e}{\partial \xi} - 2u \frac{\partial \tau}{\partial \eta} \right] d\eta = 0\,. \quad \text{(A.19)}$$

The last term in the latter equation is integrated using the rule of integration by parts to get the dissipation integral $\mathcal{D}$

$$-2\int_0^\delta u \frac{\partial \tau}{\partial \eta}\, d\eta = 2\int_0^\delta \tau \frac{\partial u}{\partial \eta}\, d\eta = 2\mathcal{D}\,. \quad \text{(A.20)}$$

The terms

$$\int_0^\delta 2u \frac{\partial u}{\partial \eta} \left[\int_0^\eta \frac{\partial \varrho u}{\partial \xi}\, d\eta \right] d\eta = \int_0^\delta \left(u_e^2 - u^2\right) \frac{\partial \varrho u}{\partial \xi}\, d\eta\,, \quad \text{(A.21)}$$

and

$$\int_0^\delta 2u \frac{\partial u}{\partial \eta} \left[\int_0^\eta \frac{\partial \varrho}{\partial t}\, d\eta \right] d\eta = \int_0^\delta \left(u_e^2 - u^2\right) \frac{\partial \varrho}{\partial t}\, d\eta\,, \quad \text{(A.22)}$$

are rewritten in a more convenient form similar to the derivation of the integral momentum equation. Rearranging gives,

$$\int_0^\delta \left[\frac{\partial}{\partial t}\left[\left(u_e - u\right) \varrho u \right] + \frac{\partial}{\partial t}\left[u_e \left(\varrho_e u_e - \varrho u\right) \right] - \frac{\partial}{\partial t}\left[u_e^2 \left(\varrho_e - \varrho\right) \right] \right] d\eta$$
$$+ \int_0^\delta \left[2u_e \left(\varrho_e - \varrho\right) \frac{\partial u_e}{\partial t} - 2\varrho_e \left(u_e - u\right) \frac{\partial u_e}{\partial t} \right] d\eta$$
$$+ \int_0^\delta \left[\frac{\partial}{\partial \xi}\left[(u_e^2 - u^2) \varrho u \right] + 2(\varrho_e - \varrho) u u_e \frac{\partial u_e}{\partial \xi} \right] d\eta - 2\mathcal{D} = 0\,. \quad \text{(A.23)}$$

In addition to the expressions in Eq. (A.10), the definitions of kinetic energy thickness θ^*, density thickness δ^{**} and a sixth integral thickness δ_u^* solely related to the velocity,

$$\varrho_e u_e^3 \theta^* = \int_0^\delta \left(u_e^2 - u^2\right) \varrho u\, d\eta, \qquad \varrho_e u_e \delta^{**} = \int_0^\delta \left(\varrho_e - \varrho\right) u\, d\eta, \qquad u_e \delta_u^* = \int_0^\delta \left(u_e - u\right)\, d\eta, \quad \text{(A.24)}$$

are introduced. Applying the Leibniz integral rule to Eq. (A.23) gives

$$\frac{\partial}{\partial t}\left[\varrho_e u_e^2 \theta\right] + \frac{\partial}{\partial t}\left[\varrho_e u_e^2 \delta^*\right] - \frac{\partial}{\partial t}\left[\varrho_e u_e^2 \theta_\varrho\right] + 2\varrho_e u_e \theta_\varrho \frac{\partial u_e}{\partial t} - 2\varrho_e u_e \delta_u^* \frac{\partial u_e}{\partial t} + \frac{\partial}{\partial \xi}\left[\varrho_e u_e^3 \theta^*\right] + 2\varrho_e u_e^2 \delta^{**} \frac{\partial u_e}{\partial \xi} - 2\mathcal{D} = 0\,. \quad \text{(A.25)}$$

Using $\delta^{**} = \delta^* - \delta_u^*$, the latter equation is formulated in compact notation as

$$\frac{\partial \theta}{\partial t} + \mathcal{T}_\theta = -u_e \left(\mathcal{S}_\theta - \mathcal{S}_{\delta^*}\right)\,, \quad \text{(A.26)}$$

where the operators $\mathcal{S}_\theta$ and $\mathcal{T}_\theta$ are

$$\mathcal{S}_\theta = \theta \frac{\partial H^*}{\partial \xi} + H^* \frac{\partial \theta}{\partial \xi} + \left(2H^{**} + H^*\left(3 - M_e^2\right)\right) \frac{\theta}{u_e} \frac{\partial u_e}{\partial \xi} - 2C_D \quad \text{(A.27)}$$

and

$$\mathcal{T}_\theta = \left(2 + 2H^{**} - H\right) \frac{\theta}{u_e} \frac{\partial u_e}{\partial t} + \frac{\theta}{\varrho_e} \frac{\partial \varrho_e}{\partial t} \quad \text{(A.28)}$$

respectively. Also, the integral momentum equation given in Eq. (A.12) is applied. The kinetic energy shape parameter H^*, the density thickness shape parameter H^{**} and the dissipation coefficient C_D are defined as

$$H^* = \frac{\theta^*}{\theta}\,, \quad \text{(A.29)}$$

$$H^{**} = \frac{\delta^{**}}{\theta} \quad \text{(A.30)}$$

and

$$C_D = \frac{\mathcal{D}}{\varrho_e u_e^3}\,. \quad \text{(A.31)}$$

The operator $\mathcal{S}_\theta$ is the steady integral mean kinetic energy equation in compressible notation as can be found standard literature. The operator $\mathcal{T}_\theta$ contains the temporal derivatives of the inviscid edge solution and is broken down in dependencies on the primary unknowns.

Stress Transport Equation

The stress transport equation in the boundary layer model used to account for history effects in nonequilibrium turbulent boundary layer flows is a simplified adaptation of the "lag" equation introduced in [91]. This equation is derived from the transport equation for the turbulence kinetic energy k with appropriate thin–layer assumptions for two dimensional flow [75, 96],

$$u \frac{\partial k}{\partial \xi} + v \frac{\partial k}{\partial \eta} \approx \left(-\overline{u'v'}\right) \frac{\partial u}{\partial \eta} - \varepsilon - \frac{\partial \mathcal{D}}{\partial \eta}\,, \quad \text{(A.32)}$$

where the first term on the right–hand side denotes production, ε is dissipation and $\mathcal{D}$ is diffusion. Following [89, 90] a stress–transport equation of the form,

$$\frac{u}{2a_1}\frac{\partial(-\overline{u'v'})}{\partial\xi} + \frac{v}{2a_1}\frac{\partial(-\overline{u'v'})}{\partial\eta} = (-\overline{u'v'})\frac{\partial u}{\partial\eta} - \varepsilon - \frac{\partial\mathcal{D}}{\partial\eta} \tag{A.33}$$

is introduced by relating the turbulence kinetic energy and the Reynolds stress as proportional with $2a_1$ as constant factor of proportionality. In addition, the dissipation term is written as

$$\varepsilon = \frac{a_2}{L}(-\overline{u'v'})^{1.5} \tag{A.34}$$

where the factor a_2 is used to account for an increased dissipation length L in the free wake. The factor is set to unity on solid walls. In [91] the point of maximum Reynolds stress, $(-\overline{u'v'})_{\max}$, is considered to be appropriate to model the Reynolds stress level of the entire boundary layer. The shear–stress coefficient C_τ as nondimensional represention of the maximum Reynolds stress is introduced,

$$u_e^2 C_\tau = (-\overline{u'v'})_{\max}\,, \tag{A.35}$$

and the dissipation length scale L is assumed to be equivalent to the conventional mixing length l_{mix} for equilibrium flows at the point of the maximum Reynolds stress. Taking the definition of the conventional mixing length with $l_{\text{mix}} = L$ shows,

$$\begin{aligned} L\frac{\partial u}{\partial\eta} &= (-\overline{u'v'})^{0.5}_{\max} \\ &= u_e C^{0.5}_{\tau_{eq}}, \end{aligned} \tag{A.36}$$

where the subscript eq denotes equilibrium conditions. Substituting Eqs. (A.35) and (A.36) into Eq. (A.33) applied at maximum Reynolds stress, while neglecting normal convection, gives after some rearrangement,

$$\frac{\delta}{C_\tau}\frac{\partial C_\tau}{\partial\xi} = K_c\left(C^{0.5}_{\tau_{eq}} - a_2 C^{0.5}_\tau\right) - \frac{2a_1}{uu_e^2}\frac{\delta}{C_\tau}\frac{\partial\mathcal{D}}{\partial\eta} - 2\frac{\delta}{u_e}\frac{\partial u_e}{\partial\xi}\,. \tag{A.37}$$

The diffusion term is set by considering the condition that in equilibrium flows the right–hand side should be equal to zero. Using the relation

$$\frac{\partial C_\tau}{\partial\xi} = 2C^{0.5}_\tau\frac{\partial C^{0.5}_\tau}{\partial\xi} \tag{A.38}$$

applied to Eq. (A.37) results in

$$\frac{2\delta}{C^{0.5}_\tau}\frac{\partial C^{0.5}_\tau}{\partial\xi} = K_c\left(C^{0.5}_{\tau_{eq}} - a_2 C^{0.5}_\tau\right) + 2\delta\left(\left(\frac{1}{u_e}\frac{\partial u_e}{\partial\xi}\right)_{eq} - \frac{1}{u_e}\frac{\partial u_e}{\partial\xi}\right). \tag{A.39}$$

The additional unknowns, i.e. the boundary layer thickness δ, the equilibrium shear–stress coefficient $C_{\tau_{eq}}$ and the equilibrium velocity gradient $\left((1/u_e)(\partial u_e/\partial\xi)\right)_{eq}$, are modelled following [87]. The factor K_c given by

$$K_c = 2a_1 \frac{u_e}{u} \frac{\delta}{L} \tag{A.40}$$

is set to $K_c = 5.6$ following [91].

To derive the time–dependent form of the stress transport equation, the turbulence kinetic energy equation given in Eq. (A.32) is simply written in its unsteady formulation,

$$\frac{\partial k}{\partial t} + u\frac{\partial k}{\partial \xi} + v\frac{\partial k}{\partial \eta} \approx (-\overline{u'v'})\frac{\partial u}{\partial \eta} - \varepsilon - \frac{\partial \mathcal{D}}{\partial \eta}. \tag{A.41}$$

Proceeding with the derivation as done before gives

$$\begin{aligned} &\frac{\partial C_\tau^{0.5}}{\partial t} + \frac{C_\tau^{0.5}}{u_e}\frac{\partial u_e}{\partial t} \\ &+ u\left\{\frac{\partial C_\tau^{0.5}}{\partial \xi} - K_c\frac{C_\tau^{0.5}}{2\delta}\left(C_{\tau_{eq}}^{0.5} - a_2 C_\tau^{0.5}\right) - C_\tau^{0.5}\left(\left(\frac{1}{u_e}\frac{\partial u_e}{\partial \xi}\right)_{eq} - \frac{1}{u_e}\frac{\partial u_e}{\partial \xi}\right)\right\} = 0. \end{aligned} \tag{A.42}$$

In compact form write

$$\frac{\partial C_\tau^{0.5}}{\partial t} + \mathcal{T}_{C_\tau^{0.5}} = -u_e \mathcal{S}_{C_\tau^{0.5}} \tag{A.43}$$

following the notation of the integral equations for momentum and mean kinetic energy. Here, the spatial operator $\mathcal{S}_{C_\tau^{0.5}}$ is,

$$\mathcal{S}_{C_\tau^{0.5}} = \frac{u}{u_e}\left\{\frac{\partial C_\tau^{0.5}}{\partial \xi} - K_c\frac{C_\tau^{0.5}}{2\delta}\left(C_{\tau_{eq}}^{0.5} - a_2 C_\tau^{0.5}\right) - C_\tau^{0.5}\left(\left(\frac{1}{u_e}\frac{\partial u_e}{\partial \xi}\right)_{eq} - \frac{1}{u_e}\frac{\partial u_e}{\partial \xi}\right)\right\}, \tag{A.44}$$

where the expression in brackets clearly corresponds to the steady stress transport equation as defined in Eq. (A.39). The factor u_e/u is set to 1.5 as given in [91]. According to the integral momentum and mean kinetic energy equations, the temporal operator $\mathcal{T}_{C_\tau^{0.5}}$ of the inviscid edge solution is broken down in primary dependencies on the velocity potential.

Empirical Closure Relations

The primary unknowns of the boundary layer model are chosen to be the displacement thickness δ^*, the momentum thickness θ and, in the turbulent part of the boundary layer, the maximum shear–stress coefficient $C_\tau^{0.5}$. The quantities at the edge of the boundary layer (taken at the solid wall in a first order boundary layer approximation) are given by the outer inviscid solution and are not considered as additional boundary layer unknowns. Thus, closure of the system requires representing the additional un-

knowns in the integral system in terms of the primary unknowns, in which the inviscid solution is given by the momentum thickness Reynolds number Re_θ and the local edge Mach number M_e.

The momentum thickness Reynolds number Re_θ is defined in dimensionless notation as

$$Re_\theta = \frac{\varrho_e u_e \theta}{\mu_e} Re. \tag{A.45}$$

Combining the equation of state in Eq. (2.4) and the standard expression for isentropic flows in Eq. (2.20), the temperature is written as a function of density only, $T_e = \varrho_e^{\gamma-1}$. Using the power law relation for the dynamic viscosity $\mu_e = T_e^{\Omega}$, with $\Omega = 2/3$ as the constant of the power law for air, the momentum thickness Reynolds number is expressed as,

$$Re_\theta = \varrho_e^{(5-2\gamma)/3}\, u_e\, \theta\, Re, \tag{A.46}$$

where Re is the chord Reynolds number based on reference freestream values.

The local Mach number at the edge of the boundary layer is defined as

$$M_e^2 = \frac{u_e^2}{a_e^2} = \frac{u_e^2}{\varrho_e^{\gamma-1}} M_r^2\,, \tag{A.47}$$

where the definition of the speed of sound, $a = \sqrt{\varrho^{\gamma-1}/M_r^2}$, is applied to express the local edge Mach number as a function of the velocity, i.e. the velocity potential $\boldsymbol{q} = \nabla\Phi$, and density only.

The closure relations for the additional boundary layer unknowns follow the detailed discussion in [87]. Herein, only an overview is provided for completeness.

The kinematic shape parameter H_k was given in [84] as,

$$H_k = \frac{H - 0.290\, M_e^2}{1 + 0.113\, M_e^2}, \tag{A.48}$$

where the shape parameter $H = \delta^*/\theta$ is defined in Eq. (A.15). In [84] this expression was derived as a curve–fit for numerical evaluations of an analytical velocity profile given in [84, 86]. The kinematic shape parameter is defined with the density taken constant across the boundary layer, and all the correlations are expressed in terms of this parameter. Thus, the boundary layer correlations depend on the velocity profile only and not the density profile [88].

The density thickness shape parameter H^{**} follows [84],

$$H^{**} = \left(\frac{0.064}{H_k - 0.8} + 0.251\right) M_e^2, \tag{A.49}$$

and is used for both laminar and turbulent boundary layers. It is negligible for subsonic flow and only has a small influence in transonic flow.

The kinetic energy shape parameter H^* was derived in [88]. The laminar formulation is written as,

$$H^* = 0.0111\,\frac{(H_k-4.35)^2}{H_k+1} - 0.0278\,\frac{(H_k-4.35)^3}{H_k+1} - 0.0002\,(H_k-4.35)^2\,H_k^2 + 1.528 \qquad (H_k < 4.35)$$
$$H^* = 0.015\,\frac{(H_k-4.35)^2}{H_k} + 1.528 \qquad (H_k \geq 4.35) \tag{A.50}$$

and was derived as a curve–fit to match finite difference solutions of the Falkner–Skan one–parameter profile family to represent all flows of interest.

The corresponding turbulent formulation is expressed as,

$$H_k^* = \left(0.5 - \frac{4}{Re_\theta}\right)\left(\frac{H_0-H_k}{H_0-1}\right)^2 \frac{1.5}{H_k+0.5} + 1.5 + \frac{4}{Re_\theta}, \qquad (H_k < H_0)$$
$$H_k^* = (H_k-H_0)^2\left(\frac{0.007\,\ln(Re_\theta)}{(H_k-H_0+4/\ln(Re_\theta))^2} + \frac{0.015}{H_k}\right) + 1.5 + \frac{4}{Re_\theta}, \quad (H_k \geq H_0), \tag{A.51}$$

and was obtained in [87] following trial and error to provide a curve–fit for numerical solutions using an analytical velocity profile. Here, the parameter H_0 defines the onset of separation,

$$H_0 = \min\left(3 + \frac{400}{Re_\theta}, 4\right). \tag{A.52}$$

These expressions are based on a two–parameter family of turbulent velocity profiles, which is composed of two overlapping asymptotic solutions for the inner and outer layers of the boundary layer, in combination with the turbulent skin friction formula given hereafter [84, 86]. The additional minor compressibility correction,

$$H^* = \frac{H_k^* + 0.028\,M_e^2}{1 + 0.014\,M_e^2}, \tag{A.53}$$

follows the expression given in [84].

The laminar skin friction coefficient C_f is based, like the laminar kinetic energy shape parameter H^* and the laminar dissipation coefficient C_D, on the one–parameter profile family of Falkner and Skan [87],

$$Re_\theta\,C_f = 0.0727\,\frac{(5.5-H_k)^3}{H_k+1} - 0.07 \qquad (H_k < 5.5)$$
$$Re_\theta\,C_f = 0.015\left(1 - \frac{1}{H_k-4.5}\right)^2 - 0.07 \qquad (H_k \geq 5.5). \tag{A.54}$$

For turbulent flows the skin friction coefficient is

$$F_c\, C_f = \frac{0.3\, e^{-1.33 H_k}}{\left(\log_{10}\left(Re_\theta / F_c\right)\right)^{1.74+0.31 H_k}} + 1.1 \times 10^{-4}\left(\tanh\left(4 - \frac{H_k}{0.875}\right) - 1\right), \quad \text{(A.55)}$$

where

$$F_c = \sqrt{1 + \frac{\gamma - 1}{2} M_e^2}. \quad \text{(A.56)}$$

This expression was given in [86]. The first term describes the attached region and follows the expression used in [96], while the second term provides estimates for separated flow based on a correlation with a (small) set of experimental data. This formulation was found to be convenient as one smooth functional expression is used for the skin friction which allows the evaluation of both attached and separated velocity profiles required for numerical solutions to fit the kinetic energy shape parameter.

The laminar dissipation coefficient C_D follows the curve–fit for solutions of the Falkner–Skan profile family and is written as

$$\begin{aligned} \frac{2}{H^*} C_D &= \frac{1}{Re_\theta}\left(0.207 + 0.00205\left(4 - H_k\right)^{5.5}\right) && (H_k < 4) \\ \frac{2}{H^*} C_D &= \frac{1}{Re_\theta}\left(0.207 - 0.0016\, \frac{\left(H_k - 4\right)^2}{1 + 0.02\left(H_k - 4\right)^2}\right) && (H_k \geq 4), \end{aligned} \quad \text{(A.57)}$$

whereas the turbulent closure formulation is based on the equilibrium boundary layer concept.

Following [162] a class of turbulent boundary layers was experimentally shown to be similar when a pressure gradient parameter was constant. In [87] these equilibrium flows, having constant velocity and shear–stress profiles in the streamwise direction, were the basis to derive an expression for the dissipation coefficient. Here, the dissipation coefficient is expressed as the sum of a turbulent wall layer contribution, a turbulent wake layer contribution, and a (small) laminar stress contribution,

$$C_D = \frac{C_f}{2} U_s + C_\tau\left(0.995 - U_s\right) + \frac{0.15}{Re_\theta}\left(0.995 - U_s\right)^2, \quad \text{(A.58)}$$

each contribution of which is composed of a shear–stress and a velocity scale. The second term accounts for upstream history effects on the Reynolds stresses through the shear–stress coefficient $C_\tau^{0.5}$, which is governed by the transport equation as given in Eq. (2.29), while the wall layer, quickly adapting to flow changes, is independent of such history effect following the idea of the universal law of the wall [87].

The equivalent normalised wall slip velocity U_s modelled by,

$$U_s = \frac{H^*}{2}\left(1 - \frac{4}{3}\frac{H_k - 1}{H}\right), \quad \text{(A.59)}$$

and the equilibrium shear–stress coefficient $C_{\tau_{eq}}$ given by,

$$C_{\tau_{eq}} = H^* \frac{0.015}{1 - U_s} \frac{(H_k - 1)^3}{H H_k^2}, \tag{A.60}$$

were also derived from the equilibrium boundary layer approach [87]. The equilibrium velocity gradient $\left((1/u_e)(\partial u_e/\partial \xi)\right)_{eq}$ was given in [92] as

$$\left(\frac{1}{u_e}\frac{\partial u_e}{\partial \xi}\right)_{eq} = \frac{4}{3\delta^*}\left(\frac{C_f}{2} - \left(\frac{H_k - 1}{6.7 a_2 H_k}\right)^2\right), \tag{A.61}$$

where the factor a_2 is used to account for an increased dissipation length in a free wake. The estimated boundary layer thickness δ was taken from [91],

$$\delta = \left(3.15 + \frac{1.72}{H_k - 1}\right)\theta + \delta^*. \tag{A.62}$$

Finally, a relation for the auxiliary density shape factor H_{θ_ϱ} given by,

$$H_{\theta_\varrho} = (0.185 H_k + 0.150)\, M_e^2, \tag{A.63}$$

was offered in [163].

All closure relations are applied to free wakes setting the skin friction coefficient to zero, which was justified on the ground that the wake layer of a boundary layer is similar to a free wake (hence the name). The detailed discussion of this point can be found in [87].

To form the exact Jacobian matrix terms of the boundary layer model, used for both the Newton approach to converge the flow solution and the eigenvalue solver for the stability analysis, the closure correlations are differentiated analytically with respect to the boundary layer unknowns of displacement thickness δ^*, momentum thickness θ, and shear–stress coefficient $C_\tau^{0.5}$. Also, the derivatives with respect to the inviscid edge solution, represented by the momentum thickness Reynolds number Re_θ and the local edge Mach number M_e, are required. The differentiation with respect to the density ϱ and the velocity potential Φ is straightforward using the definitions provided in Eqs. (A.46) and (A.47).

Blowing Velocity Model

The primary effect of the boundary layer on the outer potential flow is the displacing effect. Two basic approaches are generally used to model this effect, i.e. the effective "displacement body" model and the "transpiration velocity" (wall blowing) model. These two coupling concepts are derived from conservation of mass by comparing a real viscous flow with an equivalent fictitious flow.

Consider an actual flow with a density $\varrho(\xi,\eta,t)$ and a streamwise velocity component $u(\xi,\eta,t)$ inside the boundary layer. Assuming an impermeable wall with no–slip condition, the wall normal velocity component $v_e = v(\xi,\eta_e,t)$ at the edge of the boundary layer $\eta_e = \delta$ is calculated from the continuity equation,

$$\begin{aligned}
(v_e)_{\text{real}} &= -\frac{1}{\varrho_e}\left(\int_0^\delta \frac{\partial \varrho u}{\partial \xi}\,d\eta + \int_0^\delta \frac{\partial \varrho}{\partial t}\,d\eta\right) \\
&= \frac{1}{\varrho_e}\left(\int_0^\delta \frac{\partial}{\partial \xi}\left[\varrho_e u_e - \varrho u\right]d\eta - \int_0^\delta \frac{\partial}{\partial \xi}\left[\varrho_e u_e\right]d\eta + \int_0^\delta \frac{\partial}{\partial t}\left[\varrho_e - \varrho\right]d\eta - \int_0^\delta \frac{\partial \varrho_e}{\partial t}\,d\eta\right) \\
&= \frac{1}{\varrho_e}\frac{\partial}{\partial \xi}\left[\varrho_e u_e \delta^*\right] - \frac{\delta}{\varrho_e}\frac{\partial}{\partial \xi}\left[\varrho_e u_e\right] + \frac{1}{\varrho_e}\frac{\partial}{\partial t}\left[\varrho_e \theta_\varrho\right] - \frac{\delta}{\varrho_e}\frac{\partial \varrho_e}{\partial t},
\end{aligned} \tag{A.64}$$

with displacement thickness δ^* and auxiliary density thickness θ_ϱ.

Now, consider the transpiration velocity model, proposed in [97] as the "equivalent source" concept and referred to in this report as blowing velocity concept to avoid confusion with the transpiration boundary condition. Assume a fictitious flow with wall blowing velocity v_b. Inside the boundary layer, the density $\varrho(\xi,t) = \varrho_e(\xi,\eta_e,t)$ and the streamwise velocity component $u(\xi,t) = u_e(\xi,\eta_e,t)$ are only dependent on the streamwise location and moment in time. Then, the wall normal edge velocity is calculated as follows,

$$\begin{aligned}
(v_e)_{\text{fict}} &= v_b - \frac{1}{\varrho_e}\left(\int_0^\delta \frac{\partial \varrho u}{\partial \xi}\,d\eta + \int_0^\delta \frac{\partial \varrho}{\partial t}\,d\eta\right) \\
&= v_b - \frac{1}{\varrho_e}\left(\int_0^\delta \frac{\partial}{\partial \xi}\left[\varrho_e u_e\right]d\eta + \int_0^\delta \frac{\partial \varrho_e}{\partial t}\,d\eta\right) \\
&= v_b - \frac{\delta}{\varrho_e}\frac{\partial}{\partial \xi}\left[\varrho_e u_e\right] - \frac{\delta}{\varrho_e}\frac{\partial \varrho_e}{\partial t}
\end{aligned} \tag{A.65}$$

Comparing the wall normal edge velocities of actual and fictitious flows gives the desired relation for the wall blowing velocity,

$$v_b = \frac{1}{\varrho_e}\frac{\partial}{\partial \xi}\left[\varrho_e u_e \delta^*\right] + \frac{1}{\varrho_e}\frac{\partial}{\partial t}\left[\varrho_e \theta_\varrho\right]. \tag{A.66}$$

Only the first term on the right–hand side is kept for convenience.

Appendix B

Full Potential Flow Solver

The unsteady full potential equations are discretised using a two dimensional, unstructured triangular, finite–volume scheme. The unknowns ϱ and Φ are stored at the vertices while fluxes are evaluated at the edges of the dual cells formed around the vertices and defining the non–overlapping control volumes. An edge of a dual cell is defined as the line connecting the centres of neighbouring triangles adjacent to the considered vertex. Centres of triangles are equivalent to dual cell vertices.

Write the continuity equation defined in Eq. (2.16) for constant domains V with nonmoving boundaries ∂V as

$$\frac{d\varrho}{dt} = -\frac{1}{V}\int_{\partial V} \varrho \nabla\Phi \cdot \boldsymbol{n}\, dS \tag{B.1}$$

For each control volume (dual cell) k, the latter equation is approximated in two dimensions by a second order spatial scheme as

$$\frac{d\varrho_k}{dt} = \left(\mathcal{R}_\varrho\right)_k = -\frac{1}{V_k}\sum_{j=1}^{J} \left(\varrho_j \nabla\Phi_j \cdot \boldsymbol{n}_j\right)\Delta S_j \tag{B.2}$$

where $\boldsymbol{n}_j$ is the outward unit normal vector and ΔS_j is the length of the jth edge of the kth dual cell built from J edges. The expression inside brackets is the flux through the jth edge. The right–hand side $\left(\mathcal{R}_\varrho\right)_k$ is referred to as residual of the continuity equation. The velocity vector $\nabla\Phi_j$ and the density ϱ_j have to be evaluated at the dual edge centres. The velocity vector is approximated by an edge–based reconstruction from Φ at the four vertices of the two neighbouring triangles connected by the jth dual cell edge. The density is evaluated by a vertex–based, slope–limited upwind scheme using the values of ϱ at the upwind vertex and all its surrounding first neighbours.

Generally for ease of use on unstructured meshes, a reconstruction stencil can consist of an arbitrary number of vertices. Then, an unweighted least squares reconstruction, details of which are discussed in [164], is used to calculate a piecewise linear polynomial

of the form

$$\Phi(\Delta \boldsymbol{x}) = C_0 + C_1\,\Delta x + C_2\,\Delta y \tag{B.3}$$

by solving a linear least squares problem for the three unknowns C_n. Here, $\Delta \boldsymbol{x}$ is the distance between the reconstruction point and the point of interest, and the coefficients C_1 and C_2 are the Cartesian velocity components $\nabla\Phi = [u_1, u_2]^T$ for the reconstruction of Φ. Using the latter equation, the quantity Φ can be evaluated at any location in the vicinity of the reconstruction point of the polynomial. A linear system

$$(a)_{nm}\,C_n = b_n \tag{B.4}$$

is formed by applying the constrained equation to all vertices in the stencil and minimising the sum of the squared errors. Inverting the matrix $(a)_{nm}$ gives the coefficients, for instance,

$$u_1 = C_1 = a'_{21}\,b_1 + a'_{22}\,b_2 + a'_{23}\,b_3, \tag{B.5}$$

where $(a)'_{nm}$ denotes the inverse. Here, the right–hand side b_n depends on both the geometric values $\Delta \boldsymbol{x}$ and the values of Φ in the stencil. Importantly, the matrix $(a)_{nm}$ for the reconstruction only depends on geometric values, and in combination with the employed transpiration boundary condition, discussed hereafter, it is inverted and stored for each reconstruction on the computational grid as a preprocessing step. Weighting the formulation is not required since only first neighbours of a reconstruction location are included in a stencil.

The dependence of the computed coefficients on the ith value of Φ in the stencil is calculated analytically by writing

$$\frac{\partial u_1}{\partial \Phi_i} = \frac{\partial C_1}{\partial \Phi_i} = a'_{21} + a'_{22}\,\Delta x_i + a'_{23}\,\Delta y_i, \tag{B.6}$$

and accordingly for C_2. This step is required to form the Jacobian matrix as an essential part of the methods discussed herein. Thus, for the Jacobian matrix contribution of the jth edge to the kth dual cell write

$$\frac{\partial \left(\mathcal{R}_\varrho\right)_k}{\partial \Phi_{ji}} = -\varrho_j \frac{\Delta S_j}{V_k}\left(\frac{\partial u_{1j}}{\partial \Phi_{ji}}\,n_{xj} + \frac{\partial u_{2j}}{\partial \Phi_{ji}}\,n_{yj}\right), \tag{B.7}$$

where i runs over all elements of the stencil to dull cell edge j. Each individual contribution is added to the Jacobian matrix.

Using an equivalent least squares reconstruction for the density, the coefficients C_1 and C_2 constitute the components of the density gradient $\nabla\varrho = [\varrho_x, \varrho_y]^T$. Then, the density at the jth dual cell edge centre is formed by an upwind formulation,

$$\varrho_j = \varrho_j^{\mathrm{up}} + \psi_j^{\mathrm{up}}\left(\nabla\varrho_j^{\mathrm{up}} \cdot \Delta \boldsymbol{x}_j\right), \tag{B.8}$$

where ϱ_j^{up} and $\nabla\varrho_j^{\mathrm{up}}$ are the density and its reconstructed gradient at the upwind vertex to edge j, and $\Delta\boldsymbol{x}_j$ is the distance from the upwind vertex to edge centre j. The applied density upwind scheme was found to be essential in obtaining a stable eigenvalue spectrum of the system Jacobian matrix in the current formulation. To prevent spurious oscillations around shock waves, a slope limiter is used to reduce the spatial scheme to first order where necessary. The slope limiter ψ_j^{up} at the upwind vertex is based on a modification of the original Barth–Jespersen slope limiter [165] by applying the finite–element formulation discussed in [166] to a dual cell.

In general, the idea behind a limiter is to bound the reconstructed function between extreme values. In particular, local extrema for a linear reconstruction based at the dual cell centre are found at the dual cell vertices. For an arbitrary dual cell k, let $\varrho_l = \varrho_k + \nabla\varrho_k \cdot \Delta\boldsymbol{x}_l$ be the unbounded reconstructed value at the lth dual cell vertex, and $\Delta_2 = \varrho_l - \varrho_k$. Then, the limiter is written as

$$\psi_k = \min_l \begin{cases} \min\left(1, \Delta_{\max}/\Delta_2\right), & \text{if } \Delta_2 > 0 \\ 1, & \text{if } \Delta_2 = 0 \\ \min\left(1, \Delta_{\min}/\Delta_2\right), & \text{if } \Delta_2 < 0 \end{cases} \tag{B.9}$$

with $\Delta_{\max} = \varrho_{\max} - \varrho_k$, $\Delta_{\min} = \varrho_{\min} - \varrho_k$ and the index l looping over all the dual cell vertices. The values of $\varrho_{\max}/\varrho_{\min}$ are given by the maximum/minimum values of the three vertices corresponding to the lth dual cell vertex.

The dependence of the density gradient on the ith value of ϱ in the stencil of an upwind vertex follows the formulation in Eq. (B.6), for instance,

$$\frac{\partial\varrho_x}{\partial\varrho_i} = \frac{\partial C_1}{\partial\varrho_i} = a'_{21} + a'_{22}\,\Delta x_i + a'_{23}\,\Delta y_i, \tag{B.10}$$

with ϱ_x as the gradient component in the x–direction. Thus, for the Jacobian matrix contribution of the jth upwind vertex to the kth dual cell write

$$\begin{aligned} \frac{\partial\left(\mathcal{R}_\varrho\right)_k}{\partial\varrho_j^{\mathrm{up}}} &= -\nabla\Phi_j \cdot \boldsymbol{n}_j \frac{\Delta S_j}{V_k} \\ \frac{\partial\left(\mathcal{R}_\varrho\right)_k}{\partial\varrho_{ji}^{\mathrm{up}}} &= -\nabla\Phi_j \cdot \boldsymbol{n}_j \frac{\Delta S_j}{V_k}\,\psi_j^{\mathrm{up}} \left(\frac{\partial\varrho_{xj}^{\mathrm{up}}}{\partial\varrho_{ji}^{\mathrm{up}}}\,\Delta x_j + \frac{\partial\varrho_{yj}^{\mathrm{up}}}{\partial\varrho_{ji}^{\mathrm{up}}}\,\Delta y_j \right) \end{aligned} \tag{B.11}$$

where i runs over all elements of the upwind vertex stencil to edge j. The latter two contributions are added to the Jacobian matrix. For ease of use, the limiter is not dealt with explicitly in the Jacobian matrix but is kept fixed once the iterative solution is converged by some orders of magnitude.

Using a vertex–based reconstruction for the velocity components, the discretisation of the unsteady Bernoulli equation as given in Eq. (2.21) is straightforward. For each

control volume k, write

$$\frac{d\Phi_k}{dt} = \left(\mathcal{R}_\Phi\right)_k = \frac{1 - q_k^2}{2} - \frac{\varrho_k^{\gamma-1} - 1}{(\gamma - 1)\, M_r^2} \tag{B.12}$$

where $q_k = \left(\nabla\Phi_k \cdot \nabla\Phi_k\right)^{1/2}$ is the magnitude of the velocity vector reconstructed in the dual cell centre, ϱ_k is the solution of Eq. (B.2), and $\left(\mathcal{R}_\Phi\right)_k$ is referred to as the residual of the Bernoulli equation. The formulation of the Jacobian matrix terms follows the continuity equation,

$$\begin{aligned} \frac{\partial\left(\mathcal{R}_\Phi\right)_k}{\partial\varrho_k} &= -\frac{\varrho_k^{\gamma-2}}{M_r^2}, \\ \frac{\partial\left(\mathcal{R}_\Phi\right)_k}{\partial\Phi_{ki}} &= -u_{1k}\frac{\partial u_{1k}}{\partial\Phi_{ki}} - u_{2k}\frac{\partial u_{2k}}{\partial\Phi_{ki}}, \end{aligned} \tag{B.13}$$

with the index i running over the elements of the reconstruction stencil to the kth vertex.

The circulation convection equation of the wake model is discretised using a first order upwind scheme. Starting from the first vertex off the trailing edge gives for the kth vertex of the ordered wake system,

$$\frac{d\Gamma_k}{dt} = \left(\mathcal{R}_\Gamma\right)_k = -\frac{\Phi_k - \Phi_{k-1}}{\xi_k - \xi_{k-1}}\,\frac{\Gamma_k - \Gamma_{k-1}}{\xi_k - \xi_{k-1}}, \tag{B.14}$$

where ξ is defined along the wake cut. The streamwise derivative of the velocity potential is the average of upper and lower wake side. The value of Γ_{k-1} at the first station is set by the Kutta condition. The evaluation of the Jacobian matrix terms is straightforward, and this is not exercised again for reasons of brevity.

Starting from the stagnation point around the leading edge of the aerofoil two boundary layers (including the free wakes) develop, on the suction and pressure side. The integral boundary layer equations are discretised along the ordered edges of the solid surface and the wake cut forming the boundary layer system. To discretise the residuals, for instance the momentum equation in Eq. (2.26), write

$$\mathcal{R}_{\delta^*} = -u_e\left(\frac{\xi}{\theta}\frac{\partial\theta}{\partial\xi} + \left(H + 2 - M_e^2\right)\frac{\xi}{u_e}\frac{\partial u_e}{\partial\xi} - \frac{\xi}{\theta}\frac{C_f}{2}\right)\frac{\theta}{\xi}. \tag{B.15}$$

This allows logarithmic differentiation, for instance for the jth edge,

$$\frac{\xi}{\theta}\frac{\partial\theta}{\partial\xi} = \frac{\ln(\theta_j/\theta_{j-1})}{\ln(\xi_j/\xi_{j-1})}, \tag{B.16}$$

which is convenient especially at the first stations of the boundary layer system. At the stagnation point similar flow is assumed and the derivatives are set to their known values from similar boundary layer theory [87, 98]. All other quantities are taken or

evaluated at the current boundary layer station. To form the Jacobian matrix terms analytically, the closure correlations, for instance the skin friction coefficient C_f in Eq. (B.15), are differentiated with respect to the primary boundary layer unknowns as well as the unknowns of the other flow models.

As pointed out in [93], neither the inviscid nor the viscous equations constrain the unstable sawtooth mode (grid–to–grid oscillation) in the displacement thickness distribution in the vicinity of separation. A distinction between laminar and turbulent separation is irrelevant [167] in the discussion of this so–called Goldstein singularity [168]. This is a common problem and an artefact of the chosen discretisation causing an ill–conditioned system. A remedy suggested in [93] places local sources/sinks with strengths equal to the local wall blowing velocity between successive boundary layer locations. These sources/sinks provide the required perturbation Δu_e in the edge velocity to cure the problem.

Boundary Conditions

Boundary conditions are set using a layer of halo vertices (subscript h) on the outside of domain boundaries. The halo values provide the required behaviour on the boundary itself.

Freestream conditions for density and velocity potential at an individual boundary edge are enforced by setting the corresponding halo vertex h to freestream values. Therefore, write

$$\varrho_h = 1 \quad \text{and} \quad \Phi_h = x_h \cos\alpha + y_h \sin\alpha \tag{B.17}$$

where α is the freestream flow angle. This treatment assumes that the boundary is located far enough to allow the flow to return to far field conditions.

A transpiration boundary condition is used to set the flow tangency condition at solid surfaces. For unsteady simulations with moving surfaces, the so–called transpiration normal $\widetilde{\boldsymbol{n}}$ of the deflected geometry is applied at the original location which remains fixed at all times. Obviously, in the steady undeflected case, the transpiration normal is equal the geometric (original) normal $\widetilde{\boldsymbol{n}} = \boldsymbol{n}$. Thus, at an individual edge the boundary condition is implemented as

$$u_1 \widetilde{n}_x + u_2 \widetilde{n}_y = v_W + v_b \tag{B.18}$$

where $v_W = \dot{x}\widetilde{n}_x + \dot{y}\widetilde{n}_y$ is the normal wall velocity with the Cartesian wall velocity components $\dot{x}$ and $\dot{y}$. The wall normal blowing velocity v_b for the boundary layer coupling as given in Eq. (2.31) is evaluated by a first order backward difference along the boundary without dependence on halo values.

The stencil for the reconstruction of the velocity at a boundary edge includes three internal vertices (with two vertices on the boundary itself) plus the halo vertex. The

dependence on the halo vertex is isolated, for instance for the velocity component u_1,

$$\begin{aligned} u_1 = C_1 &= \left(a'_{21}\,\widetilde{b}_1 + a'_{22}\,\widetilde{b}_2 + a'_{23}\,\widetilde{b}_3\right) + \left(a'_{21} + a'_{22}\,\Delta x_h + a'_{23}\,\Delta y_h\right)\Phi_h \\ &= c_1 + d_1\,\Phi_h \end{aligned} \tag{B.19}$$

where $\widetilde{b}_n$ are the right–hand side terms in Eq. (B.4) reduced by the halo contribution. Then, rewrite Eq. (B.18) for the halo value of the velocity potential

$$\Phi_h = \frac{v_W + v_b - c_1\,\widetilde{n}_x - c_2\,\widetilde{n}_y}{d_1\,\widetilde{n}_x + d_2\,\widetilde{n}_y}. \tag{B.20}$$

The density is directly reconstructed at the halo vertex. Using the principle in Eq. (B.19) of isolating the halo contribution for the coefficient C_0, which is equivalent to the reconstructed density, the halo value becomes

$$\varrho_h = \frac{c_0}{1 - d_0}, \tag{B.21}$$

which is equivalent to a linear (first order) extrapolation.

At any boundary edge of the wake cut there are corresponding edges on the upper and lower wake side laying on top of each other with geometric normal $\boldsymbol{n}$ (thus being independent of the transpiration system). The two wake conditions, i.e. a jump in the velocity potential according to the circulation and a normal flux equal the jump due to boundary layer coupling, are written as

$$\begin{aligned} \Phi^u - \Phi^l &= -\Gamma \\ u_1^u\,n_x + u_2^u\,n_y - \left(u_1^l\,n_x + u_2^l\,n_y\right) &= \Delta v_b, \end{aligned} \tag{B.22}$$

where $\Delta v_b = v_b^u + v_b^l$ with the sign of the lower blowing velocity following from defining the normal velocity component positive upward. Using Eq. (B.19) to isolate the halo contributions from the left–hand side terms gives

$$\begin{pmatrix} d_0^u & -d_0^l \\ d_1^u\,n_x + d_2^u\,n_y & -d_1^l\,n_x - d_2^l\,n_y \end{pmatrix} \begin{pmatrix} \Phi_h^u \\ \Phi_h^l \end{pmatrix} = \begin{pmatrix} -\Gamma - c_0^u + c_0^l \\ \Delta v_b - \left(c_1^u - c_1^l\right) n_x - \left(c_2^u - c_2^l\right) n_y \end{pmatrix} \tag{B.23}$$

which is easily solved for Φ_h^u and Φ_h^l. Finally for the density, upper halo values are set to corresponding lower internal values and vice versa. This gives the required continuous density across the wake.

The Kutta condition is implemented by applying the solid surface boundary condition of the velocity potential to the first edge off the trailing edge on upper and lower wake side. This sets the direction of the flow to leave the trailing edge smoothly. The corresponding circulation defining the upstream boundary condition of the circulation convection model is simply the potential jump between the trailing edge vertices.

The various stencils for the reconstruction of the density and velocity values in the preceding discussion of the discretisation scheme can contain halo information. Thus, the dependence of halo vertices on interior vertices, using the product rule, is required to evaluate the Jacobian matrix correctly. Consider Eq. (B.20) for setting a halo vertex for an edge of the solid surface. Here, the halo vertex depends on interior values of the velocity potential,

$$\frac{\partial \Phi_h}{\partial \Phi_i} = \frac{-1}{d_1 \widetilde{n}_x + d_2 \widetilde{n}_y} \left(\frac{\partial c_1}{\partial \Phi_i} \widetilde{n}_x + \frac{\partial c_2}{\partial \Phi_i} \widetilde{n}_y \right), \tag{B.24}$$

where i runs over all the elements in the stencil excluding the halo vertex itself. Also, the blowing velocity v_b at edge j is dependent on the velocity potential, density and displacement thickness,

$$\begin{aligned} \frac{\partial \Phi_h}{\partial \Phi_i} &= \frac{\partial \Phi_h}{\partial v_b} \frac{\partial v_b}{\partial \Phi_i}, & \frac{\partial \Phi_h}{\partial \varrho_i} &= \frac{\partial \Phi_h}{\partial v_b} \frac{\partial v_b}{\partial \varrho_i}, \\ \frac{\partial \Phi_h}{\partial \delta_j^*} &= \frac{\partial \Phi_h}{\partial v_b} \frac{\partial v_b}{\partial \delta_j^*}, & \frac{\partial \Phi_h}{\partial \delta_{j-1}^*} &= \frac{\partial \Phi_h}{\partial v_b} \frac{\partial v_b}{\partial \delta_{j-1}^*}. \end{aligned} \tag{B.25}$$

Here, the index i loops the three vertices of edge j and its upstream edge $j-1$. The blowing velocity v_b, the wall normal velocity v_W and the transpiration normal $\widetilde{\boldsymbol{n}}$ depend on the structural solution (here represented by the pitch angle α),

$$\frac{\partial \Phi_h}{\partial \alpha} = \frac{\partial \Phi_h}{\partial v_W} \frac{\partial v_W}{\partial \alpha} + \frac{\partial \Phi_h}{\partial v_b} \frac{\partial v_b}{\partial \alpha} + \frac{\partial \Phi_h}{\partial \widetilde{n}_x} \frac{\partial \widetilde{n}_x}{\partial \alpha} + \frac{\partial \Phi_h}{\partial \widetilde{n}_y} \frac{\partial \widetilde{n}_y}{\partial \alpha}. \tag{B.26}$$

The dependencies for the other boundary conditions follow accordingly.

Remarks on Coupled Inviscid/Viscous Flow Solver

Several schemes to couple an outer inviscid flow solver with an inner integral boundary layer solver have been discussed in the literature [61,169]. These include direct, inverse, semi–inverse, quasi–simultaneous, and fully–simultaneous coupling. In the classical direct approach the viscous solver uses the inviscid solution to calculate the boundary layer and wake, particularly the displacement thickness. The displacing effect of the viscous layer is then imposed on the outer flow. This hierarchical iterative procedure continues until convergence of both the inviscid and viscous solutions is achieved. Besides the slow convergence especially for strongly interacting flows in the sub- and transonic regime, the method becomes unstable when separation is encountered. The semi–inverse coupling defines a suitable scheme for separated flow. Here, the hierarchy of the viscous solver is inverted to have the pressure distribution calculated from a given displacement thickness which is updated, for instance, by comparing inviscid and viscous pressure distributions using the relaxation scheme presented in [170].

Dropping the hierarchical order of inviscid and viscous flow as well as the space–marching boundary layer calculations at each iteration, opens the way to the simultaneous schemes. While the quasi–simultaneous approach solves a simplified formulation for either flow model together with a complete formulation of the other model simultaneously, the fully–simultaneous coupling does not require any approximate and simplified interaction laws by solving both sets of equations simultaneously. As pointed out in [61], fully–simultaneous coupling has essentially a Newton structure with the inviscid, the viscous as well as the mixed sensitivities and boundary layer dependencies included in a fully–coupled global Jacobian matrix. Fully–simultaneous coupling is the natural choice due to its robustness and convergence characteristics. In addition, the Jacobian matrix of the coupled fluid solution is straightforwardly used in the methods discussed herein. More details about the various coupling schemes can be found in the cited literature.

Appendix C

Typical Section Aerofoil

The "typical section" aerofoil model with oscillating pitching and plunging motion represents the torsional and bending behaviour of a wing structure. It is a realistic model for a wing with a high aspect ratio and low sweep angle. The two degrees–of–freedom model is generally idealised as a point mass defining the centre of gravity (cg), as well as a torsional and a translational spring attached to the elastic centre (ec) located the dimensionless distance $x_\alpha/2$ from the centre of gravity, where x_α is measured in semichords and negative for an elastic centre ahead of the centre of gravity. The aerofoil structural model is illustrated in Fig. 5.1.

Conveniently, the equations of motion are derived through Lagrange's equation,

$$\frac{d}{dt}\left(\frac{\partial L}{\partial \dot{\eta}_j}\right) - \frac{\partial L}{\partial \eta_j} = \frac{\partial W}{\partial \eta_j}\,, \tag{C.1}$$

where the Lagrangian L is defined as the difference between the kinetic energy E_K and potential energy E_P of the system. The expression W is the work done by the generalised forces acting on the system and η_j are the generalised independent variables of plunge h and pitch α.

The potential energy of the two degrees–of–freedom system expressed in dimensionless notation is given by

$$E_P = \frac{1}{2}\,\omega_h^2\,h^2 + \frac{1}{8}\,r_\alpha^2\,\omega_\alpha^2\,\alpha^2, \tag{C.2}$$

where ω_h and ω_α are the natural frequencies of the uncoupled plunging and pitching motion, respectively, and r_α is the radius of gyration about the elastic centre as a nondimensional parameter for the moment of inertia. The dimensionless form is found throughout using the chord length and mass of the aerofoil as well as freestream values of the density and velocity as reference values.

The dimensionless kinetic energy is generally written as

$$E_K = \frac{1}{2}\,\boldsymbol{v}_{cg}\cdot\boldsymbol{v}_{cg} + \frac{1}{8}\,r_{cg}^2\,\dot{\alpha}^2, \tag{C.3}$$

where r_{cg} is the radius of gyration about the centre of gravity and $\boldsymbol{v}_{cg}$ is the velocity of the aerofoil at the centre of gravity given by,

$$\boldsymbol{v}_{cg} = -\begin{pmatrix} 0 \\ 0 \\ \dot{\alpha} \end{pmatrix} \times \begin{pmatrix} -\frac{x_\alpha}{2}\cos\alpha \\ \frac{x_\alpha}{2}\sin\alpha \\ 0 \end{pmatrix} + \begin{pmatrix} 0 \\ \dot{h} \\ 0 \end{pmatrix} \tag{C.4}$$

Using the expression $r_\alpha^2 = r_{cg}^2 + x_\alpha^2$, the kinetic energy follows as

$$E_K = \frac{1}{2}\,\dot{h} + \frac{1}{4}\,x_\alpha\,\cos\alpha\,\dot{\alpha}\,\dot{h} + \frac{1}{8}\,r_\alpha^2\,\dot{\alpha}^2. \tag{C.5}$$

The work W done by aerodynamic loads and damping forces is given in nondimensional notation as

$$W = \left(\frac{2}{\mu_s \pi}\,C_l - 2\,\zeta_h \frac{2\,\omega_r}{\bar{u}}\,\dot{h}\right) h + \left(\frac{2}{\mu_s \pi}\,C_m - \zeta_\alpha \frac{r_\alpha^2}{\bar{u}}\,\dot{\alpha}\right) \alpha, \tag{C.6}$$

where C_l and C_m are the lift and moment coefficients, respectively, μ_s is the aerofoil–to–fluid mass ratio, and $\omega_r = \omega_h/\omega_\alpha$ is the ratio of natural frequencies. The dimensionless parameter ζ_h and ζ_α are the structural damping ratios.

Substituting the expressions of the potential and kinetic energy as well as the work in Lagrange's equation gives the desired equations of motion of the two degrees–of–freedom system,

$$\begin{aligned} \ddot{h} + \frac{x_\alpha}{2}\cos\alpha\,\ddot{\alpha} - \frac{x_\alpha}{2}\sin\alpha\,\dot{\alpha}^2 + 2\,\zeta_h \frac{2\,\omega_r}{\bar{u}}\,\dot{h} + \frac{4\,\omega_r}{\bar{u}^2}\,h &= \frac{2}{\mu_s \pi}\,C_l \\ x_\alpha\cos\alpha\,\ddot{h} + \frac{r_\alpha^2}{2}\,\ddot{\alpha} + 2\,\zeta_\alpha \frac{r_\alpha^2}{\bar{u}}\,\dot{\alpha} + \frac{2\,r_\alpha^2}{\bar{u}^2}\,\alpha &= \frac{4}{\mu_s \pi}\,C_m, \end{aligned} \tag{C.7}$$

with $\bar{u} = 2/\omega_\alpha$ as the dimensionless reduced velocity. This is a coupled, nonlinear system of second order ordinary differential equations in time which linearises to

$$\begin{aligned} \ddot{h} + \frac{x_\alpha}{2}\,\ddot{\alpha} + 2\,\zeta_h \frac{2\,\omega_r}{\bar{u}}\,\dot{h} + \frac{4\,\omega_r}{\bar{u}^2}\,h &= \frac{2}{\mu_s \pi}\,C_l \\ x_\alpha\,\ddot{h} + \frac{r_\alpha^2}{2}\,\ddot{\alpha} + 2\,\zeta_\alpha \frac{r_\alpha^2}{\bar{u}}\,\dot{\alpha} + \frac{2\,r_\alpha^2}{\bar{u}^2}\,\alpha &= \frac{4}{\mu_s \pi}\,C_m, \end{aligned} \tag{C.8}$$

assuming small angles in the pitching motion, i.e. $\sin\alpha \approx \alpha$, $\cos\alpha \approx 1$ and $\dot{\alpha}\alpha \approx 0$. In compact notation write

$$M\,\ddot{\boldsymbol{\eta}} + C\,\dot{\boldsymbol{\eta}} + K\,\boldsymbol{\eta} = \boldsymbol{f}, \tag{C.9}$$

with $\boldsymbol{\eta} = [h, \alpha]^T$ containing the unknowns (generalised coordinates) and

$$\boldsymbol{f} = \frac{1}{\mu_s \pi}\,[2\,C_l,\ 4\,C_m]^T \tag{C.10}$$

as the vector of integrated aerodynamic forces. The matrices given by,

$$M = \begin{pmatrix} 1 & \frac{x_\alpha}{2} \\ x_\alpha & \frac{r_\alpha^2}{2} \end{pmatrix}, \quad C = \begin{pmatrix} 2\,\zeta_h \frac{2\,\omega_r}{\bar{u}} & 0 \\ 0 & 2\,\zeta_\alpha \frac{r_\alpha^2}{\bar{u}} \end{pmatrix}, \quad K = \begin{pmatrix} \frac{4\,\omega_r^2}{\bar{u}^2} & 0 \\ 0 & \frac{2\,r_\alpha^2}{\bar{u}^2} \end{pmatrix}, \tag{C.11}$$

are the matrices of mass, damping and stiffness, respectively.

Estimation of Natural Frequencies

The natural coupled frequencies of the two degrees–of–freedom system are found from the system given in Eq. (C.9) neglecting aerodynamic loads and structural damping. A general solution of $\boldsymbol{\eta}$ for the homogeneous (wind–off) system is assumed to be a complex–valued exponential function in time, represented by $\boldsymbol{\eta} = \boldsymbol{p}_\eta\, e^{\lambda\tau}$, and thus,

$$\left(\lambda^2 I + M^{-1}K\right) \boldsymbol{p}_\eta\, e^{\lambda\tau} = 0\,, \tag{C.12}$$

with I as the identity matrix. For a nontrivial solution to exist, the determinant of the coefficient matrix must be equal to zero,

$$\left|\lambda^2 I + M^{-1}K\right| = 0. \tag{C.13}$$

A system with n degrees–of–freedom has n natural frequencies. Expansion of the determinant gives a polynomial equation of order $2n$ in λ. The $2n$ roots of the polynomial characterise the system's n complex conjugate eigenvalues $\lambda_j = \sigma_j \pm i\omega_j$, the imaginary parts of which are related to the circular frequency. This gives for the two degrees–of–freedom system,

$$\lambda_{1,2} = \pm i\,\omega_{1,2} = \pm i \left(\frac{1}{\bar{u}^2 \det M} \left(r_\alpha^2 \left(\omega_r^2 + 1\right) \pm \sqrt{r_\alpha^4 \left(\omega_r^2 - 1\right)^2 + 4\,\omega_r^2\, x_\alpha^2\, r_\alpha^2} \right) \right)^{1/2} \tag{C.14}$$

which are purely imaginary eigenvalues without modal damping. The frequencies, i.e. the imaginary parts, are ordered in ascending order. The lower frequency ω_1 typically refers to a dominant bending motion, whereas the second frequency ω_2 describes a dominant torsion motion.

The coupling of the homogeneous system arises from the inertia terms due to the static unbalance x_α. The uncoupled natural frequencies of the aerofoil model are

$$\omega_h = \frac{2}{\bar{u}}\,\omega_r \quad \text{and} \quad \omega_\alpha = \frac{2}{\bar{u}}, \tag{C.15}$$

which can easily be seen.